UNIVERSIDAD DE CHILE
FACULTAD DE CIENCIAS FÍSICAS Y MATEMÁTICAS
DEPARTAMENTO DE GEOLOGÍA

SEÑALES SÍSMICAS LENTAS EN EL MARGEN CHILENO

TESIS PARA OPTAR AL GRADO DE DOCTOR EN CIENCIAS, MENCIÓN GEOLOGÍA

MIGUEL ANTONIO SÁEZ ARIAS

PROFESOR GUÍA:

SERGIO RUIZ TAPIA

MIEMBROS DE LA COMISIÓN:

GABRIEL EASTON VARGAS

JUAN CARLOS BÁEZ SOTO

ANDRÉS TASSARA ODDO

Este trabajo ha sido financiado por

CONICYT-PCHA/Doctorado Nacional/2017 – 21171480

SANTIAGO DE CHILE

2024

RESUMEN

En las últimas dos décadas, el desarrollo y densificación de instrumentos sísmicos de alta precisión a nivel mundial han permitido entender que la energía sísmica puede liberarse en diversas escalas temporales a través de complejos procesos de ruptura conocidos como terremotos. Dependiendo de su duración, los terremotos se clasifican como ordinarios (T.O.) o lentos (T.L.). Los T.O. se caracterizan por rupturas repentinas, duraciones máximas de hasta un par de minutos y la emisión de ondas sísmicas de alta frecuencia. Por otro lado, los T.L. corresponden a rupturas graduales que pueden prolongarse desde varias decenas de minutos hasta años, produciendo ondas sísmicas de baja frecuencia y pequeña amplitud, difíciles de detectar. En la actualidad, se ha logrado identificar en diversos ambientes tectónicos una amplia variedad de manifestaciones de tipo sísmicas y geodésicas asociadas a T.L. Debido a la relación espacial y temporal observada con los T.O. de gran magnitud, el estudio de los T.L. se ha convertido en uno de los tópicos más importantes de la sismología a nivel mundial.

En esta investigación, nos centramos en la búsqueda, caracterización y localización de señales sísmicas lentas a lo largo del margen chileno, utilizando datos recopilados por redes sísmicas desplegadas en la región de Atacama, frente a las costas de Pichilemu, sobre el punto triple chileno y a lo largo de la porción centro-sur del sistema de fallas Liquiñe-Ofqui. El análisis de los datos permitió detectar la ocurrencia de señales sísmicas lentas en todas las redes analizadas. En particular, tremores superficiales de origen tectónico fueron detectados frente a las costas de Pichilemu y sobre el punto triple chileno, mientras que, terremotos repetitivos fueron identificados en el sistema de fallas Liquiñe-Ofqui, en la región de Atacama y sobre el punto triple chileno.

Las observaciones realizadas muestran que las señales sísmicas lentas chilenas se desarrollan tanto en la parte superficial como profunda del contacto. Sus características son similares a las observadas en otras zonas del mundo y la presencia de fluidos es un factor de primer orden para su generación. Además, rasgos geomorfológicos que facilitan el movimiento de fluidos o alteren las propiedades friccionantes de los materiales (ej: subducción de ridge, montes submarinos, etc) también juegan un papel crucial en la generación de estas señales.

DEDICATORIA

“*A todas aquellas personas que han sufrido o perdido a un ser querido por la ocurrencia de terremotos”*

AGRADECIMIENTOS

Es difícil resumir en una página, la gratitud que siento al finalizar esta linda y extensa etapa, la cual duró ~7 años. Comienzo agradeciendo a mi familia, por ser el pilar fundamental de todo este camino, quienes estuvieron en las buenas y en las malas. Mamá, papá y hermana, gracias por el apoyo incondicional durante todos estos años, por estar conmigo en los momentos más tristes y felices. Agradecimiento especial a mi madre, quién ha hecho de mí y mi hermana dos profesionales a punta de esfuerzo, gracias por creer en nosotros, por entregar tu vida y felicidad es post de la nuestra, gracias por demostrarme que el amor desinteresado y genuino existe.

Gracias a mis amigos de la universidad y la vida, en especial a aquellos que me han acompañado en largas jornadas de estudio y diversión: Rogelio, Leoncio, Franz, Panchito Pastén, Javier, Kellen, Efra, Christian Flores, y tantos otros. Mención especial a Rogelio y Leoncio, con quienes tuve la oportunidad de formar una amistad más allá de lo académico, y con quienes he podido compartir grandes momentos de mi vida.

Gracias a los profesores que formaron parte de esta comisión: Gabriel Easton, Juan Carlos Báez y Andrés Tassara. Un agradecimiento especial al profesor Sergio Ruiz, quien fue el guía de este trabajo y demuestra con su ejemplo, que un gran científico también puede ser una gran persona.

Gracias a todas aquellas personas que de alguna u otra manera han formado parte de este camino, y han contribuido a mi crecimiento personal y académico. Perdón por no poder nombrarlas a todas.

A la Comisión Nacional de Investigación Científica y Tecnológica (CONICYT) por financiar este trabajo mediante CONICYT-PCHA/Doctorado Nacional/2017 – 21171480.

Finalmente, quiero agradecer a mi mujer Luz y mi hijo Alonso, a quienes dedico este trabajo. Gran parte de este logro se los debo a ellos, tanto por la motivación, así como también por el apoyo. A mi mujer, gracias por toda la compresión, la incondicionalidad, la solidaridad y el amor brindado durante todo este proceso. Gracias por ser la madre y mujer que eres. A mi hijo, gracias por tu inocencia, por tus risas infinitas y por mostrarme que el amor en la vida tiene distintas formas, y tú eres la más grande. Espero que en un

tiempo puedas leer estás páginas y sepas que fuiste el motor de este trabajo, y ojalá te inspire a dejar un grano de arena en este mundo.

Gracias a la vida, por darme la oportunidad de vivir este proceso, de caer, aprender y mejorar.

Tabla de Contenido

Índice de Figuras

1 Introducción

La actividad sísmica a lo largo del margen chileno está controlada principalmente por la subducción de la placa de Nazca bajo la placa Sudamericana a una razón de 6.8 cm/año (Vigny et al., 2009). Esta alta tasa de convergencia es la responsable de que la subducción chilena sea uno de los entornos tectónicos más activos sísmicamente a nivel mundial. Grandes y destructivos terremotos de tipo interplaca (M_w >8.0) azotan a las costas chilenas en promedio una vez cada 10 años (Ruiz & Madariaga, 2018). En la última década, tres grandes terremotos han ocurrido en el margen chileno: Maule 2010 M_w 8.8 (Moreno et al., 2010), Iquique 2014 M_w 8.1 (Ruiz et al., 2014) e Illapel 2015 M_w 8.3 (Tilmann et al., 2016). La densificación de redes sísmicas multiparamétricas a lo largo del territorio nacional, compuestas por estaciones GPS y sismómetros-acelerómetros, ha permitido observar que en ocasiones algunos de estos grandes terremotos son precedidos por un complejo proceso de nucleación.

El terremoto de Iquique M_w 8.1 ocurrido el año 2014, es un ejemplo claro de lo señalado anteriormente. Este evento tuvo un largo de ruptura de ~150 km aproximadamente y rompió una zona que no era afectada por un gran terremoto desde el año 1877 (Métois et al., 2016). El uso de estaciones GPS desplegadas en las costas chilenas permitió observar que el terremoto de Iquique fue precedido por un deslizamiento lento, el cual comenzó ocho meses antes del evento principal (Socquet et al., 2017) y tuvo su mayor expresión 14 días antes de dicho evento (Ruiz et al., 2014).

En la Figura 1-1b se presentan los deslizamientos registrados por algunas estaciones GPS cercanas a la zona de ruptura del terremoto de Iquique. En dicha figura, se observa que a partir del día 16 de marzo del año 2014, la estación Pisagua (PSGA) inicia un deslizamiento hacia el oeste con una tendencia similar a la que generaría en dicha estación un terremoto ordinario. La particularidad de esta señal es que evidencia un deslizamiento total para la estación PSGA cercano a los 15 mm en un periodo de 14 días. Esta observación anómala, corresponde al primer registro de un deslizamiento lento en el territorio nacional (Ruiz et al., 2014). Este fenómeno, recibe el apellido de lento, debido a que la señal registrada se desarrolla en un tiempo considerablemente mayor en comparación con un terremoto ordinario de similar magnitud.

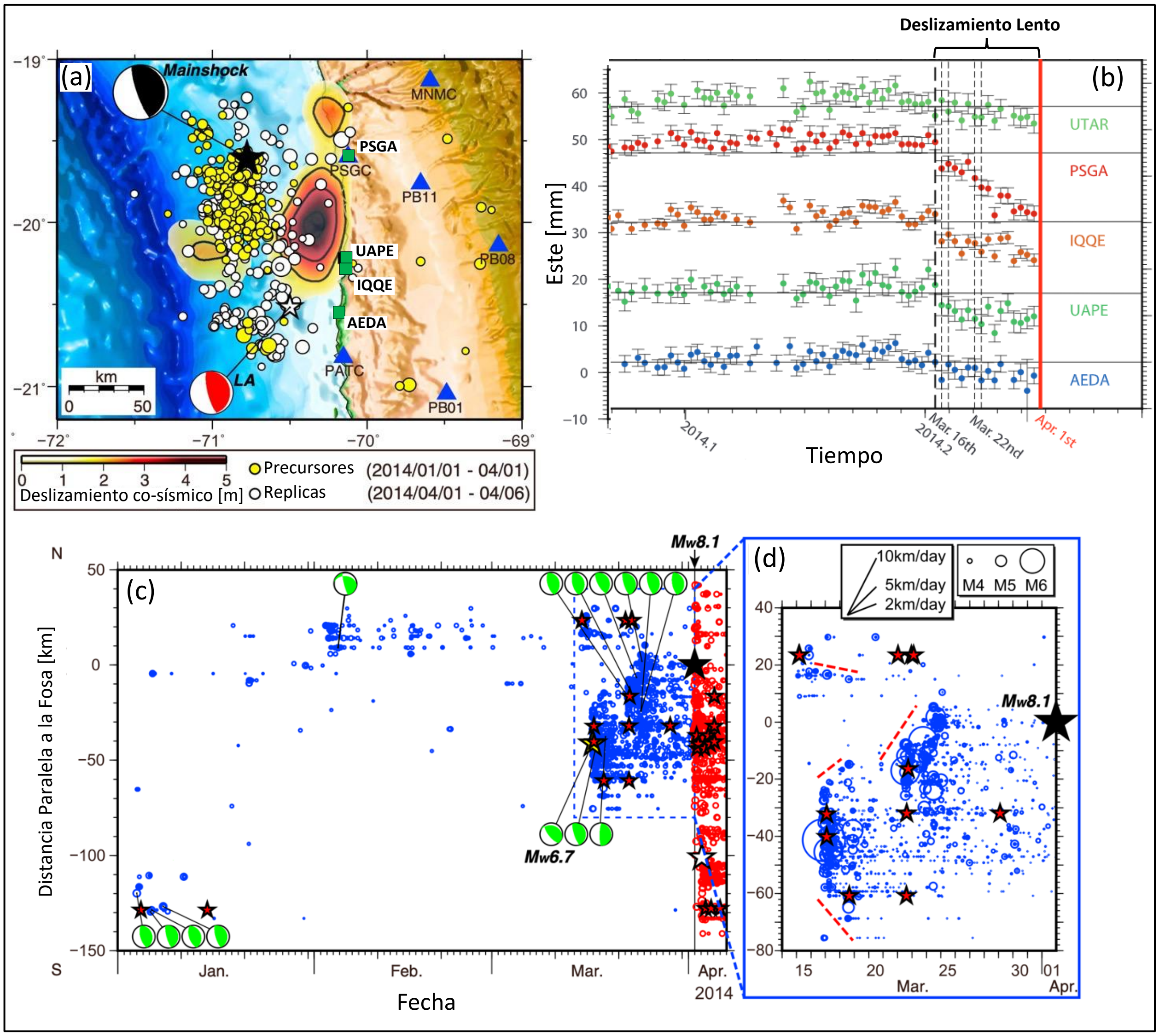

Figura 1-1: Terremoto de Iquique 2014 Mw 8.1. (a) Distribución de deslizamiento de la ruptura principal, epicentros asociados a la sismicidad precursora (círculos amarillos) y replicas (círculos blancos). Con cuadrados verdes se representan las estaciones GPS, mientras que, con triángulos azules se indican estaciones sísmicas. (b) Señales geodésicas registradas por estaciones GPS. (c) Distribución temporal de la sismicidad precursora y réplicas del terremoto de Iquique y (d) zoom periodo comprendido entre 13 de marzo y el 01 de abril del 2014, con estrellas rojas se presentan los terremotos repetitivos. Modificado de Kato & Nakagawa (2014) y Ruiz et al. (2014).

La señal geodésica lenta observada durante el terremoto de Iquique estuvo acompañada por un aumento y migración de la sismicidad precursora además de la presencia de enjambres y terremotos repetitivos (Figura 1-1c y Figura 1-1d), estos últimos interpretados como rupturas repetitivas dentro de una falla (Kato & Nakagawa, 2014). Las manifestaciones sísmicas y geodésicas detalladas anteriormente dan cuenta de que el terremoto de Iquique fue precedido por la ocurrencia de un terremoto lento, el cual estresó la zona donde el 16 del marzo del 2014 rompe el precursor principal M_w 6.7 para finalmente gatillar el 01 de abril el evento principal (Ruiz et al., 2014; Socquet et al., 2017).

Señales lentas o también denominados terremotos lentos (T.L.), por su duración en comparación a terremotos ordinarios de similar magnitud, han sido observadas en distintas etapas del ciclo sísmico (Brodsky & Mori, 2007). En particular, deslizamientos lentos han sido identificados previo a la ruptura principal de grandes terremotos: Tohoku-Oki 2011 M_w 9.0 (Kato et al., 2012), Papanoa 2014 M_w 7.3 (Radiguet et al., 2016) y Valparaíso 2017 M_w 6.9 (Ruiz et al., 2017). Debido a la relación espacial y temporal observada con los terremotos ordinarios de gran magnitud (Obara & Kato, 2016), el estudio de los terremotos lentos se ha convertido en uno de los tópicos más importantes de la sismología a nivel mundial (Nishikawa et al., 2023).

En las últimas dos décadas, se han observado manifestaciones sísmicas y geodésicas lentas en múltiples ambientes tectónicos, incluyendo zonas de subducción ubicadas alrededor del Cinturón de Fuego del Pacífico. Ejemplos notables de estas manifestaciones se encuentran en Japón (Nishikawa et al., 2023), Cascadia (Dragert et al., 2001), Costa Rica (Walter et al., 2013), México (Rousset et al., 2017), Chile (Gallego et al., 2013), Nueva Zelanda (Romanet & Ide, 2019), y Alaska (Rousset et al., 2019). Además, estas manifestaciones también se han detectado en fallas transformantes como San Andreas (Nadeau & Dolenc, 2005) y en zonas de colisión entre continentes, como la cordillera central de Taiwán (Peng & Chao, 2008).

A pesar de que Chile experimenta una de las tasas de actividad sísmica más altas del mundo, manifestaciones asociadas a T.L. a lo largo del país han sido escasamente estudiadas. En esta investigación, nos enfocamos en la detección, caracterización y localización de señales sísmicas lentas a lo largo del margen chileno. Para ello, empleamos datos recopilados por redes sísmicas desplegadas en el fondo del mar (OBS) y sismómetros de banda ancha instalados en tierra.

1.1 Hipótesis de Trabajo

En el margen de subducción chileno ocurren distintas manifestaciones sísmicas asociadas a terremotos lentos cuya distribución y características están influenciada por la geología, estructura tectónica y las condiciones locales a lo largo del margen.

1.2 Objetivo General

Buscar, localizar y caracterizar señales sísmicas lentas y ordinarias-lentas a lo largo del margen chileno, utilizando para ello estaciones sísmicas desplegadas en el fondo del mar (OBS) y en tierra (estaciones banda ancha y acelerómetros).

1.3 Objetivos Específicos

- Desarrollar e implementar metodologías computacionales para el procesamiento de grandes volúmenes de datos y detección de señales sísmicas ordinarias y lentas.
- Caracterizar las propiedades dinámicas y espacio-temporales de las señales lentas identificadas, incluyendo su tamaño, profundidad, frecuencia y patrones de ocurrencia.
- Investigar la relación entre las manifestaciones de terremotos lentos, la sismicidad ordinaria y la actividad tectónica a lo largo del margen chileno.

2 Terremotos Lentos

Hasta hace unos pocos años se pensaba que las fallas podían liberar el estrés acumulado a partir de un deslizamiento continuo asísmico (sin emisión de ondas sísmicas) o a través de una ruptura instantánea (terremotos ordinarios). El despliegue y densificación de redes sismológicas compuestas por estaciones GPS y sismómetros-acelerómetros desplegados tanto en tierra como en el fondo marino, han permitido comprender que el deslizamiento de una falla es mucho más complejo, abarcando un amplio rango de escalas temporales y espaciales.

Cuando el deslizamiento en una falla es lo suficientemente rápido, las fuerzas dinámicas predominan y ondas sísmicas de alta frecuencia son emanadas. La energía generada por este proceso es suficiente para vencer las fuerzas friccionales que mantienen a la falla bloqueada (Brodsky & Mori, 2007), generando como resultado un gran deslizamiento en un corto periodo de tiempo. Este proceso es lo que conocemos como ruptura dinámica o terremoto ordinario.

Mientras la ocurrencia de terremotos ordinarios se relaciona con velocidades de deslizamiento que oscilan generalmente entre 10^{-4} y 1 m/s (Bürgmann, 2018) y duraciones totales que varían entre un par de segundos hasta un par de minutos dependiendo de la magnitud del terremoto, las fallas también son capaces de liberar la energía almacenada de forma gradual y lenta, en eventos denominados terremotos lentos, los cuales pueden durar desde decenas de minutos hasta un par de años (Obara, 2020).

Debido a su baja velocidad de ruptura, los terremotos lentos no son capaces de alcanzar las condiciones dinámicas para producir ondas sísmicas de alta frecuencia, por el contrario, son procesos tan lentos, que generan ondas sísmicas ricas en contenidos de baja frecuencia y de pequeña amplitud, las que generalmente son muy difíciles de observar en sismogramas (Peng & Gomberg, 2010). A pesar de lo anterior, y gracias al desarrollo de instrumentos sismológicos de alta sensibilidad, en los últimos años ha sido posible identificar una rica variedad de manifestaciones sísmicas y geodésicas asociadas con la ocurrencia de terremotos lentos.

A continuación, se presenta un resumen de las señales sísmicas y geodésicas lentas identificadas hasta la fecha, junto con sus principales características.

2.1 Tipos de Terremotos Lentos

Existen diferentes manifestaciones (señales) asociadas con la ocurrencia de terremotos lentos, las cuales pueden ser divididas según su duración y forma de observación en señales sísmicas o geodésicas. Ambas señales reciben el apellido de “lento” debido a que su duración es superior a la de un terremoto ordinario de similar magnitud. En este sentido, es importante destacar que todas las características asociadas a los terremotos lentos se basan en una comparación respecto de las propiedades de terremotos ordinarios. A continuación, se describen las principales características de cada una de las manifestaciones lentas.

2.1.1 Señales Sísmicas

Las señales sísmicas lentas se caracterizan por duraciones que varían desde unos segundos hasta un par de minutos, y pueden ser observadas a partir de la traza sísmica registrada por estaciones sismológicas desplegadas tanto en tierra como en el fondo marino. Hasta la fecha, tres señales lentas de tipo sísmica han sido identificadas en distintos ambientes tectónicos. Las señales sísmicas detectables a partir de sismómetros de alta sensibilidad corresponden a terremotos de baja frecuencia o low-frequecy earthquakes (LFE), terremotos de muy baja frecuencia o very low frequency earthquakes (VLFE) y tremores no-volcánicos o non-volcanic tremor (NVT). A continuación, se describen las señales sísmicas lentas.

2.1.1.1 Terremotos de Baja Frecuencia (LFE)

Los terremotos de baja frecuencia fueron detectados por primera vez en la fosa de Nankai en Japón a 30-40 km de profundidad (Katsumata & Kamaya, 2003; Nishide et al., 2000).

Los analistas de la agencia meteorológica de Japón (JMA) descubrieron eventos de baja amplitud, que no poseían un arribo claro de la onda P, pero sí de la onda S. Estos eventos, parecidos al "ruido sísmico", mostraban arribos consistentes en distintas estaciones sísmicas, pero su contenido de frecuencia era claramente inferior al de terremotos ordinarios de similar magnitud, por lo que recibieron el nombre de terremotos de baja frecuencia o Low Frequency Earthquakes (LFE) (Beroza & Ide, 2011).

Los LFE corresponden a una de las manifestaciones sísmicas de terremotos lentos, poseen magnitudes aproximadas de M_w 1.5, duración de la fuente ~0.3 s, un contenido de frecuencia predominante entre 1-10 Hz (Obara, 2020) y son generados a partir de fallas por cortes (Ide et al., 2007). En la Figura 2-1b se ilustra la traza generada por un LFE.

2.1.1.2 Tremores No-Volcánicos (NVT)

Los tremores no-volcánicos o tremores de origen tectónico (NVT) fueron descubiertos, al igual que los LFE, en la zona de subducción de Nankai (Obara, 2002). Los NVT son señales débiles, no impulsivas, de baja amplitud y persistentes en el tiempo, con duraciones de decenas de segundos. El contenido de frecuencia predominante de los NVT es de 1 a 10 [Hz]. En la Figura 2-1b se presenta un sismograma característico de un NVT. Al igual que los LFE, los NVT fueron descubierto en la parte profunda del contacto interplaca (30-40 km) bajo la zona donde ocurren los grandes terremotos en Japón.

Dos familias de NVT han sido detectadas hasta el momento. La primera familia se localiza bajo la zona sismogénica, donde se generan deformaciones por corte asociadas al contacto entre placas, mientras que, la segunda familia se relaciona a deformaciones producidas en el prisma de acreción (Obana & Kodaira, 2009; Obara, 2020), razón por la cual reciben el nombre de NVT superficiales. Para ambas familias, se ha identificado que su actividad puede ser gatillada por el paso de ondas superficiales generadas por terremotos lejanos (Chao et al., 2019; Wallace et al., 2017), así como también, por cambios en el nivel de las mareas (Rubinstein et al., 2008), siendo los NVT superficiales los más sensibles a estos cambios de esfuerzo. Lo anterior, sustenta la idea de que los NVT se producen en fallas lo suficientemente estresadas para que pequeñas variaciones de esfuerzos generen su ruptura (Gallego et al., 2013).

Utilizando técnicas de correlaciones cruzadas, diversos autores han mostrados que los NVT corresponden a enjambres de LFE (Shelly et al., 2006, 2007; Tang et al., 2010).

2.1.1.3 Terremotos de Muy Baja Frecuencia (VLFE)

Los terremotos de muy baja frecuencia o very low-frequency earthquakes (VLFE) fueron descubiertos en la zona superficial de la subducción de Nankai, Japón (Ishihara, 2003). Estas señales sísmicas están caracterizadas por un contenido de energía rico en bajas frecuencias, con periodos en torno 10-100 [s], magnitudes que varían entre M_W 3-4, y un escaso o nulo contenido de alta frecuencia (Nishikawa et al., 2023; Obara & Ito, 2005). Los mecanismos focales estimados para los VLFE son consistentes con fallas por corte producidos por el contacto entre placas (Obara, 2020). En la Figura 2-1c se presenta un sismograma asociado a la ocurrencia de un VLFE.

Al igual que los NVT, se han identificado dos familias de VLFE. La primera familia detectada en la parte profunda del contacto entre placas, bajo la zona donde se producen los grandes terremotos interplaca, mientras que, la segunda familia se identifica en el prisma de acreción, producto de la deformación de este último (Obara & Ito, 2005).

Diversos autores han mostrado que los VLFE ocurren simultáneamente con los NVT y LFE, evidenciando una correlación temporal y espacial entre las distintas manifestaciones sísmicas lentas (Y. Ito et al., 2007; Masuda et al., 2020).

2.1.2 Señales Geodésicas

Los deslizamientos lentos o slow slip event (SSE) corresponden a deslizamientos transientes a lo largo de un plano de falla, lo suficientemente lento como para no generar ondas sísmicas, por lo tanto, pueden ser observados solo a través de señales geodésicas

(Obara, 2002). En general, estos eventos involucran deslizamiento que varían desde unos pocos milímetros hasta decenas de centímetros en periodos de tiempos que oscilan entre días a años (Wallace, 2020). Los SSEs fueron descubiertos en la zona de subducción de Cascadia el año 2001, utilizando para ello, redes regionales de GPS (Dragert et al., 2001). Hasta la fecha, dos señales lentas de tipo geodésicas han sido identificadas, las cuales, pueden ser clasificadas según su duración en deslizamientos de corta duración o short-term SSEs (STSSE) y deslizamientos lentos de larga duración o long-term SSEs (LTSSE). Deslizamientos lentos han sido observados en distintos ambientes tectónicos, siendo las zonas de subducción los entornos donde se han identificado una mayor cantidad de estas señales. A continuación, se presenta una breve descripción de cada señal.

2.1.2.1 Deslizamientos Lentos de Corta Duración (STSSE)

Los SSEs de corta duración o short term slow slip event (STSSE) corresponden a deslizamientos por corte que pueden durar desde unos pocos días hasta un mes (Nishikawa et al., 2023) y han sido identificado tanto en la parte superficial del contacto interplaca (Perez-Silva et al., 2022; Wallace, 2020), así como también, en la zona profunda del contacto entre placa, bajo la zona sismogénica (Khoshmanesh et al., 2020; Wallace & Eberhart-Phillips, 2013). Los deslizamientos reportados para los STSSE varían desde milímetros hasta un par de centímetros con magnitudes de momento generalmente menores a M_w 7.0 (Nishikawa et al., 2023). En la Figura 2-1e se presenta la deformación generada por un STSSE y registrada por un inclinómetro.

2.1.2.2 Deslizamientos Lentos de Larga Duración (LTSSE)

Los SSEs de larga duración o long term slow slip event (LTSSE) corresponden a deslizamientos lentos con duraciones que varían desde un par de meses hasta un par de años (Obara, 2020). Estos eventos han sido identificados tanto en la parte superficial del contacto interplaca (Yokota & Ishikawa, 2020), así como también, bajo la zona sismogénica (Hirose & Obara, 2005). Las magnitudes reportadas para estos eventos varían entre M_W 6.5-7.5 con deslizamientos en torno a decenas de centímetros (Nishikawa et al., 2023). En la Figura 2-1f se presenta la deformación generada por un LTSSE y registrada por un instrumento geodésico.

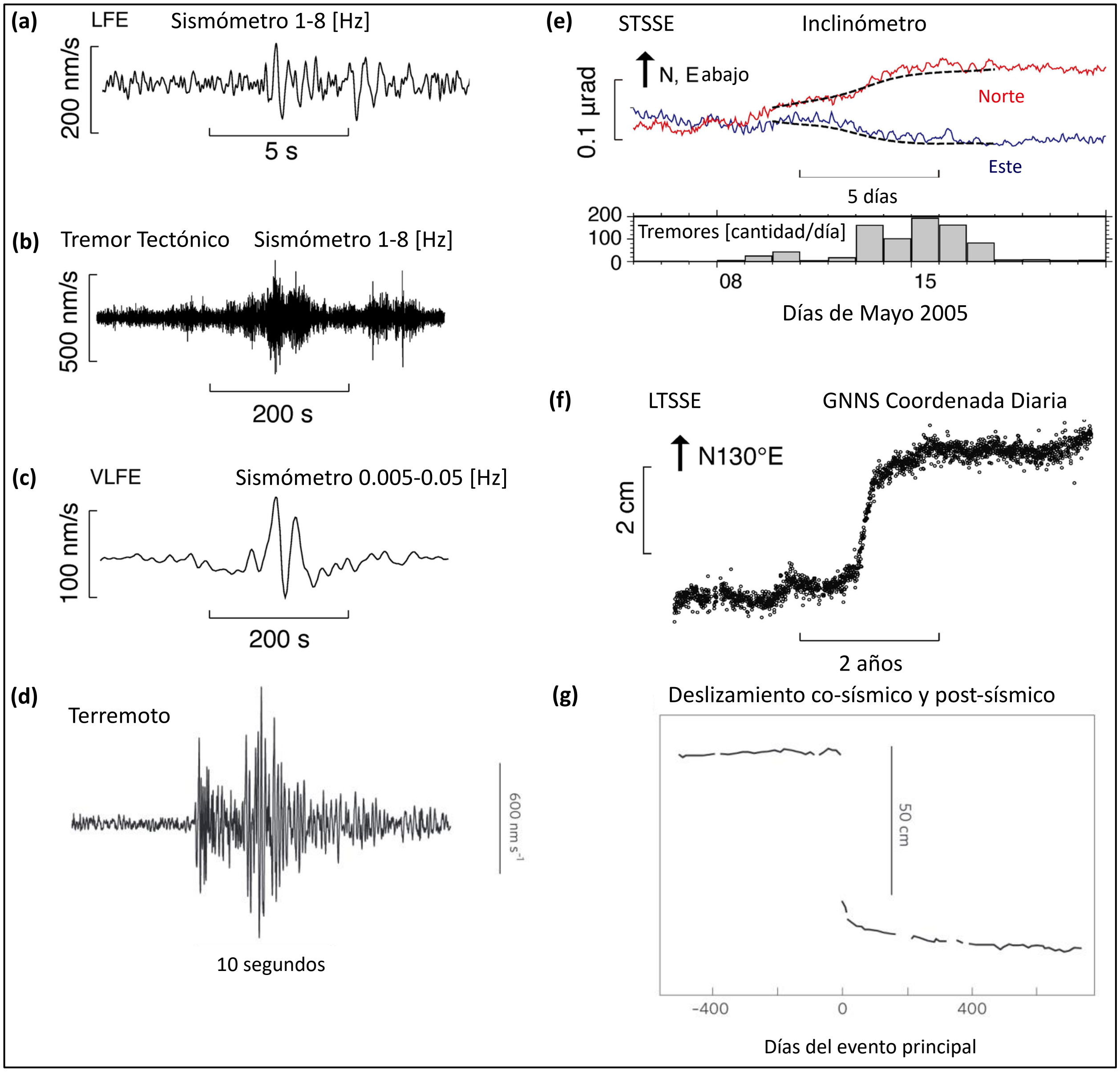

Figura 2-1: Familia de terremotos lentos. Manifestaciones sísmicas (a), (b) y (c) y geodésicas (e) y (f) asociada a la ocurrencia de terremotos lentos. Registros sísmicos de (a) terremoto de baja frecuencia (LFE), (b) tremor tectónico (NVT) y (c) terremoto de muy baja frecuencia (VLFE). Señales geodésicas asociadas a (e) deslizamiento lento de corta duración (STSSE) y (f) deslizamiento lento de larga duración. (SLSSE). (d) Señal sísmica y (g) geodésica asociada a un terremoto ordinario. Modificado de Nishikawa et al. (2023) y Peng & Gomberg (2010).

2.1.3 Señales Sísmicas Ordinarias Asociadas a Deslizamientos Lentos

Diversos autores han mostrado que en ocasiones los deslizamientos lentos están involucrados en procesos de cargas asísmicas que gatillan la ocurrencia de sismicidad ordinaria en forma de enjambres sísmicos o sismicidad repetitiva. A continuación, se describen las manifestaciones ordinarias gatilladas por la ocurrencia de deslizamientos lentos.

2.1.3.1 Terremotos Repetitivos

Los terremotos repetitivos, corresponden a eventos sísmicos que poseen una ubicación y geometría idéntica pero que ocurren en diferentes periodos de tiempo (Uchida & Bürgmann, 2019). Estos eventos son causados por un parche sísmico que acumula y libera esfuerzos, en una zona asísmica o de creeping, de forma repetitiva (Uchida, 2019). Debido a que estos eventos corresponden a rupturas repetitivas, la manera de identificarlos se basa en comparar la similitud de formas de ondas o a través de la co-locación de áreas de ruptura. En la Figura 2-2 se ilustran los sismogramas y áreas de rupturas generadas por un terremoto repetitivo que ocurre en distintos periodos de tiempo durante 15 años.

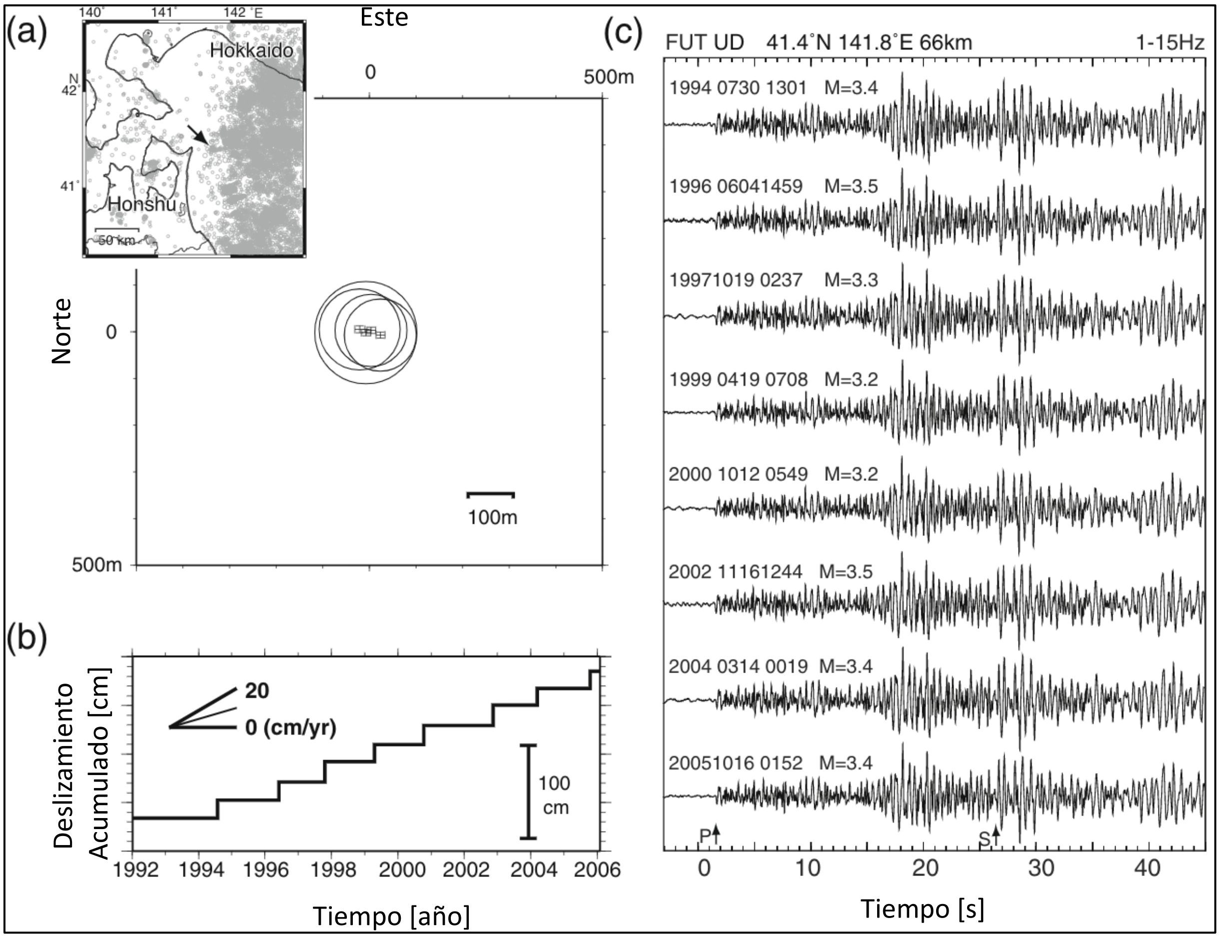

Figura 2-2: Ejemplo de terremoto repetitivo. (a) Ubicación de la fuente, (b) deslizamiento acumulado y (c) forma de ondas generadas por un terremoto repetitivo ocurrido en la zona noreste de Japón. Modificado de Uchida (2019).

El mecanismo capaz de generar estas rupturas repetitivas correspondería a un deslizamiento lento que es capaz de cargar el parche sísmico hasta generar su falla. Por lo tanto, el deslizamiento sísmico acumulado por la ocurrencia de terremotos repetitivos está relacionado con el deslizamiento generado de forma asísmica (deslizamiento lento), ver Figura 2-3.

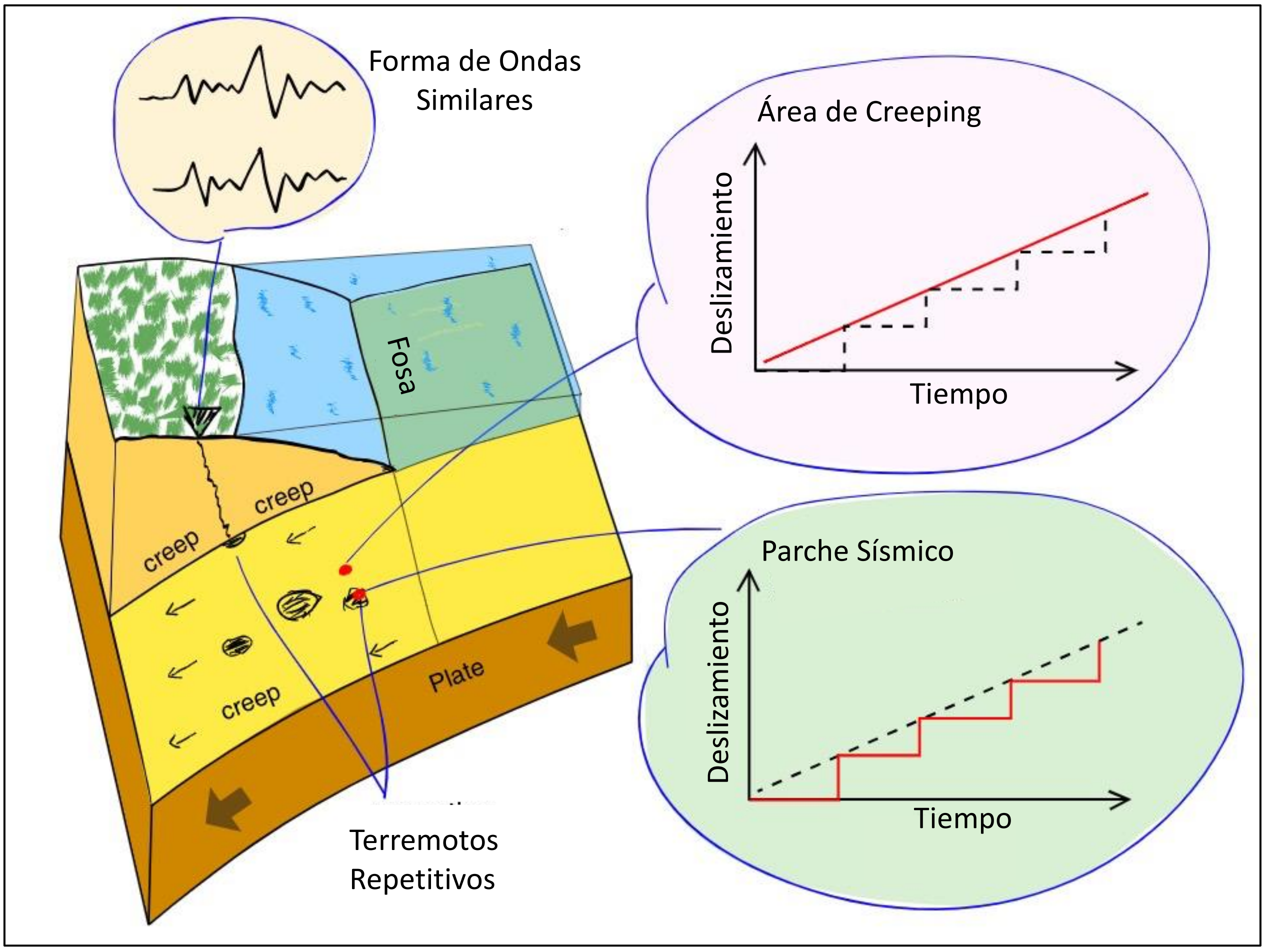

Figura 2-3: Modelo esquemático para la ocurrencia de terremotos repetitivos. Los terremotos repetitivos ocurren en parches sísmicos que son estresados por un movimiento asísmico. El deslizamiento acumulado por la ruptura repetitiva de estos eventos está relacionado con el deslizamiento generado de forma asísmica. Modificado de Uchida (2019).

2.1.3.2 Enjambres Sísmicos

Los enjambres sísmicos se definen como aquellos episodios donde la tasa de sismicidad en un área específica aumenta por sobre la actividad sísmica normal sin la presencia clara de un evento principal (Hill, 1977). En la Figura 2-4 se presenta la evolución temporal de un enjambre sísmico ocurrido en Vanuatu (Holtkamp & Brudzinski, 2011).

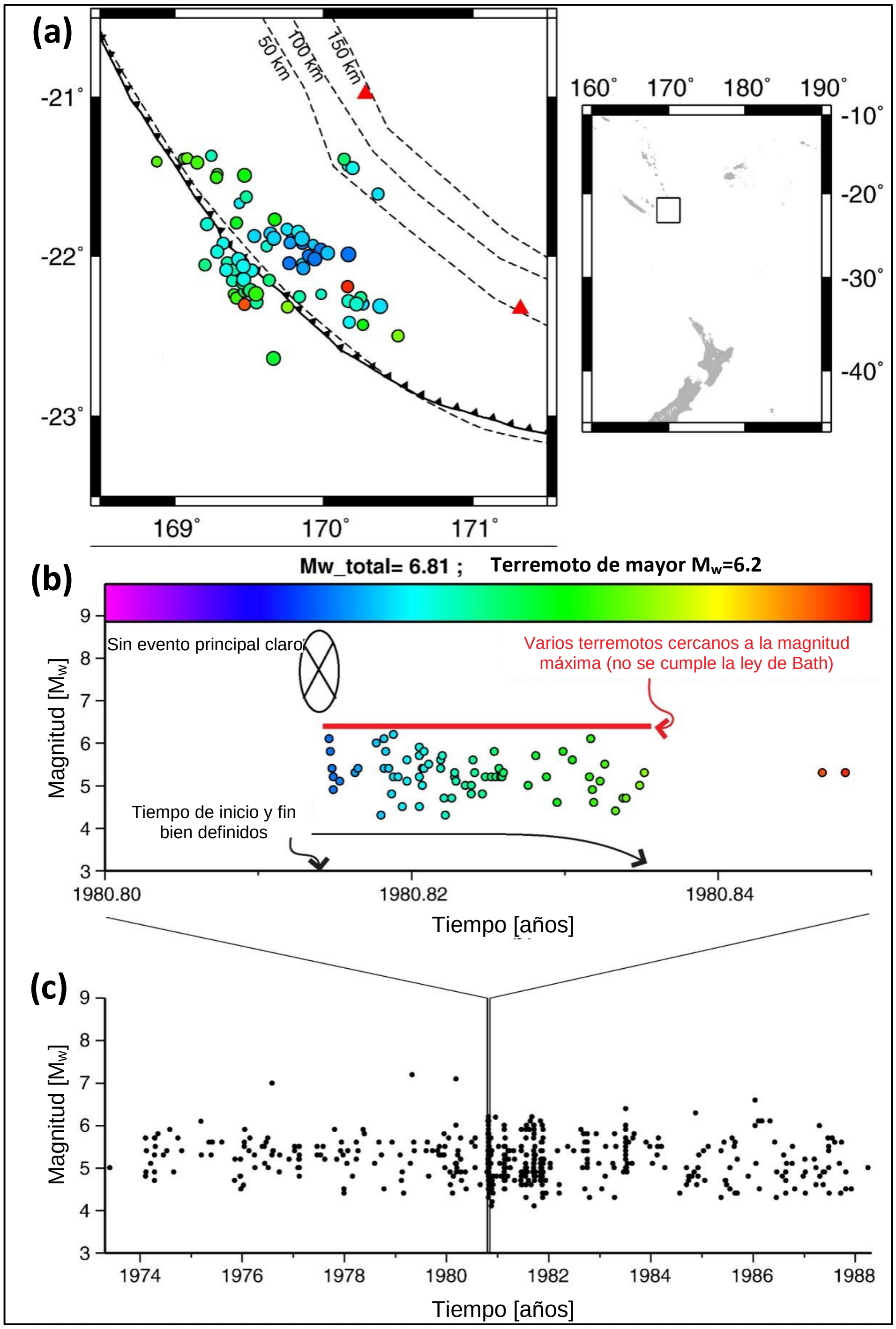

Figura 2-4: Ejemplo de enjambre sísmico. (a) Distribución en planta del enjambre sísmico ocurrido en Vanatau en 1980. (b) Magnitud de los eventos según el tiempo de ocurrencia considerando un periodo de tres semanas. (c) Evolución temporal de la magnitud de eventos ocurridos en el área de estudio mostrado en (a) considerando una ventana temporal de 15 años. Líneas verticales indican la ventana temporal analizada en (b). Círculos de colores indican los eventos ocurridos según la barra temporal mostrada en (b). Modificado de Holtkamp & Brudzinski (2011).

La ocurrencia de enjambres sísmicos está asociado a procesos asísmicos transientes, tales como, migración de fluidos y episodios de deslizamientos lentos a lo largo de las fallas (Nishikawa et al., 2021). Por un lado, la migración de fluidos puede incrementar la presión de poros y reducir de esta manera el esfuerzo efectivo normal y la resistencia al corte de las fallas, facilitando de esta manera la ruptura y generación de terremotos (Yamashita, 1998). Por otro lado, un deslizamiento lento puede gatillar cambios de esfuerzos capaces de cargar la zona hasta su falla y con ello generar actividad tipo enjambre (Fukuda, 2018).

2.2 Distribución de Terremotos Lentos en Profundidad

La manera en que desliza una falla varía en profundidad según las propiedades friccionales de los materiales que la componen. Estas propiedades presentan un comportamiento complejo y dependiente de las condiciones de presión, temperatura, presencia de fluido, sedimentos, rugosidad, minerales y tipos de rocas presentes en el ambiente tectónico donde se ubica la falla (Lay et al., 2012; Lay & Bilek, 2007). Adicionalmente, las propiedades friccionales pueden variar según las condiciones dinámicas que se desarrollen durante la ruptura, las que incluyen el tiempo de deslizamiento, velocidad de ruptura y deslizamiento total.

Si la resistencia por fricción durante la ruptura disminuye más rápido que la tensión, el deslizamiento puede producirse en forma repentina con caídas de tensión asociadas, proceso conocido como terremoto ordinario. La zona que muestra este comportamiento friccional, conocido como, velocity-weakening, y es capaz de generar terremotos ordinarios se denomina zona sismogénica. Por otro lado, si la resistencia en la falla no disminuye con el deslizamiento se producirá un deslizamiento estable. Este comportamiento friccional es conocido como velocity-strengthening.

Aunque los terremotos no se originan fuera de la zona sismogénica, se ha observado que la propagación de la ruptura sísmica se extiende a los regímenes friccionales de deslizamiento estable ubicados tanto hacia arriba como abajo de dicha zona. La propiedad de fricción de estas regiones de la falla que pueden propagar la ruptura sísmica pero no nuclearla se conoce como estabilidad condicional, mientras que, la zona que alberga dichos materiales se denomina zona de transición.

La variación en profundidad de las propiedades friccionales determina la forma en que una falla es capaz de romper y las características físicas que tendrá el proceso de ruptura. En la Figura 2-5 se presenta un esquema con la variación en profundidad de las propiedades friccionales en un ambiente tectónico de subducción.

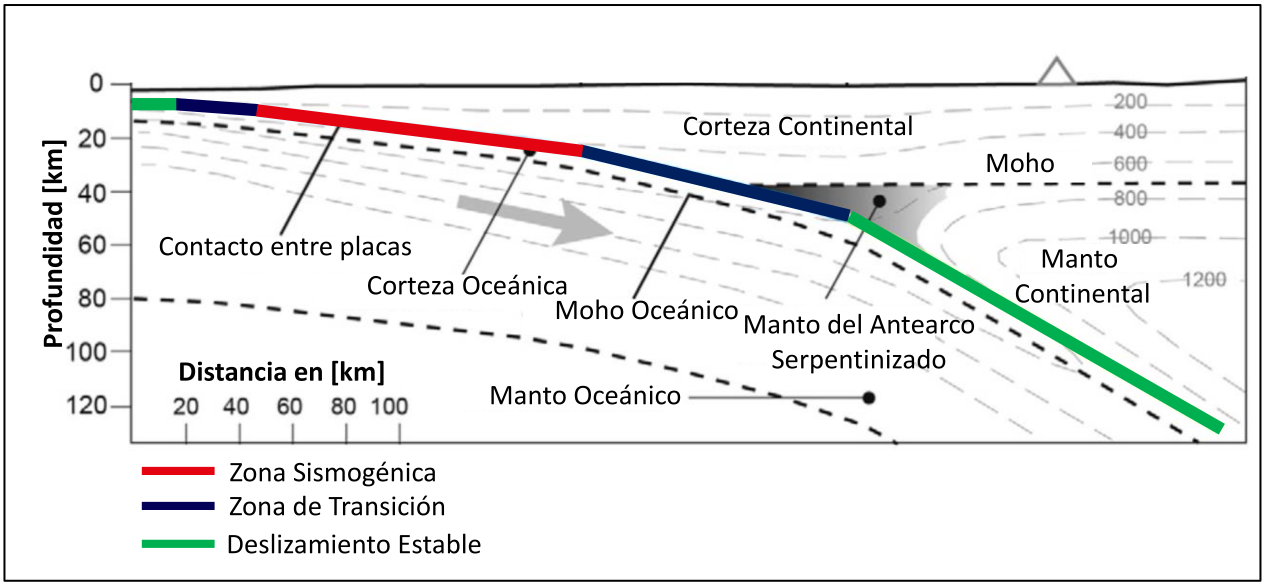

Figura 2-5: Representación esquemática de la variación en profundidad de las propiedades friccionales. Las profundidades son referenciales. Modificado de Audet & Kim (2016) y Peacock et al. (2011).

Como se mencionó en el acápite anterior, terremotos lentos han sido identificados bajo y sobre la zona sismogénica. Las condiciones de presión y temperatura de ambas zonas son considerablemente distintas. A modo de ejemplo, en la zona de subducción de Nankai, manifestaciones lentas han sido identificadas en la zona superficial del contacto entre placas a menos de 10 km de profundidad, donde la temperatura varía entre 100-200 °C, y también, bajo la zona donde ocurren los mega terremotos (25-40 km de profundidad) con temperaturas que oscilan entre 350-450 °C (Peacock, 2009). Lo anterior, permite comprender que la distribución bimodal de los terremotos lentos guarda relación con la variación en profundidad de las propiedades friccionales a lo largo del contacto entre placas, y en particular, con la ubicación de las zonas de transición donde se desarrollan comportamientos condicionalmente estables. En ambas zonas la presencia de fluidos facilita el deslizamiento lento a través de presiones de poros casi litostáticas que reducen la tensión normal efectiva y permiten que se produzca el deslizamiento en condiciones que, de otro modo, serían friccionalmente estables (Audet & Kim, 2016). En el caso de la zona superficial, la deshidratación de los sedimentos y minerales subductados forman parte de las fuentes aportantes de fluidos (Tonegawa et al., 2022), mientras que, para la zona profunda, la presencia de estratos saturados de baja velocidad sobre la placa subductante y reacciones metamórficas de deshidratación son las principales fuentes de fluido (Behr & Bürgmann, 2021; Wallace, 2020). En la Figura 2-6 se presenta un esquema con la distribución en profundidad de las distintas manifestaciones asociadas a terremotos lentos.

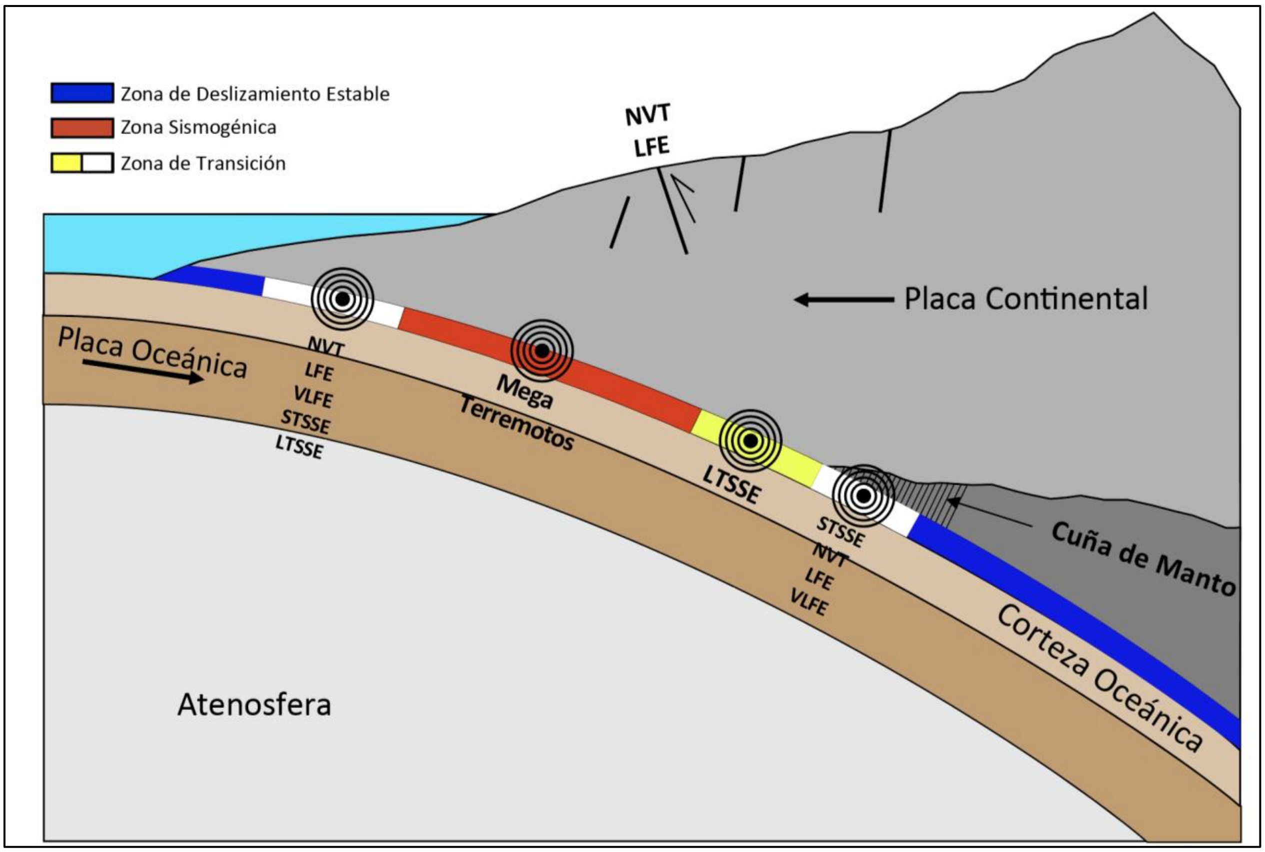

Figura 2-6: Esquema con la variación en profundidad de las distintas manifestaciones asociadas a terremotos lentos y propiedades friccionales en un ambiente tectónico de subducción. Señales sísmicas: tremores tectónicos (NVT), terremotos de baja frecuencia (LFE), terremotos de muy baja frecuencia (VLFE). Señales geodésicas: deslizamientos lentos de corta duración (STSSE) y deslizamientos lentos de larga duración (LTSSE).

2.3 Relación entre Terremotos Lentos

Las observaciones desarrolladas permiten señalar que diferentes manifestaciones lentas ocurren simultáneamente, tanto temporal como espacialmente, lo que sugiere que son generadas por una fuente común (Kaneko et al., 2018).

La primera relación establecida entre la familia de terremotos lentos corresponde a la observada entre los tremores tectónicos y los deslizamientos lentos de corta duración en Cascadia (Rogers & Dragert, 2003). En dicha zona, se observó que episodios de tremores tectónicos ocurrían solo cuando se desarrollaba un deslizamiento lento, mientras que, en el periodo intersísmico, la actividad de tremores era menor o nula (ver Figura 2-7). Además de la correlación temporal se determinó que ambas señales provenían de una fuente común, ubicada en la parte profunda del contacto interplaca. La correlación temporal y espacial observada entre ambas manifestaciones generó que los autores denominaran a este fenómeno como “Episodic Tremor and Slip” o ETS. Actualmente, ETS profundos han sido reportados en Japón (Obara et al., 2004), México (Brudzinski et al., 2016) y Alaska (Rousset et al., 2019).

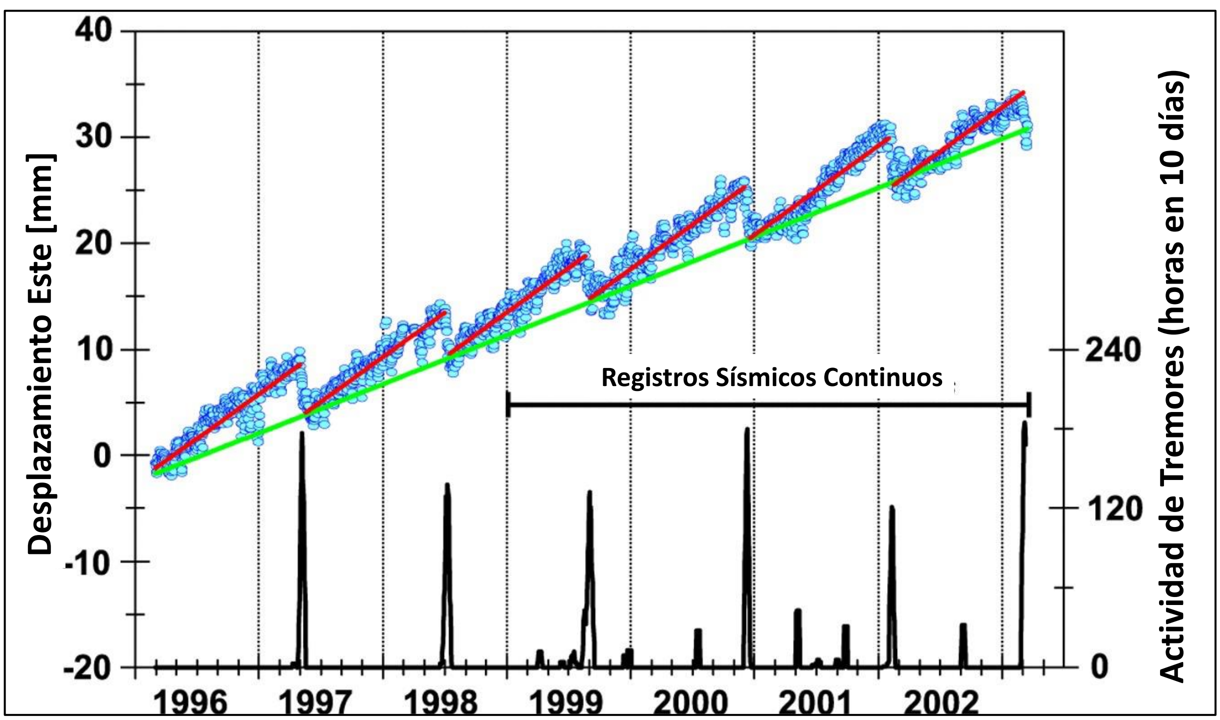

Figura 2-7: Comparación entre deslizamiento y actividad de tremores en el área de Victoria, Canadá. Modificado de Rogers & Dragert (2003).

El despliegue de instrumentación sísmuca sobre el fondo del mar (ocean bottom seismometer, OBS) ha permitido identificar episodios de tremores tectónicos y deslizamiento lentos también en la zona superficial del contacto entre placa. ETS superficiales han sido observados en Japón (Y. Ito et al., 2015), México (Plata-Martínez et al., 2021), Costa Rica (Walter et al., 2013) y Nueva Zelanda (Todd et al., 2018).

Por otro lado, Shelly et al. (2006) demostraron que los LFE se generan en el contacto entre placas, en la misma zona donde ocurren los tremores tectónicos. Además de tener una fuente común, los LFE ocurren casi exclusivamente durante episodios de tremores. Al comparar la similitud de ambas señales sísmicas, fue posible concluir que los tremores tectónicos corresponden a enjambres de LFE (Brown et al., 2008; Shelly et al., 2007). Posteriormente, utilizando una red densa de sismómetros de alta sensibilidad, Ito et al., (2007) mostraron que los terremotos de muy baja frecuencia (VLFE) ocurren y migran con los tremores tectónicos y los deslizamientos lentos en la zona profunda del contacto entre placas.

Las correlaciones temporales y espaciales observadas entre los distintos tipos de señales lentas han permitido entender que todas corresponden a diferentes manifestaciones de un deslizamiento lento por corte (Ide et al., 2007; Masuda et al., 2020). Por ejemplo, al filtrar en los rangos de frecuencia adecuados, es posible observar todas señales sísmicas lentas (NVT, LFE y VLFE) en un solo sismograma. Además, durante los periodos en los que ocurren estas manifestaciones sísmicas lentas, se puede detectar la presencia de un deslizamiento lento (ver Figura 2-8).

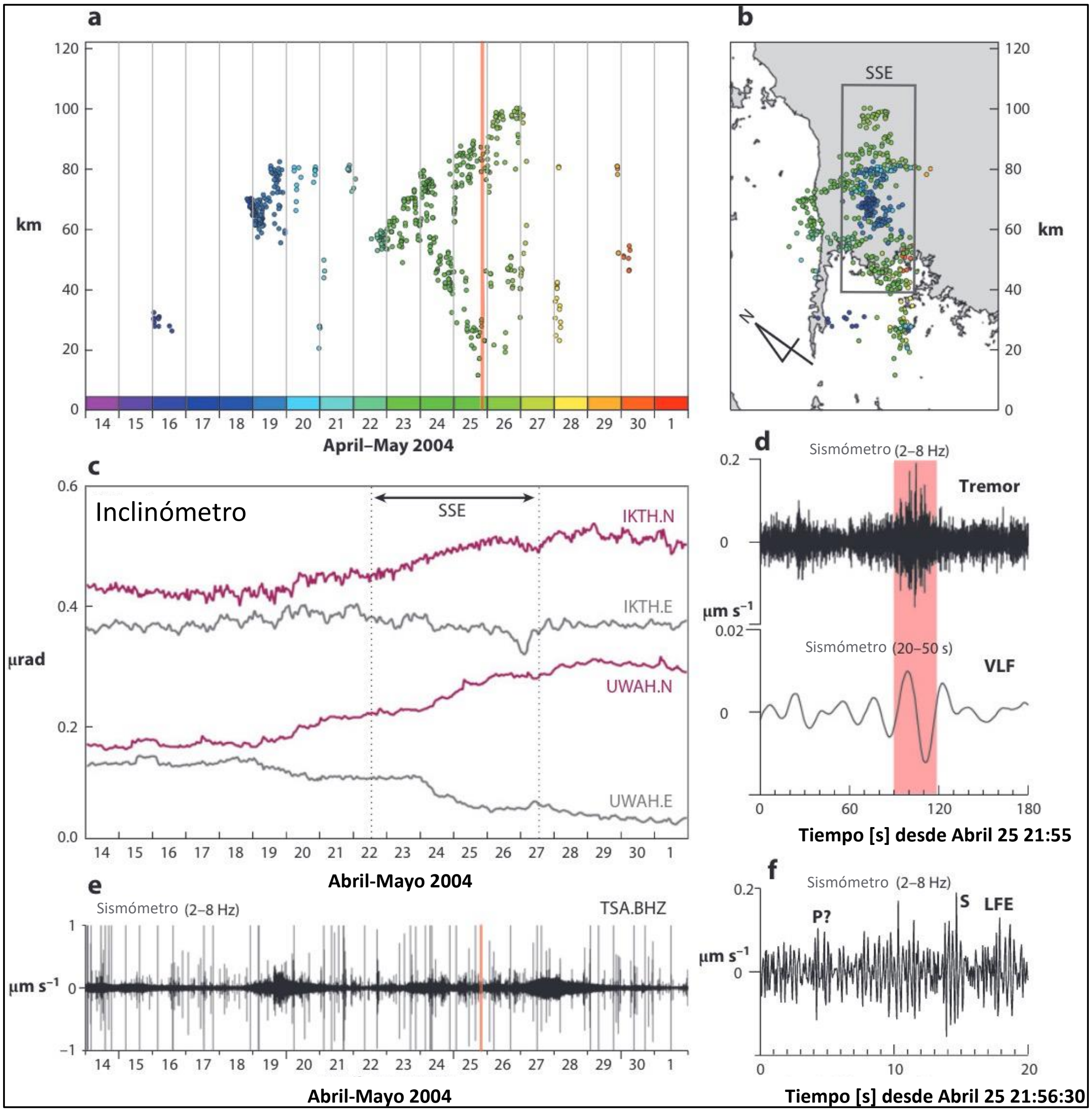

Figura 2-8: Actividad ETS en Shikoku, Japón. (a) Distribución espacio-tiempo de tremores tectónicos y (b) distribución en planta de (a). (c) Registros de inclinómetros asociados al ETS. (d) Zoom al registro sísmico de un tremor presentado en (e) y filtrado entre 2-8 [Hz] (arriba) y 0.02-0.05 [Hz] (abajo). (f) Zoom al registro sísmico presentado en (d). Modificado de Beroza & Ide (2011)

Debido a que las distintas manifestaciones poseen una fuente común de generación, algunos autores han propuesto nombrar al conjunto de estas señales como “broadband slow earthquakes” (Ide & Yabe, 2019; Kaneko et al., 2018; Masuda et al., 2020), argumentando que cada señal representa la observación del terremoto lento en un contenido de frecuencia particular. A pesar de lo anterior, es posible que un terremoto lento genere deslizamientos pobres en algún contenido de frecuencia, y que, por ello, alguna de las manifestaciones no pueda ser observada, como es el caso de la ocurrencia de VLFE sin tremores tectónico (Hutchison & Ghosh, 2016; Y. Ito et al., 2007).

La visión unificada de los terremotos lentos ha permitido comprender que las manifestaciones sísmicas lentas corresponderían a pequeñas rupturas generadas por parches sísmicos embebidos en un medio con comportamiento friccional del tipo condicionalmente estable. Este tipo de comportamiento, observado sobre y bajo la zona sísmogenica, es favorecida por la presencia de fluidos provenientes de sedimentos no-consolidados, estratos de baja velocidad, reacciones metamórficas, deshidratación de minerales, entre otras. En la Figura 2-9 se presenta un modelo esquemático con la distribución en profundidad de los terremotos lentos en una zona de subducción.

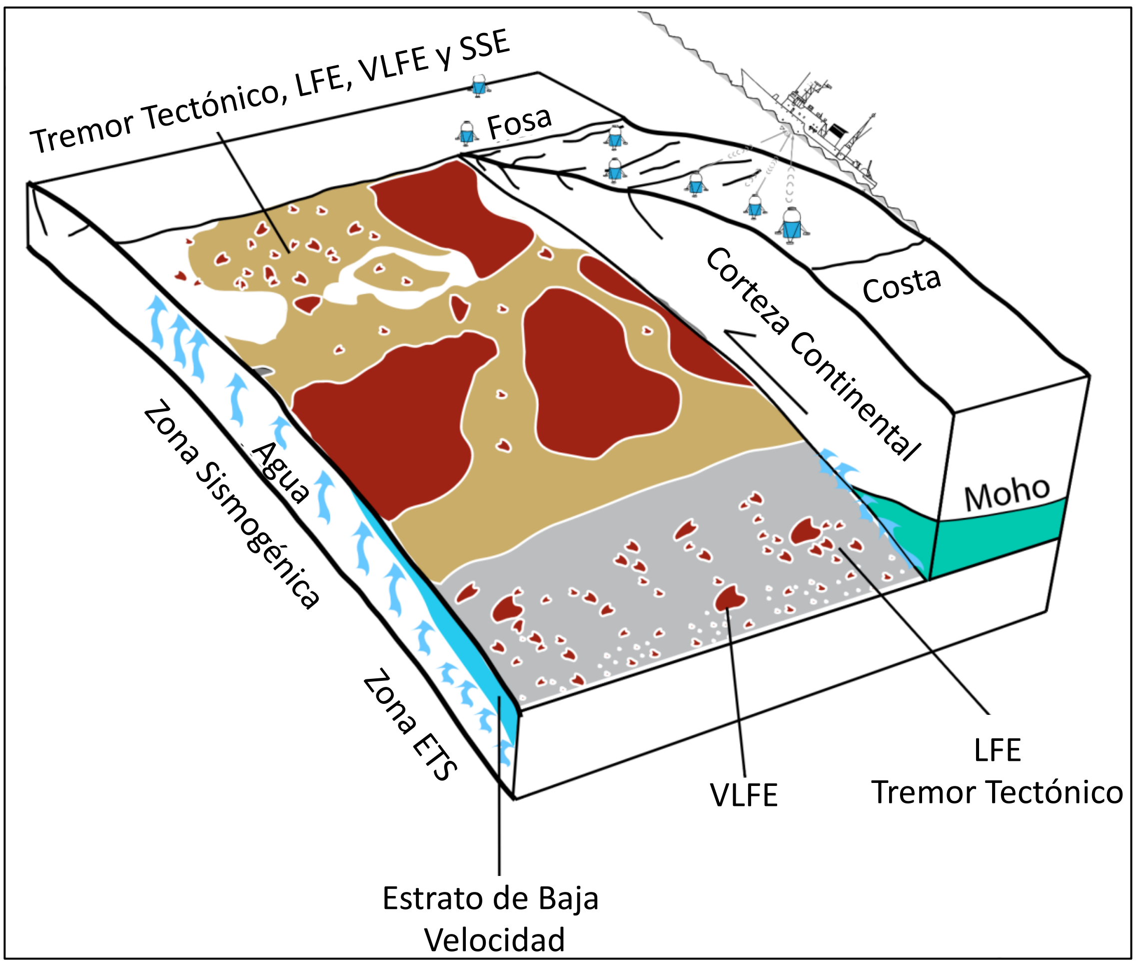

Figura 2-9: Modelo esquemático con la distribución de deslizamientos asísmicos y sísmicos en una zona de subducción. Modificado de Behr & Bürgmann (2021) y Lay et al. (2012).

2.4 Propiedades y Modelos Físicos de Terremotos Lentos

Los terremotos lentos, al igual que los ordinarios, se producen a partir de fallas por cortes. La diferencia principal entre ambos procesos guarda relación con la duración de la ruptura y la energía sísmica emanada en dicho proceso.

El estudio de terremotos ordinarios ha permitido comprender que existe una relación proporcional entre el momento sísmico o energía liberada durante la ruptura y el cubo de su duración ($M_0 \propto T^3$) (Aki, 1967, 1972), tal como se muestra con línea roja en la Figura 2-10. Lo anterior, conocido como ley de escalamiento, permite comprender a los terremotos ordinarios como un proceso que escala en tamaño según el cubo de su duración.

Por otro lado, caracterizando los parámetros de la fuente de distintas manifestaciones lentas, Ide et al. (2007a) proponen una relación lineal entre el momento sísmico y la duración de los terremotos lentos ($M_0 \propto T$), la cual se expresa con línea azul en la Figura 2-10.

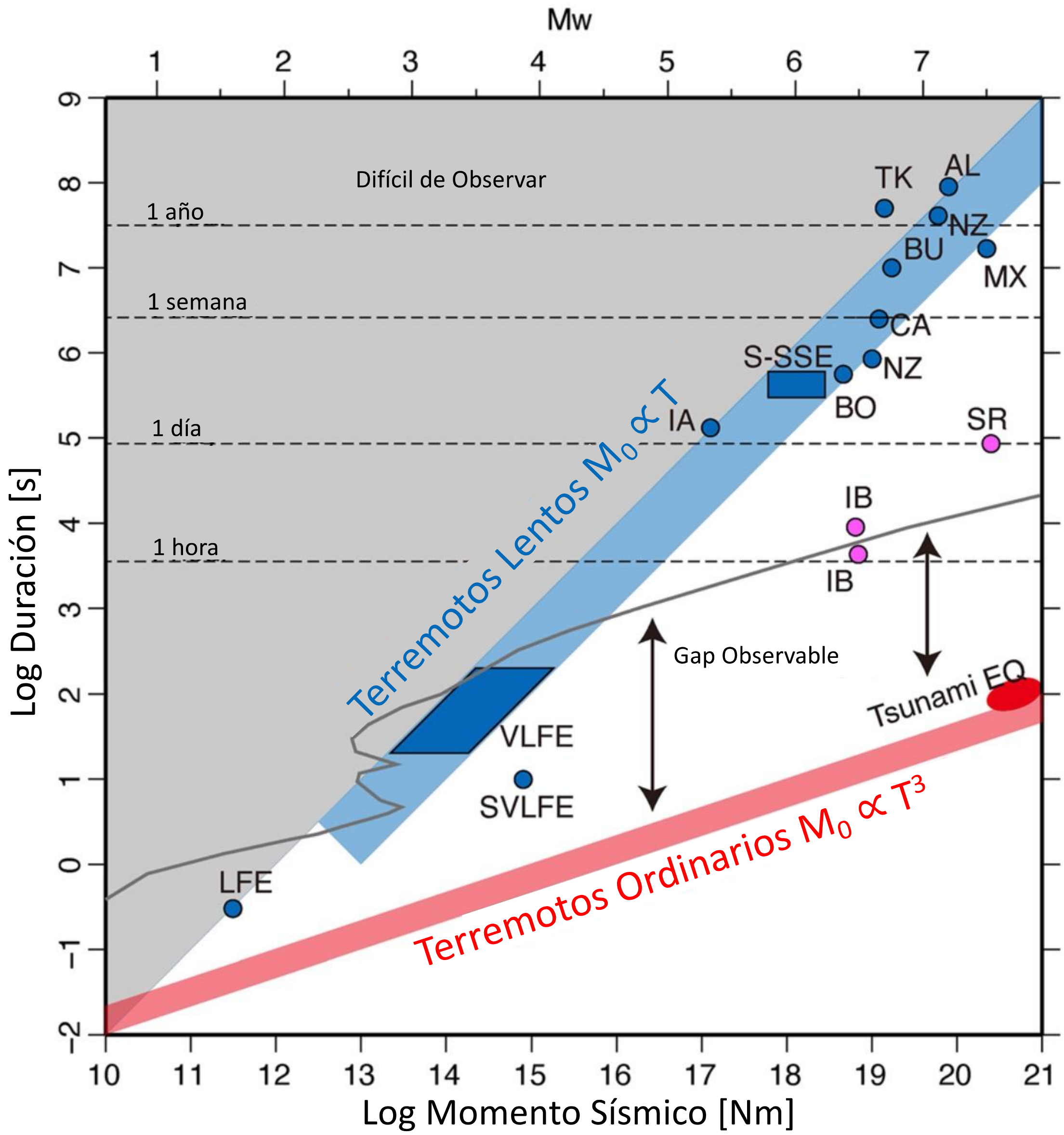

Figura 2-10: Ley de escalamiento para terremotos lentos y ordinarios. Símbolos azules y magenta representan terremotos lentos ocurridos en zonas como Japón, Cascadia, México, Nueva Zelanda y Costa Rica. Para más detalle revisar Nishikawa et al. (2023). Modificado de Ide (2014) y Nishikawa et al. (2023).

Adicionalmente, las observaciones desarrolladas en distintos ambientes tectónicos permiten señalar que el espectro de las señales sísmicas lentas (VLFE, LFE y tremores) decaen en la alta frecuencia con f^{-1} (Masuda et al., 2020) a diferencia de los terremotos ordinarios que lo hacen con f^{-2}, ver Figura 2-11. Lo anterior, es consistente con una relación lineal entre el momento sísmico y la duración de la fuente y por ende una tasa de momento $\dot{M}_0(t)$ constante (Ide, Beroza, et al., 2007).

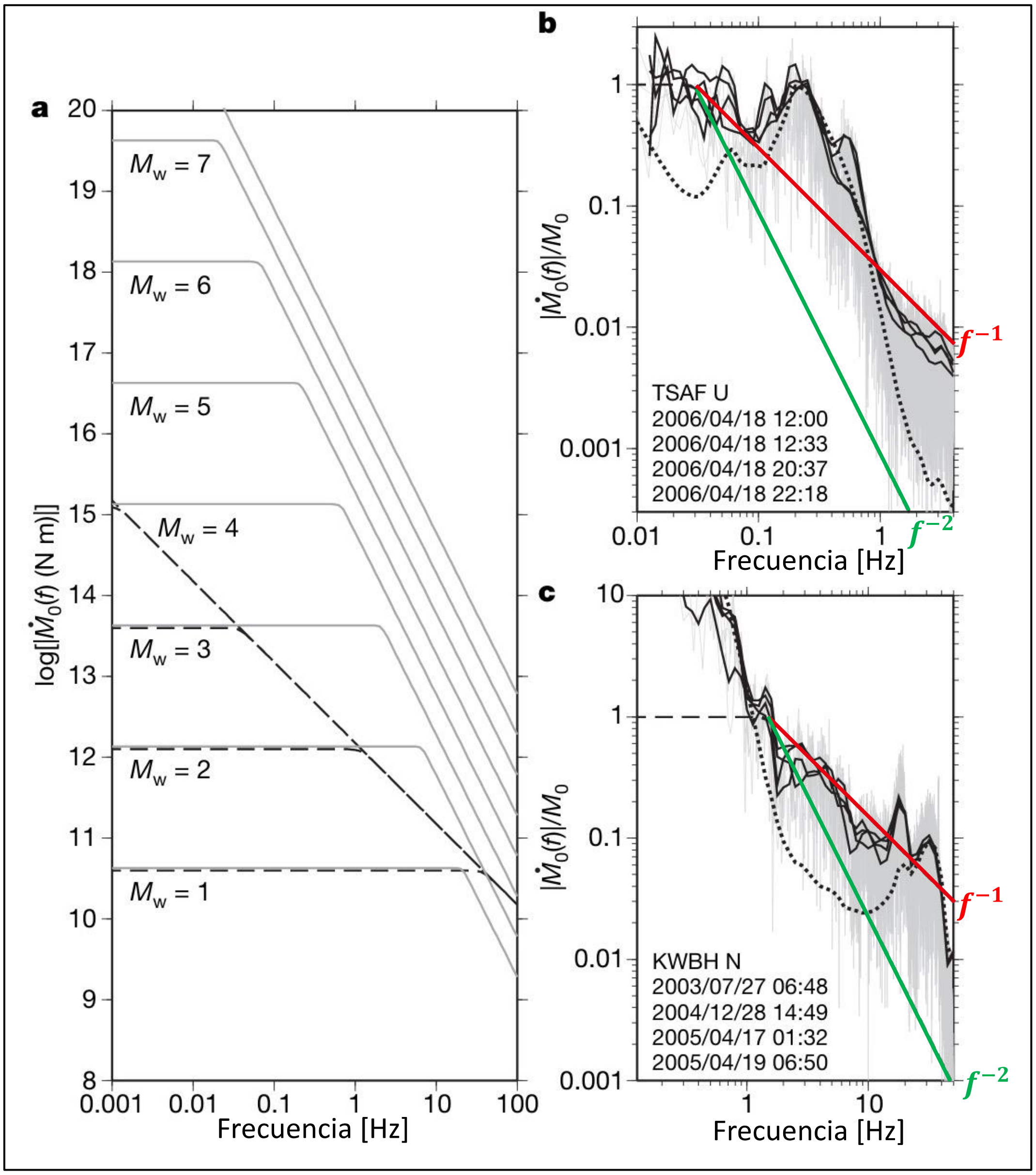

Figura 2-11: Espectro de la tasa de momento para terremotos lentos. (a) Escalamiento del espectro de la tasa de momento para terremotos lentos (línea negra punteada) y terremotos ordinarios (línea gris continua). Ejemplo de espectro de la tasa de momento para (b) VLFE y (c) LFE. Modificado de Ide & Beroza, et al. (2007).

La ley de escalamiento propuesta, las características espectrales y la correlación temporal-espacial observada permiten comprender a las señales lentas como distintas manifestaciones de un proceso físico común. A partir de lo anterior, la diferencia entre las señales lentas estaría dada solo por el tamaño final que podría alcanzar la ruptura (Ide, et al. 2007a).

2.5 Ubicación de Terremotos Lentos a Nivel Mundial

Desde su descubrimiento en el año 2002 (Obara, 2002), manifestaciones sísmicas y geodésicas lentas han sido reportadas en distintas zonas del mundo. Si bien, en las zonas de subducción del cinturón del fuego del Pacífico es donde se han observado la mayor cantidad y variedad de manifestaciones lentas (Obara, 2020), estas, también han sido reportadas en ambientes tectónicos transformantes como las fallas de San Andrés (Thomas et al., 2009) y Alpine (Wech et al., 2012), así como también, en zonas de colisión entre continentes (Chao et al., 2012). En la Figura 2-12 se presenta un resumen con las manifestaciones sísmicas lentas observadas hasta el momento a nivel mundial.

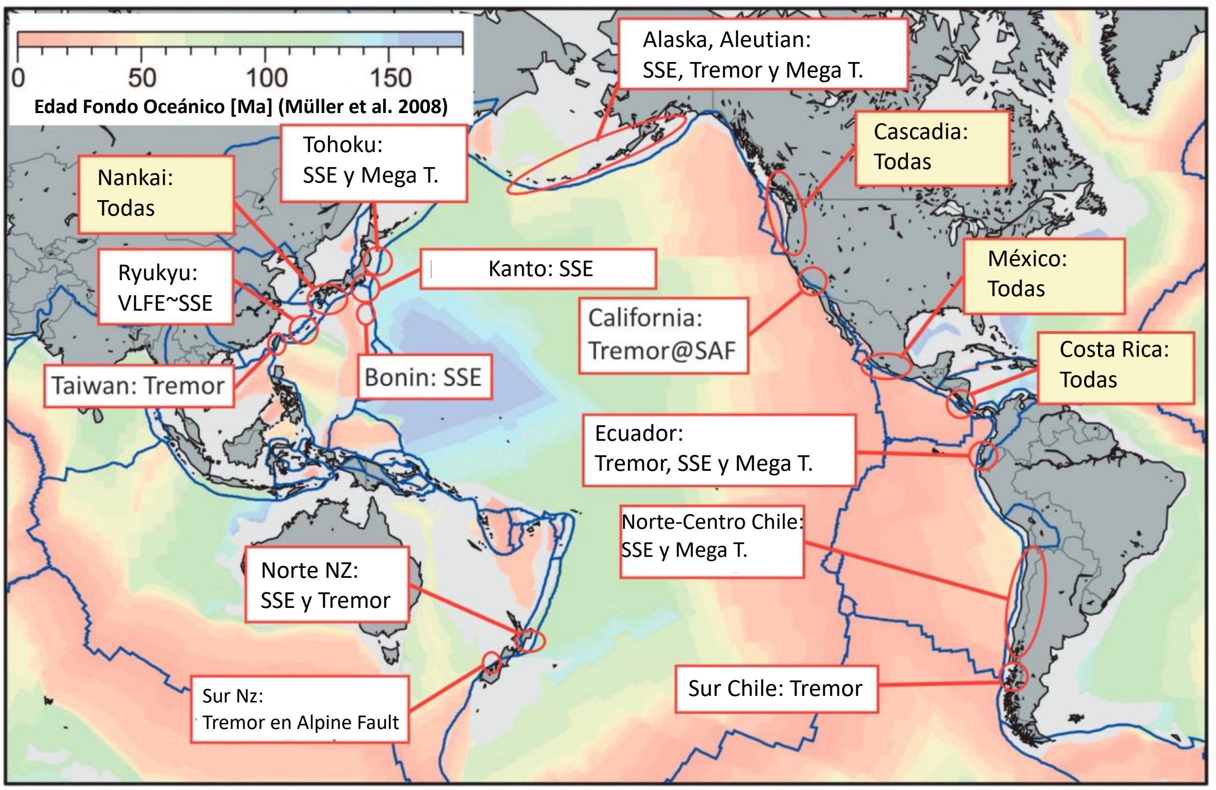

Figura 2-12: Distribución de terremotos lentos a nivel mundial. Nomenclatura utilizada: deslizamiento lento (SSE), terremoto de muy baja frecuencia (VLFE), Mega T.: Mega terremotos. Tremor incluye la ocurrencia de terremotos de baja frecuencia (LFE). Edad del fondo marino obtenido a partir de Müller et al., (2008). Modificado de Obara (2020).

De la Figura 2-12 es posible observar que los terremotos lentos corresponden a fenómenos globales que se desarrollan en diversos ambientes, donde interactúan placas tectónicas jóvenes y calientes como la de Filipinas (~15 Ma), así como también, viejas y frías como la de Nueva Zelanda (120 Ma) (Ide, 2012). Si bien hasta el momento no se ha podido correlacionar la ocurrencia de terremotos lentos con alguna característica tectónica en particular (edad de placas, velocidad de placas, presencia de sedimentos, etc), es de esperar que la densificación de estaciones a nivel mundial permita esclarecer las condiciones necesarias para la generación de estas manifestaciones.

3 Terremotos Lentos en Chile

3.1 General

A pesar de ser uno de los entornos tectónicos con mayor actividad sísmica a nivel mundial, la ocurrencia de terremotos lentos en el margen chileno ha sido escasamente estudiada. La primera señal lenta observada en el margen chileno corresponde a los tremores tectónicos que ocurren en la zona sur del país, cercano al punto triple (Gallego et al., 2013; Ide, 2012). La densificación de estaciones GPS y sismológicas, posterior a la ocurrencia del terremoto del Maule 2010 M_w 8.8, ha permitido detectar señales lentas de tipo sísmica y geodésica en otras zonas del margen chileno. A continuación, se detallan y describen los tipos de señales lentas identificadas hasta el año 2024 a lo largo del margen chileno.

3.2 Señales Geodésicas

Deslizamientos lentos de corta y larga duración han sido detectados en la zona norte y centro del margen chileno. En particular, tres eventos de deslizamiento de corta duración y dos de larga duración han sido observados a lo largo del país. Los eventos de corta duración corresponden a los detectados previo al terremoto de Iquique 2014 (Ruiz et al., 2014), fase post-sísmica del terremoto de Illapel 2015 (Tissandier et al., 2023) y Valparaíso 2017 (Ruiz et al., 2017). Por otro lado, los deslizamientos lentos de larga duración corresponden a los detectados en Copiapó (Klein et al., 2018, 2023) y en Iquique

(Socquet et al., 2017), este último observado ocho meses antes del terremoto del 01 de abril del 2014 M_w 8.1.

En algunos casos, estos deslizamientos lentos han sido acompañados de señales sísmicas ordinarias, tales como, terremotos repetitivos y sismicidad tipo enjambre. A continuación, se entrega una breve descripción de las señales geodésicas lentas identificadas a lo largo del margen chileno.

3.2.1 Deslizamientos Lentos de Corta Duración

3.2.1.1 Terremoto de Iquique 2014 M_w 8.1

La primera señal geodésica lenta detectada en Chile corresponde al deslizamiento de corta duración ocurrido 14 días antes de la ruptura principal del terremoto de Iquique M_w 8.1 2014 (Ruiz et al., 2014), ver Figura 1-1b. La señal geodésica estuvo asociado a un terremoto lento con un área de ruptura que coincide espacialmente con los parches de mayor deslizamiento generados por el evento principal y generó un desplazamiento máximo de ~1 cm en la estación de Pisagua (Figura 1-1b). El deslizamiento lento tuvo una magnitud de M_w 7.0 (Socquet et al., 2017) y estuvo acompañado por un aumento de la tasa de sismicidad, la ocurrencia de terremotos repetitivos y actividad tipo swarm (Kato et al., 2016). Estas señales precursoras ordinarias estuvieron caracterizadas por un proceso de migración que comenzó en la zona somera del contacto entre placas y finalizó rodeando la parte superficial de la ruptura principal (Kato & Nakagawa, 2014; Ruiz et al., 2014), ver Figura 1-1a y Figura 1-1c.

Utilizando un catalogó de alta resolución, Kato et al. (2016) mostraron que el deslizamiento durante la fase precursora del terremoto fue liberado en partes iguales por un proceso asísmico (terremotos repetitivos) y sísmico (sismicidad ordinaria). La correlación espacial y temporal observada entre la sismicidad precursora y las zonas con mayores deslizamientos de tipo asísmicos (ver Figura 3-1) permiten inferir que la fase de nucleación del terremoto de Iquique estuvo controlada por un deslizamiento lento de corta duración el cual estresó la zona donde finalmente rompe el terremoto principal (Meng et al., 2015; Ruiz et al., 2014).

Hasta la fecha de publicación de la presente tesis, no se han identificado señales sísmicas lentas (tremores tectónicos, LFE o VLFE) asociadas a la ocurrencia del terremoto de Iquique. El hecho de no detectar este tipo de señales no implica que manifestaciones sísmicas no se hayan desarrollado. En este contexto, es posible que la amplitud de estas señales no pueda ser detectada debido a la alta tasa de sismicidad observada en la fase precursora o que la señal se encuentre oculta bajo el ruido ambiental.

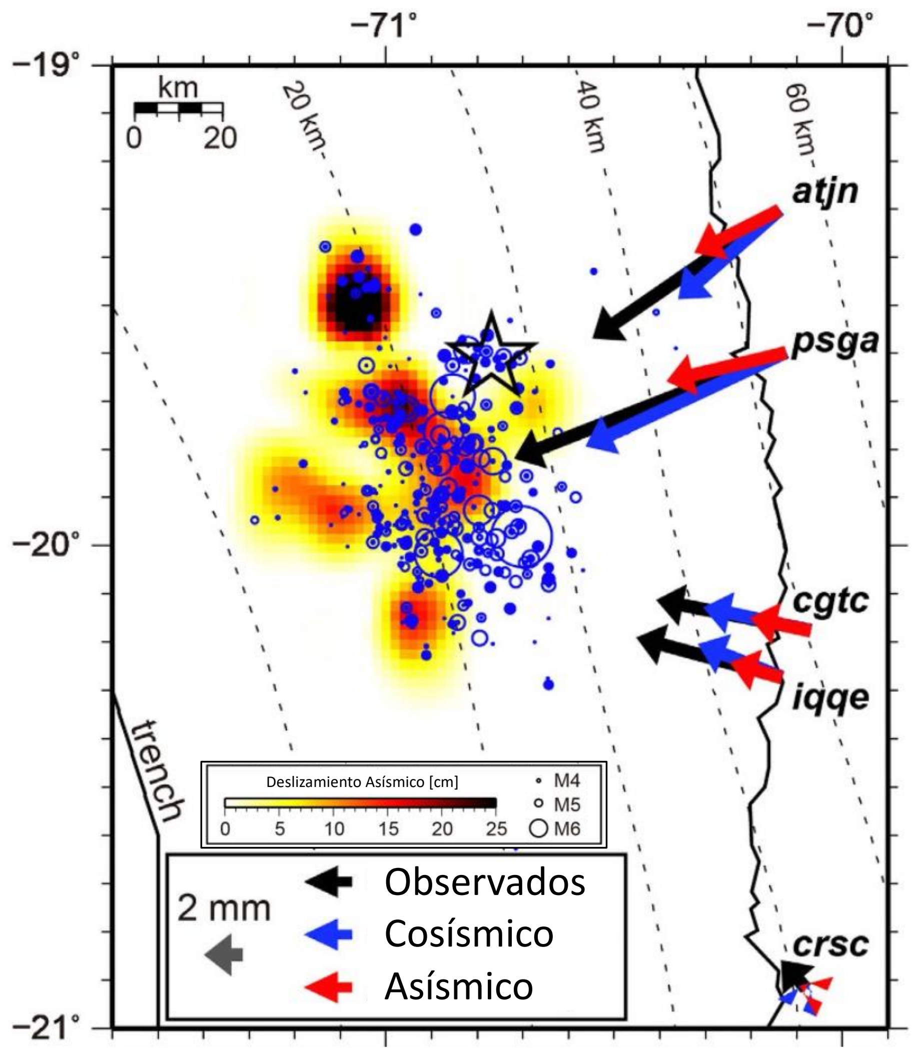

Figura 3-1: Deformación superficial 17 días antes del terremoto de Iquique 2014 M_W 8.1. Las flechas indican la deformación superficial medida con estaciones GPS ubicadas en las cercanías de la zona donde se detectó la actividad precursora. Con círculos azules escalados según magnitud se identifican los epicentros de la actividad precursora ocurrida 17 días antes del evento principal. Modificado de Kato et al. (2016).

3.2.1.2 Terremoto de Valparaíso 2017 M_W 6.9

El día 24 de abril del año 2017 ocurre frente a Valparaíso, un terremoto tipo interplaca M_W 6.9, el cual, rompió un área aproximada de 50 km^2 a 28 km de profundidad (Ruiz et al., 2017). Dos días antes del evento principal se detectó el inicio de una fase precursora, que estuvo caracterizada por la ocurrencia de un deslizamiento lento de corta duración, terremotos repetitivos y un aumento de la sismicidad ordinaria (Caballero et al., 2021; Ruiz et al., 2017). Al igual que en el caso del terremoto de Iquique, el deslizamiento lento se generó en la misma zona donde posteriormente rompe el evento principal (Ruiz et al., 2017).

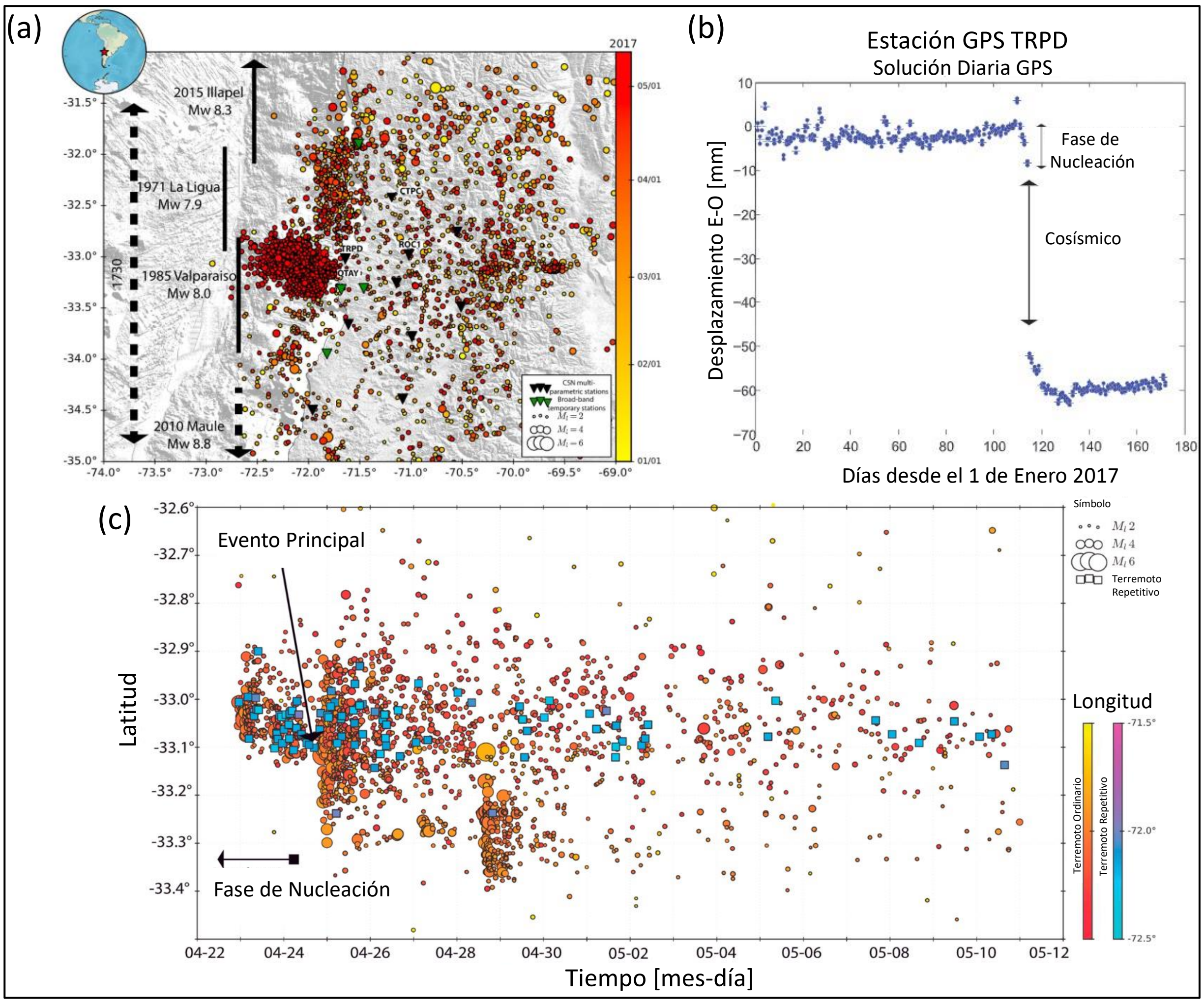

Figura 3-2: Terremoto de Valparaíso 2017 M_w 6.9. (a) Sismicidad detectada entre el 01 de enero y 12 de mayo del 2017. Triángulos invertidos negros y verde indican la ubicación de estaciones multiparamétricas y banda ancha, respectivamente. (b) Serie temporal de GPS asociada a la

estación TRPD durante la secuencia sísmica de Valparaíso 2017. (c) Distribución temporal de la sismicidad asociada a la fase de nucleación del terremoto de Valparaíso 2017 y sus réplicas. Modificado de Ruiz et al. (2017).

La comparación entre los desplazamientos observados y modelados muestra que solo la mitad del desplazamiento total puede ser explicado por la contribución de la sismicidad ordinaria precursora (Caballero et al., 2021). Lo anterior sugiere que tanto la actividad ordinaria como asísmica observada durante la secuencia de Valparaíso 2017 puede ser interpretada como el resultado de un deslizamiento lento que inicio antes del evento principal y que se extendió luego de este (Moutote et al., 2023).

Al igual que en el terremoto de Iquique, durante la secuencia sísmica de Valparaíso 2017 no se reportó la ocurrencia de ninguna manifestación lenta de tipo sísmica (tremores tectónicos, LFE y VLFE).

3.2.1.3 After slip terremoto de Illapel 2015 M_w 8.3

Utilizando datos GNSS en continuo, Tissandier et al. (2023) estudiaron el deslizamiento post-sísmico (afterslip) generado por el terremoto de Illapel M_w 8.3. Durante los dos meses posteriores al evento principal, los autores identifican que el afterslip se desarrolla en tres zonas, la cuales rodean la ruptura co-sísmica y albergan terremotos repetitivos y réplicas (Figura 1-1). Adicionalmente, los autores detectan un deslizamiento asísmico con una duración de un par de días, el cual ocurre al sur de la ruptura principal. Este deslizamiento lento, se correlaciona espacial y temporalmente con un burst de sismicidad. Finalmente, los autores concluyen que las zonas donde se desarrollan los deslizamientos post-sísmicos se correlacionan con sectores donde recurrentemente ocurrieron enjambres de sismicidad previo al terremoto de Illapel 2015 (Poli et al., 2017). Estas zonas estarían caracterizadas por altas presiones de poros y por tener un comportamiento asísmico recurrente.

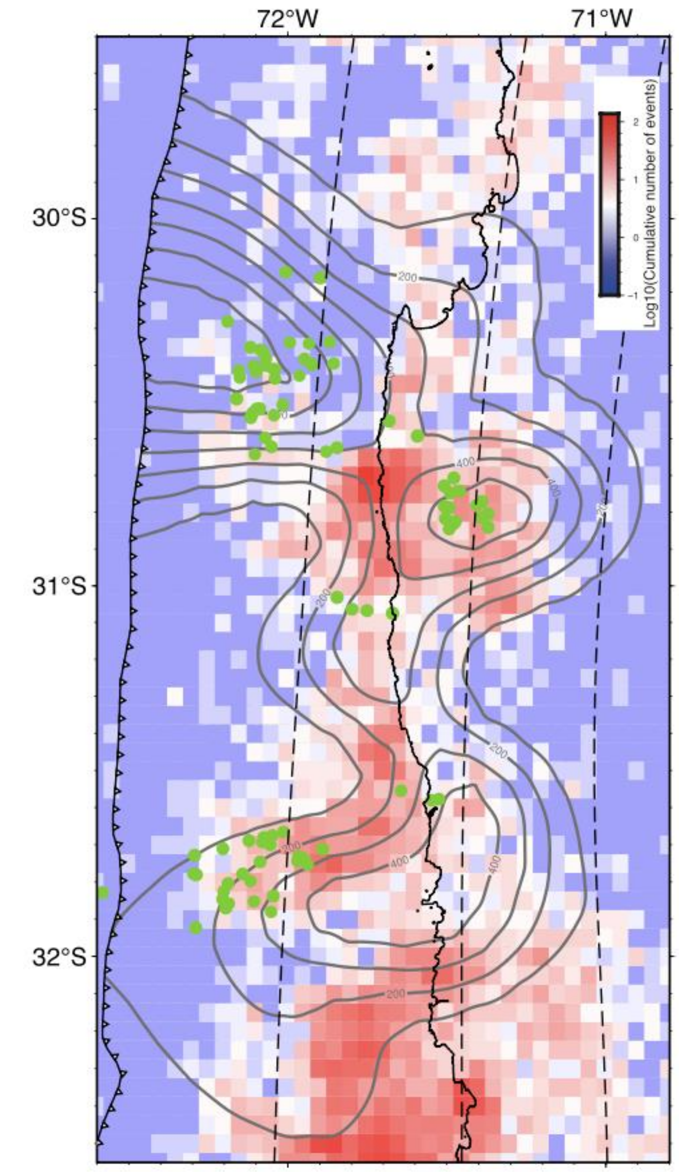

Figura 3-3: Comparación entre deslizamiento post-sísmico (líneas continuas grises) y sismicidad intersísmica de tipo repetitiva (Poli et al., 2017). Modificado de Tissandier et al. (2023).

3.2.2 Deslizamientos Lentos de Larga Duración

3.2.2.1 Terremoto de Iquique 2014 M_w 8.1

Utilizando estaciones GPS y sismómetros desplegados en las cercanías del área de ruptura del terremoto de Iquique 2014, Socquet et al. (2017) postulan que la fase precursora del evento comenzó ocho meses antes de la ruptura principal.

Al analizar 2 años de datos geodésicos y sísmicos, Socquet et al. (2017) detectan que un grupo de estaciones GPS comienza a acelerar hacia el oeste, ocho meses antes del evento principal, ver Figura 3-4. El deslizamiento detectado (interpretado como lento, ya que generó una desviación de 2 mm/year) tuvo una M_W de 6.5 y se localizó en el contacto entre placas, rodeando la zona de ruptura del terremoto de Iquique.

El deslizamiento lento estuvo acompañado de un aumento de la sismicidad, una disminución del "b-value" y una reducción del contenido de alta frecuencia de los terremotos. Todos estos cambios se interpretan como respuestas ordinarias frente a un deslizamiento lento, el cual genera rupturas sísmicas que se vuelven cada vez más suaves o lentas y tal vez facilitado por la migración de fluidos (Socquet et al., 2017).

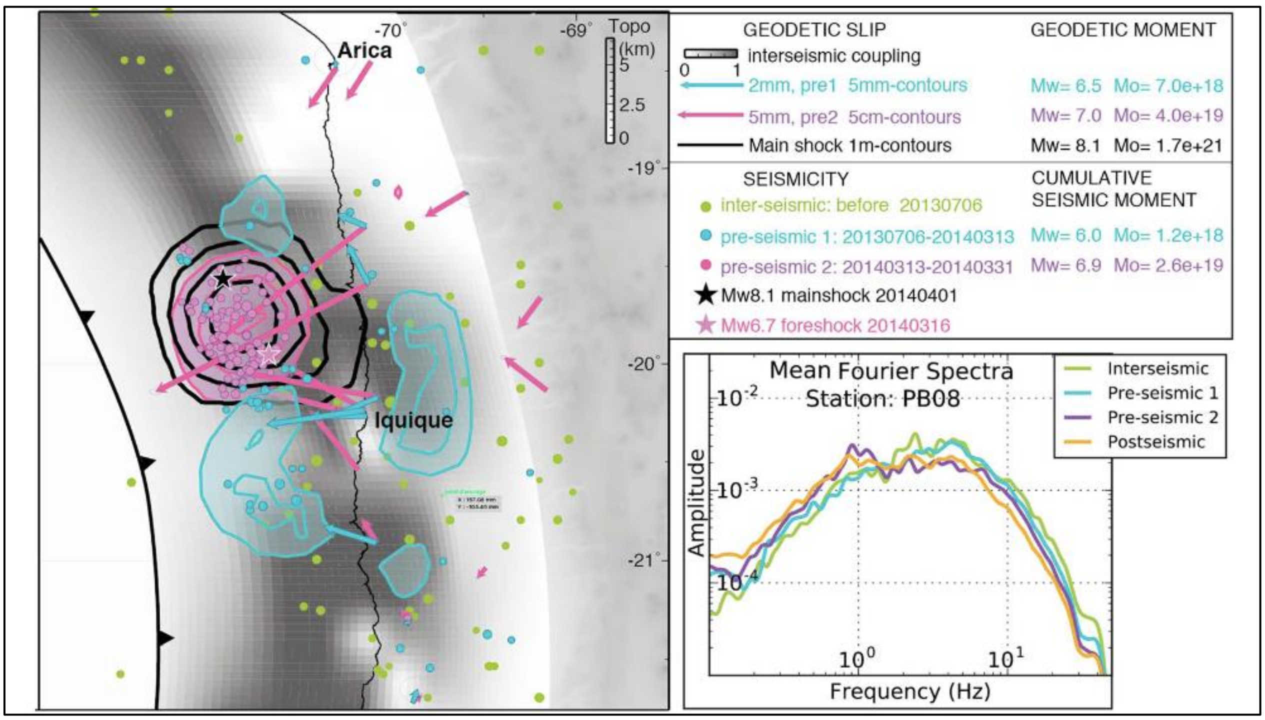

Figura 3-4: Deslizamientos lentos de corta y larga duración previo a la ocurrencia del terremoto de Iquique 2014 M_W 8.1. Modificado de Socquet et al. (2017).

3.2.2.2 Atacama

En el margen chileno, el primer deslizamiento lento profundo de larga duración fue observado en la región de Atacama, donde el ridge de Copiapó se encuentra subductando bajo la placa Sudamericana (Klein et al., 2018, 2023). El deslizamiento lento ocurrió en la parte profunda de la zona de subducción (40-60 km), tuvo una duración aproximada de 18 meses (2014 a 2016) y una magnitud equivalente M_W 6.9 (Klein et al., 2023).

Utilizando solo una estación GPS, Klein et al. (2018) observan que deslizamientos similares habían ocurrido los años 2005 y 2009, sugiriendo un periodo de recurrencia para el evento de aproximadamente 5 años. En la Figura 3-5 se ilustran los periodos de tiempos donde se ha identificado la ocurrencia del deslizamiento lento profundo. Basados en esta observación, el año 2019 se desplegó en la zona una red densa de estaciones GPS, la que permitió detectar la ocurrencia del deslizamiento lento el año 2020 (ver Figura 3-6), validando de esta manera la periodicidad de 5 años observada en periodos anteriores (Klein et al., 2023).

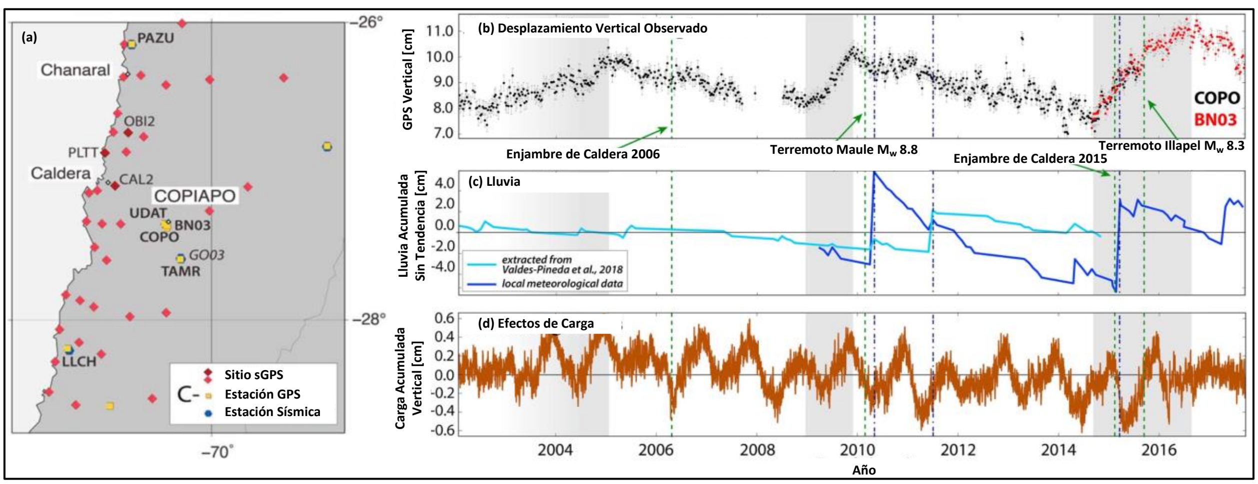

Figura 3-5: Deslizamiento lento profundo de larga duración en Atacama. (a) Mapa de estaciones GPS y sísmicas. (b) Serie de tiempo para el desplazamiento vertical en las estaciones COPO (negro) y BN03 (rojo). (b) Serie de tiempo acumulada sin tendencia para lluvia según Valdés-Pineda et al. (2018). (c) Cargas acumuladas para la estación COPO. Los periodos identificados como deslizamiento lento se destacan con áreas grises. Modificado de Klein et al. (2018).

Otras manifestaciones asociadas a terremotos lentos como tremores tectónicos, eventos repetitivos y enjambres han sido detectadas en la zona. Estas manifestaciones lentas se encuentran limitando la parte superior del área de ruptura generada por el deslizamiento lento (Pastén-Araya et al., 2022) y su distribución en profundidad se relaciona con la subducción del ridge de Copiapó el cual genera una segmentación de la sismicidad en profundidad. En particular, aquellas zonas donde ocurren manifestaciones lentas coinciden con anomalías de baja velocidad de V_p y V_s, indicando la posible presencia de fluidos. A pesar de lo anterior, hasta la fecha, no se ha observado una correlación temporal entre la ocurrencia del deslizamiento lento y manifestaciones sísmicas del mismo tipo.

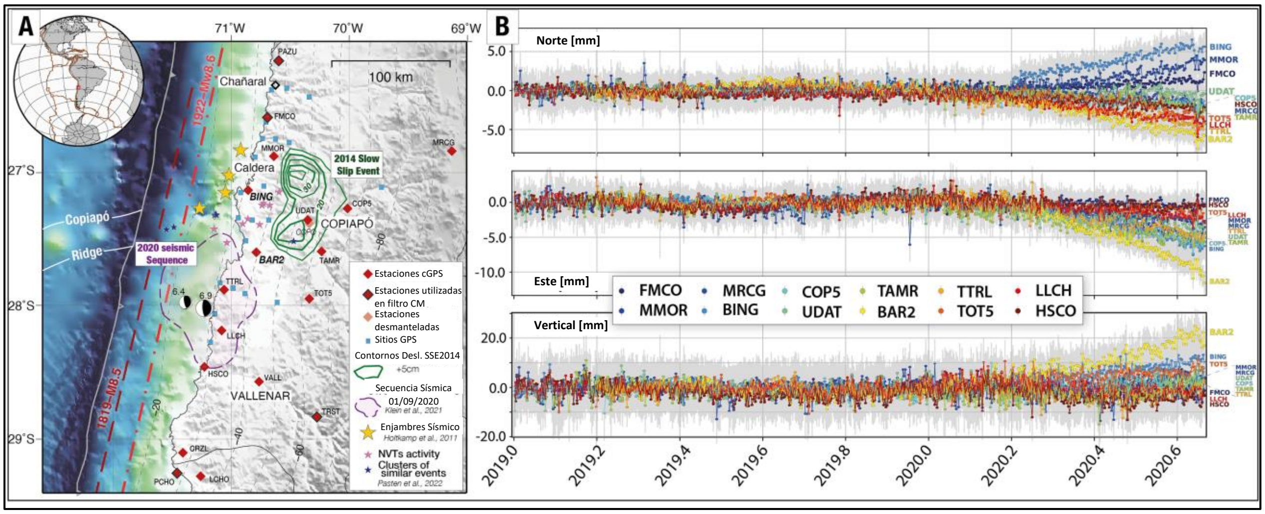

Figura 3-6: Deslizamiento lento profundo de larga duración en Atacama detectado el año 2020. (a) Contexto sismotectónico. (b) Series de tiempos de GPS para las estaciones mostradas en (a) sin tendencia y filtradas. Modificado de Klein et al. (2023).

En la misma zona, Ojeda et al. (2023) estudiaron el enjambre de Copiapó 2006 utilizando datos sísmicos y geodésicos. Durante el enjambre los autores detectan la migración de sismicidad a lo largo del contacto entre placas, la ocurrencia de potenciales eventos repetitivos y un potencial deslizamiento lento, este último observado en solo una estación GPS. Los autores proponen que el comportamiento dual (ordinario y lento) de este enjambre se debe a la subducción del Ridge de Copiapó, el cual afecta tanto a la interfaz entre placas como a la placa superior al inducir interacciones complejas entre procesos sísmicos y asísmicos, estos últimos favorecidos por la presencia de fluidos.

3.3 Señales Sísmicas Lentas

Hasta la fecha de publicación de la presente investigación, solo señales sísmicas lentas de tipo tremores tectónicos han sido reportadas a lo largo del margen chileno. Tremores superficiales se han reportados en la zona centro-sur (Tréhu et al., 2020) y sur (Sáez et al., 2019), mientras que, tremores profundos se han observado en la zona norte (Pastén-Araya et al., 2022) y sur de Chile (Gallego et al., 2013; Ide, 2012).

A continuación, se presenta un resumen de los tremores tectónicos identificados hasta la fecha y se adjuntan los trabajos realizados como primer autor o co-autor.

3.3.1 Tremores Tectónicos

3.3.1.1 Trabajos Previos

La primera observación de señales sísmicas lentas realizada en Chile corresponde al trabajo desarrollado por Ide (2012), quién utilizando una red temporal de estaciones sísmicas, identificó la ocurrencia de tremores tectónicos en las cercanías del punto triple, donde las placas de Nazca y Antártica subductan bajo la placa Sudamericana.

Los tremores tectónicos detectados presentan amplitudes relativamente bajas, con duraciones que varían desde horas hasta días y un escaso contenido de alta frecuencia (Gallego et al., 2013; Ide, 2012). En la Figura 3-7 se presenta un ejemplo de tremor tectónico detectado en el sur de Chile.

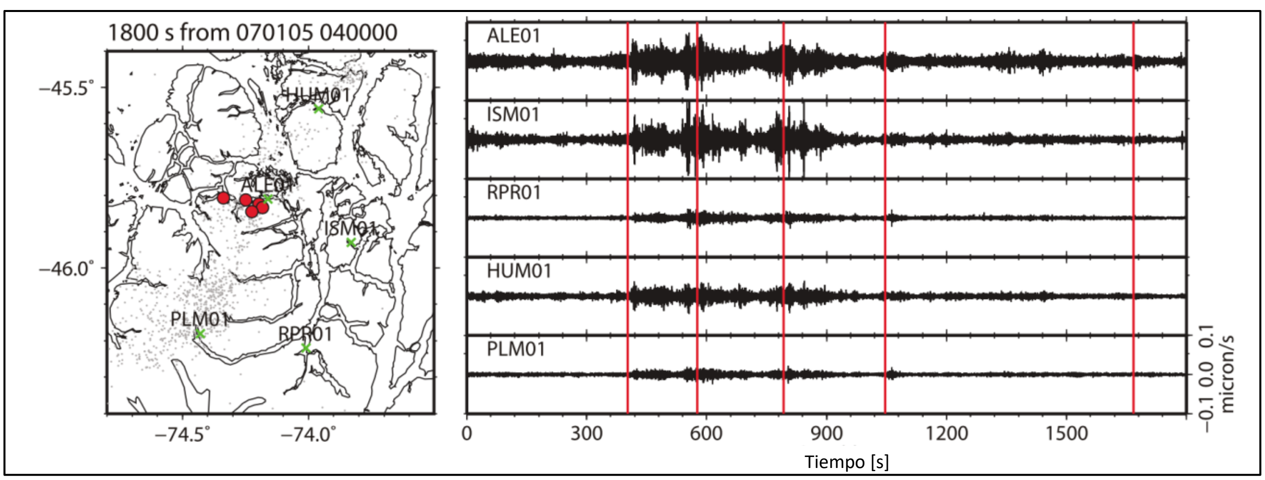

Figura 3-7: Ejemplos de tremores tectónicos detectados en el sur de Chile. Modificado de Ide (2012).

La distribución hipocentral de los tremores muestra que estos se generan a profundidades cercanas a los 30 km en la zona próxima al punto triple, y se empiezan a profundizar a medida que se alejan de dicho sector, alcanzando profundidades en torno a los ~50 km (Ide, 2012). La ubicación y profundidades estimadas permiten concluir que los tremores tectónicos ocurren en el contacto entre las placas de Nazca y Sudamericana.

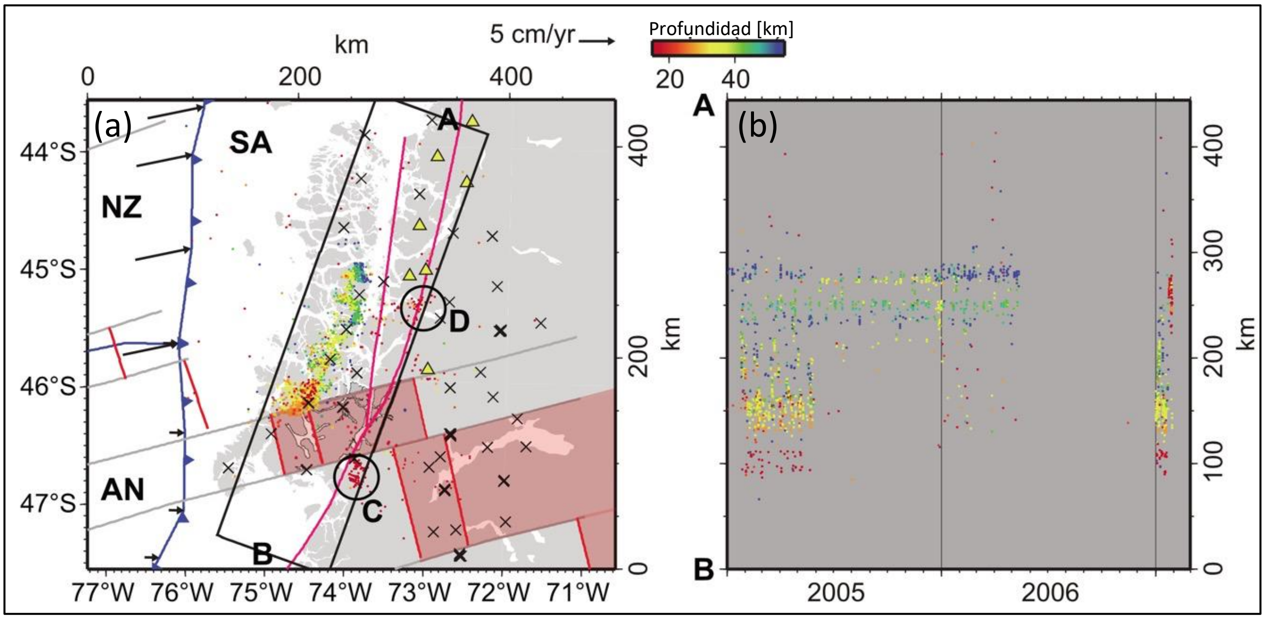

Figura 3-8: Tremores tectónicos detectados en el sur de Chile. (a) Distribución espacial y (b) distribución temporal. Modificado de Ide (2012).

De acuerdo, con Gallego et al. (2013) dentro de los tremores tectónicos es posible distinguir la ocurrencia de LFE, pero estos presentan en ocasiones diferencias de tiempo entre la llegada de la onda S y P cercanos a 1 [s]. Lo anterior, no es consistente con la localización de los tremores a profundidades mayores a 30 km. Los posibles LFE detectados por Gallego et al. (2013), corresponderían a terremotos superficiales que ocurren dentro de la placa Sudamericana.

Una de las principales características de los tremores tectónicos profundos del sur de Chile, es que presentan un alto grado de sensibilidad frente a cambios de mareas (Gallego et al., 2013) o el paso de ondas superficiales generadas por terremotos lejanos (Chao et al., 2019). En la Figura 3-9 se presentan dos ejemplos donde se muestra la correlación entre el aumento de esfuerzos debido a cambios de marea o el paso de ondas superficiales y la ocurrencia de tremores tectónicos.

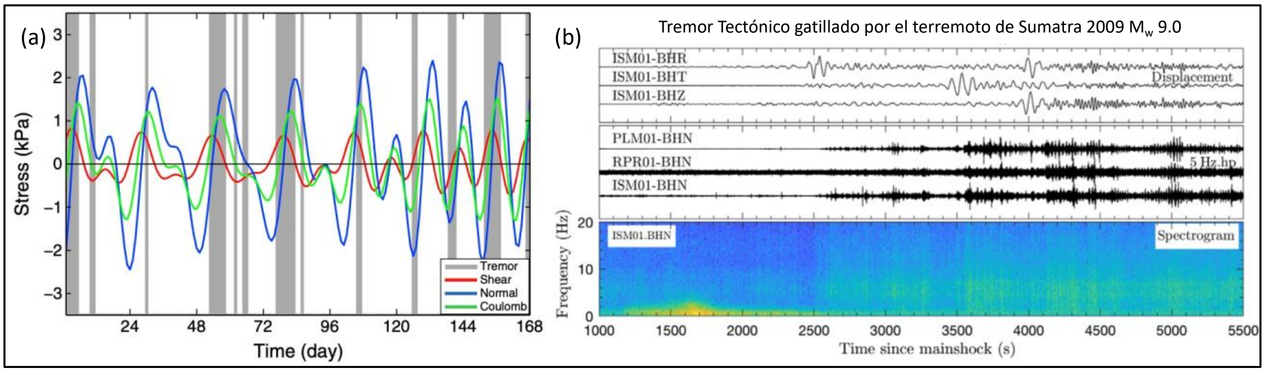

Figura 3-9: (a) Correlación entre la ocurrencia de tremores tectónicos (áreas grises) y esfuerzos tidales según componente. (b) Ejemplo de tremor tectónico gatillado por el paso de ondas superficiales generadas por el terremoto de Sumatra 2009 M_W 9.0. Modificado de Gallego et al. (2013) y Chao et al. (2019).

La sensibilidad detectada entre los tremores tectónicos y pequeñas variaciones de estrés, reflejan que estas manifestaciones lentas ocurren en fallas débiles que están muy cerca de romper (Rubinstein et al., 2008). Lo anterior, se podría generar si las altas presiones de confinamiento son mitigadas por la presencia de agua y presiones de poro casi litostáticas (Nishikawa et al., 2023; Rubinstein et al., 2010).

3.3.2 Resumen Señales Sísmicas Lentas en Chile

Hasta el año 2024, en Chile se han identificado las siguientes manifestaciones lentas y ordinarias-lentas:

- Deslizamientos lentos de larga duración;
- Deslizamientos lentos de corta duración;
- Tremores tectónicos;
- Terremotos de baja frecuencia;
- Terremotos repetitivos.

A la fecha, los terremotos de muy baja frecuencia (VLFE) corresponden a la única señal sísmica lenta no identificada.

3.3.2.1 Método de Búsqueda Señales Lentas

Una de las principales tareas desarrolladas durante la presente investigación fue la búsqueda de tremores tectónicos a lo largo del margen chileno. La búsqueda se realizó en redes sismológicas desplegadas en el fondo del mar, así como también, en tierra.

El carácter no impulsivo de los tremores tectónicos genera que en ocasiones estos se confundan con otros tipos de señales, tales como, frentes de ondas superficiales generadas por terremotos lejanos (Romanet & Ide, 2019) u ondas de tipo T-Phases (Katakami et al., 2017). Estas últimas, corresponden a ondas de sonido de alta frecuencia (2-8 Hz) que se generan por la conversión de las ondas sísmicas P y S al entrar en contacto con la interfaz continente-mar (Talandier & Okal, 1998). Al convertirse en ondas de sonido, la T-Phase es atrapada por un canal de baja velocidad (SOFAR) que le permite viajar grandes distancias con una atenuación despreciable (Thorp, 1965).

Diversos autores han mostrado las dificultades que presenta el discernir señales asociadas a tremores tectónicos respecto de formas de ondas generadas por el paso de la T-Phase (Katakami et al., 2017; Obana & Kodaira, 2009; Plata-Martinez et al., 2021). Dada esta problemática, el primer trabajo desarrollado durante la investigación fue la detección y caracterización de ondas T-Phase generadas por terremotos chilenos y detectadas en la isla Juan Fernández. Los trabajos desarrollados respecto de este tema son Sáez & Ruiz, (2018) y Carrasco et al., (2019), los cuales se presentan en el Anexo 1 y 2, respectivamente. Los trabajos mencionados permitieron concluir que la T-Phases generadas en el margen chileno presentan un contenido de frecuencia rico entre los 2-8 [Hz] (similar al tremor tectónico) y que su atenuación al entrar en contacto con el continente es muy fuerte, no siendo posible identificar su arribo en estaciones sismológicas desplegadas en la costa.

La segunda parte de la investigación se enfocó en el desarrollo de rutinas computacionales para la detección de tremores tectónicos. Las rutinas desarrolladas corresponden a una modificación de la metodología temporal propuesta por Ide (2010, 2012), la cual se basa en estimar el grado de correlación que existe entre las envolventes de las señales registradas en una red sismológica. A continuación, se detalla el procedimiento utilizado en todos los trabajos en los que se realizó la búsqueda de tremores tectónicos a lo largo de Chile.

1. Los datos obtenidos se transforman a formato SAC, se verifica que cada archivo posea la siguiente información: tiempo de origen, latitud, longitud, profundidad y frecuencia de muestreo. Adicionalmente, se comprueba que cada archivo a procesar posea la cantidad de datos correspondiente a un día de medición. En el caso de que existan gaps de información menores a 6 horas, estos se rellenan con ruido blanco.
2. A los datos que cumplen las condiciones señaladas anteriormente, se les remueve la tendencia y se le aplica un taper tipo “tukeywin” utilizando para ello una longitud igual al 1% del largo total.
3. Posteriormente, los datos son filtrados en el rango de frecuencia donde los tremores tectónicos pueden ser diferenciados de los terremotos locales. Generalmente, el filtro utilizado corresponde a un Butterworth pasa banda entre 2-8 [Hz] de cuarto orden. Las trazas filtradas son elevadas al cuadrado, filtradas con un filtro pasa bajo de frecuencia esquina 10 s y resampleadas a 1 muestra por segundo. En la Figura 3-10 se ilustra un ejemplo con la envolvente calculada para una traza temporal.
4. Los pasos detallados anteriormente se realizan para todas las componentes horizontales disponible en cada arreglo sísmico. Se utiliza solo esta componente debido a que los tremores tectónicos están dominados principalmente por ondas S (Ide, 2012).
5. Para todas las combinaciones posible dentro del arreglo, se calcula la correlación cruzada entre las envolventes, utilizando para ello ventanas de 300 [s] y un traslape de 150 [s]. El coeficiente de correlación $C_{ij}(\Delta t_{ij})$ entre las envolventes horizontales y_i e y_j se calcula según la siguiente formula:

$$C_{ij}(\Delta t_{ij}) = \sum_{k=1}^{n} \frac{y_i(t_k)y_j\left(t_k + \Delta t_{ij}\right)}{\sqrt{\sum_{k=i}^{n}\left(y_i(t_k)\right)^2 \left(y_j\left(t_k + \Delta t_{ij}\right)\right)^2}} \quad (1)$$

6. Si el máximo coeficiente de correlación excede un valor en un determinado número de estaciones, la ventana pasa a la siguiente etapa. Tanto el coeficiente de correlación como el número de estaciones se definen según la calidad de los datos y la cantidad de sensores disponibles en cada arreglo, pero en general, estos valores oscilan entre 0.5-0.65 para el coeficiente de correlación en al menos 4 estaciones.
7. El set de tiempos Δt_{ij} que maximiza el coeficiente de correlación para los distintos pares de estaciones es almacenado y utilizado para la determinación de los hipocentros. Para un evento x_0 su hipocentro es determinado a partir de minimizar mediante mínimos cuadrados la siguiente ecuación:

$$\Delta t_{ij} = T(x_j, x_0) - T(x_i, x_0) \tag{2}$$

Donde $T(x_1, x_2)$ es el tiempo de viaje de la onda S entre x_1 y x_2. Debido a que $T(x_1, x_2)$ es una función no lineal se utilizó el método Levenberg-Mardquardt para resolver la Ecuación (2). Para más detalles respecto de la resolución revisar Ide (2012).

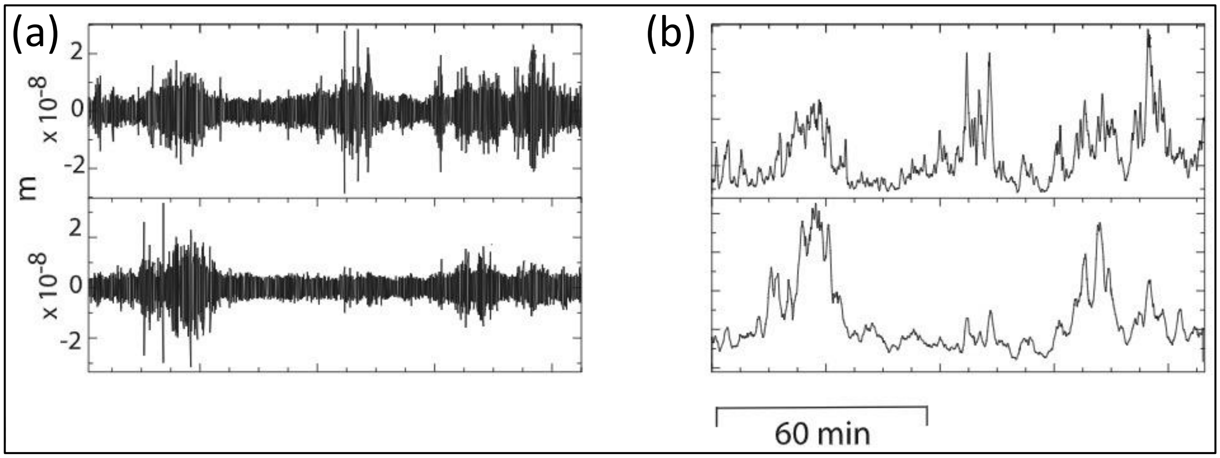

Figura 3-10: Metodología para la búsqueda de tremores tectónicos. (a) Traza temporal y (b) envolvente de la traza mostrada en (a). Modificado de Schwartz & Rokosky (2007).

Utilizando la metodología detallada anteriormente se realizó la búsqueda de tremores tectónicos en los siguientes arreglos:

- Instrumentos OBS desplegados sobre el punto triple chileno (Sáez et al., 2019);
- Instrumentos OBS desplegados frente a las costas de Pichilemu (Tréhu et al., 2019);
- Instrumentos banda ancha desplegados en las cercanías de Copiapó, Región de Atacama (Pastén-Araya et al., 2022).
- Instrumentos banda ancha desplegados en el sistema de fallas Liquiñe-Ofqui (Sáez et al., 2024 *en preparación*).

A continuación, se presentan los artículos científicos generados a partir de las observaciones realizadas, detallando en cada uno de ellos el trabajo realizado.

3.3.2.2 Tremores Tectónicos sobre el Punto Triple

El objetivo de esta investigación era comprender qué tipo de manifestaciones sísmicas lentas y ordinarias se generaban durante la subducción del Ridge de Chile. Para lo anterior, se utilizó un arreglo de estaciones OBS desplegados sobre el punto triple en marzo del año 2009. El arreglo estuvo compuesto por cinco estaciones de periodo corto, las cuales registraron de manera continua ruido sísmico por un periodo de seis meses.

El trabajo realizado en la investigación consistió en el desarrollo de la hipótesis de trabajo, procesamiento de datos, análisis de resultados y escritura del artículo. A continuación, se presenta el articulo científico publicado, en el cual, participé como primer autor.

Ⓔ

Shallow Nonvolcanic Tremor Activity and Potential Repeating Earthquakes in the Chile Triple Junction: Seismic Evidence of the Subduction of the Active Nazca–Antarctic Spreading Center

by Miguel Sáez, Sergio Ruiz, Satoshi Ide, and Hiroko Sugioka

ABSTRACT

In southern Chile, at ∼46.2°S and ∼75.2°W, the active spreading center between the Nazca and Antarctic plates is colliding with the South American plate, forming the Chile triple junction (CTJ). For 1 yr, from March 2009 to February 2010, five ocean-bottom seismometers (OBSs) were deployed over the CTJ. We used a portion of the OBS data to study the seismic signatures of the subduction of the active Nazca–Antarctic spreading center. Using the envelope technique, we detected long episodes of shallow nonvolcanic tremor (NVT) activity. To improve the identified location of the NVT activity, we cross-correlated the vertical and horizontal components of all located NVTs. In different months, we measured the local maximum of the lag-time correlation near 2 s, which is associated with the lag between the S and P waves ($S - P_{\mathrm{time}}$). Furthermore, we observed that in the days with intense tremor activity, the maxima corresponding to $S - P_{\mathrm{time}}$ emerged in windows without observable NVTs. We suggest that days with intense tremor activity correspond to an almost continuous slow slip, which may accelerate and decelerates nearly randomly, with spatial and temporal heterogeneity. In addition, we detected some potential repeating earthquakes with an $S - P_{\mathrm{time}}$ near 2 s, as well as NVTs. The detected NVT activity and potential repeating earthquakes suggest the existence of a shallow region close to the CTJ that is able to generate brittle (earthquakes) and brittle–ductile (potential repeating earthquakes and NVTs) ruptures.

Supplemental Content: Catalogs of nonvolcanic tremors (NVTs), local earthquakes, and repeating earthquakes detected using the ocean-bottom seismometer (OBS) data, and figure showing the hypocenters of localized earthquakes.

INTRODUCTION

The subduction of an active spreading center beneath a continental plate is a peculiar phenomenon in subduction environments. Currently, in southern Chile (at ∼46.2°S and 75.2° W), the Chile ridge (Nazca–Antarctic spreading center) is subducting beneath the continental South America plate, thereby forming the Chile triple junction (CTJ; Cande and Leslie, 1986; Bourgois *et al.*, 1996; Fig. 1). The collision of the CTJ with the continent has generated local tectonic erosion, rapid uplift, normal faulting, and sedimentary mass wasting in the last 14 Ma (Maksymowicz *et al.*, 2012; Folguera *et al.*, 2018). The presence of a slab window south of the CTJ and beneath the South American plate is another unusual signature of the actual subduction of the Chile ridge (Breitsprecher and Thorkelson, 2009; Russo *et al.*, 2010). Furthermore, some authors have proposed that the CTJ behaved as a barrier to the propagation of the 1960 Valdivia M_{w} 9.5 megathrust earthquake (Barrientos and Ward, 1990; Moreno *et al.*, 2009).

Seismically, the region around the CTJ has been characterized by a low rate of tectonic seismicity mostly related to shallow events ($M_{\mathrm{w}} \sim 0.5$–3.4) occurring in the overriding South American plate (Agurto-Detzel *et al.*, 2014). In addition, signatures of slow earthquakes such as deep nonvolcanic tremors (NVTs; Ide, 2012; Gallego *et al.*, 2013; Idehara *et al.*, 2014) and low-frequency earthquakes (LFEs; Gallego *et al.*, 2013) have been detected east of the CTJ (Fig. 1) at depths ranging between 30 and 50 km (Ide 2012; Idehara *et al.*, 2014). Tectonic tremor activity around the CTJ occurs on the plate boundary interface and is controlled by tidal stress (Ide 2012; Gallego *et al.*, 2013).

Slow earthquakes occur in areas surrounding the seismogenic zone, where large tsunamigenic and destructive

doi: 10.1785/0220180394

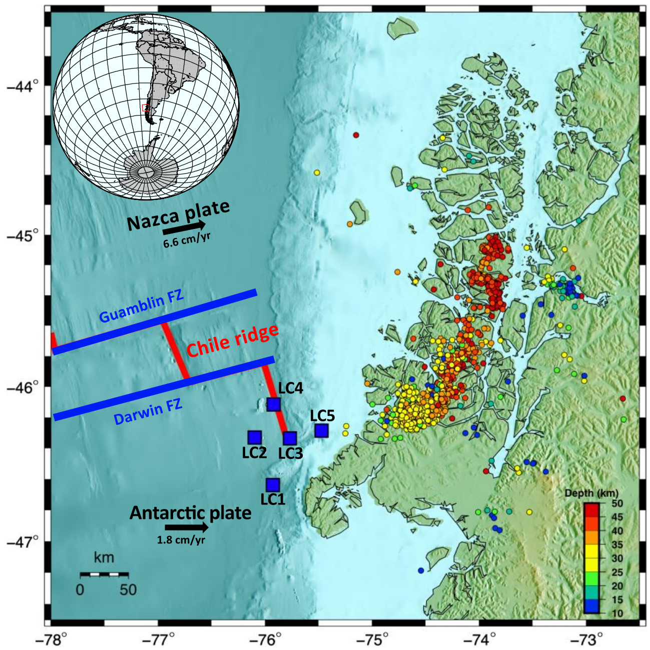

▲ **Figure 1.** Study area, seismic array, and distribution of slow-slip signatures. Blue squares show the locations of ocean-bottom seismometers (OBSs). Red and blue lines represent the Chile ridge spreading center and its fracture zones (FZs), respectively. Colored circles represent the distribution of nonvolcanic tremors (NVTs) according to Ide (2012) and obtained from Idehara *et al.* (2014). Red square in the inset corresponds to the study area. The color version of this figure is available only in the electronic edition.

megathrust earthquakes occur (Obara and Kato, 2016). Shallow tremor, LFEs, and very low-frequency earthquakes (VLFEs) occur in the shallow part of the plate boundary (Obana and Kodaira, 2009; Sugioka *et al.*, 2012; Nakano *et al.*, 2018) where tsunamigenic earthquakes occur (Lay *et al.*, 2012). On the other hand, different slow earthquakes signatures such as VLFEs, LFEs, and slow-slip event have been detected in the deepest zone of the seismogenic contact (Obara and Kato, 2016, and reference therein). Huge earthquakes such as the 2011 Tohoku-Oki M_w 9.0 and the 2014 Iquique M_w 8.1 were preceded by the occurrence of slow earthquakes (Kato *et al.*, 2012; Ito *et al.*, 2013; Kato and Nakagawa, 2014; Ruiz *et al.*, 2014). Studying the occurrence of slow earthquakes is crucial to better understand the generation of megathrust earthquakes. In this sense, in the present study, we attempt to answer the following questions:

1. What kind of seismic signature can be observed when an active spreading center begins to subduct?
2. Can the subduction of an active spreading center generate a slow earthquake?

To answer these questions, we analyzed six months of data recorded by five ocean-bottom seismometers (OBSs) deployed above the current CTJ position (Fig. 1).

This article is organized as follows. Descriptions of the data and instruments used are given in the Data section. In the NVTs in the CTJ section, we show the occurrence of shallow NVTs in the region. Later, in the $S-P$ Time in NVTs section, we apply the $S-P$ technique to the NVTs to constrain the tremor depth. In the Local Seismicity and Potential Repeating Earthquakes section, we show some examples of local earthquakes and repeaters. In the Discussion and Conclusions section, we discuss our results and analyze the relationship between the different observed seismic signatures. Finally, we propose that close to the CTJ, a region that is prone to break in a brittle–ductile manner generates potential repeating earthquakes and shallow NVT activity.

DATA

In March 2009, during the trans-Pacific Mirai cruise (MR08-08 Leg1), a temporary array of OBSs was installed near the CTJ (Abe, 2009). The array was composed of five 1 s Lennartz LE-3Dlite short-period instruments with a maximum aperture of ~50 km. The spatial distribution of the stations is shown in Figure 1. Stations LC2 and LC4 were located west of the trench, whereas stations LC5 and LC1 were located east of the trench. Station LC3 was located very close to the current position of the CTJ. The five OBS stations continuously recorded the horizontal (H1 and H2) and vertical (UD) directions at a rate of 200 samples per second from 2 March 2009 to 18 August 2009 and were removed in February 2010. Unfortunately, stations LC3 and LC4 stopped recording on 18 August 2009 and 26 January 2010, respectively.

NVTs IN THE CTJ

To look for NVT activity, the envelope correlation method (Ide, 2010, 2012) was performed with the OBS data. This methodology, which is used to detect NVTs, follows the following steps (Ide, 2012).

1. Original velocity records are band-pass filtered between 2 and 8 Hz.
2. The filtered velocity data are squared, low-pass filtered at 0.1 s, and resampled at 1 sample per second. The square root of this output is the envelope data.
3. The envelopes are cross-correlated using 300 s time windows with a 150 s overlap.

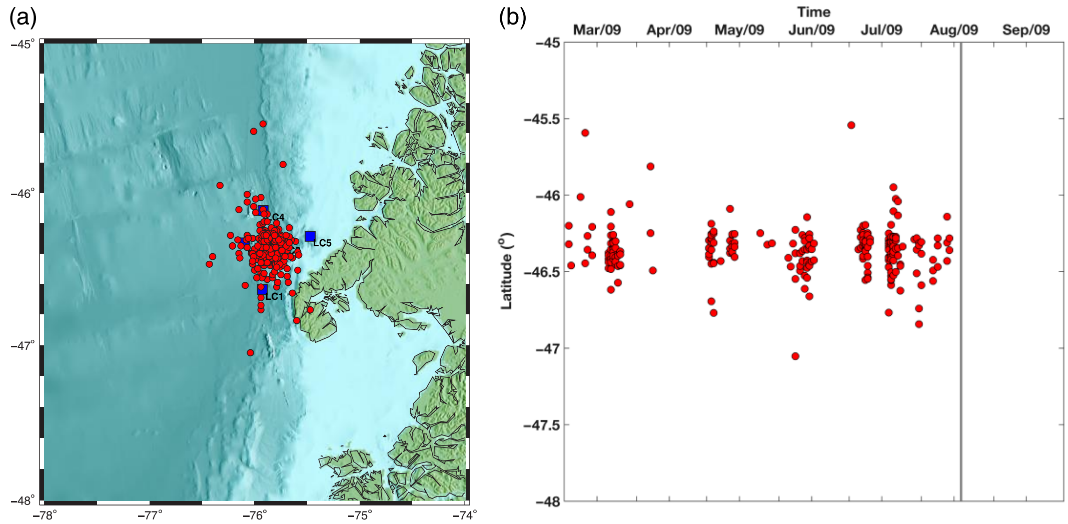

▲ **Figure 2.** Spatiotemporal distribution of NVTs in the Chile triple junction (CTJ) (Ⓔ Table S1, available in the supplemental content to this article). (a) Red circles represent the NVTs detected using the envelope technique and blue squares show the location of OBS stations. (b) Temporal distribution of the NVTs shown in (a). Gray line shows the time at which station LC3 stopped recording. The color version of this figure is available only in the electronic edition.

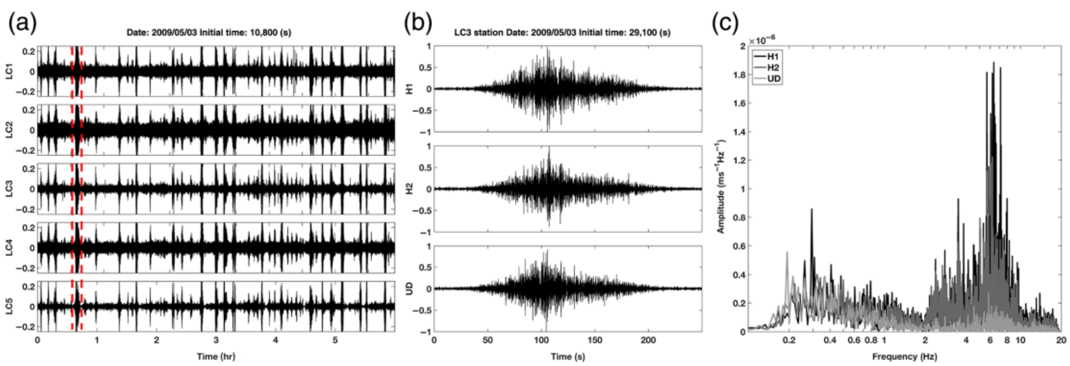

▲ **Figure 3.** Examples of detected nonvolcanic activity. (a) About 6 hr of intense tremor activity recorded by the five OBS stations on 5 May from 3 a.m. to 9 a.m. (b) Three components of the NVTs that are highlighted with red dotted lines in (a). (c) Spectrum of tremor signals shown in (b). H, horizontal component; UD, vertical component. The color version of this figure is available only in the electronic edition.

4. An event is identified if the maximum cross correlation is greater than or equal to 0.6 in more than five pair stations.
5. The event location is determined by minimizing the set of differential arrivals Δt^{ij} and solving a nonlinear least-squares problem, and the duration is measured using the half-value width of the stacked envelope.
6. If the duration is longer than 80 s and the root mean square is less than 2.5 (see Ide, 2012), we regard the event as a tremor.

The epicentral distribution of the detected NVTs according to latitude and longitude is shown in Figure 2a. This figure shows that tremors are located mainly within the array, and the most intense activity occurs around station LC3. In addition, intense tremor activity was observed in the months of March, May, June, and July (Fig. 2b). Information for 6 hr of a day with intense NVT activity is shown in Figure 3a. The detected NVTs are characterized by the generation of a nonimpulsive

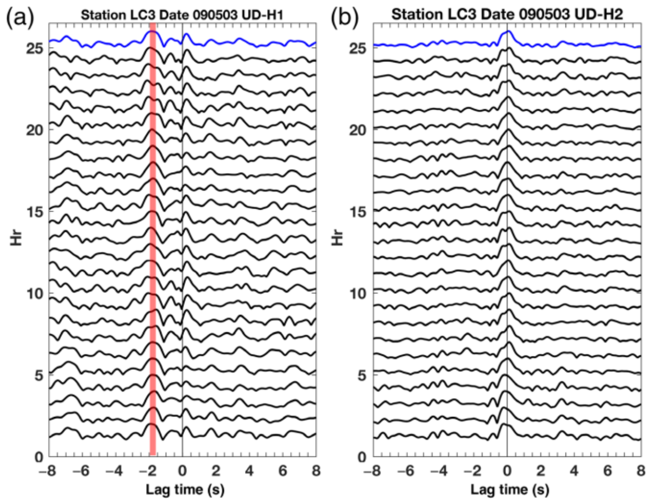

▲ **Figure 4.** Envelope of the cross correlation between the (a) UD–H1 and (b) UD–H2 components, as recorded by station LC3, in a day with intense NVT activity. Black lines show the hourly stacking of 5 min windows (see the NVTs in the CTJ section for more details), whereas blue lines represent the average envelope of the day. The red line indicates the maximum of the envelope function and is interpreted as the lag between the S and P waves ($S - P_{\mathrm{time}}$). The color version of this figure is available only in the electronic edition.

signal (it is not possible to distinguish the arrival of the P wave or S wave) with durations greater than 150 s (Fig. 3b). These signal features are typical of tectonic tremors and have been observed at various sites worldwide (Beroza and Ide, 2011; Ide, 2012; Obara and Kato, 2016). A catalog of tremor is presented in Ⓔ Table S1 (available in the supplemental content to this article).

$S - P$ TIME IN NVTs

Because of the nonimpulsive nature of the tremor signal, traditional methodologies used to locate NVTs have poor depth resolution (Rubinstein *et al.*, 2009). To overcome this limitation, it is possible to measure the S minus P time ($S - P_{\mathrm{time}}$) of an NVT signal using the cross correlation between the vertical and horizontal components. The $S - P$ technique (La Rocca *et al.*, 2009) has been used successfully in Japan (Yabe and Ide, 2013) and Cascadia (La Rocca *et al.*, 2009, 2010), where the technique allowed researchers to locate NVTs near or on the subducting slab interface. Because our aperture array is greater than 20 km, we modified the original methodology proposed by La Rocca *et al.* (2009). The $S - P_{\mathrm{time}}$ was calculated following the next steps.

1. Continuous daily traces are demeaned, detrended, and band-pass filtered between 5 and 8 Hz using a fourth-order Butterworth filter.
2. The daily filtered traces are divided into 5 min windows.
3. One-bit normalization (all positive amplitudes are replaced by 1, whereas all negative amplitudes are replaced with −1) is performed in each available window.
4. Cross correlation between UD–H1 and UD–H2 is conducted in every normalized window. Cross correlation is calculated by shifting the horizontal components.
5. Stacking of the cross-correlated windows each hour is performed, and finally, the envelope is calculated.

The results of the application of the $S - P$ method to the UD–H1 and UD–H2 components recorded at the LC3 station on a day with intense tremor activity are shown in Figure 4a and 4b, respectively. In Figure 4a, it is possible to measure a local maximum lag-time correlation near −2 s that is associated with the lag between the S and P waves ($S - P_{\mathrm{time}}$). The correlations between the UD and H1 components are antisymmetric, and the corresponding maximum is associated with negative lag times. This result can be interpreted as indicative that the UD components are composed mainly of P waves, whereas the horizontal (H1) components are composed mainly of S waves. When we cross-correlated the UD–H2 components, the $S - P_{\mathrm{time}}$ did not emerge (Fig. 4b). Furthermore, the $S - P$ methodology only worked at the LC3 station, which probably suggests that tremor activity is occurring with a particular radiation pattern below LC3 (Yabe and Ide, 2013).

LOCAL SEISMICITY AND POTENTIAL REPEATING EARTHQUAKES

The seismicity of the region around the CTJ is mainly associated with volcanic activity. In a secondary order, it is possible to observe tectonic activity east of the CTJ related to low-magnitude shallow earthquakes ($M_{\mathrm{w}} \sim 0.5$–3.4) occurring within the South American plate (Agurto-Detzel *et al.*, 2014). Using the OBS data and visual inspection, we were able to detect the occurrence of 40 local earthquakes (see Ⓔ Table S2). The detected earthquakes show a low amplitude and can be clearly observed only at station LC3, whereas at the other stations, it is possible to observe the arrival of a high-frequency content, but it is not possible to clearly distinguish the arrival of the first P wave or S wave (Fig. 5a). Using the SEISAN software, we were able to locate 8 of the 40 available local earthquakes. The localized events are concentrated around LC3 and aligned with the Chile Rise (Ⓔ Fig. S1). The depth of local earthquakes varies between 14 and 21 km, whereas their local magnitude varies between $M_{\mathrm{L}} - 0.3$ and −1.2 (Ⓔ Table S3). Local earthquakes recorded at station LC3 are characterized by $S - P_{\mathrm{time}}$ values from 1.5 to 2 s, and the P wave is impulsive only in the UD component (Fig. 5b). The $S - P_{\mathrm{time}}$ near 2 s obtained in local earthquakes is similar to the $S - P_{\mathrm{time}}$ on day with intense

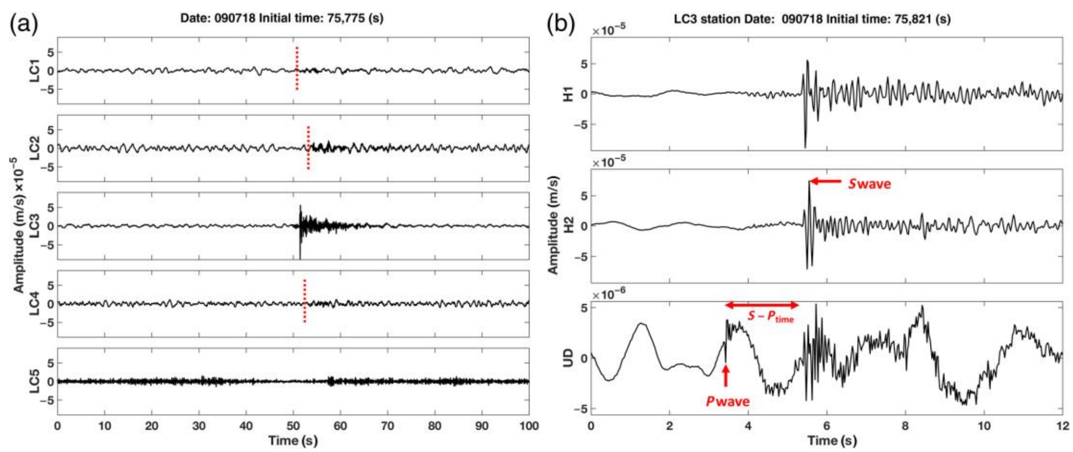

▲ **Figure 5.** Example of a local earthquake. (a) H1 component of the seismogram recorded by the five OBS stations. A local earthquake is clearly visible only at station LC3, whereas at stations LC1, LC2, and LC4, it is possible to observe the arrival of a high-frequency content (dotted red line). (b) H1, H2, and UD components of the local earthquake shown in (a) and recorded by station LC3. The arrivals of *P* and *S* waves are indicated by red arrows, whereas the time difference between both phases is called $S - P_{time}$. Notably, the *P* wave is clearly visible in only the UD component. The color version of this figure is available only in the electronic edition.

tremor activity. Because of the particular signatures of these local seismic activities, we selected local earthquakes as templates to find repeating earthquakes. To detect repeaters, we followed the methodology proposed by Kato and Nakagawa (2014). First, we filtered the daily waveform data with a Butterworth band-pass filter from 2 to 8 Hz and 4 to 8 Hz. As template events, we selected the 40 detected local earthquakes, and then the waveform was cut 2 s before and 8 s after the arrival of the *P* wave. The template was cross-correlated with six months of filtered daily waveform data. If the cross-correlation coefficient exceeded 0.95 at station LC3, we identified the event as a "potential repeating earthquake." Traditional methodologies consider an event as repeaters if the correlation coefficient is major than 0.95 in more than two stations (Uchida and Matsuzawa, 2013; Kato and Nakagawa, 2014). In this work, we used only the waveforms recorded by station LC3 because in the other stations it was not possible to distinguish the arrival of the impulsive *P* and *S* phases; therefore, low correlation coefficients were obtained. Figure 6 shows some examples of potential repeating earthquakes. A catalog of potential repeating earthquakes is presented in Ⓔ Tables S4 and S5.

DISCUSSION AND CONCLUSIONS

Local and Potential Repeating Earthquakes

The $S - P_{time}$ calculated for a large number of local earthquakes varies between 1.5 and 2 s (Fig. 5b). These $S - P_{time}$ values suggest that brittle ruptures are occurring at shallow depths. On the other hand, the occurrence of potential repeating earthquakes (Fig. 6) can be interpreted as the seismic evidence of a possible shallow slow slip occurring in a hydrated and fractured zone close to the CTJ (Kato *et al.*, 2012; Kato and Nakagawa, 2014; Poli *et al.*, 2017; Nishikawa and Ide, 2018). The occurrence of local and potential repeating earthquakes is observed only at station LC3, whereas the *P* wave is recorded only in the UD component (Fig. 5b). Based on these observations, we propose that local and potential repeating earthquakes with a similar rupture pattern are occurring close to station LC3.

Shallow NVT Activity in the CTJ

Seismic signatures of slow earthquakes such as NVTs and LFEs have been detected east of the CTJ at depths ranging between 30 and 50 km (Ide, 2012; Gallego *et al.*, 2013; Fig. 1). Deep NVTs are produced in the plate interface and are modulated by tidal stress (Ide, 2012; Gallego *et al.*, 2013). In this study, using OBS data, we detected episodes of intense NVT activity with an $S - P_{time}$ near 2 s (Fig. 4a). This observation corresponds to the first evidence of shallow NVT activity in the Chilean margin (Obara and Kato, 2016). Tremors in the CTJ are characterized by no impulsive signals, with a duration ranging from ten seconds to minutes and a frequency content between 2 and 20 Hz (Fig. 3).

The NVT activity in the CTJ is not persistent. We detected consecutive days in the months of March, May, June, and July during which the $S - P_{time}$ was ~2 s (Fig. 7a). These days are characterized by intense tremor activity (Fig. 7c). On the other hand, we observed days without tremor activity (Fig. 7b) during which the $S - P_{time}$ did not emerge (Fig. 7a). On a day with intense tremor activity, the proposed $S - P$ methodology does not distinguish whether

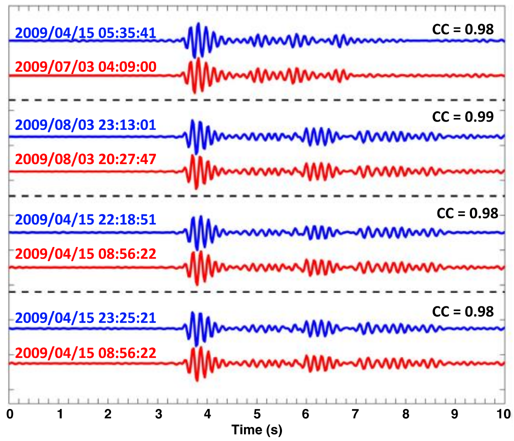

▲ **Figure 6.** Examples of detected potential repeating earthquakes. Red and blue colors represent the template and detected repeating earthquakes, respectively. Each trace is normalized by the maximum amplitude value. The cross-correlation coefficient (CC) is indicated in the upper right part of each panel. Templates were filtered between 4 and 8 Hz. The color version of this figure is available only in the electronic edition.

the cross-correlated windows have an observable NVT. The cross correlation of a window without an observable NVT (Fig. 8c) has a maximum at a lagged time near 2 s. Similar $S - P_{\text{time}}$ values are obtained when windows with observable NVTs are cross-correlated (Fig. 8a). We suggest that days with intense tremor activity correspond to an almost continuous slow slip, which may accelerate and decelerates nearly randomly, with spatial and temporal heterogeneity. Changes in the rupture velocity of this slow slip are observed as intense and observable NVT activity. When the velocity of the slow slip is nearly constant, visible tremors are lost in the ambient seismic noise; however, the tremors are detectable using the $S - P_{\text{time}}$ cross-correlation technique. On a day with intense tremor activity, the continuous slow slip can be observed as a rich and persistent high-frequency content between 2 and 10 Hz (Fig. 8b). On the other hand, observable NVTs can be distinguished as the arrival of a high-frequency content between 2 and 20 Hz. Because this frequency content is greater than the typical 2–8 Hz observed in deep and shallow NVTs (Obana and Kodaira, 2009; Ide, 2012; Kaneko *et al.*, 2018), we suggest that the tremor source in the CTJ is close to the OBS array.

Where Are the Observed Seismic Signals Being Generated?

We detected the occurrence of local earthquakes, potential repeating earthquakes, and NVTs close to the CTJ. The $S - P_{\text{time}}$ near 2 s observed in the different seismic signals suggests that close to the CTJ, there is probably a shallow zone that is able to generate brittle (earthquakes) and brittle–ductile (repeating earthquakes and NVTs) ruptures. This zone may be fractured and hydrated, which would facilitate the occurrence of shallow NVTs (Toh *et al.*, 2018) and repeating earthquakes (Poli *et al.*, 2017). Unfortunately, there are no 2D velocity models under the CTJ that allow us to understand where the observed signal comes from. Maksymowicz *et al.* (2012) obtained a seismic reflection profile north and very close to the LC3 station. The profile shows the presence of a structure interpreted as a frontal accretionary prism that could generate these observed seismic signals (Maksymowicz *et al.*, 2012). Shallow NVTs associated with reverse faults in a shallow accretionary prism (Obana and Kodaira, 2009) or by shear failure in the décollement zone along the plate interface (Sugioka *et al.*, 2012) have been detected in Japan. Furthermore, shallow VLFEs (Nakano *et al.*, 2018; Toh *et al.*, 2018) and LFEs (Obana and Kodaira, 2009) have been detected accompanying shallow tremor activity and shallow slow slips. Unfortunately, we were not able to detect VLFEs and LFEs probably because the OBS stations use short-period instruments; despite this, we do not discard the possible

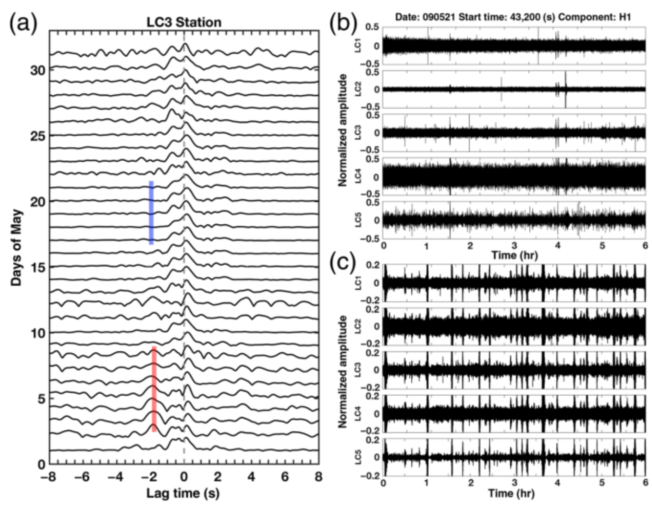

▲ **Figure 7.** (a) Daily envelope of the cross correlation between the UD and H1 components for the days of May. The vertical red line indicates consecutive days during which the $S - P_{\text{time}}$ near 2 s emerges, and the vertical blue line shows consecutive days during which $S - P_{\text{time}}$ cannot be identified. (b) About 6 hr of a day during which the $S - P_{\text{time}}$ does not emerge; (c) 6 hr of a day during which the $S - P_{\text{time}}$ emerges. The color version of this figure is available only in the electronic edition.

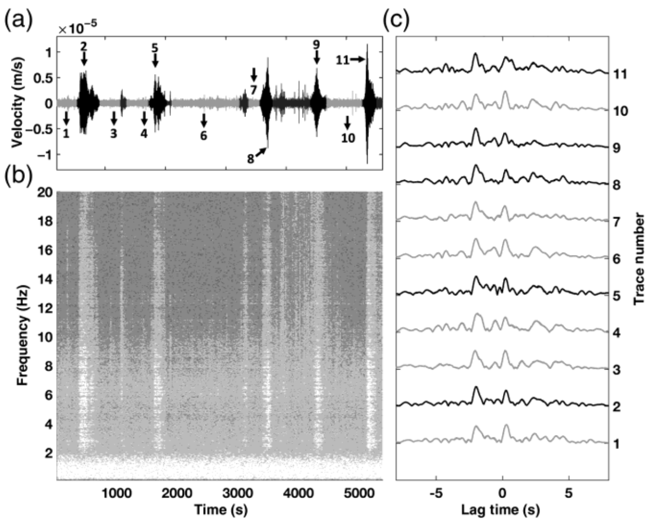

▲ **Figure 8.** (a) H1 component recorded by station LC3 in a day with intense tremor activity. Arrows indicate the number of traces shown in (c). (b) Spectrogram of the waveform shown in (a). (c) Envelopes of the cross correlations between the UD and H1 components of the traces shown in (a).

occurrence of another slow-slip earthquake signature in the CTJ. Another possibility is that the different observed seismic signals come from transforming faults which are seismically active before subducting under the South American plate.

DATA AND RESOURCES

The data used in the present work were obtained during the trans-Pacific Mirai cruise (MR08-08 Leg1). The seismic array was composed of five 1 s Lennartz LE-3Dlite short-period ocean-bottom seismometers (OBSs). The array recorded continuously from March 2009 to February 2010. The cruise report is available at http://www.godac.jamstec.go.jp/catalog/data/doc_catalog/media/MR08-06_leg1_all.pdf. The event data are available at http:/p21.jamstec.go.jp/chobs/. The authors are happy to share the continuous data upon request. All websites were last accessed May 2019.

ACKNOWLEDGMENTS

Miguel Sáez thanks the scholarship PCHA/Doctorado Nacional/2017-21171480, granted by Comisión Nacional de Investigación Científica y Tecnológica (CONICYT). S. R. thanks the support of Chilean Fondo Nacional de Desarrollo Científico y Tecnológico (FONDECYT), Grant Number 1170430, and CONICYT Programa de Investigación Asociativa (PIA)/Anillo de Investigación en Ciencia y Tecnología ACT172002. Authors thank Japan Society for the Promotion of Science (JSPS) Inter-University Exchange Project (Sciece and Engineering Exchange program with Latin America [SEELA]), JSPS Grants-in-Aid for Scientific Research (KAKENHI) (16H02219), and the Ministry of Education, Culture, Sports, Science and Technology (MEXT) KAKENHI (16H06477).

REFERENCES

Abe, N. (2009). Preliminary report on MR08-06 Leg1 Marine Geological and Geophysical Research: A complete trans-Pacific Cruise, *AGU Fall Meeting Abstracts*, San Francisco, California, 14–18 December 2019, Abstract ID OS13A-1191.

Agurto-Detzel, H., A. Rietbrock, K. Bataille, M. Miller, H. Iwamori, and K. Priestley (2014). Seismicity distribution in the vicinity of the Chile triple junction, Aysén region, southern Chile, *J. S. Am. Earth Sci.* **51,** 1–11.

Barrientos, S. E., and S. N. Ward (1990). The 1960 Chile earthquake: Inversion for slip distribution from surface deformation, *Geophys. J. Int.* **103,** no. 3, 589–598.

Beroza, G. C., and S. Ide (2011). Slow earthquakes and nonvolcanic tremor, *Annu. Rev. Earth Planet. Sci.* **39,** 271–296.

Bourgois, J., H. Martin, Y. Lagabrielle, J. Le Moigne, and J. Frutos Jara (1996). Subduction erosion related to spreading-ridge subduction: Taitao peninsula (Chile margin triple junction area), *Geology* **24,** no. 8, 723–726.

Breitsprecher, K., and D. J. Thorkelson (2009). Neogene kinematic history of Nazca–Antarctic–Phoenix slab windows beneath Patagonia and the Antarctic Peninsula, *Tectonophysics* **464,** nos. 1/4, 10–20.

Cande, S. C., and R. B. Leslie (1986). Late Cenozoic tectonics of the southern Chile trench, *J. Geophys. Res.* **91,** no. B1, 471–496.

Folguera, A., E. Contreras-Reyes, N. Heredia, A. Encinas, S. B. Iannelli, V. Oliveros, F. M. Dávila, G. Collo, L. Giambiagi, and A. Maksymowicz (2018). *The Evolution of the Chilean–Argentinean Andes*, Springer, Berlin, Germany.

Gallego, A., R. M. Russo, D. Comte, V. Mocanu, R. E. Murdie, and J. C. Vandecar (2013). Tidal modulation of continuous nonvolcanic seismic tremor in the Chile triple junction region, *Geochem. Geophys. Geosys.* **14,** no. 4, 851–863.

Ide, S. (2010). Striations, duration, migration and tidal response in deep tremor, *Nature* **466,** no. 7304, 356.

Ide, S. (2012). Variety and spatial heterogeneity of tectonic tremor worldwide, *J. Geophys. Res.* **117,** no. B3, doi: 10.1029/2011JB008840.

Idehara, K., S. Yabe, and S. Ide (2014). Regional and global variations in the temporal clustering of tectonic tremor activity, *Earth Planets Space* **66,** no. 1, 66.

Ito, Y., R. Hino, M. Kido, H. Fujimoto, Y. Osada, D. Inazu, Y. Ohta, T. Iinuma, M. Ohzono, and S. Miura (2013). Episodic slow slip events in the Japan subduction zone before the 2011 Tohoku-Oki earthquake, *Tectonophysics* **600,** 14–26.

Kaneko, L., S. Ide, and M. Nakano (2018). Slow earthquakes in the microseism frequency band (0.1–1.0 Hz) off Kii Peninsula, Japan, *Geophys. Res. Lett.* **45,** no. 6, 2618–2624.

Kato, A., and S. Nakagawa (2014). Multiple slow-slip events during a foreshock sequence of the 2014 Iquique, Chile M_w 8.1 earthquake, *Geophys. Res. Lett.* **41,** no. 15, 5420–5427.

Kato, A., K. Obara, T. Igarashi, H. Tsuruoka, S. Nakagawa, and N. Hirata (2012). Propagation of slow slip leading up to the 2011 M_w 9.0 Tohoku-Oki earthquake, *Science* 335**,** no. 6069, 705–708.

La Rocca, M., K. C. Creager, D. Galluzzo, S. Malone, J. E. Vidale, J. R. Sweet, and A. G. Wech (2009). Cascadia tremor located near plate interface constrained by *S* minus *P* wave times, *Science* **323,** no. 5914, 620–623.

La Rocca, M., D. Galluzzo, S. Malone, W. Mccausland, and E. Del Pezzo (2010). Array analysis and precise source location of deep tremor in Cascadia, *J. Geophys. Res.* **115,** no. B6, doi: 10.1029/2008JB006041.

Lay, T., H. Kanamori, C. J. Ammon, K. D. Koper, A. R. Hutko, L. Ye, H. Yue, and T. M. Rushing (2012). Depth-varying rupture properties of subduction zone megathrust faults, *J. Geophys. Res.* **117,** no. B4, doi: 10.1029/2011JB009133.

Maksymowicz, A., E. Contreras-Reyes, I. Grevemeyer, and E. R. Flueh (2012). Structure and geodynamics of the post-collision zone between the Nazca–Antarctic spreading center and South America, *Earth Planet. Sci. Lett.* **345,** 27–37.

Moreno, M. S., J. Bolte, J. Klotz, and D. Melnick (2009). Impact of megathrust geometry on inversion of coseismic slip from geodetic data: Application to the 1960 Chile earthquake, *Geophys. Res. Lett.* **36,** no. 16, doi: 10.1029/2009GL039276.

Nakano, M., T. Hori, E. Araki, S. Kodaira, and S. Ide (2018). Shallow very-low-frequency earthquakes accompany slow slip events in the Nankai subduction zone, *Nat. Comm.* **9,** no. 1, 984.

Nishikawa, T., and S. Ide (2018). Recurring slow slip events and earthquake nucleation in the source region of the M 7 Ibaraki-Oki earthquakes revealed by earthquake swarm and foreshock activity, *J. Geophys. Res.* **123,** no. 9, 7950–7968.

Obana, K., and S. Kodaira (2009). Low-frequency tremors associated with reverse faults in a shallow accretionary prism, *Earth Planet. Sci. Lett.* **287,** nos. 1/2, 168–174.

Obara, K., and A. Kato (2016). Connecting slow earthquakes to huge earthquakes, *Science* **353,** no. 6296, 253–257.

Poli, P., A. M. Jeria, and S. Ruiz (2017). The M_w 8.3 Illapel earthquake (Chile): Preseismic and postseismic activity associated with hydrated slab structures, *Geology* **45,** no. 3, 247–250.

Rubinstein, J. L., D. R. Shelly, and W. L. Ellsworth (2009). Non-volcanic tremor: A window into the roots of fault zones, in *New Frontiers in Integrated Solid Earth Sciences*, Springer, Dordrecht, The Netherlands, 287–314.

Ruiz, S., M. Metois, A. Fuenzalida, J. Ruiz, F. Leyton, R. Grandin, C. Vigny, R. Madariaga, and J. Campos (2014). Intense foreshocks and a slow slip event preceded the 2014 Iquique M_w 8.1 earthquake, *Science* **345,** no. 6201, 1165–1169.

Russo, R. M., A. Gallego, D. Comte, V. I. Mocanu, R. E. Murdie, and J. C. Vandecar (2010). Source-side shear wave splitting and upper mantle flow in the Chile ridge subduction region, *Geology* **38,** no. 8, 707–710.

Sugioka, H., T. Okamoto, T. Nakamura, Y. Ishihara, A. Ito, K. Obana, M. Kinoshita, K. Nakahigashi, M. Shinohara, and Y. Fukao (2012). Tsunamigenic potential of the shallow subduction plate boundary inferred from slow seismic slip, *Nature Geosci.* **5,** no. 6, 414.

Toh, A., K. Obana, and E. Araki (2018). Distribution of very low frequency earthquakes in the Nankai accretionary prism influenced by a subducting-ridge, *Earth Planet. Sci. Lett.* **482,** 342–356.

Uchida, N., and T. Matsuzawa (2013). Pre- and postseismic slow slip surrounding the 2011 Tohoku-oki earthquake rupture, *Earth Planet. Sci. Lett.* **374,** 81–91.

Yabe, S., and S. Ide (2013). Repeating deep tremors on the plate interface beneath Kyushu, southwest Japan, *Earth Planets Space* **65,** no. 1, 17–23.

Miguel Sáez
Sergio Ruiz
Department of Geophysics
University of Chile
Avenue Blanco Encalada 2002
Santiago, Chile
msaez@dgf.uchile.cl

Satoshi Ide
Department of Earth and Planetary Science
University of Tokyo
Hongo 7-3-1, Bunkyo
Tokyo 113-0033, Japan

Hiroko Sugioka
Department of Planetology
Kobe University
Rokkodai-cho, Nada-ku, Kobe
Hyogo 657-8501, Japan

Published Online 24 July 2019

3.3.2.3 Tremores Tectónicos frente a Pichilemu

El objetivo de este trabajo era comprender la deformación dinámica que se genera en el prisma de acreción de una zona que fue fuertemente afectada durante el terremoto del Maule 2010 M_W 8.8. Para la investigación, se utilizaron 10 estaciones OBS desplegadas sobre el fondo del mar frente a las costas de Pichilemu. Las estaciones OBS estaban equipadas con sismómetros de banda intermedia, manómetros de presión y caudalímetros de fluidos.

En la investigación se analizó la sismicidad ordinaria, lenta y cambios de presiones generados por la deformación del prisma de acreción. Mi aporte a esta investigación fue la búsqueda, localización y caracterización de tremores tectónicos. A continuación, se presenta el articulo científico publicado, en el cual, participé como co-autor.

Research Paper

THEMED ISSUE: Subduction Top to Bottom 2

GEOSPHERE

GEOSPHERE; v. 16, no. 1

https://doi.org/10.1130/GES02102.1

12 figures; 4 tables; 1 set of supplemental files

CORRESPONDENCE: trehu@coas.oregonstate.edu

CITATION: Tréhu, A.M., de Moor, A., Mieres Madrid, J., Sáez, M., Chadwell, C.D., Ortega-Culaciati, F., Ruiz, J., Ruiz, S., and Tryon, M.D., 2020, Post-seismic response of the outer accretionary prism after the 2010 Maule earthquake, Chile: Geosphere, v. 16, no. 1, p. 13–32, https://doi.org/10.1130/GES02102.1.

Science Editor: Shanaka de Silva
Guest Associate Editor: Laura M. Wallace

Received 10 December 2018
Revision received 10 August 2019
Accepted 14 October 2019

Published online 11 December 2019

GOLD OPEN ACCESS

THE GEOLOGICAL SOCIETY OF AMERICA®

Post-seismic response of the outer accretionary prism after the 2010 Maule earthquake, Chile

Anne M. Tréhu[1], Alexander de Moor[1,*], José Mieres Madrid[2], Miguel Sáez[2], C. David Chadwell[3], Francisco Ortega-Culaciati[2], Javier Ruiz[2], Sergio Ruiz[2], and Michael D. Tryon[3,†]

[1]College of Earth Ocean and Atmospheric Sciences, Oregon State University, Corvallis, Oregon 97331, USA
[2]Department of Geophysics, University of Chile, Santiago, Chile
[3]Marine Physical Lab, Scripps Institution of Oceanography, La Jolla, California 92093, USA

ABSTRACT

To investigate the dynamic response of the outer accretionary prism updip from the patch of greatest slip during the 2010 M_w 8.8 Maule earthquake (Chile), 10 ocean-bottom seismometers (OBSs) were deployed from May 2012 to March 2013 in a small network with an inter-instrument spacing of 7–10 km. Nine were recovered, with four recording data from intermediate-band three-component seismometers and differential pressure gauges, and five recording data from absolute pressure gauges (APGs). All instruments were also equipped with fluid flow meters designed to detect very low rates of flow into or out of the seafloor. We present hypocenters for local earthquakes that have S-P times <17 s (i.e., within ~125 km of the network), with a focus on events located beneath or near the network. Most of the seismicity occurred either near the boundary between the active accretionary prism and continental basement or in the outer rise seaward of the trench. For many outer-rise earthquakes, the P and S arrivals are followed by a distinctive T-phase arrival. Very few earthquakes, and none located with hypocenters deemed "reliable," were located within the active accretionary prism or on the underlying plate boundary. Nonvolcanic tremor-like pulses and seafloor pressure transients (but no very-low-frequency earthquakes or fluid flow) were also detected. Many of the tremor observations are likely T-phases or reverberations due to soft seafloor sediments, although at least one episode may have originated within the accretionary prism south of the network. The transient seafloor pressure changes were observed simultaneously on three APGs located over the transition from the active prism to the continental basement and show polarity changes over short distances, suggesting a shallow source. Their duration of several hours to days is shorter than most geodetic transients observed using onshore GPS networks. The results demonstrate the need for densely spaced and large-aperture OBS networks equipped with APGs for understanding subduction zone behavior.

*Now at Canyonlands Field Institute, Moab, Utah 84532, USA
†Retired

INTRODUCTION

On 27 February 2010, a M_w 8.8 megathrust earthquake ruptured the central Chilean margin. This event, termed the Maule earthquake, filled a well-documented seismic gap that had not ruptured in a major earthquake since 1835 (Campos et al., 2002; Lomnitz, 2004; Ruegg et al., 2009; Ruiz and Madariaga, 2018). A large number of slip models have been published for this event based on seismic, geodetic, satellite, and tsunami data (e.g., Moreno et al., 2010; Lay et al., 2010; Delouis et al., 2010; Tong et al., 2010; Lorito et al., 2011; Vigny et al., 2011; Lin et al., 2013; Yue et al., 2014). While the models differ in their details, a common feature of most of the models is that the patch of greatest slip occurred to the northwest of the epicenter (Fig. 1). Still debated, however, are the cross-strike location of greatest slip, the relationship between slip in the main shock and aftershock activity, and whether slip propagated to the trench or was arrested when it reached the accretionary prism, which is thought to be ~30 km wide in this region. Resolution of these questions is important for understanding the conditions under which coseismic slip can propagate beneath or through the accretionary wedge and the implications for tsunamigenesis.

Until the 2011 Tohoku earthquake (Japan), slip during megathrust earthquakes was generally not expected to propagate to the deformation front because of the assumed velocity-strengthening rheology of the trench sediments that are accreted to form the outer accretionary wedge (Lallemand et al., 1994; Wang and Hu, 2006), with the exception being rare "tsunami" earthquakes characterized by slow, shallow slip and generation of a tsunami much larger than expected based on the radiated seismic energy (for a review, see Ye et al. [2016]). The M_w 9.0 Tohoku earthquake, however, indicated that under some conditions, the outer accretionary wedge can lurch seaward by tens of meters (Sato et al., 2011; Kodaira et al., 2012). Assuming that subduction is driven primarily by slab pull, the accretionary prism would be in the stress shadow generated by a locked segment of the plate boundary and would therefore appear to be locked prior to an earthquake (Wang and Dixon, 2004). For this reason, it is difficult to anticipate whether seismogenic slip is likely to extend to the trench or be arrested as it reaches the accretionary prism based on preseismic observations. In the latter case, stress would increase in the accretionary prism

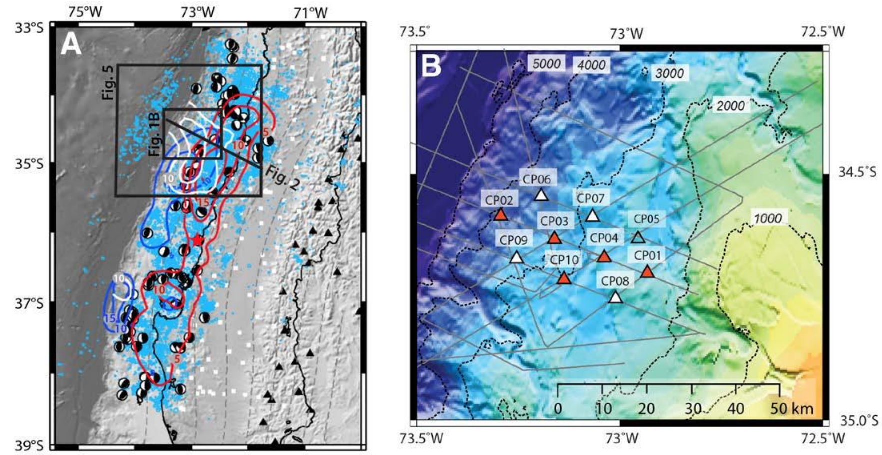

Figure 1. (A) Map showing several representative slip models for the 2010 Mw 8.8 Maule earthquake (Chile) and aftershock distribution. (Modified from Figure 1 of Rietbrock et al. (2012) to add the slip model of Yue et al. (2014) and the location of the maps in Figures 1B and 5 and the cross-section of Figure 2.) Slip models: 5, 10, and 15 m slip contours from Lorito et al. (2011) in red; 10 and 15 m slip contours from Vigny et al. (2011) in blue; 10 and 15 m slip from Yue et al. (2014) in white. Red star is the main shock epicenter. Light blue dots are aftershock epicenters. Source mechanisms of selected aftershocks are also shown. White squares are seismic stations deployed onshore for the international aftershock monitoring network known as IMAD. Black triangles are volcanos. Black lines represent the coastline of Chile and its border with Argentina. Grey dashed lines are contours to the plate boundary at 20 km intervals from model Slab1.0 of Hayes et al. (2012). (B) Location of the ChilePEPPER network overlain on bathymetry. Red triangles show locations of absolute pressure gauges (APG); white triangles are intermediate-band three-component seismometers and differential pressure gauges (DPG). Open triangle (site CP05) indicates a site where the instrument package was not recovered, although it was still responding to acoustic release commands when the site was revisited in February 2017 during cruise MGL1701 of RV *Marcus Langseth* (nearly 4 yr after the initial recovery attempt). Data from sites CP02 and CP03 were sensitive to seismic frequencies for only 10 and 100 days after deployment, respectively, because of instrument malfunction. Grey lines are high-resolution multichannel seismic reflection lines collected during R/V *Melville* cruise MV1206. Background bathymetry (contoured in meters) is from Global Multi-Resolution Topography (Ryan et al., 2009).

immediately after the earthquake and would be relaxed through postseismic creep on the plate boundary and within the prism. Few in situ observations are available of this process because, with the exception of the continental margin offshore Japan (Nakano et al., 2016), most subduction zones are not adequately instrumented to detect slow slip, nonvolcanic tremor, and other subtle clues to the postseismic response of the outer accretionary prism.

The aftershocks in the months immediately after the Maule earthquake (Fig. 1A) were recorded on a dense network of temporary seismic stations, known as IMAD (International Maule Aftershock Deployment) (e.g., Lange et al., 2012; Rietbrock et al., 2012; Hayes et al., 2013). This effort was complemented by networks of ocean-bottom seismometers (OBSs) with interstation spacing of 25 km or more to record aftershocks and provide data for improved velocity models (Lieser et al., 2014; Hicks et al., 2014). While many offshore aftershocks were observed, few were located beneath the outer accretionary wedge, and no observations of low-frequency earthquakes or nonvolcanic tremor have been reported from the OBS data. ChilePEPPER (Project Evaluating Prism Post-Earthquake Response) was designed to test the hypothesis that compressive stress in the accretionary prism increased as a result of >15 m of sudden plate boundary slip to the east and that this stress was being relaxed through internal wedge deformation, which would be expected to result in slow earthquakes, microseismicity, and fluid expulsion driven by increased pore-fluid pressure. When the project was conceived, coseismic slip models and the relatively small far-field tsunami generated by the earthquake suggested that slip had not propagated to the trench, although some subsequent work challenged that conclusion (Yue et al., 2014). To capture the dynamic response of the accretionary wedge to the expected change in stress, 10 OBSs equipped with intermediate or broadband three-component seismometers, absolute or differential pressure gauges, and chemical aqueous transport (CAT) meters (Tryon et al., 2001) were deployed updip of the patch of greatest slip in May 2012 and recorded data until March 2013. Instruments were arranged in a small-aperture network with an inter-instrument spacing of 7–10 km (Fig. 1B). High-resolution swath bathymetric (Maksymowicz et al., 2017), potential field (Maksymowicz et al., 2015), and multi-channel seismic reflection data (Tréhu and Tryon, 2012; Tréhu et al., 2019) were also acquired.

BACKGROUND

Tectonic Setting

The western boundary of the South American plate is characterized by subduction of the Nazca plate below the South American plate at the Peru-Chile trench. Historically, it is the most seismically active subduction zone in the world, nucleating events >M 8 roughly every 10 yr (Campos et al., 2002), with three since 2010. The short seismic cycle, long historical record (Lomnitz, 2004; Ruiz and Madariaga, 2018), along-strike variability in trench sediment fill and slab dip (e.g., Contreras-Reyes and Osses, 2010), and complex topography of the incoming plate make this region a natural laboratory for understanding seismogenesis and the segmentation of plate-boundary faults. Proposed causes for seismic segmentation (i.e., zones that repeatedly rupture in earthquakes separated by zones that are frequently barriers to rupture propagation) include subducting ridges and seamounts on the incoming plate (Contreras-Reyes et al., 2010; Contreras-Reyes and Carrizo, 2011), peninsulas and bends in the coastline of the overriding plate (Loveless et al., 2010), variations in sediment subduction and thickness (Ruff, 1989; Scholl et al., 2015), and fractured zones in the incoming oceanic plate (Poli et al., 2017).

The 100 km × 500 km region that ruptured during the Maule earthquake was a well-documented, mature seismic gap that had last ruptured in a large event (M ~8.5) in 1835 (Ruegg et al., 2009). This segment, which is bounded to the south by the rupture zone of the 21 and 22 May 1960 M_w 8.0 Concepción and M_w 9.5 Valdivia earthquakes and to the north by the rupture zone of the 1985 Valparaiso earthquake, is characterized by subduction in a N78°E direction at 66 mm/yr (Angermann et al., 1999). High sedimentation rates linked to deglaciation and erosion of the Andes mountains since the Pliocene (e.g., Kukowski and Oncken, 2006; Völker et al., 2013) and blocking of sediment transport to the north by the Juan Fernández Ridge (Contreras-Reyes et al., 2010) has led to a sediment-filled trench and construction of an accretionary wedge composed primarily of terrigenous sediments with rare interbedded ash layers (Mix et al., 2003). Along-strike variability within the accretionary wedge has been attributed to episodic phases of trench sediment accretion and erosion (Bangs and Cande, 1997; Contardo et al., 2008; Contreras-Reyes et al., 2017).

Along the segment of margin where the OBS network was deployed, a 20–50-km-wide wedge with a subduction channel <1 km thick and a subduction zone backstop correlated with the slope break has been inferred based on several large-aperture seismic transects (Moscoso et al., 2011; Contreras-Reyes et al., 2017). The ChilePEPPER network straddles one of these transects (Moscoso et al., 2011). This profile has been interpreted to show an accretionary wedge defined by P-wave velocity <4.5 km/s adjacent to a paleo–accretionary complex with velocity of 4.5–6 km/s overlain by a slope basin up to 2 km thick that extends from the shelf break to the coast (Fig. 2). The solid white lines indicate the top and bottom of the subducted oceanic crust and the short-dashed white line shows the base of the continental crust interpreted from the velocity model (Moscoso et al., 2011). The long dashed line shows the interpreted boundary between the active accretionary prism and a Cretaceous paleo-accretionary complex that forms the continental backstop in this region (Contreras-Reyes et al., 2017). More regionally, a subducting seamount near the hypocenter of the

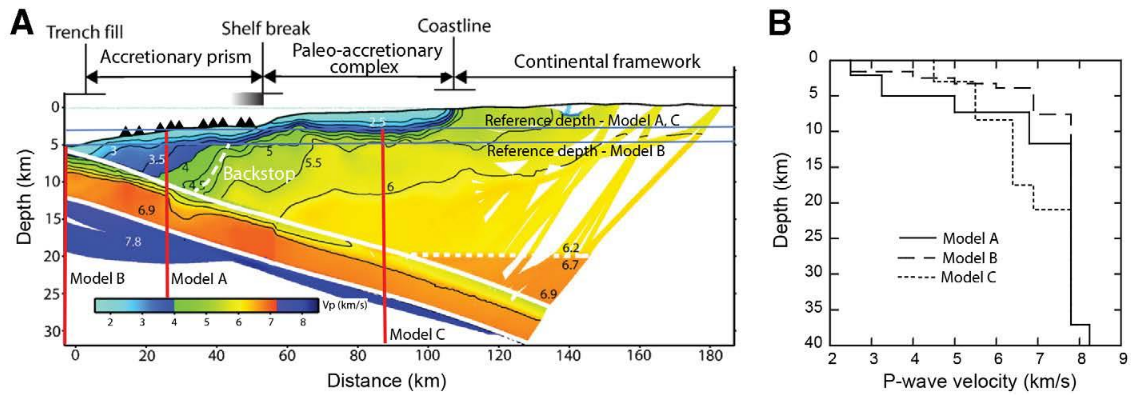

Figure 2. (A) P-wave velocity (Vp) model of Moscoso et al. (2011). Solid white lines indicate the top and bottom of the subducted oceanic crust and short-dashed white line shows the base of the continental crust interpreted from the velocity model (Moscoso et al., 2011). Velocities are in units of km/s. Depth is relative to sea level. The locations of the three velocity-depth profiles discussed in the text and shown in B are indicated by vertical red lines, and the reference depths used for locating earthquakes with these models are shown by horizontal blue lines. The boundary between active accretionary prism and the paleo-accretionary rocks that form the continental basement, which is interpreted based on the position of a strong lateral velocity gradient, is shown as a long-dash white line. Contreras-Reyes et al. (2017) interpreted this boundary to be co-located with the slope break and used the slope break as a proxy for the position of the backstop along strike. High-resolution multichannel seismic data have shown that the projection to the seafloor of this gradient is a complex zone of transpression and transtension located seaward of the slope break (Tréhu et al., 2019), indicated by the shaded rectangle shown above the cross-section. Locations of the ChilePEPPER ocean-bottom seismometers (see Fig. 1B for location) projected onto the cross-section are shown by the black triangles. (B) P-wave velocity versus depth below sea level for models A, B and C.

earthquake has been interpreted from a high P-velocity anomaly in the upper plate by Hicks et al. (2014), who speculated that this feature may have caused frictional heterogeneities on the plate interface that promoted the initial nucleation of the Maule event. Other local density and gravity anomalies have also been correlated with the patch of greatest slip, suggesting that subducting or obducted seamounts may act as asperities (Maksymowicz et al., 2015). Cubas et al. (2013a) and Maksymowicz et al. (2015) have estimated the basal friction using Coulomb wedge theory and have concluded that the frictional coefficient was lower on the patch of highest slip. Their conclusion that low basal friction is correlated with interseismic coupling and/or large coseismic slip is consistent with studies along other subduction margins (e.g., Hikurangi [New Zealand]: Fagereng, 2011; Tohoku [Japan]: Cubas et al., 2013b).

Seismological Constraints on the Maule Earthquake and Its Aftershocks

The along-strike distribution and downdip limit of slip during the M_w 8.8 Maule event are well constrained based on regional seismic, teleseismic, GPS, and interferometric synthetic-aperture radar (InSAR) data and show that the earthquake was a bilateral rupture that extended along ~500 km of the Chilean coastline, with the largest slip patches occurring to the north and south of the epicenter (e.g., Tong et al., 2010; Pollitz et al., 2011; Vigny et al., 2011; Moreno et al., 2012; Lin et al., 2013; Yue et al., 2014). The updip extent of seismogenic slip, however, varies depending on model parameterization because of limited offshore data. Even when data from offshore DART (Deep-Ocean Assessment and Reporting of Tsunamis) buoys are included in the data set used to constrain the model, different investigators obtain different solutions (Fig. 1A). For example, the model of Lin et al. (2013) suggests that coseismic slip did not propagate through the shallowest 15–20 km of the plate boundary, suggesting that the plate boundary beneath the accretionary wedge slips aseismically during the interseismic period. In contrast, Yue et al. (2014) concluded that >10 m of slip locally extended to the trench along the portion of the plate boundary updip from the patch of greatest slip. Understanding whether slip propagated to the trench is important for understanding aftershock distribution, frictional properties of the megathrust, forearc structure of the region, effects of subducting topography, and future seismic hazard assessment.

In response to the Maule event, seismologists from Chile, Europe, and the United States deployed a temporary 164-station network onshore for seven months to monitor aftershock activity (Russo et al., 2011). Several groups also deployed short-period OBSs for several months during the year following the earthquake (Lieser et al., 2014; Hicks et al. 2014). Over 100,000 aftershocks have been located and >400 focal mechanisms have been constructed from these data sets (Agurto et al., 2012; Lange et al., 2012; Rietbrock et al., 2012; Hayes et al., 2013). The OBS data have been used for joint inversion of velocity structure and seismicity (Hicks et al., 2014; Lieser et al., 2014) with a resolution controlled by the relatively sparse inter-instrument spacing of several tens of kilometers. Despite its importance for understanding plate-boundary slip, no attempts to detect nonvolcanic tremor, which is commonly interpreted to be a short-period proxy for slow slip, have been reported from these offshore data.

Aftershock seismicity from Rietbrock et al. (2012) is shown in in Figure 1A. Most of the seismicity was located on or near the plate boundary between 40 and 140 km landward of the deformation front, with a second, less-continuous band of events at greater depth; most source mechanisms for earthquakes in this band indicate low-angle thrust motion on or near the plate interface. Aftershocks with normal faulting mechanisms were recorded beneath the outer rise seaward of the trench, especially along the northern end of the rupture zone. Evidence for an offshore splay fault along the northern boundary of the rupture zone was reported by Lieser et al. (2014) based on OBS data. All studies document a notable dearth of aftershock activity within or beneath the forearc within ~40 km of the trench. Rietbrock et al. (2012) interpreted this to indicate that slip models in which the largest slip magnitude is within 40 km of the trench and the highest downdip gradient in slip is correlated with greatest moment release in aftershocks were most consistent with global patterns in the relationship between slip during large earthquakes and aftershock distribution. In contrast, Lange et al. (2012) and Moscoso et al. (2011) argued that this pattern suggested that the outer forearc did not slip during the main shock and was accommodating plate motion aseismically.

INSTRUMENTATION

Ten (10) Lamont-Doherty Earth Observatory (Palisades, New York, USA) OBSs from the Ocean Bottom Seismograph Instrument Pool (OBSIP; http://www.obsip.org/) were available on short notice for ChilePEPPER (Table 1). Five OBSs (SL-OBSs) were equipped with a three-component L4C 1 Hz geophone with a low-noise amplifier and a differential pressure gauge (DPG). The other five OBSs (CI-OBSs) each contained a Trillium Compact broadband seismometer and a Paroscientific absolute pressure gauge (APG). The SL-OBSs recorded 40 samples/s (sps) and the CI-OBSs recorded 125 sps. CAT flow meters (Tryon et al., 2001), which are designed to detect flow rates of 0.01–1.5 cm/yr into or out of the seafloor, were integrated into the OBS packages by using the patch of seafloor covered by the OBS anchor as the collection area monitored by the CAT meter, which was attached to the side of the OBS and recovered with it (Tréhu and Tryon, 2012).

Nine of the 10 OBSs that were deployed in May 2012 during R/V *Melville* cruise MV1206 were recovered in March 2013 during on R/V *Point Sur* cruise PS1306. One SL-OBS (site CP05) responded to the release command but remains on the seafloor. The remaining SL-OBSs (sites CP06–CP09) generally performed well and recorded data for the entire deployment, although CP07 and CP08 had occasional artifacts that intermittently distorted the waveforms. Unfortunately, the seismometers in the CI-OBSs did not record data, so only pressure data from these instruments were used for this study (Fig 1B). Three of the APGs (at sites CP01, CP04, and CP10) recorded good-quality data for

TABLE 1. SITE LOCATIONS (SEE FIG. 1B), SAMPLE RATE, AND COMPONENTS RECORDED

Site	Latitude (S)			Longitude (W)			Water depth (m)	Sample rate (sps)	Comments
	Decimal degrees	Degrees	Minutes	Decimal degrees	Degrees	Minutes			
CP01	34.70182	34	42.1091	72.93232	72	55.9394	2395	125	APG
CP02	34.58622	34	35.1734	73.29314	73	17.5884	3924	125	APG (to 17 Aug 2012)
CP03	34.63270	34	37.9617	73.16094	73	9.6565	3272	125	APG (to 29 May 2012)
CP04	34.67109	34	40.2652	73.03790	73	2.2739	2673	125	APG
CP05	34.61964	34	37.1786	72.95682	72	57.4089	2550	40	Not recovered
CP06	34.54564	34	32.7382	73.19254	73	11.5524	3623	40	X, Y, Z, DPG
CP07	34.58792	34	35.2754	73.06748	73	4.0486	2790	40	X, Y, Z, DPG
CP08	34.75379	34	45.2271	73.00970	73	0.5817	2398	40	X, Y, Z, DPG
CP09	34.67334	34	40.4004	73.25416	73	15.2494	3224	40	X, Y, Z, DPG
CP10	34.71460	34	42.8759	73.13726	73	8.2356	2967	125	APG

Notes: X, Y, and Z refer to three orthogonal geophone components. APG—absolute pressure gauge; DPG—differential pressure gauge; sps—samples per second.

seismic frequencies <2 Hz for the entire deployment. Rapidly increasing instrument noise for frequencies >20 Hz (Webb and Nooner, 2016), however, limited the utility of the APGs for detecting local earthquakes with magnitude <~3 (Fig. 3). Unfortunately, two of the APGs lost sensitivity to seismic frequencies after ~10 and 100 days, respectively, because of internal corrosion. For more details on OBS performance, see Tréhu (2013).

Timing for the OBSs was provided by an internal clock that was calibrated to a GPS clock before deployment and after recovery, and timing was corrected assuming a linear drift rate. Total clock drift ranged from –0.87 to 1.16 s. As a secondary, qualitative check on the timing accuracy of the instruments, we looked at four large, deep teleseismic events (deMoor, 2015), two from Argentina and two from Colombia, with origin times distributed over the duration of the ChilePEPPER deployment to see whether the time lags between instruments remained constant, as they should have if they were due only to differences in local crustal structure and the distance between the source and the receiver. Deep events were chosen because of their impulsive P-wave and steep incident angles. Unfortunately, only five stations recorded all four events. Using cross-correlation of waveforms from these events, bandpass

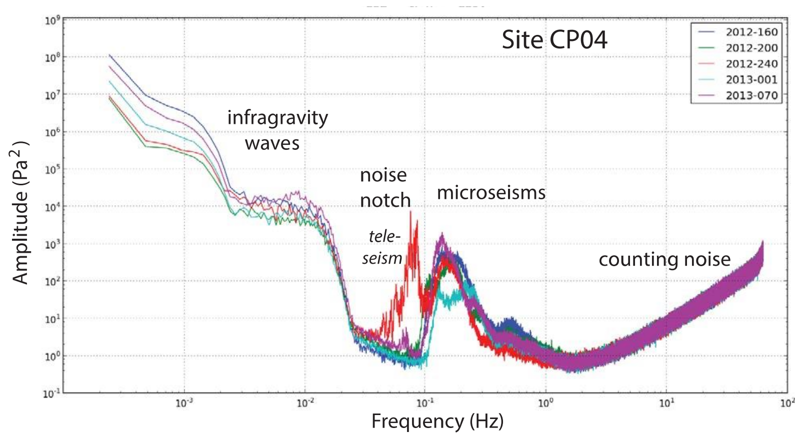

Figure 3. Power spectra of absolute pressure gauge data for day-long records at site CP04 (see Fig. 1B for location) on five different days distributed through the deployment. The legend indicates color coding by year and Julian day. Similar spectra were observed at sites CP01 and CP10. These spectra are not corrected for counting noise (Webb and Nooner, 2016).

filtered at 0.1–1 Hz, we concluded that the APG at site CP10 contained a timing error. This was confirmed by examining P-wave residuals at CP10 after initially locating earthquakes using Hypo71 software (Lee and Lahr, 1975) without including a timing correction for CP10. A decrease in the residual at CP10 with time was observed, leading to an empirical clock drift correction for CP10 of -0.004s/day and initial time offset of 1.5 s (deMoor et al., 2015). A timing correction based on this analysis was applied to picks from CP10. Average residuals for stations other than at CP10 are <0.2 s and show no systematic temporal variation throughout the deployment. Because the network was sampling a single quadrant of the radiation pattern for the direct P-wave from these deep events, these observations also served as a check on polarity. The APG data were multiplied by −1 for consistency with the seismometer data.

Figure 4A shows vertical component (BHZ) or pressure (HDH) across the network from one of the largest earthquakes to occur beneath the network and illustrates several characteristics of the data. This event is the second of a pair of approximately collocated events with M_b 4.7 and 4.5 that occurred on 15 September 2012 at 00:40 and 00:50 UTC and were reported in the U.S. Geological Survey Comprehensive Earthquake Catalog (ComCat; https://earthquake.usgs.gov/earthquakes/search). A third event from the same location with M_L 3.4 was reported by the Chilean National Seismological Center (CSN) at

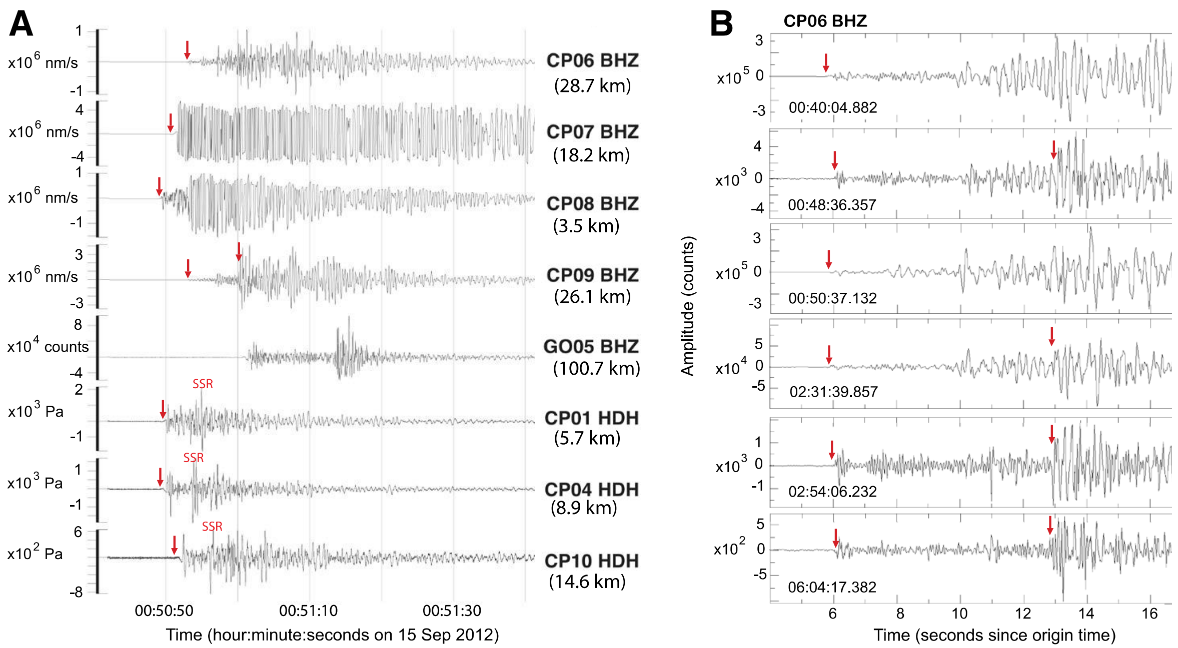

Figure 4. (A) Vertical ground velocity (BHZ) and pressure (HDH) data recorded across the ChilePEPPER network (see Fig. 1B for location) from an earthquake within the network on 15 September 2012; time is shown as hour:minute:second UTC. Source-receiver distance is indicated below the station name. Red arrows show the P- and S-wave arrival-time pick used for locations. SSR indicates the reflection of the P-wave from the sea surface above the instrument. GO05 is an onshore station (35.01°S, 71.93°S; Fig. 5A) that was not used for the catalog of Table S1 (see footnote 1) but is shown here to illustrate the difference in code length between an onshore station that is well coupled to the ground and an ocean-bottom seismometer emplaced on soft seafloor sediment. (B) Seismograms recorded at station CP06 for six approximately co-located earthquakes on 15 September 2012, showing variation in amplitude, waveform, and frequency content of events in this sequence. Data have been filtered with a passband of 1–15 Hz. P- and S-wave arrival time picks used for locations are marked by red arrows. All S-waves were picked using horizontal as well as vertical component data.

02:31. We located several additional smaller earthquakes very near these three events. Figure 4B shows the vertical component at site CP06 for several events in this sequence, including the three reported by ComCat and CSN. The two largest events were recorded across the network, but the signal was clipped on the two closest seismometers so that shear-wave arrival times could not be identified at these two sites (Fig. 4A); absolute pressure sensors at these distances (HDH) did not clip, demonstrating their ability to measure strong, high-frequency, local signals as well as very-long-period signals. On the other hand, the signal on the pressure sensors did not rise above background noise level for smaller, high-frequency earthquakes, even though these were well recorded by the seismometers. Note that the waveforms from these earthquakes at CP06 differ (Fig. 4B), indicating different fault mechanisms. The most complete data set was obtained for the event at 02:31, for which both P- and S-wave arrivals were clear on all four instruments equipped with seismometers and P-wave arrivals were clear on the three pressure sensors functioning at that time, resulting in a total of 11 travel-time picks for that event.

DATA ANALYSIS

Local Earthquakes

Hypocenters

Data were input into an Antelope database for display and phase picking. Events were detected automatically using the ratio of the long term to the short term amplitude average, but all arrival times used for locations were picked manually. The picks were then exported and reformatted for input to Hypo71 (Lee and Lahr, 1975) for calculating event locations. This classic program was used because it is well documented, flexible, and suitable for the small network aperture and relatively small number and local nature of the events being located. A one-dimensional P-wave velocity model was extracted from kilometer 28 in the model of Moscoso et al. (2011), which corresponds to the center of the ChilePEPPER network (model A in Fig. 2B). The reference depth for the top of the velocity model was placed at the mean depth of the stations (2.9 km below sea level [bsl]), and station delays or advances were defined by the difference between the reference depth and the station depth divided by the velocity of the first layer in the velocity model. This method assumes that the ray paths in layer 1 are vertical, an assumption that would be violated for very shallow, local events. Different station delays were used for P- and S-wave picks.

While P-wave velocities (Vp) for the study area are well constrained, the S-wave velocity (Vs) for the outer accretionary wedge is poorly constrained by the controlled source results. To estimate the regional Vp/Vs ratio, we located the 15 September earthquake at 02:31 for a series of Vp/Vs ratios from 1.6 to 2.6 and for hypocentral depths from 1 to 17 km relative to our reference depth of 2.87 km bsl. The minimum root mean squared (RMS) travel-time misfit for this event was for a depth of 7 km and a Vp/Vs ratio of 2.0–2.2 (Table 2, event 1). This relatively high Vp/Vs ratio is consistent with the Vp/Vs ratio for the outer accretionary wedge in this region obtained by Hicks et al. (2014) and with Vp/Vs ratios measured in cores from the Nankai accretionary wedge, Japan (Hashimoto et al., 2011). The low S-wave velocity is probably due to the presence of unconsolidated sediments in the accretionary wedge. In contrast, for an event located in the trench ~40 km west of the network, the minimum RMS travel-time residual was for a depth of 9–13 km and a Vp/Vs ratio of 1.8 (Table 2, event 2).

All events with at least five arrival-time picks and a location within ~125 km of the ChilePEPPER network (as indicated by an S-P time <17s) were identified and located (de Moor, 2015). In addition, events with only four P-wave

TABLE 2. ROOT MEAN SQUARED MISFIT AS A FUNCTION OF RATIO OF P- TO S-WAVE VELOCITY (Vp/Vs) AND SOURCE DEPTH FOR AN EVENT BENEATH THE ChilePEPPER ARRAY (EVENT 1) AND ONE LOCATED WEST OF THE ARRAY BENEATH THE OUTER RISE (EVENT 2)

Depth* (km)	Event 1 Vp/Vs					Depth* (km)	Event 2 Vp/Vs				
	1.60	1.80	2.00	2.20	2.40		1.60	1.80	2.00	2.20	2.40
1	1.21	0.62	1.00	1.00	2.38	1	1.27	1.48	1.19	1.19	1.18
3	0.59	0.52	0.66	0.66	0.95	3	1.27	1.47	1.22	1.22	1.14
5	0.59	0.56	0.46	0.46	0.72	5	1.27	1.45	1.28	1.28	1.17
7	0.55	0.47	0.44	0.44	0.80	7	0.44	1.48	1.26	1.26	1.17
9	0.58	0.48	0.50	0.50	0.71	9	0.44	0.42	1.24	1.24	1.17
11	0.58	0.52	0.51	0.51	0.79	11	0.44	0.42	1.31	1.31	1.17
13	0.58	0.52	0.50	0.50	0.90	13	0.44	0.42	0.53	0.53	1.19
15	0.58	0.53	0.58	0.58	1.02	15	0.44	0.43	0.52	0.52	1.31
17	0.59	0.55	0.50	0.50	1.15	17	0.44	0.43	0.51	0.51	1.33

*Relative to reference depth of 2.9 km below sea level.
Note: Cell outlines highlight combination of depth and Vp/Vs that minimizes the root mean squared travel-time misfit.

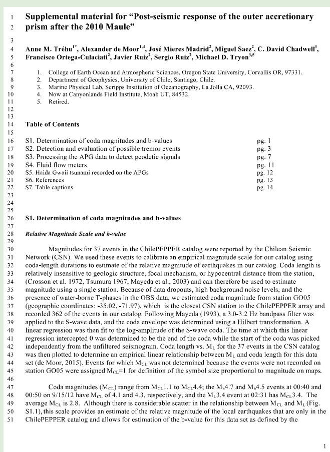
Supplemental material for "Post-seismic response of the outer accretionary prism after the 2010 Maule"

Anne M. Tréhu[1*], Alexander de Moor[1,4], José Mieres Madrid[2], Miguel Saez[2], C. David Chadwell[3], Francisco Ortega-Culaciati[2], Javier Ruiz[2], Sergio Ruiz[2], Michael D. Tryon[3,5]

1. College of Earth Ocean and Atmospheric Sciences, Oregon State University, Corvallis OR, 97331.
2. Department of Geophysics, University of Chile, Santiago, Chile.
3. Marine Physical Lab, Scripps Institution of Oceanography, La Jolla CA, 92093.
4. Now at Canyonlands Field Institute, Moab UT, 84532.
5. Retired.

Table of Contents

S1. Determination of coda magnitudes and b-values

Relative Magnitude Scale and b-value

Magnitudes for 37 events in the ChilePEPPER catalog were reported by the Chilean Seismic Network (CSN). We used these events to calibrate an empirical magnitude scale for our catalog using coda-length durations to estimate of the relative magnitude of earthquakes in our catalog. Coda length is relatively insensitive to geologic structure, focal mechanism, or hypocentral distance from the station, (Crosson et al. 1972, Tsumura 1967, Mayeda et al., 2003) and can therefore be used to estimate magnitude using a single station. Because of data dropouts, high background noise levels, and the presence of water-borne T-phases in the OBS data, we estimated coda magnitude from station GO05 (geographic coordinates: -35.02, -71.97), which is the closest CSN station to the ChilePEPPER array and recorded 362 of the events in our catalog. Following Mayeda (1993), a 3.0-3.2 Hz bandpass filter was applied to the S-wave data, and the coda envelope was determined using a Hilbert transformation. A linear regression was then fit to the log-amplitude of the S-wave coda. The time at which this linear regression intercepted 0 was determined to be the end of the coda while the start of the coda was picked independently from the unfiltered seismogram. Coda length vs. M_L for the 37 events in the CSN catalog was then plotted to determine an empirical linear relationship between M_L and coda length for this data set (de Moor, 2015). Events for which M_{CL} was not determined because the events were not recorded on station GO05 were assigned M_{CL}=1 for definition of the symbol size proportional to magnitude on maps.

Coda magnitudes (M_{CL}) range from M_{CL}1.1 to M_{CL}4.4; the M_b4.7 and M_b4.5 events at 00:40 and 00:50 on 9/15/12 have M_{CL} of 4.1 and 4.3, respectively, and the M_L3.4 event at 02:31 has M_{CL}3.4. The average M_{CL} is 2.8. Although there is considerable scatter in the relationship between M_{CL} and M_L (Fig. S1.1), this scale provides an estimate of the relative magnitude of the local earthquakes that are only in the ChilePEPPER catalog and allows for estimation of the b-value for this data set as defined by the

1

[1]Supplemental Material. Technical details related to determination of coda magnitudes and b-values, detection and evaluation of possible non-volcanic tremor events, and processing of absolute pressure gauge data to detect geodetic signals. Table of hypocentral parameters for the earthquakes in the ChilePEPPER catalog and a discussion of the fluid flow. Please visit https://doi.org/10.1130/GES02102.S1 or access the full-text article on www.gsapubs.org to view the Supplemental Material.

arrival time picks and no S-wave picks were included in our catalog if the high-frequency content of the signal suggested a nearby source. Hypocentral parameters were calculated for a starting depth of 8 km relative to the reference depth of 2.9 km below sea level. After an initial run in which all earthquakes were located using velocity model A (Fig. 2B) and a Vp/Vs ratio of 2.2, earthquakes west of −73.2° were relocated using model B (Fig. 2B) and a Vp/Vs ratio of 1.78. As an empirical test of the reliability of the hypocentral parameters, events with an RMS travel-time misfit <1.0 s and nominal horizontal errors <20 km were relocated using a starting depth of 13 km, and only events with a solution located within 15 km of the first solution were retained. This second test yielded a catalog of 453 events, including 147 events with RMS residuals <0.5 s and epicenters located within 16 km of a ChilePEPPER station. Of these, 35 were located using at least six arrival-time picks. The average RMS travel-time misfit for all events is 0.19 s; for events with at least six picks, RMS misfit is 0.22 s; for events with eight or more picks, it is 0.35 s. Coda magnitudes were estimated as described in Section S1 of the Supplemental Material[1]. The complete catalog is provided as Table S1 (footnote 1); however, actual uncertainties in the hypocentral parameters for most of the events in Table S1 are large and poorly defined, and the catalog should be used primarily as a tool to help initiate future studies.

Comparison to Other Catalogs

The distribution of epicenters in our catalog (Fig. 5A) is generally consistent with the distribution of epicenters in the ComCat catalog for the time period of the ChilePEPPER deployment (Fig. 5B), and with the catalog of Lieser et al. (2014) developed from OBS data from 20 September to 25 December 2012 (Fig. 5C). All three catalogs show a low level of seismicity beneath the outermost wedge (note that two "outer wedge" events in the ComCat catalog are likely mislocated, as discussed below). Most of the activity is focused near the boundary between the inner and outer wedge or seaward of the deformation front beneath the outer rise.

To examine possible biases in locations of offshore earthquakes located using only onshore observations, we compared hypocenters for events in the ComCat catalog that were located within or near the ChilePEPPER network (i.e., events between 34.5° and 35.0°S and between 72.8° and 73.8°W). Figure 6A suggests that ComCat epicenters may be systematically too far east and too deep along a transect perpendicular to the coast and overlying the ChilePEPPER network. A similar systematic bias has been documented for earthquakes occurring offshore central Cascadia (Pacific coast of North America) and attributed to the difference in crustal structure between the Oregon Coast

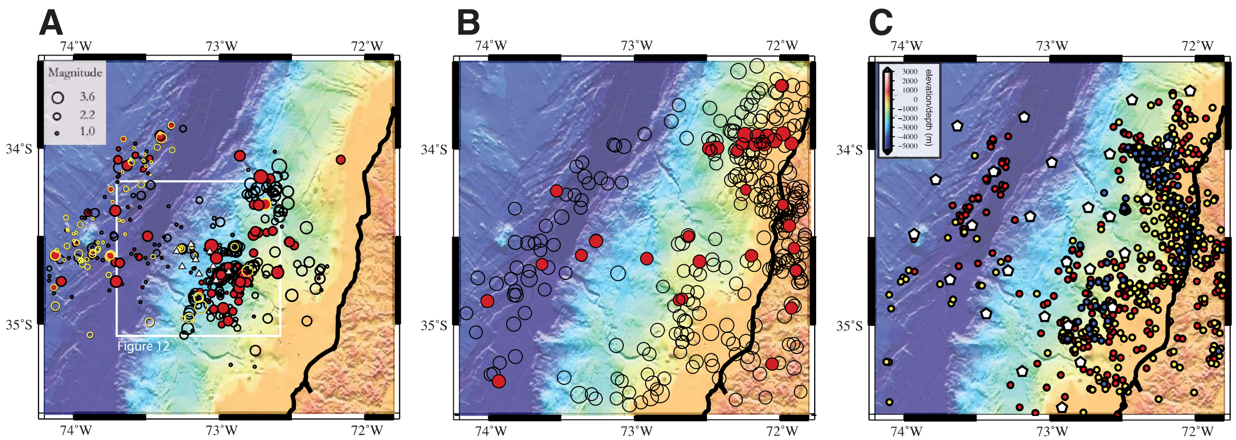

Figure 5. (A) Events located during ChilePEPPER deployment (see Fig. 1 for location) overlain on bathymetry. Open circles indicate events located using only four or five P and S-wave arrival time picks. Red filled circles indicate events located with six or more phase picks. Circle radius is determined by the local coda magnitude determined as described the Supplemental Material (see footnote 1). Yellow outlines indicate events for which a T-phase was observed. White triangles show the stations of the ChilePEPPER network. (B) Events in the U.S. Geological Survey Comprehensive Catalog (ComCat; https://earthquake.usgs.gov/earthquakes/search/) for the period during which the ChilePEPPER network was active (red filled circles) and from 1 March 2010 until the beginning of ChilePEPPER deployment (open circles). Magnitudes range from 4.1 to 5.2. (C) Events reported by Lieser et al. (2014) based an ocean-bottom seismometer (OBS) network deployed from 20 September to 25 December 2010; white hexagons are OBS locations. Events are color coded by location quality: blue—excellent; yellow—very good; red—good. The elevation/depth scale applies to all three maps.

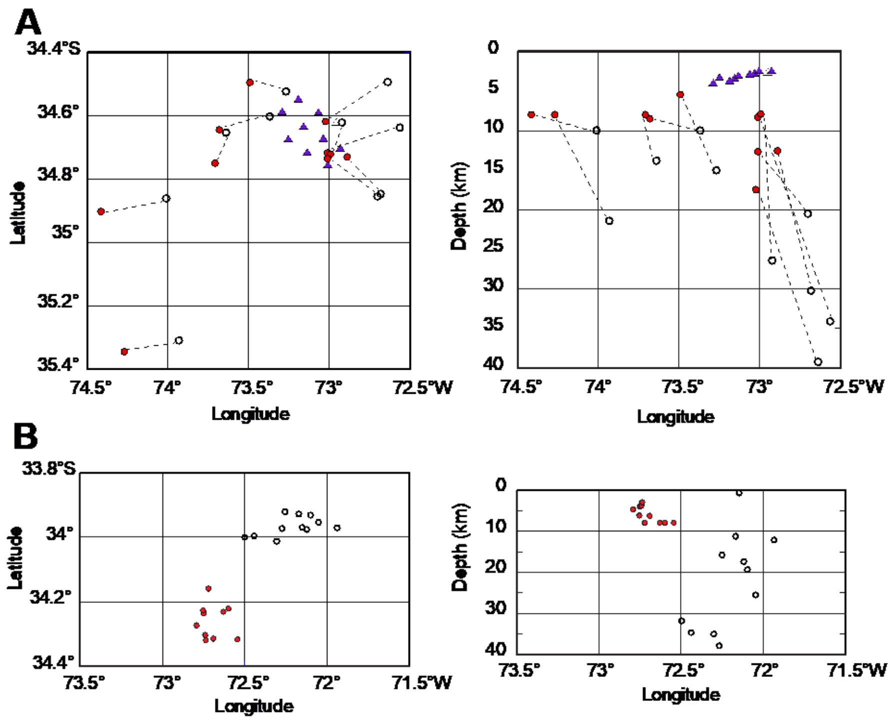

Figure 6. (A) Comparison between hypocenters reported in the U.S. Geological Survey ComCat catalog (https://earthquake.usgs.gov/earthquakes/search/) (open circles) and those determined from the ChilePEPPER network (see Fig. 1B for location) (red filled circles). Depth is relative to sea level. Purple triangles indicate the locations of ChilePEPPER instruments. Because the events do not define two distinctly different populations, a dashed line is used to connect hypocenters for the same event. (B) Same as A for events located north of the ChilePEPPER network. For reasons discussed in the text, it is likely that both sets of hypocenters have systematic biases.

Range and the continental margin as well as to the lack of close stations when only onshore data are available (Williams et al., 20 11; Tréhu et al., 2015).

A cluster of relatively large-magnitude earthquakes in Figure 5A located near 34.2°S, 72.7°W corresponds to earthquakes near 34.0°S, 72.2°W in Figure 5B. Figure 6B shows the difference between ComCat hypocenters and our hypocenters for these earthquakes. The epicenters in our catalog for these events are probably systematically biased to be too close to the network because of the high Vp/Vs ratio we used for locating all events east of 73.2°W. Although a high Vp/Vs ratio is appropriate for the events originating in the wedge beneath the network, it is likely too high for events outside the network, for which the ray path is primarily in the crust and upper mantle. Depths for events in Figure 6B are poorly resolved for both catalogs. Relocation of these events in an accurate three-dimensional velocity model and using travel time observed both onshore and offshore is needed to obtain more accurate hypocentral parameters for these events. In the subsequent discussion, we focus on earthquakes located within or near the ChilePEPPER network.

Depth Uncertainty and Fault Mechanisms for Selected Earthquakes

To further examine depth resolution, three of the events that occurred on 15 September 2012 near site CP08 (Fig. 1B) were relocated for fixed depths at 2 km intervals from 2 to 30 km assuming velocity model A (Fig. 2B) and a Vp/Vs ratio of 2.2 (Fig. 7A). A similar exercise was run for two earthquakes located in the outer rise west of the deformation front assuming model B and a Vp/Vs ratio of 1.78 (Fig. 7B). The smallest RMS travel-time misfits occur for the 15 September events at ~8 km relative to sea level (compared to depths of 8.3, 7.9, and 7.2 km for these events when depth was not constrained). Although

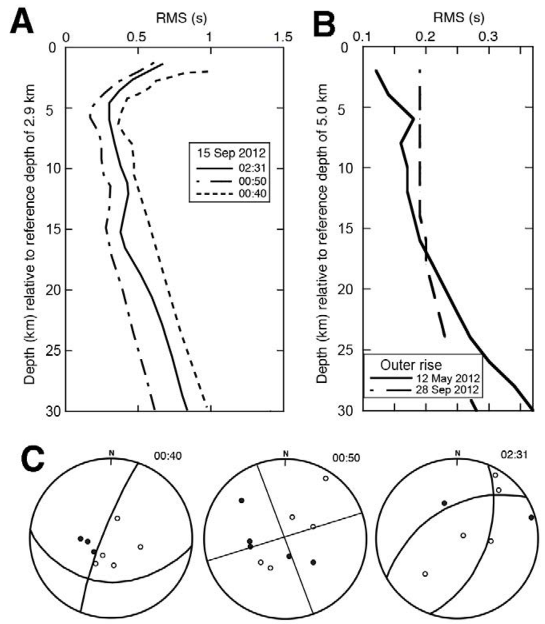

Figure 7. (A) Root mean squared (RMS) travel-time residuals as a function of source depth relative to the reference depth of 2.9 km below sea level for the three largest events on 15 September 2012 assuming velocity model A (Fig. 2). The best-recorded event was at 02:31 UTC (M_b 3.4), which was large enough to be recorded on the absolute pressure gauges and small enough to be on scale on the seismometers. The events at 00:40 (M_b 4.7) and 00:50 (M_b 4.5) were clipped on several seismometers. (B) Residuals as a function of source depth for two outer rise earthquakes located ~24 and 37 km from the closest station, assuming velocity model B. Although depth is not well resolved, the best fit is for shallow depth. (C) First-motion diagrams for three events on 15 September 2012. Lower-hemisphere projection. Filled circles are compressional first motions; open circles are dilatational first motions. Takeoff angle and azimuth were calculated for the solution in Table S1 (see footnote 1). Orthogonal nodal planes were fit by eye.

depth is not well constrained for the outer-rise earthquakes, a shallow depth is suggested.

To explore the impact of our choice of velocity model and Vp/Vs ratio, we relocated five earthquakes in the 15 September cluster for which at least six arrival time picks were available using a Vp/Vs ratio of 1.8 rather than 2.2; we also relocated these earthquakes using a P-wave model representative of the crustal structure near the coast (model C in Fig. 2; Table 3). The outer-accretionary-wedge P-wave velocity model with a Vp/Vs ratio of 2.2 yielded the shallowest source and the smallest travel-time misfit, supporting our choice of velocity model. The average horizontal and vertical uncertainties in the estimated hypocentral parameters with model A and Vp/Vs = 2.2 are 3.7 km and 3.3 km, respectively.

First-motion polarities are shown in Figure 7C for the three largest events on 15 September. Each event has a different mechanism, consistent with the observation that waveforms at a particular station differ among the events (e.g., Fig. 4B). Although the uncertainty in these mechanism estimates may be large because of the sensitivity of take-off angle and azimuth to local velocity structure, all three events are consistent with a scenario in which the greatest compressive stress is approximately horizontal and oriented NW-SE, and the intermediate and least compressive stresses are of similar magnitude.

T-Phase Observations

Nearly 50% of the events located beneath the outer rise show a distinctive T (tertiary) phase that is rarely observed for events located east of the deformation front (Fig. 8); events with T-phases are indicated in Table S1 (footnote 1) and outlined by a yellow circle in Figure 5A. T-phases are commonly observed from earthquakes originating in ocean basins and are generally thought to represent energy traveling in the SOFAR (sound fixing and ranging) channel, which occurs because the speed of sound in the ocean has a minimum at ~1000 m water depth, forming an efficient waveguide for transmitting sound in the ocean. Because of low attenuation, the T-phase may be the only phase observed for smaller events in submarine earthquake swarms (e.g., Dziak et al., 1995, 2004; Dziak, 2001; Blackman et al., 2000; Bohnenstiehl et al., 2002; Forsyth et al., 2003; Tréhu et al., 2018). They are characterized by their high-frequency content (>3 Hz), emergent nature, and a propagation velocity of 1.5 km/s. Although the mechanism for coupling P- or S-wave energy from earthquakes into the SOFAR channel remains controversial (e.g., de Groot-Hedlin and Orcutt, 2001; Balanche et al., 2009), spatial correlation of T-phase observations with outer-rise events suggests a shallow source depth (Wech et al., 2018) and/or a source where crystalline basement is at or near the seafloor for these events. That not all outer-rise events generate T-phases may indicate a range of source depths.

Possible Nonvolcanic Tremor

The importance of observations of nonvolcanic tremor as a proxy for slow slip motivated a search for tremor in the ChilePEPPER data. Wech et al. (2013) have discussed the challenges of detecting tremor from OBSs. One of the challenges is distinguishing tremor offshore from T-phases from regional or teleseismic earthquakes for which the body and surface waves are too low in amplitude or frequency to rise above the background noise level in the

TABLE 3. COMPARISON OF ROOT MEAN SQUARED (RMS) TRAVEL-TIME MISFIT AND HYPOCENTRAL DEPTH FOR VELOCITY MODELS A AND C (FIG. 2B) AND RATIOS OF P- TO S-WAVE VELOCITIES (Vp/Vs) OF 1.8 AND 2.2

15 Sep 2012	No. of picks	Model A, Vp/Vs = 1.8		Model A, Vp/Vs = 2.2		Model C, Vp/Vs = 1.8		Model C, Vp/Vs = 2.2	
(hr:min)		RMS (s)	Depth (km)	RMS (s)	Depth (km)	RMS (s)	Depth (km)	RMS (s)	Depth (km)
0:40	9	0.50	10.70	0.59	5.50	0.52	15.00	0.78	21.68
0:48	6	0.26	10.52	0.17	9.31	0.32	3.77	0.26	13.58
0:50	8	0.44	4.28	0.12	5.00	0.49	14.86	0.46	19.99
2:31	11	0.56	7.19	0.42	5.37	0.60	14.33	0.62	15.00
2:54	6	0.20	10.72	0.05	5.68	0.08	10.83	0.18	12.54
Average of five events		0.39	8.68	0.27	6.17	0.40	12.41	0.46	16.56
Depth below sea level			13.70		10.48		15.28		19.43

Notes: Depths are relative to the reference depth of 2.9 km except where indicated in the bottom row. Model A with Vp/Vs = 2.2 is the preferred model for events located beneath the network in the accretionary wedge. Time zone is UTC.

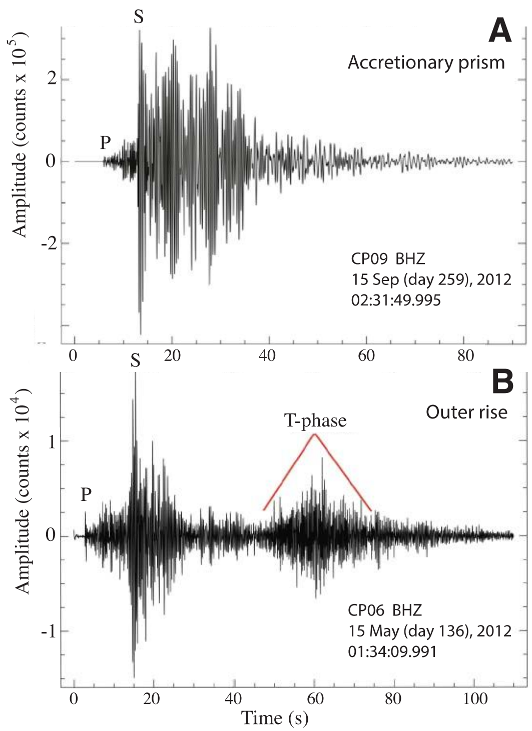

2–8 Hz passband. Because of efficient propagation of high-frequency sound in the SOFAR channel, the T-phase is sometimes the only phase observed. This phenomenon has been observed in OBS networks on the coast of Oregon (USA) for earthquakes from the Explorer Ridge (offshore British Columbia, Canada) (Czoski et al., 2012) and Blanco transform fault (offshore Oregon) (Tréhu et al., 2018). Another challenge is distinguishing tremor from the extended coda for earthquake signals recorded on seismometers emplaced on the seafloor on continental margins compared to signals recorded on well-coupled stations on land. For example, note the much longer signal recorded on the OBSs and APGs in Figure 4A compared to the signal from the same earthquake recorded onshore at station GO05.

Signals resembling nonvolcanic tremor are observed at stations CP06, CP07, and CP09 throughout the deployment. These signals were identified by bandpass filtering the data at 2–8 Hz, squaring the signal, low-pass filtering below 0.1 s and resampling at 1 sample/s, and taking the square root of this signal to produce the signal envelope. The signal envelopes from the three stations were cross-correlated using a 300 s time window with a 150 s overlap. A potential "tremor" event was detected if the maximum normalized cross-correlation between the three stations was ≥0.6. Finally, to rule out local earthquakes, the cross-correlation had to remain above 80% of its maximum value for at least 20 s. This procedure resulted in >800 events. The procedure is described in more detail in Section S2 (footnote 1), and the times and duration of tremor-like pulses detected thus are listed in Table S2. The number of tremor events per day is compared to the number of earthquakes per day in our catalog in Figure 9.

Figure 8. Examples of data recorded on the broadband vertical component (BHZ) for two typical local earthquakes. (A) An earthquake in the accretionary prism. (B) An earthquake from the outer rise, showing a distinct T-phase; P and S phases are observed for both events. The station, date (including Julian day), and time (UTC) of the first sample are shown for each event.

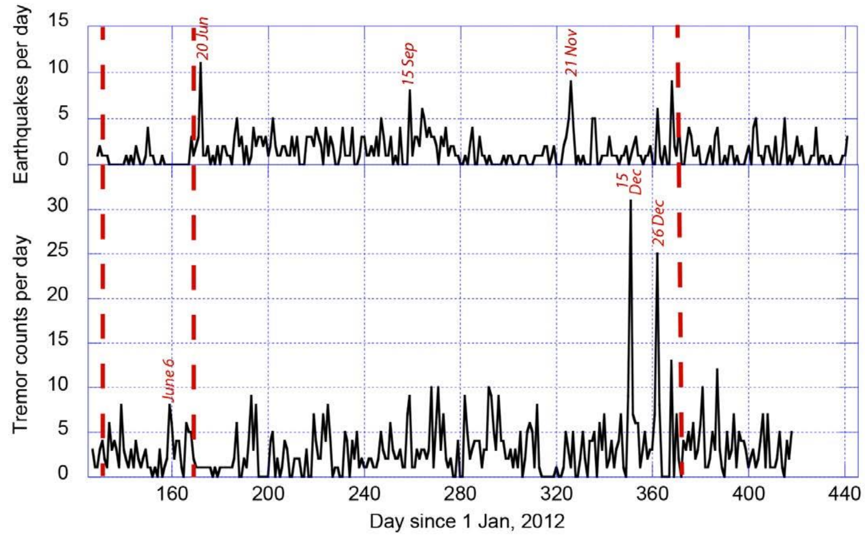

Figure 9. Comparison between the number of earthquakes per day in the catalog of Table S1 (see footnote 1) and the number of tremor events per day in the catalog of Table S2. No correlation is observed between the two catalogs. The times of the three transients observed on the absolute pressure gauges are indicated with a dashed red line.

The largest number of potential tremor events detected through this procedure occurred on 16 December 2012 (day 351 of the year 2012). Four hours of data showing possible nonvolcanic tremor (Fig. 10A) are compared to a typical 4 h window of data, which contains local and regional earthquakes (Fig. 10B). Although tremor-like signals were coherent across the ChilePEPPER network on 16 December, no such signals were recorded onshore at station GO05 (Fig. 10A), suggesting an offshore source. This is in marked contrast to tremor-like signals observed following a M_w 6.0 earthquake on 6 June that was located ~270 km southeast of the network (Fig. S2.2 [footnote 1]). For 6 June, the tremor-like signals are closely correlated with aftershock and other local earthquake activity recorded at GO05 (Fig. S2.3).

Time lags between stations picked from cross-correlations were used to try to locate the source of the tremor pulses using several techniques used to locate tremor onshore. In general, apparent tremor sources could not be localized. Lags calculated for several time windows during the 16 December tremor "swarm," however, allow us to place some constraints on the source location. Figures 10C and 10D show that cross-correlation lags are similar regardless of whether a single pulse or multiple pulses are included in the analysis, indicating that the tremor pulses on this day were coming from the same source. Picks at station CP07 are advanced relative to those at station CP09, whereas those at station CP06 are delayed. Picking the delay time for CP06 is complicated by the asymmetric nature of the cross-correlation. The peak lag is ~15 s, which implies a velocity of no more than 1 km/s to cover the 15 km distance between CP09 and CP06. However, if the lag is measured from the midpoint of the cross-correlation pulse, the lag is decreased to ~8 s, implying a velocity of at most 1.88 km/s. Picking the advance for CP07 is complicated by the double pulse of the cross-correlation. The advance of the first peak is too large for any reasonable velocity. The second peak is advanced by 5.5–6 s, implying a maximum velocity of 3.5 km/s. One reason for the asymmetric lags between tremor pulses recorded on different OBSs may be variable OBS-seafloor coupling resonances due to the relatively massive instrument packages deployed on seafloor sediment with very low shear modulus (e.g., Tréhu, 1985). The peak frequency of the signal observed on the OBSs is systematically different on different instruments (~4.5 Hz at CP06, ~3 Hz at CP09, and no distinct peak at CP07). This is likely a site rather than a source characteristic and may affect the accuracy with which lag times between events can be measured. Although the uncertainties in the lag times preclude a precise location, they are compatible with a source at a distance of a few tens of kilometers to the south or southeast of the network and with a path either in the ocean or in the shallow accretionary prism.

Although we cannot conclusively rule out a source in the water, the apparent source location landward of the deformation front for the 16 December

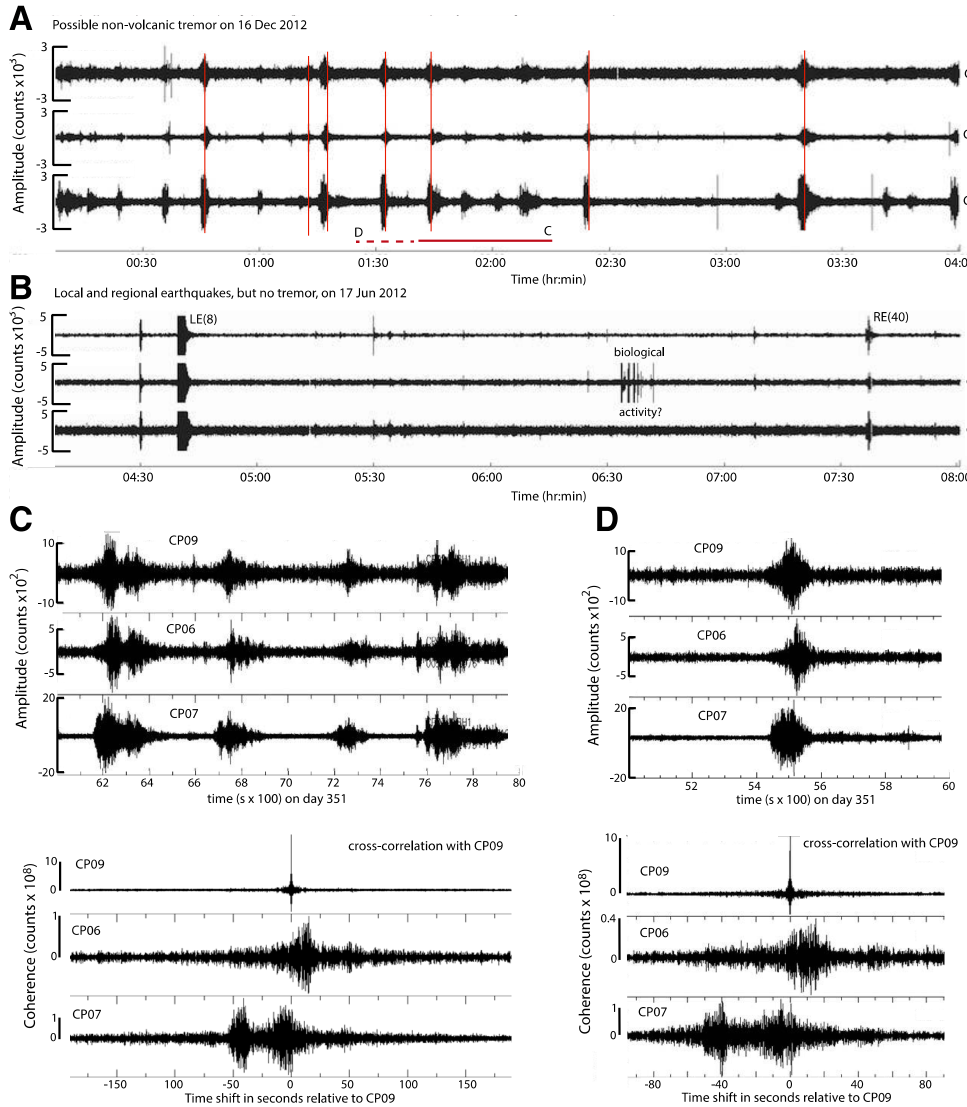

Figure 10. (A) Possible nonvolcanic tremor observed at sites CP06, CP07, and CP09 (see Fig. 1B for location) on 16 December 2012 (Julian day 351). A 4-h-long sample of data on channel BH1 is shown, bandpass filtered at 1–20 Hz. Amplitudes are shown as counts. Data have not been corrected for instrument response; all instruments had the same sensor and recording electronics, but the site response may differ because of soil-structure interaction, as discussed in the text. No data in this time window are clipped, in contrast to the data shown in B. Vertical red lines indicate tremor times detected by the automated tremor detection procedure described in the text. Horizontal solid red line shows the time window displayed in C; horizontal dashed red line shows the time window displayed in D. (B) A 4-h-long sample of data on 17 June 2012, prior to the onset of the transient event shown in Figure 11. Spikes in data from site CP07 may reflect biological activity on or near the ocean-bottom seismometer. Several local events, including a local earthquake (LE) with an S-P time of 8 s and a regional earthquake (RE) with an S-P time of 40 s, are observed in this time window. The local event has a maximum peak-to-peak amplitude of 1,200,000 counts and is clipped on this display; the envelope of the unclipped coda of the local event (not shown) is characterized by a sharp onset and rapid exponential decay, in contrast to the possible tremor shown in A. (C,D) Examples of tremor pulses on 16 December and the cross-correlations used to estimate lag times between stations, as discussed in the text. All times UTC.

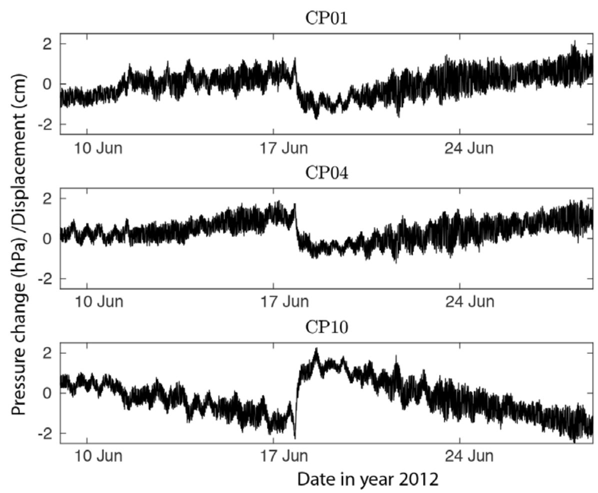

Figure 11. Transient event observed on 17 June 2012 at stations CP1, CP04, and CP10 (see Fig. 1B for location). Data have been processed as described in Section S3 in the Supplemental Material (see footnote 1).

tremor pulses and the general absence of T-phases observed in our data for earthquakes originating in the accretionary prism suggest that these apparent tremor pulses are not T-phases. Moreover, the absence in the CSN catalog of a large earthquake within a few hundred kilometers of the network on 16 December suggests that these events are not aftershocks that look like tremor because of OBS-seafloor coupling resonances. We conclude that it is likely that the ChilePEPPER network recorded nonvolcanic tremor originating in the forearc on 16 December, although we cannot rule out the possibility that some of the pulses detected are due to T-phases from earthquakes. We include these inconclusive results here both as a tantalizing suggestion and a cautionary note. Reliable detection of offshore tremor likely requires both close spacing of stations to detect tremor located within the network and a large aperture to rule out T-phases.

Seafloor Deformation Transients

Slow slip near the deformation front updip of the main slip patch after large earthquakes has been noted in several subduction zones, most notably after the 2005 Nias-Simeulue earthquake (Sumatra, Indonesia), where continuous GPS on islands overlying the outer wedge captured the outer-wedge deformation (Hsu et al., 2006). Shallow slow slip beneath the offshore accretionary prism that was not preceded by a megathrust earthquake downdip has been detected on APGs in the Hikurangi subduction zone (Wallace et al., 2016).

To evaluate whether slow slip events with periods of days to weeks occurred during the post–Maule earthquake deployment, the APG data were processed through a sequence of steps described in Section S3 (footnote 1), which included deterministic removal of the tides (Egbert and Erofeeva, 2002), removal of a long-period drift signal, and reduction of noise using principal component analysis (Dong et al., 2006). This procedure resulted in detection of three episodes of possible transient deformation on 10 May and 17 June 2012 and on 5 January 2013. The processed time series for the largest event (event B) is shown in Figure 11, and the approximate duration and offset observed at each instrument are given in Table 4. The 17 June 2012 transient lasted <24 h, with most of the displacement occurring within 4 h. Subsidence occurred at sites CP01 and CP04 and uplift occurred at site CP10. The pattern of uplift and subsidence is different for the three events, suggesting shallow-rooted deformation of the seafloor.

The second and third transients show a temporal correlation with times of relatively high seismicity (Fig. 9), although in the first case the transient precedes the seismicity, and in the second case the transient follows the seismicity. In both cases, Table S1 (footnote 1) indicates that the earthquakes responsible for the peaks in Figure 9 were small (locations based on four to five observations) and located near the ChilePEPPER network. In contrast, the seismicity peak on 21 November was due to events located well to the north of the network. Although the seismicity peak on 15 September was located near the

TABLE 4. DATE AND DURATION OF THE DETECTED TRANSIENTS IN THE VERTICAL DISPLACEMENT TIME SERIES

	Date	Time of onset (UTC)	Duration	Amplitude Site CP01 (cm)	Amplitude Site CP04 (cm)	Amplitude Site CP10 (cm)
Event A	10 May 2012	23:05	Instantaneous	−1.06 ± 0.01	0.66 ± 0.01	0.32 ± 0.01
Event B	17 Jun 2012	19:40	~1 day	−1.65 ± 0.003	−1.67 ± 0.01	2.95 ± 0.003
Event C	05 Jan 2013	10:00	Two events ~5 days apart	0.85, 0.15	−1.95, −0.35	0.9, 0.30

Notes: Event C is actually two short transients ~5 days apart; the offset during each transient is listed, separated by a comma. See Figure 1B for site locations.

network, no transient was detected around that time. Possible explanations for these transients will be discussed in the concluding section of the paper, which integrates the various observations reported here with the structural framework derived from swath bathymetry and high-resolution multichannel seismic (MCS) data, which are discussed in detail by Tréhu et al. (2019).

Very Low Frequency (VLF) Earthquakes

In 2002, a new class of seismic signals was discovered in the accretionary wedge adjacent to the Nankai Trough offshore Japan (Ishihara, 2003). These events are characterized by peak energy at periods of 10–100 s and little short-period energy and are referred to as VLF (very low frequency) earthquakes. Because of the dearth of high-frequency energy, these events are generally not detected by detection algorithms optimized to find high-frequency events. The spatial occurrence of these events typically overlaps documented aftershock areas in the Nankai Trough, and the unusual properties of these events have been attributed to release of fluid overpressure through fluid expulsion along reverse faults within the accretionary wedge (Obara and Ito, 2005). One of the objectives of ChilePEPPER was to determine whether VLF events were occurring in the accretionary wedge updip as a response to anticipated increased pore pressure in the accretionary wedge induced by slip further downdip during the Maule earthquake.

The APG data from sites CP01, CP04, and CP10 were bandpassed at 0.003–0.07 Hz and visually scanned on all instruments. Forty-three (43) episodes of low-frequency energy were noted (Table S3 [footnote 1]). The times of these events were then compared to times and locations of large seismic events in the U.S. Geological Survey ComCat catalog. All but one of the events corresponded to the expected arrival times of Rayleigh waves. The waveform of the single event that could not be correlated with the catalog was similar to the other interpreted Rayleigh waves, suggesting that it also was a Rayleigh wave from a distant earthquake. We conclude that at most one VLF event (but likely none) large enough to be detected above the background noise level occurred in the vicinity of the ChilePEPPER network during its deployment. Although no VLF events were observed, the ChilePEPPER APG network clearly recorded the tsunami generated by the 2012 Haida Gwaii earthquake (British Columbia, Canada), which generated coherent signals with a primary period of ~20 min (0.0008 Hz) and a peak-to-peak amplitude of ~80 Pa (~8 mm) on the APGs (Fig. S4 [footnote 1]), illustrating the sensitivity of the APGs to very small pressure changes at time scales intermediate between those detected by seismology and geodesy.

Fluid Flow Measurements

According to the dynamic wedge theory of Wang and Hu (2006), stress should increase in the outer accretionary wedge after a great earthquake if the plate boundary beneath the outer wedge is velocity strengthening and slip is arrested downdip of the trench during the main shock. The increased stress should increase pore-fluid pressure within the wedge and induce fluid flow through the sediment-water interface. Slow slip episodes on the plate boundary should also result in pulses of fluid flow. In the Nankai Trough, gradual pore-pressure changes at the toe of the wedge suggest that pore-pressure re-equilibration may take >60 yr (Davis et al., 2013). CAT flow meters designed to detect very low rates of flow into or out of the seafloor (Tryon et al., 2001) were deployed next to OBSs on the outer wedge offshore Costa Rica and recorded oscillating flow of 0.2–1 cm/yr into and out of the seafloor. This flow was correlated with increases in seismic noise (Brown et al., 2005). Modeling suggests that the flow was driven by an episode of localized slow slip on the plate boundary (LaBonte et al., 2009).

For ChilePEPPER, CAT flow meters were integrated into the OBS packages by using the OBS anchor as the collection chamber and attaching the meter to the side of the OBS (Tréhu and Tryon, 2012). The data show that settling of the instruments into the sediments took several months and varied considerably from site to site, yielding in situ records lasting 2–6 months. Once equilibration had been achieved, in situ flow rates were <±0.01 cm/yr (Fig. S5.1 [footnote 1]), and no significant temporal variation was detected. These flow rates are two to three orders of magnitude smaller than rates observed on the Costa Rican margin (Brown et al., 2005, LaBonte et al., 2009) and approach the detection limit of the CAT flow meters. It is difficult to evaluate the significance of this result because of uncertainty about how well the collection chamber was coupled to the seafloor with this instrument configuration.

DISCUSSION

Figure 12A shows the locations of earthquakes in our catalog overlain on structural features of the accretionary prism interpreted from the high-resolution MCS data (Tréhu et al., 2019). As in Figure 5, open circles represent earthquakes located with four or five phases, and filled circles represent earthquakes located with six or more phases. Magenta dots are considered reliable; orange dots are earthquakes for which the epicenters derived from ChilePEPPER data are likely biased to the south, as discussed above. The three APGs on which transients were observed are indicated by yellow triangles outlined in black, and the three seismometers that were used to detect tremor are shown by white triangles outlined in black. Two APGs and one seismometer, outlined in yellow or white, respectively, and filled with gray, were affected by instrumentation problems; although they may have intermittently provided arrival times used for hypocenter locations, they were not used for the tremor and transient analyses. Figure 12B shows hypocenters based on six or more phase picks and at latitudes between 34.8°S and 34.5°S overlain on the velocity model of Moscoso et al. (2011).

One of the more surprising results from the MCS data acquired during ChilePEPPER was an abrupt transition from subduction of nearly all sediment on the incoming plate at the deformation front south of 34.42°S to accretion of nearly all sediment to the north (Tréhu et al., 2019). This transition in the structure at the deformation front is correlated with a change in the morphology of the active accretionary prism (shown by a magenta line in Fig. 12A) that extends to the boundary between the active prism and continental backstop. Tréhu et al. (2019) argued that this change in deformation front structure cannot be explained by changes in the trench sediment and attributed it to a history of subduction of topographic roughness. They concluded that the abrupt downward step in the plate boundary at this transition affected both the updip and along-strike propagation of slip during the Maule earthquake. Both of these outer-prism segments were quiet during the ChilePEPPER deployment, with only a few epicenters based on fewer than six arrival-time readings located within the active accretionary prism in either segment.

The MCS data also indicate that the boundary between the active wedge and the continental basement in this region is a complex zone marked by transpressional structures near the seafloor immediately north and south of the ChilePEPPER network. These are indicated by the blue lines in Figure 12A, which are solid where flower structures are imaged on MCS data and dashed where transpressional ridges are inferred based on bathymetry. The ChilePEPPER network was deployed in a region where the transpressional ridges are not observed. The MCS data suggest that this region is characterized by a pull-apart basin (labeled PAB in Figs. 12A and 12B) formed in response to an extensional stepover in a dominantly right-lateral transpressional shear zone that follows the boundary between the active accretionary prism and the continental framework. Fault mechanisms from first motions for the three largest events of the 15 September 2012 earthquake sequence are roughly consistent with this tectonic setting. Landward of this shear zone, the depth to the paleo-accretionary rocks that comprise the continental basement in this region varies significantly along strike. An uplifted basement dome is present immediately east of the network (labeled DBU in Fig. 12A). The cluster of earthquakes recorded on 15 September 2012, which are among the largest and best located in our catalog, occurred on the boundary between the active accretionary prism and the continental basement as defined by a strong lateral gradient in velocity. Other earthquakes are scattered over a range of depths landward of this boundary or in the subducting crust (with a few additional earthquakes in the upper mantle below 25 km, which are not shown here).

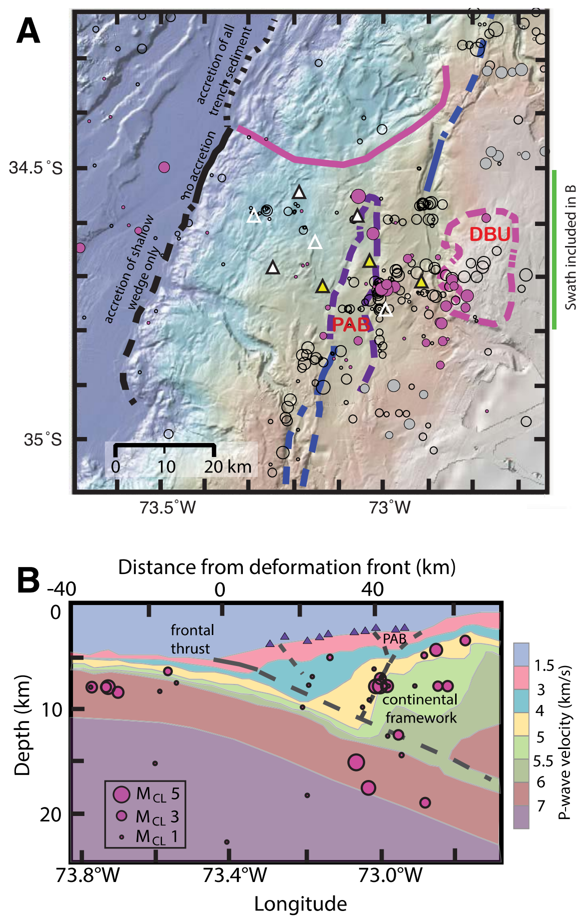

Figure 12. (A) Earthquakes located using data from the ChilePEPPER network. Open circles are events located with fewer than six arrival time picks; magenta and grey filled circles are located with six to 11 arrival-time picks. Grey circles are likely mislocated with a bias toward the network for reasons discussed in the text. Circle diameters are proportional to coda magnitude determined as discussed in Section S1 in the Supplemental Material (see footnote 1). See B for scale. Triangles are ChilePEPPER ocean-bottom seismometer locations. White indicates seismometers used for tremor analysis; yellow indicates absolute pressure gauges used for transient analysis; all stations were used to locate earthquakes. Blue lines indicate transpressional structures near the seafloor (solid line for flower structures, dashed line for transpressional ridges inferred from bathymetry). Magenta line delimits a region of disrupted topography interpreted to indicate subduction of a large topographic feature at ~2 Ma (Tréhu et al., 2019). PAB—pull-apart basin; DBU—domal basement uplift. See text for further discussion. (B) Depth below sea level versus longitude for earthquakes (magenta filled circles) with latitude between 34.5°S and 34.8°S and located using at least six arrival-time picks, compared to the velocity model of Moscoso et al. (2011). Long dashed line is the plate boundary interpreted by Moscoso et al. (2011), modified to incorporate results of Tréhu et al. (2019) near the deformation front (solid line). Purple triangles are the projected location of the ChilePEPPER instruments. Short dashed lines are upper plate structures discussed by Tréhu et al. (2019).

We interpret the three transients detected on the APGs to represent adjustments in response to motion on the boundary between the active prism and the continental basement. The detailed nature of the deformation resulting in these observations is poorly constrained. They could reflect slumping of near-surface topography generated in response to faulting at greater depth or a response to motion on shallow faults that reach the seafloor. Given the complexity of the local structure, the variability in the observations, and the expected anelastic behavior of the sediments, we did not attempt to model these results. Given the increasing interest in seafloor geodesy and the small number of results reported from seafloor APGs, we nonetheless think they merit being reported as additional evidence documenting the promise of APGs as a tool for seafloor geodesy as well as evidence for continuing tectonic activity on the boundary between the active accretionary wedge and the continental basement.

Many pulses of energy in the 2–8 Hz range that resemble nonvolcanic tremor were detected throughout the deployment, but techniques developed for locating tremor on land were not successful at locating the source of the tremor. Detailed examination of the lag times of tremor pulses during the 16 December "swarm" indicates a source located in either the ocean or the shallow forearc wedge several tens of kilometers south or southeast of the ChilePEPPER network, although the precision with which lag times can be picked precludes a precise determination of the source location. Based on the observation that most earthquakes that generated T-phases during the ChilePEPPER deployment were located seaward of the deformation front, an apparent source landward of the deformation front suggests that these tremor pulses may have a shallow subseafloor source. More detailed analysis of the azimuth of approach and apparent velocity of tremor pulses throughout the experiment is underway. These tantalizing results (as well as the transients observed on the APGs) illustrate the need for large-aperture networks with small interstation spacing, requiring larger numbers of seafloor instruments.

CONCLUSIONS

We have located earthquakes with S-P times <17 s (i.e., within ~125 km of the network), with 34 earthquakes located with at least six phase picks, RMS residual <0.5 s, and the closest station within 16 km of the epicenter. Most of the seismicity occurred either near the boundary between the inner and outer wedge or in the outer rise of the subducting plate seaward of the deformation front. For ~50% of the outer-rise earthquakes, the P- and S-wave arrivals were followed by a distinctive T-phase arrival traveling in the ocean. T-phases were rare for earthquakes located landward of the deformation front. Very few earthquakes, and none located with hypocenters deemed "reliable," were located within the active accretionary wedge or on the underlying plate boundary. Comparison of hypocenters for earthquakes within the ChilePEPPER network with hypocenters for the same events reported by onshore catalogs suggests that depths determined with only onshore data and using velocity models appropriate for the coastal region are systematically overestimated.

Application of techniques used to detect nonvolcanic tremor resulted in identification of many potential tremor events. For offshore events recorded on offshore seismometers, distinguishing between nonvolcanic tremor from sources beneath the seafloor and T-phases from tectonic earthquakes is challenging with a small-aperture network. Because of uncertainties in defining the lag time of these arrivals between stations in the network, we were not able to locate the source of the nonvolcanic tremor or conclusively rule out the possibility of T-phases. Close examination of the lag times across the network on the day with the largest number of apparent tremor events indicates that the source of the observations was south or southeast of the network, either along the boundary between the accretionary prism and the continental framework or within the continental framework. The maximum velocities compatible with the observed lags suggest that the source depths were within either the ocean or near-seafloor sediments. In addition to T-phases, P and S waves from earthquakes that reverberate in the uppermost layer of very low-velocity sediments on the seafloor can resemble nonvolcanic tremor. Misidentification as tremor of aftershocks that trigger these reverberations is the likely explanation for an episode of apparent triggered tremor following a M 6 earthquake near the Chile-Argentina border ~270 km from the network.

Analysis of the APG data resulted in several important observations. First, although the APGs were not a good sensor for detecting small, local earthquakes because of a rapid increase in background noise level at frequencies <2 Hz, they did serve as strong-motion instruments for larger, local earthquakes that saturated the seismometers. At longer periods, they proved to be very sensitive, and were used to detect several transient events with a duration of several hours to a few days on instruments that straddled the boundary between the active prism and the continental framework. Because the polarity of the transients differs between stations and between events, we conclude that they represent readjustments of forearc basin sediments in response to tectonic motion along a buried shear zone.

No VLF earthquakes or fluid flow into or out of the seafloor were detected, suggesting that if pore pressures in the outer accretionary prism were elevated in response to the Maule earthquake, release of pressure by flow through the seafloor was below the detection threshold of our instruments.

In spite of limitations due to the small number of stations, the results demonstrate the value of deploying networks of seismometers and APGs in the ocean after major earthquakes in order to document postseismic deformation and understand interplate dynamics. While close instrument spacing was required to obtain good constraints on the depth of earthquakes within the network as well as for detecting tremor and spatially varying transients, all of these measurements would have benefited from a larger-aperture network; however, ten instruments equipped with broadband seismometers, APGs, and flow meters were available for deployment on short notice, resulting in a tradeoff between spacing and aperture. The results underscore the need for large numbers of OBSs capable of measuring seafloor deformation over a wide range of time scales.

ACKNOWLEDGMENTS

We thank the captains and crews of the R/V *Melville* and R/V *Point Sur* and the staff of the U.S. Ocean Bottom Instrument Facility at Lamont-Doherty Earth Observatory for their support for this project. Funding was provided by U.S. National Science Foundation grants OCE1130013 to Oregon State University (OSU; A.M. Tréhu) and OCE1129574 to Scripps Institution of Oceanography (SIO; M.D. Tryon). Support for J. Mieres Madrid to visit OSU and SIO was provided by CONICYT/FONDECYT grant 11170047 (Un. Chile; J. Ruiz and E. Contreras-Reyes). The paper benefitted greatly from thoughtful and probing reviews from Guest Associate Editor Laura Wallace and two annonymous reviewers. All OBS data are available from the IRIS Data Management Center (http://ds.iris.edu/). Underway data and cruise reports are available from the Rolling Deck to Repository (https://www.rvdata.us/).

REFERENCES CITED

Agurto, H., Rietbrock, A., Ryder, I., and Miller, M., 2012, Seismic-afterslip characterization of the 2010 M_w 8.8 Maule, Chile, earthquake based on moment tensor inversion: Geophysical Research Letters, v. 39, L20303, https://doi.org/10.1029/2012GL053434.

Angermann, D., Klotz, J., and Reigber, C., 1999, Space-geodetic estimation of the Nazca–South America Euler vector: Earth and Planetary Science Letters, v. 171, p. 329–334, https://doi.org/10.1016/S0012-821X(99)00173-9.

Balanche, A., Guennou, C., Goslin, J., and Mazoyer, C., 2009, Generation of hydroacoustic signals by oceanic earthquakes: A mechanical model: Geophysical Journal International, v. 177, p. 476–480, https://doi.org/10.1111/j.1365-246X.2009.04146.x.

Bangs, N.L., and Cande, S.C., 1997, Episodic development of a convergent margin inferred from structures and processes along the southern Chile margin: Tectonics, v. 16, p. 489–503, https://doi.org/10.1029/97TC00494.

Blackman, D.K., Nishimura, C.E., and Orcutt, J.A., 2000, Seismoacoustic recordings of a spreading episode on the Mohns Ridge: Journal of Geophysical Research, v. 105, p. 10,961–10,973, https://doi.org/10.1029/2000JB900011.

Bohnenstiehl, D.R., Tolstoy, M., Dziak, R.P., Fox, C.G., and Smith, D.K., and 2002, Aftershock sequences in the mid-ocean ridge environment: An analysis using hydroacoustic data: Tectonophysics, v. 354, p. 49–70, https://doi.org/10.1016/S0040-1951(02)00289-5.

Brown, K.M., Tryon, M.D., DeShon, H.R., Dorman, L.M., and Schwartz, S.Y., 2005, Correlated transient fluid pulsing and seismic tremor in the Costa Rica subduction zone: Earth and Planetary Science Letters, v. 238, p. 189–203, https://doi.org/10.1016/j.epsl.2005.06.055.

Campos, J., Hatzfeld, D., Madariaga, R., Lopez, G., Kausel, E., Zollo, A., Iannacone, R., Fromm, R., Barrientos, S., and Lyon-Caen, H., 2002, A seismological study of the 1835 seismic gap in south-central Chile: Physics of the Earth and Planetary Interiors, v. 132, p. 177–195, https://doi.org/10.1016/S0031-9201(02)00051-1.

Contardo, X., Cembrano, J., Jensen, A., and Díaz-Naveas, J., 2008, Tectono-sedimentary evolution of marine slope basins in the Chilean forearc (33°30′–36°50′S): Insights into their link with the subduction process: Tectonophysics, v. 459, p. 206–218, https://doi.org/10.1016/j.tecto.2007.12.014.

Contreras-Reyes, E., and Carrizo, D., 2011, Control of high oceanic features and subduction channel on earthquake ruptures along the Chile–Peru subduction zone: Physics of the Earth and Planetary Interiors, v. 186, p. 49–58, https://doi.org/10.1016/j.pepi.2011.03.002.

Contreras-Reyes, E., and Osses, A., 2010, Lithospheric flexure modeling seaward of the Chile trench: Implications for oceanic plate weakening in the trench outer rise region: Geophysical Journal International, v. 182, p. 97–112, https://doi.org/10.1111/j.1365-246X.2010.04629.x.

Contreras-Reyes, E., Flueh, E.R., and Grevemeyer, I., 2010, Tectonic control on sediment accretion and subduction off south central Chile: Implications for coseismic rupture processes of the 1960 and 2010 megathrust earthquakes: Tectonics, v. 29, TC6018, https://doi.org/10.1029/2010TC002734.

Contreras-Reyes, E., Maksymowicz, A., Lange, D., Grevemeyer, I., Munoz-Linford, P., and Moscoso, E., 2017, On the relationship between structure, morphology and large coseismic slip: A case study of the Mw 8.8 Maule, Chile 2010 earthquake: Earth and Planetary Science Letters, v. 478, p. 27–39, https://doi.org/10.1016/j.epsl.2017.08.028.

Cubas, N., Avouac, J.P., Souloumiac, P., and Leroy, Y.M., 2013a, Megathrust friction determined from mechanical analysis of the forearc in the Maule earthquake area: Earth and Planetary Science Letters, v. 381, p. 92–103, https://doi.org/10.1016/j.epsl.2013.07.037.

Cubas, N., Avouac, J.P., Leroy, Y.M., and Pons, A., 2013b, Low friction on the high slip patch of the 2011 Mw 9.0 Tohoku-Oki earthquake required from the wedge structure and extensional splay faults: Geophysical Research Letters, v. 40, p. 4231–4237, http://doi.org/10.1002/grl.50682.

Czoski, P.A., Tréhu, A.M., Williams, M.C., Dziak, R.P., and Embley, R.W., 2012, The August and October 2008 earthquake swarms on the Explorer/Pacific plate boundary [abs.]: Seismological Research Letters, v. 83, p. 425–426.

Davis, E.E., Kinoshita, M., Wang, K., Asano, Y., Ito, Y., and Becker, K., 2013, Episodic deformation and inferred slow slip at the Nankai subduction zone during the first decade of CORK borehole pressure and VLFE monitoring: Earth and Planetary Science Letters, v. 368, p. 110–118, https://doi.org/10.1016/j.epsl.2013.03.009.

de Groot-Hedlin, C.D., and Orcutt, J.D., 2001, Excitation of T-phases by seafloor scattering: Journal of the Acoustical Society of America, v. 109, p. 1944–1954, https://doi.org/10.1121/1.1361057.

Delouis, B., Nocquet, J.-M., and Vallee, M., 2010, Slip distribution of the February 27, 2010 Mw = 8.8 Maule earthquake, central Chile, from static and high-rate GPS, InSAR, and broadband seismic data: Geophysical Research Letters, v. 37, L17305, https://doi.org/10.1029/2010GL043899.

de Moor, A., 2015, Local seismicity recorded by ChilePEPPER: Implications for dynamic accretionary prism response and long-term prism evolution [M.S. thesis]: Corvallis, Oregon State University, 79 p., https://ir.library.oregonstate.edu/concern/graduate_thesis_or_dissertations/00000354x.

Dong, D., Fang, P., Bock, Y., Webb, F., Prawirodirdjo, L., Kedar, S., and Jamason, P., 2006, Spatiotemporal filtering using principal component analysis and Karhunen-Loeve expansion approaches for regional GPS network analysis: Journal of Geophysical Research, v. 111, B03405, https://doi.org/10.1029/2005JB003806.

Dziak, R.P., 2001, Empirical relationship of T-wave energy and fault parameters of northeast Pacific Ocean earthquakes: Geophysical Research Letters, v. 28, p. 2537–2540, https://doi.org/10.1029/2001GL012939.

Dziak, R.P., Fox, C.G., and Schreiner, A.E., 1995, The June-July 1993 seismo-acoustic event at CoAxial segment, Juan de Fuca Ridge: Evidence for a lateral dike injection: Geophysical Research Letters, v. 22, p. 135–138, https://doi.org/10.1029/94GL01857.

Dziak, R.P., Bohnenstiehl, D.R., Matsumoto, H., Fox, C.G., Smith, D.K., Tolstoy, M., Lau, T.-K., Haxel, J.H., and Fowler, M.J., 2004, P- and T-wave detection thresholds, *Pn* velocity estimate, and detection of lower mantle and core P-waves on ocean sound-channel hydrophones at the Mid-Atlantic Ridge: Bulletin of the Seismological Society of America, v. 94, p. 665–677, https://doi.org/10.1785/0120030156.

Egbert, G.D., and Erofeeva, S.Y., 2002, Efficient inverse modeling of barotropic ocean tides: Journal of Atmospheric and Oceanic Technology, v. 19, p. 183–204, https://doi.org/10.1175/1520-0426(2002)019<0183:EIMOBO>2.0.CO;2.

Fagereng, Å., 2011, Wedge geometry, mechanical strength, and interseismic coupling of the Hikurangi subduction thrust, New Zealand: Tectonophysics, v. 507, p. 26–30, https://doi.org/10.1016/j.tecto.2011.05.004.

Forsyth, D.W., Yang, Y., Mangriotis, M.-D., and Shen, Y., 2003, Coupled seismic slip on adjacent oceanic transforms: Geophysical Research Letters, v. 30, 1618, https://doi.org/10.1029/2002GL016454.

Hashimoto, Y., Tobin, H.J., Knuth, M., and Harada, A., 2011, Data report: Compressional and shear wave velocity measurements on sediment in the hanging wall and footwall of megasplay fault, NanTroSEIZE Stage 1, *in* Kinoshita, M., Tobin, H., Ashi, J., Kimura, G., Lallemant, S., Screaton, E.J., Curewitz, D., Masago, H., Moe, K.T., and the Expedition 314/315/316 Scientists, Proceedings of the Integrated Ocean Drilling Program, Volume 314/315/316: Washington, D.C., Integrated Ocean Drilling Program Management International, Inc., https://doi.org/10.2204/iodp.proc.314315316.217.2011.

Hayes, G.P., Wald, D.J., and Johnson, R.L., 2012, Slab1.0: A new three-dimensional model of global subduction interface geometry: Journal of Geophysical Research, v. 117, https://doi.org/10.1029/2011JB008524.

Hayes, G.P., Bergman, E., Johnson, K.L., Benz, H.M., Brown, L., and Meltzer, A.S., 2013, Seismotectonic framework of the February 27, 2010 M_w 8.8 Maule, Chile earthquake sequence: Geophysical Journal International, v. 195, p. 1034–1051, https://doi.org/10.1093/gji/ggt238.

Hicks, S.P., Rietbrock, A., Ryder, I.M.A., Lee, C.-S., and Miller, M., 2014, Anatomy of a megathrust: The 2010 M8.8 Maule, Chile earthquake rupture zone imaged using seismic tomography: Earth and Planetary Science Letters, v. 405, p. 142–155, https://doi.org/10.1016/j.epsl.2014.08.028.

Hsu, Y.J., Simons, M., Avouac, J.P., Galetzka, J., Sieh, K., Chlieh, M., Natawidjaja, D., Prawirodirdjo, L., and Bock, Y., 2006, Frictional afterslip following the 2005 Nias-Simeulue earthquake, Sumatra: Science, v. 312, p. 1921–1926, https://doi.org/10.1126/science.1126960.
Ishihara, Y., 2003, Major existence of very low frequency earthquakes in background seismicity along subduction zone of south-western Japan: Eos (Transactions, American Geophysical Union), v. 84, Fall Meeting Suppl., Abstract S41C-0107.
Kodaira, S., No, T., Nakamura, Y., Fujiwara, T., Kaiho, Y., Miura, S., Takahashi, N., Kaneda, Y., and Taira, A., 2012, Coseismic fault rupture at the trench axis during the 2011 Tohoku-oki earthquake: Nature Geoscience, v. 5, p. 646–650, https://doi.org/10.1038/ngeo1547.
Kukowski, N., and Oncken, O., 2006, Subduction erosion: The "normal" mode of fore-arc material transfer along the Chilean margin?, *in* Oncken, O., Chong, G., Franz, G., Giese, P., Götze, H.-J., Ramos, V.A., Strecker, M.R., and Wigger, P., eds., The Andes: Active Subduction Orogeny: Berlin, Springer, Frontiers in Earth Sciences, v. 3, p. 217–236, https://doi.org/10.1007/978-3-540-48684-8_10.
LaBonte, A.L., Brown, K.M., and Fialko, Y., 2009, Hydrologic detection and finite element modeling of a slow slip event in the Costa Rica prism toe: Journal of Geophysical Research, v. 114, B00A02, https://doi.org/10.1029/2008JB005806.
Lallemand, S.E., Schnürle, P., and Malavieille, J., 1994, Coulomb theory applied to accretionary and nonaccretionary wedges: Possible causes for tectonic erosion and/or frontal accretion: Journal of Geophysical Research, v. 99, p. 12,033–12,055, https://doi.org/10.1029/94JB00124.
Lange, D., Tilmann, F., Barrientos, S.E., Contreras- Reyes, E., Methe, P., Moreno, M., Heit, B., Bernard, P., Vilotte, J.-P., and Beck, S., 2012, Aftershock seismicity of the 27 February 2010 Mw 8.8 Maule earthquake rupture zone: Earth and Planetary Science Letters, v. 317-318, p. 413-425, https://doi.org/10.1016/j.epsl.2011.11.034.
Lay, T., Ammon, C.J., Kanamori, H., Koper, K.D., Sufri, O., and Hutko, A.R., 2010, Teleseismic inversion for rupture process of the 27 February 2010 Chile (M_w 8.8) earthquake: Geophysical Research Letters, v. 37, L13301, https://doi.org/10.1029/2010GL043379.
Lee, W.H., and Lahr, J.C., 1975, HYPO71 (revised): A computer program for determining hypocenter, magnitude, and first motion pattern of local earthquakes: U.S. Geological Survey Open-File Report 75-311, 113 p., https://doi.org/10.3133/ofr75311.
Lieser, K., Grevemeyer, I., Lange, D., Flueh, E., Tilmann, F., and Contreras-Reyes, E., 2014, Splay fault activity revealed by aftershocks of the 2010 M_w 8.8 Maule earthquake, central Chile: Geology, v., 42, p. 823–826, https://doi.org/10.1130/G35848.1.
Lin, Y.-n.N., Sladen, A., Ortega-Culaciati, F., Simons, M., Avouac, J.-P., Fielding, E.J., Brooks, B.A., Bevis, M., Genrich, J., Rietbrock, A., Vigny, C., Smalley, R., and Socquet, A., 2013, Coseismic and postseismic slip associated with the 2010 Maule Earthquake, Chile: Characterizing the Arauco Peninsula barrier effect: Journal of Geophysical Research: Solid Earth, v. 118, p. 3142–3159, https://doi.org/10.1002/jgrb.50207.
Lomnitz, C., 2004, Major earthquakes of Chile: A historical survey, 1535–1960: Seismological Research Letters, v. 75, p. 368–378, https://doi.org/10.1785/gssrl.75.3.368.
Lorito, S., Romano, F., Atzori, S., Tong, X., Avallone, A., McCloskey, J., Cocco, M., Boschi, E., and Piatanesi, A., 2011, Limited overlap between the seismic gap and coseismic slip of the great 2010 Chile earthquake: Nature Geoscience, v. 4, p. 173–177, https://doi.org/10.1038/ngeo1073.
Loveless, J.P., Pritchard, M.E., and Kukowski, N., 2010, Testing mechanisms of subduction zone segmentation and seismogenesis with slip distributions from recent Andean earthquakes: Tectonophysics, v. 495, p. 15–33, https://doi.org/10.1016/j.tecto.2009.05.008.
Maksymowicz, A., Tréhu, A.M., Contreras-Reyes, E., and Ruiz, S., 2015, Density-depth model of the continental wedge at the maximum slip segment of the Maule Mw8.8 megathrust earthquake: Earth and Planetary Science Letters, v. 409, p. 265–277, https://doi.org/10.1016/j.epsl.2014.11.005.
Maksymowicz, A., Chadwell, C.D., Ruiz, J., Tréhu, A.M., Contreras-Reyes, E., Weinrebe, W., Díaz-Naveas, J., Gibson, J.C., Lonsdale, P., and Tryon, M.D., 2017, Coseismic seafloor deformation in the trench region during the Mw 8.8 Maule megathrust earthquake: Scientific Reports, v. 7, 45918, https://doi.org/10.1038/srep45918.
Mix, A.C., Tiedemann, R., Blum, P., et al., 2003, Proceedings of the Ocean Drilling Program, Initial Reports, Volume 202: College Station, Texas, Ocean Drilling Program, https://doi.org/10.2973/odp.proc.ir.202.2003.
Moreno, M., Rosenau, M., and Oncken, O., 2010, 2010 Maule earthquake slip correlates with pre-seismic locking of Andean subduction zone: Nature, v. 467, p. 198–202, https://doi.org/10.1038/nature09349.
Moreno, M., Melnick, D., Rosenau, M., Baez, J., Klotz, J., Oncken, O., Tassara, A., Chen, J., Bataille, K., Bevis, M., Soquet, A., Bolte, J., Vigny, C., Brooks, B., Ryder, I., Grund, V., Smalley, B., Carrizo, D., Bartsch, M., and Hase, H., 2012, Toward understanding tectonic control on the Mw 8.8 2010 Maule Chile earthquake: Earth and Planetary Science Letters, v. 321–322, p. 152–165, https://doi.org/10.1016/j.epsl.2012.01.006.
Moscoso, E., Grevemeyer, I., Contreras-Reyes, E., Flueh, E.R., Dzierma, Y., Rabbel, W., and Thorwart, M., 2011, Revealing the deep structure and rupture plane of the 2010 Maule, Chile earthquake (Mw = 8.8) using wide angle seismic data: Earth and Planetary Science Letters, v. 307, p. 147–155, https://doi.org/10.1016/j.epsl.2011.04.025.
Nakano, M., Hori, T., Araki, E., Takahashi, N., and Kodaira, S., 2016, Ocean floor networks capture low-frequency earthquake event: Eos (Transactions, American Geophysical Union), v. 97, https://doi.org/10.1029/2016EO052877.
Obara, K., and Ito, Y., 2005, Very low frequency earthquakes excited by the 2004 off the Kii peninsula earthquakes: A dynamic deformation process in the large accretionary prism: Earth, Planets, and Space, v. 57, p. 321–326, https://doi.org/10.1186/BF03352570.
Poli, P., Maksymowicz, A., and Ruiz, S., 2017, The M_w 8.3 Illapel earthquake (Chile): Preseismic and postseismic activity associated with hydrated slab structures: Geology, v. 45, p. 247–250, https://doi.org/10.1130/G38522.1.
Pollitz, F.F., Brooks, B., Tong, X., Bevis, M.G., Foster, J.H., Bürgmann, R., Smalley, R., Jr., Vigny, C., Socquet, A., Ruegg, J.-C., Campos, J., Barrientos, S., Parra, H., Baez Soto, J.C., Cimbaro, S., and Blanco, M., 2011, Coseismic slip distribution of the February 27, 2010 Mw 8.8 Maule, Chile earthquake: Geophysical Research Letters, v. 38, L09309, https://doi.org/10.1029/2011GL047065.
Rietbrock, A., Ryder, I., Hayes, G., Haberland, C., Comte, D., Roecker, S., and Lyon-Caen, H., 2012, Aftershock seismicity of the 2010 Maule Mw = 8.8, Chile, earthquake: Correlation between co-seismic slip models and aftershock distribution: Geophysical Research Letters, v. 39, L08310, https://doi.org/10.1029/2012GL051308.
Ruegg, J.C., Rudloff, A., Vigny, C., Madariaga, R., de Chabalier, J.B., Campos, J., Kausel, E., Barrientos, S., and Dimitrov, D., 2009, Interseismic strain accumulation measured by GPS in the seismic gap between Constitución and Concepción in Chile: Physics of the Earth and Planetary Interiors, v. 175, p. 78–85, https://doi.org/10.1016/j.pepi.2008.02.015.
Ruff, L.J., 1989, Do trench sediments affect great earthquake occurrence in subduction zones?: Pure and Applied Geophysics, v. 129, p. 263–282, https://doi.org/10.1007/BF00874629.
Ruiz, S., and Madariaga, R., 2018, Historical and recent large megathrust earthquakes in Chile: Tectonophysics, v. 733, p. 37–56, https://doi.org/10.1016/j.tecto.2018.01.015.
Russo, R.M., Beck, S.L., Roecker, S.W., Reusch, A.M., Velasco, A., Ebeling, C., and Bremner, P.M., 2011, EarthScope participates in open data seismic deployment following 2010 Chile earthquake: inSights (EarthScope newsletter), http://www.earthscope.org/articles/open_seismic_data_deployment (accessed August 2019).
Ryan, W.B.F., Carbotte, S.M., Copan, J.O., O'Hara, S., Melkonian, A., Arko, R., Weissel, R.A., Ferrini, V., Goodwillie, A., Nitsche, F., Bonczkowski, J., and Zemsky, R., 2009, Global Multi-Resolution Topography synthesis: Geochemistry Geophysics Geosystems, v. 10, Q03014, https://doi.org/10.1029/2008GC002332.
Sato, M., Ishikawa, T., Ujihara, N., Yoshida, S., Fujita, M., Mochizuki, M., and Asada, A., 2011, Displacement above the hypocenter of the 2011 Tohoku-Oki earthquake: Science, v. 332, p. 1395, https://doi.org/10.1126/science.1207401.
Scholl, D.W., Kirby, S.H., von Huene, R., Ryan, H., Wells, R.E., and Geist, E.L., 2015, Great (≥Mw8.0) megathrust earthquakes and the subduction of excess sediment and bathymetrically smooth seafloor: Geosphere, v. 11, p. 236–265, https://doi.org/10.1130/GES01079.1.
Tong, X., Sandwell, D., Luttrell, K., Brooks, B., Bevis, M., Shimada, M., Foster, J., Smalley, R., Jr., Parra, H., Báez Soto, J.C., Blanco, M., Kendrick, E., Genrich, J., and Caccamise, D.J., II, 2010, The 2010 Maule, Chile earthquake: Downdip rupture limit revealed by space geodesy: Geophysical Research Letters, v. 37, L24311, https://doi.org/10.1029/2010GL045805.
Tréhu, A.M., 1985, Coupling of ocean bottom seismometers to sediment: Results of tests with the U.S. Geological Survey ocean bottom seismometer: Bulletin of the Seismological Society of America, v. 75, p. 271–289.
Tréhu, A., 2013, Cruise report: R/V *Point Sur*, PS1306: https://doi.org/10.7284/903032 (last accessed August 2019).
Tréhu, A., and Tryon, M., 2012, Cruise report: R/V *Melville*, MV1206—The 2010 Maule, Chile Earthquake: Project Evaluating Prism Post-Earthquake Response (Chile-PEPPER), https://doi.org/10.7284/903827 (last accessed August 2019).
Tréhu, A.M., Braunmiller, J., and Davis, E., 2015, Seismicity of the central Cascadia Continental margin near 44.5° N: A decadal view: Seismological Research Letters, v. 86, p. 819–829, https://doi.org/10.1785/0220140207.

Tréhu, A.M., Wilcock, W.S.D., Hilmo, R., Bodin, P., Connolly, J., Roland, E.C., and Braunmiller, J., 2018, The role of the Ocean Observatories Initiative in monitoring the offshore earthquake activity of the Cascadia subduction zone: Oceanography, v. 31, p. 104–113, https://doi.org/10.5670/oceanog.2018.116.

Tréhu, A.M., Hass, B., de Moor, A., Maksymowicz, A., Contreras-Reyes, E., Vera, E., and Tryon, M.D., 2019, Geologic controls on up-dip and along-strike propagation of slip during subduction zone earthquakes from a high-resolution seismic reflection survey across the northern limit of slip during the 2010 Mw 8.8 Maule earthquake, offshore Chile: Geosphere, v. 15, https://doi.org/10.1130/GES02099.1.

Tryon, M., Brown, K., Dorman, L., and Sauter, A., 2001, A new benthic aqueous flux meter for very low to moderate discharge rates: Deep Sea Research Part I: Oceanographic Research Papers, v. 48, p. 2121–2146, https://doi.org/10.1016/S0967-0637(01)00002-4.

Vigny, C., et al., 2011, The 2010 M_w 8.8 Maule megathrust earthquake of central Chile, monitored by GPS: Science, v. 332, p. 1417–1421, https://doi.org/10.1126/science.1204132.

Völker, D., Geersen, J., Contreras-Reyes, E., and Reichert, C., 2013, Sedimentary fill of the Chile Trench (32–46°S): Volumetric distribution and causal factors: Journal of the Geological Society of London, v. 170, p. 723–736, https://doi.org/10.1144/jgs2012-119.

Wallace, L.M., Webb, S.C., Ito, Y., Mochizuki, K., Hino, R., Henrys, S., Schwarz, S.Y., and Sheehan, A.F., 2016, Slow slip near the trench at the Hikurangi subduction zone, New Zealand: Science, v. 352, p. 701–704, https://doi.org/10.1126/science.aaf2349.

Wang, K., and Dixon, T., 2004, "Coupling" semantics and science in earthquake research: Eos (Transactions, American Geophysical Union), v. 85, p. 180, https://doi.org/10.1029/2004EO180005.

Wang, K., and Hu, Y., 2006, Accretionary prisms in subduction earthquake cycles: The theory of dynamic Coulomb wedge: Journal of Geophysical Research, v. 111, B06410, https://doi.org/10.1029/2005JB004094.

Webb, S.C., and Nooner, S.L., 2016, High-resolution seafloor absolute pressure gauge measurements using a better counting method: Journal of Atmospheric and Oceanic Technology, v. 33, p. 1859–1874, https://doi.org/10.1175/JTECH-D-15-0114.1.

Wech, A.G., Sheehan, A.F., Boese, C.M., Townend, J., Stern, T.A., and Collins, J.A., 2013, Tectonic tremor recorded by ocean bottom seismometers: Seismological Research Letters, v. 84, p. 752–758, https://doi.org/10.1785/0220120184.

Wech, A., Tepp, G., Lyons, J., and Haney, M., 2018, Using earthquakes, T waves, and infrasound to investigate the eruption of Bogoslof Vocano, Alaska: Geophysical Research Letters, v. 45, p. 6918–16925, https://doi.org/10.1029/2018GL078457.

Williams, M.C., Tréhu, A.M., and Braunmiller, J., 2011, Seismicity at the Cascadia plate boundary beneath the Oregon continental shelf: Bulletin of the Seismological Society of America, v. 101, p. 940–950, https://doi.org/10.1785/0120100198.

Ye, L., Lay, T., Kanamori, H., and Rivera, L., 2016, Rupture characteristics of major and great ($M_w{}^{3}7.0$) megathrust earthquakes from 1990 to 2015: 1. Source parameter scaling relationships: Journal of Geophysical Research: Solid Earth, v. 121, p. 826–844, https://doi.org/10.1002/2015JB012426.

Yue, H., Lay, T., Rivera, L., An, C., Vigny, C., Tong, X., and Báez Soto, J.C., 2014, Localized fault slip to the trench in the 2010 Maule, Chile M_w = 8.8 earthquake from joint inversion of high-rate GPS, teleseismic body waves, InSAR, campaign GPS, and tsunami observations: Journal of Geophysical Research: Solid Earth, v. 119, p. 7786–7804, https://doi.org/10.1002/2014JB011340.

3.3.2.4 Tremores Tectónicos en la Región de Atacama

El objetivo de esta investigación era comprender los efectos sismológicos y reológicos que genera la subducción del Ridge de Copiapó en la Región de Atacama. Para lo anterior, se utilizó una red temporal de estaciones banda ancha y acelerómetros desplegadas en la zona, la cual registró de forma continua desde junio del año 2019 a enero del año 2020.

En la investigación se detectó y localizó la sismicidad ordinaria y lenta además de generar un modelo tomográfico para la zona. Mi aporte en la investigación fue la búsqueda y localización de tremores tectónicos y terremotos repetitivos. A continuación, se presenta el articulo científico publicado, en el cual, participé como co-autor.

Geophysical Research Letters

RESEARCH LETTER
10.1029/2021GL095471

Key Points:

- We identify distinct along-dip segments hosting seismicity, clusters of similar events, non-volcanic tremors and slow slip
- Low Vp and Vs velocities with moderate Vp/Vs ratio suggest the presence of fluids in the aseismic zones
- We propose these marked differences in seismic behavior are due to the subduction of the Copiapó ridge

Supporting Information:

Supporting Information may be found in the online version of this article.

Correspondence to:

F. Pastén-Araya,
fpasten@dgf.uchile.cl

Citation:

Pastén-Araya, F., Potin, B., Azúa, K., Sáez, M., Aden-Antoniów, F., Ruiz, S., et al. (2022). Along-dip segmentation of the slip behavior and rheology of the Copiapó ridge subducted in north-central Chile. *Geophysical Research Letters*, *49*, e2021GL095471. https://doi.org/10.1029/2021GL095471

Received 31 JUL 2021
Accepted 26 JAN 2022

Along-Dip Segmentation of the Slip Behavior and Rheology of the Copiapó Ridge Subducted in North-Central Chile

F. Pastén-Araya[1], B. Potin[1], K. Azúa[1], M. Sáez[1], F. Aden-Antoniów[2], S. Ruiz[1], L. Cabrera[3], J. P. Ampuero[4], J. M. Nocquet[4], L. Rivera[5], and Z. Duputel[6]

[1]Departamento de Geofísica, Facultad de Ciencias Físicas y Matemáticas, Universidad de Chile, Santiago, Chile, [2]Department of Earth, Atmospheric and Planetary Sciences, Massachusetts Institute of Technology, Cambridge, MA, USA, [3]ISTerre Institut des Sciences de la Terre, CNRS, Université Grenoble Alpes, Grenoble, France, [4]Université Côte d'Azur, IRD, CNRS, Observatoire de la Côte d'Azur, Géoazur, Valbonne, France, [5]Université de Strasbourg/CNRS, ITES, UMR 7063, Strasbourg F-67084, Strasbourg, France, [6]Observatoire Volcanologique du Piton de la Fournaise, Universite de Paris, Institut de Physique du Globe de Paris, CNRS, Paris, France

Abstract We studied the along-dip influence of the Copiapó ridge subduction in the Atacama region, North-Central Chile by building a new seismicity catalog, including similar events and non-volcanic tremors (NVTs). We also obtained a 3-D tomographic model for *P* and *S*-waves velocity (and the implied Vp/Vs ratio). We identify along-dip segmentation involving four distinct segments: a locked seismogenic zone hosting ordinary seismicity and clusters of similar events; a transition zone with NVTs and low seismicity; an aseismic zone with slow-slip events; and a deep zone with abundant intraslab seismicity. The velocity models show differences among these zones, with low velocity anomalies of Vp and Vs coinciding with aseismic slip zones, indicating the possible presence of fluids. Due to the spatial distribution along-strike and along-dip of the aseismic zones, we propose that these differences in seismogenic behavior are generated by subduction of the heterogeneous seamounts associated with the Copiapó ridge.

Plain Language Summary Several studies suggest that subduction of large bathymetric features such as seamounts and fracture zones can produce aseismic slip in the subduction zones. We investigate the possible influence of the subduction of the Copiapó ridge in north-central Chile. Our results show down-dip zones with distinct seismic and aseismic behavior. The seismic zones are distinguished by ordinary seismicity and high coupling values, while the aseismic zones are characterized by low coupling values, clusters of similar events, non-volcanic tremors and slow-slip events. In addition, by means of a three-dimensional tomography model, we suggest that fluids are present in the aseismic zones which can help to produce aseismic slip. All these consistent observations exhibit a significant spatial correlation with the Copiapó ridge. Therefore we propose these differences in the seismic behavior are due to the subduction of the Copiapó ridge.

1. Introduction

The segmentation and the probable extent of seismic ruptures of subduction earthquakes along-strike and down-dip are still under debate and remain as open questions. Several studies have proposed that the extent of seismic ruptures might be controlled by different factors such as: the presence of fluids and sediment entering the subduction zone (Baba et al., 2020; Liu & Zhao, 2018); differences in the geology of the upper plate (Bassett et al., 2016; Maksymowicz et al., 2018) and the subduction of large bathymetric features in the oceanic crust like seamounts and oceanic ridges (Kato et al., 2010; Maksymowicz, 2015; Wang & Bilek, 2011, 2014). The latter is particularly noteworthy since several megathrust earthquakes have stopped close to bathymetric features, thus leading several studies to suggest that these oceanic features act as seismic barriers along-strike of the megathrust (Bassett & Watts, 2015a, 2015b; Contreras-Reyes & Carrizo, 2011; Henstock et al., 2016; Lallemand et al., 2018; Wang & Bilek, 2011, 2014). In addition, the subduction of these bathymetric features is linked to other seismic observations like seismic swarms, non-volcanic tremors (NVTs) and slow-slip events (SSEs) (Nishikawa et al., 2019; Nishikawa & Ide, 2018; Poli et al., 2017). Tréhu et al. (2012) showed evidence of correlation between seismicity clusters and seamount subduction in the Cascadia subduction zone, while Kodaira et al. (2004) and Kato et al. (2010) established a connection between the subduction of an oceanic ridge and the frequent occurrence of SSEs in the Nankai subduction zone. Although the potential influence of bathymetric features on seismic ruptures along-strike has been abundantly discussed in past works, an accurate assessment of their influence at depth

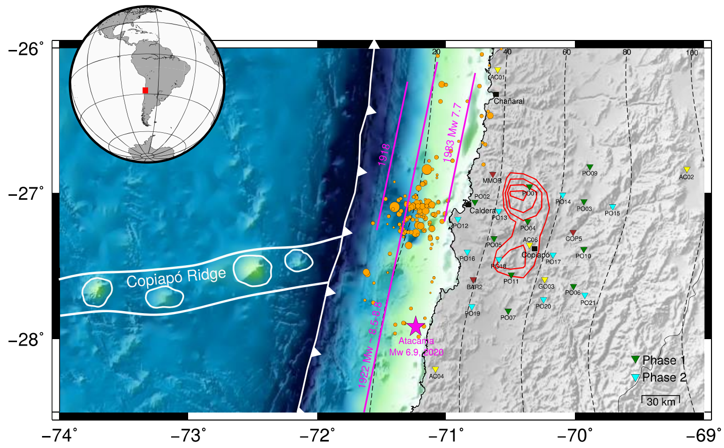

Figure 1. Seismotectonic context. The pink lines and star indicate the historical and recent earthquakes. The green and lightblue triangles correspond to the two phases of the temporary broad-band network. The brown and yellow triangles correspond to semi-permanent broad-band stations of the Strasbourg university and the permanent stations of Centro Sismológico Nacional respectively. The white line indicates de CoR and its seamounts. The orange dots indicate the seismic swarm of 2006, and the red lines are slip contours of the 2014 deep SSE, each contour is 50 mm of slip (Klein, Duputel, et al., 2018). The segmented black lines correspond to Slab2.0 model (Hayes et al., 2018) and the white triangles indicate the trench.

remains challenging. In particular, we still need to understand why some regions are more prone to aseismic slip than others.

The Atacama North-Central region of the Chilean margin (26°–28.5°S), where the Copiapó Ridge (CoR) is subducting below the South American margin, is currently characterized by a seismic gap (Ruiz & Madariaga, 2018). The CoR is made of different seamounts of diverse geometries and considerable heights (∼2,000 m high) (Figure 1). The CoR subduction coincides with a zone of low interseismic coupling, separating two areas of high coupling that could potentially generate large subduction earthquakes (Mw > 8.5) (Klein, Metois, et al., 2018). In addition, seismic swarms have been reported in this area in 1973, 1979 and 2006 (Comte et al., 2002; Holtkamp et al., 2011). The latter occurred between April and May 2006 with a total of 180 reported events (Figure 1; Comte et al., 2006). A SSE in 2014 was detected deeper along the interface, at approximately 50 km depth (Klein, Duputel, et al., 2018) with an equivalent magnitude 6.9 (Figure 1). Continuous GPS data of the global network suggest that SSEs recurrently occur every 4–5 years in that area (Klein, Duputel, et al., 2018).

Large megathrust earthquakes also occurred in the past, the largest one in 1922 (Mw ∼ 8.5–8.8), and several moderate earthquakes have occurred more frequently for example, 1796, 1918, 1983 (Beck et al., 1998; Kanamori et al., 2019; Ruiz & Madariaga, 2018). The last event, with Mw 6.9, happened on 1 September 2020 and was part of a remarkable seismic and a-seismic sequence (Klein et al., 2021) (Figure 1). Most ruptures of moderate magnitude earthquakes (<7.5) that initiated north of the CoR stopped at the CoR, although the large megathrust earthquake of 1922 appears to ruptured through it.

We deployed a temporary seismological network to study the seismicity associated with the CoR and eventually to understand how it might control the along-dip seismic behavior of the plate interface. We conducted an effective search for similar events and NVTs, clues for potential aseismic slip. Using a non-linear tomography method, we built 3-D *P*- and *S*-wave velocity models and a Vp/Vs ratio model to investigate the rheology and the possible presence of fluids along the plate interface.

2. Data, Methods and Results

Seismic monitoring is performed by five permanent stations of the Centro Sismológico Nacional (CSN) within 200 km around the study area. Three semi-permanent stations of the University of Strasbourg also monitor the region since 2019 (Zigone et al., 2019). In order to increase the detection capability for this study, we installed 10 temporary broad-band stations, in 2 different settings, during 4 months each (Figure 1). The first phase of acquisition ran from June 24th to October 8th of 2019 and the second phase from October 9th of 2019 to January 17th of 2020. In total, we acquired data for 8 months, with a total of 28 stations of which 8 were permanent during the entire experiment.

2.1. Seismic Catalog

During the 8 months of data acquisition, the network detected tens of thousands of local and regional events. In order to build a robust catalog, we implemented both manual and automatic phase-arrival picking. For the manual picking, earthquake detection was performed by a multistage approach. First, we roughly identified potential events by a conservative STA/LTA detection method on each station. Second, we filtered out the hundreds of very-low magnitude events and most of the outliers by considering only the potential wave-arrivals observed on for at least 5 stations. Finally, we gathered these potential-arrivals into potential-events and manually inspected them. We selected only events for which at least 1 station had an arrival time difference between *P* and *S*-wave smaller than 25 s, limiting the study area to approximately 200 km radius around the network. Picking was performed using Seisan (Havskov & Ottemöller, 2008). Due to the quality of the records obtained, we were able to manually picked a portion of the data between the months of August-September of the first phase and November-January of the second phase. We obtained 1,477 events made of 16,745 *P* and 14,653 *S*-wave arrival times.

To complete this catalog, we trained a neural network algorithm with the manual catalog to detect and pick arrival times. This algorithm was able to detect and pick accurately well identified events. To filter outliers, very small and quarry blasts events, we selected only events detected by at least 5 stations, with at least 7 arrival-times of which at least 1 corresponded to a *P*-wave and 1 to an *S*-wave. We located the resulting catalog to geographically select local events and uncover large arrival-time residuals potentially corresponding to misidentified data. We use this method for 35 days between September-October of the first phase and 45 days between November-December of the second phase, completing the rest of the registration that could not be done manually. This automatic approach identified 2,483 events with 18,914 *P* and 18,308 *S*-wave arrival-times. Therefore, our final catalog consists of 3,960 events between August 2019 and January 2020, with 35,659 *P*- and 32,961 *S*-wave arrival-times, with local magnitudes between 0.3 and 4.6, and the completeness magnitude of 1.45 (See catalogs in supplementary material).

In Figure 2b, we represent a projection of the seismicity on the profile A-A' identified on Figure 2a. The seismicity corresponds to all events between the two dashed black lines of Figure 2a. Three seismicity planes or double seismic zone can be recognized. This pattern has been observed in other regions along the Chilean margin (Bloch et al., 2014; Comte et al., 1999; Marot et al., 2013). The upper plane correspond to interplate seismicity and is bounded between 20 and 32 km depth. The intermediate plane, between 32 and 80 km depth, is apparently located in the oceanic crust (blue segmented line in Figure 2b). The lower plane (red segmented line in Figure 2b) is located in the upper oceanic mantle and presents most of the seismicity between 45 and 60 km depth, decaying toward 60 and 80 km depth, and increasing again between 80 and 110 km depth. The two deepest planes tend to merge between 100 and 120 km depth. The seismicity in the upper plate is scarce, with a marked eastward seismicity limit at 69.5°S. The clusters observed between 0 and 5 km depth correspond to mining activity (Figure 2b).

2.2. Clusters of Similar Events

We investigated the possible presence of repeating earthquakes or similar events which could indicate if aseismic slip takes place, especially on the interface and near the region of the recurrent deep slow-slip observed by Klein, Duputel, et al. (2018). From the manually picked catalog we selected the events located at a depth of 60 km or above for a matched-filter search (Gibbons & Ringdal, 2006). This selection resulted in 908 templates with S-P times ranging from 6 to 25 s. By doing so the *P*- and *S*-waves won't be contained in the same window (e.g., Igarashi, 2020) however the moveouts, the different arrival times with respect to the first arrival across the network,

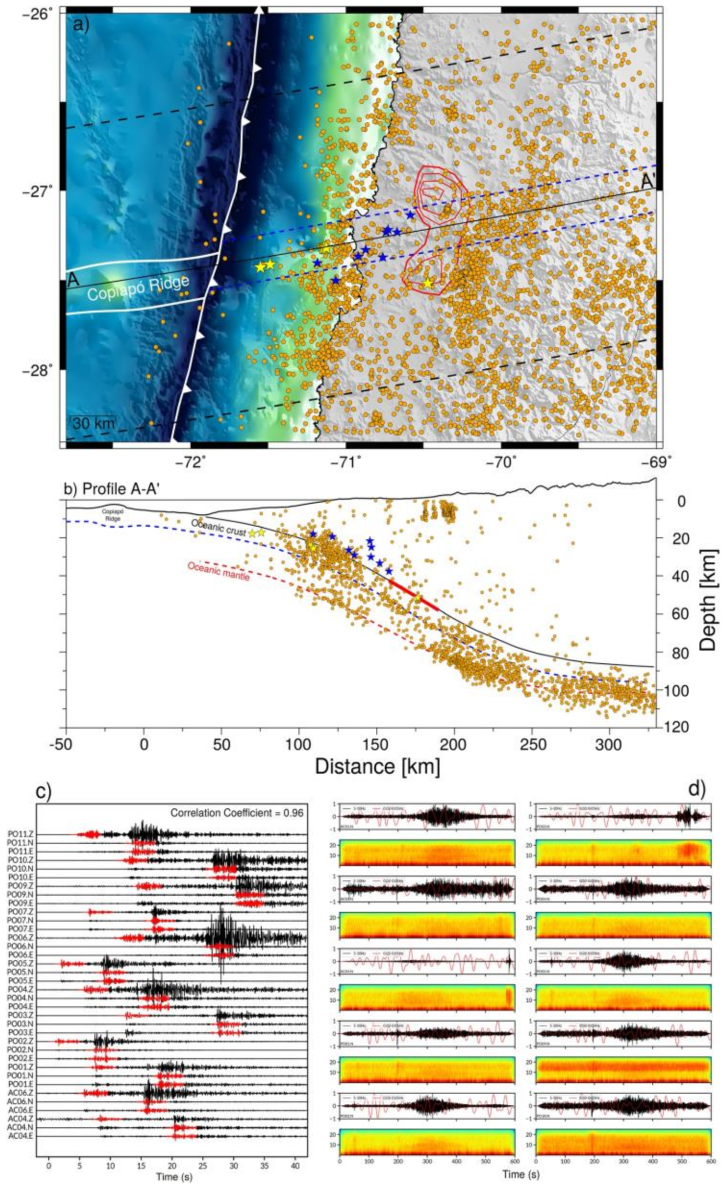

Figure 2. (a) Orange dots correspond to our seismicity catalog, yellow stars to clusters of similar events, and blue stars to NVTs activity. The red lines indicate the 2014 SSE (Klein, Duputel, et al., 2018). The segmented black lines indicate the seismicity zone in profile A-A'. Segmented blue lines indicate the zone covered by our tomographic profile in Figure 3. (b) Seismicity profile between the black segmented lines indicated in (a). Clusters of similar events, NVTs and SSE are indicated with the same colors as in (a). The black line indicates bathymetry and Slab2.0 (Hayes et al., 2018) with interplate seismicity. The blue segmented line indicates the intermediate plane of intraslab seismicity in the oceanic crust and the red segmented line indicating the lower plane of intraslab seismicity in the upper oceanic mantle. (c) Example of similar event detections (in black) and the corresponding templates (in red) and (d) Example of NVT obtained with the envelope method.

will be constant in the matched-filter search. This allow us limit the decrease of similarity by using to large template waveforms while keeping the information of the S-P times intact.

To build the templates, we cut the waveform 1 s before the *P*-wave arrival on the vertical components and 4 s after the *S*-wave arrival on the two horizontal components to limit the overlap of the different seismic arrivals. Due to the magnitudes in our catalog, we conducted the scan using three components at each station, on data filtered between 2 and 8 Hz (Uchida & Matsuzawa, 2013) and 1–15 Hz (Uchida, 2019). *P*- and *S*-waves correlations were performed on the vertical and horizontal components respectively. We found repeating events with a frequency bands between 2 and 8 Hz, in more than three stations with a correlation coefficient greater than or equal to 0.95 (Figure 2c), however we did not find any in frequency bands between 1 and 15 Hz. Due to the difference in these results, we decided to define these events as clusters of similar events. We obtained a total of 27 similar events (Table S1) for the period 24 June 2019, to 17 January 2020. Twelve of these detections seem to be related to mining activity, with local magnitudes < 1.0 and located outside our study area. The 15 remaining events represent 7 clusters of 2–3 events and are located around 27.5°S of latitude, at a depth of 18 and 29 km along the interface with one pair at a depth of 51 km, with a local magnitudes between 1.3 and 2.5 (Figure 2b). These similar events seem to be aligned with the CoR, potentially co-located with the deep SSE (Figures 1 and 2a) and in less coupled zones (Figure S1 in Supporting Information S1).

2.3. Non-Volcanic Tremor Search

To detect non-volcanic tremors (NVTs) activity, we use the envelope correlation method (Ide, 2010, 2012). Hypocenters of tremors are determined as follow: velocity data are band-pass filtered between 1 and 10 Hz. Filtered traces are squared, low-pass filtered at 0.1 Hz and resampled at 1 Hz. The distinct trace obtained is called the envelope data (Figure S2 in Supporting Information S1). For all stations separated by less than 100 km, the envelopes of horizontal components are cross-correlated using a 5-min time window with a 150 s overlap. Following Sáez et al. (2019), a tremor is identified if the cross-correlation coefficient is greater than 0.6 for more than five pairs of stations.

Because of the elevated seismicity rate in the area, many local distant earthquakes were detected. We carried out a visual inspection to eliminate false detections. Figure 2a shows the spatial distribution of NVTs activity after visual inspection (Figures S3 to S8). This NVTs activity was identified uniquely on 20 September 2019 (Table S2), with a clear lack of *P*- and *S*-wave arrivals (Figure 2d). The NVTs activity is located between 27°S and 27.5°S and 70.5°W-71°W, with dispersion in depth (Figures S9 to S20), however, most of them are concentrated toward the downdip or transition zone (Figures 2a and 2b), which exhibits low coupling values (Figure S1 in Supporting Information S1). The NVTs activity is updip of the SSE slip and, as the clusters of similar events, present a spatial correlation with the CoR subduction (Figure 2a).

2.4. 3-D Tomography Model

To build a 3-D tomographic model we use the INSIGHT code (Potin, 2016). The model consists of a set of Vp, Vs and Vp/Vs values at each node of a regularly spaced three-dimensional grid constituting the inversion grid. The inversion was carried out using a nonlinear minimization approach based on a stochastic description of the data and the model (see Text 1 in Supporting Information S1 for more details).

Using the arrival times from our catalog, we build local Vp and Vs velocity models and Vp/Vs ratio of the region from 26.5°S to 28°S and from 69°W to 72°W. These models were derived from the arrival times of 35,659 *P*-waves and 32,961 *S*-waves corresponding to 3,960 events on an inversion grid consisting of 1,175,878 cells with a longitudinal, latitudinal, and vertical resolution size of 3 km, 3 and 1.5 km, respectively (See Figure S21 and S22 for initial model used to make the Vp and Vs models and S23 to travel-time residues in the inversion in Supporting Information S1).

To visualize the velocity variations along-dip, we extracted a cross-section along profile A-A' (blue segmented lines in Figure 2a). Figure 3 shows the results of relative Vp and Vs velocities and Vp/Vs ratio. The upper plate shows higher Vp and Vs values toward shallow depths (0–20 km) and intermediate values for deeper zones (20–35 km), while the Vp/Vs ratio vary between 1.68 and 1.76. In the oceanic crust, at depths between 20 and 40 km depths, Vp and Vs values are moderate to low, with Vp/Vs ratio between 1.78 and 1.82. Between 40 and

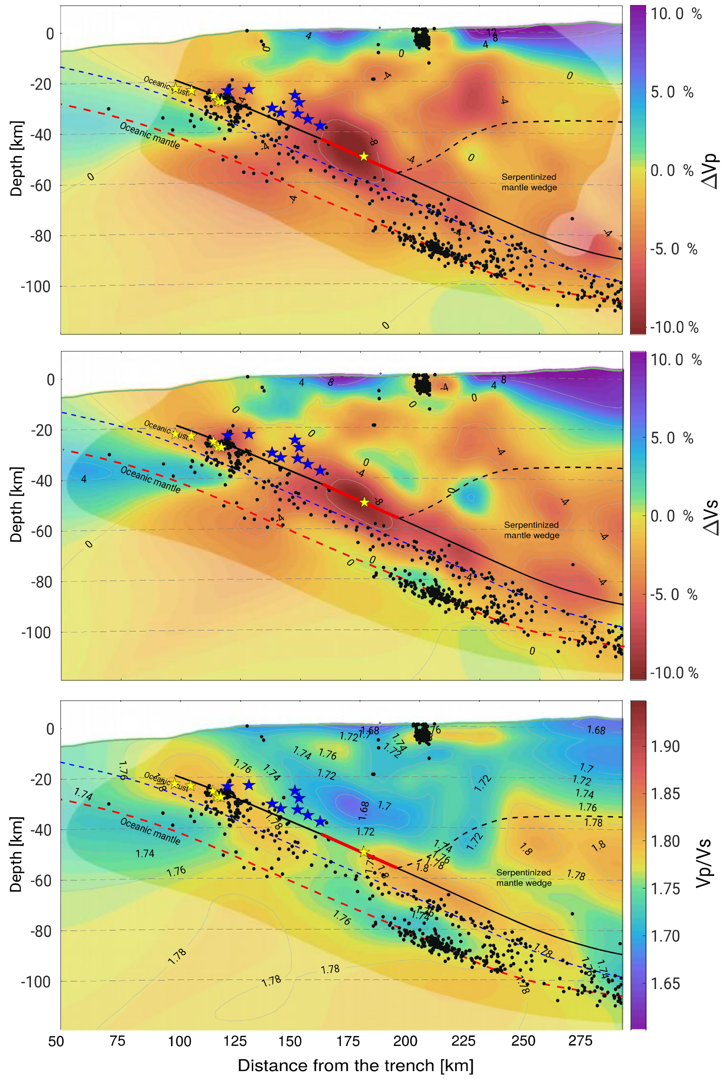

Figure 3. Cross-section of the 3-D relative tomographic velocity models. (a) Vp model, (b) Vs model and (c) Vp/Vs ratio model. Yellow and blue stars indicate clusters of similar events and NVTs activity respectively. The solid black line indicates Slab2.0 (Hayes et al., 2018), and the solid red line to SSE (Klein, Duputel, et al., 2018). The blue and red segmented lines indicate seismicity planes (black dots) in the oceanic crust and upper oceanic mantle. The less illuminated areas represent areas with lower resolution.

60 km depths, a marked anomaly is observed with remarkably low Vp and Vs values and Vp/Vs ratio between 1.74 and 1.76. Between 60 and 110 km depth, Vp and Vs values return to intermediate ranges and the Vp/Vs ratio increases from 1.78 to 1.83. Finally, in the upper oceanic mantle, Vp and Vs values are moderate and Vp/Vs ratio range from 1.76 to 1.80 (See Figures S24 to S32 for checkerboards, ray coverage resolution and restitution index tests respectively).

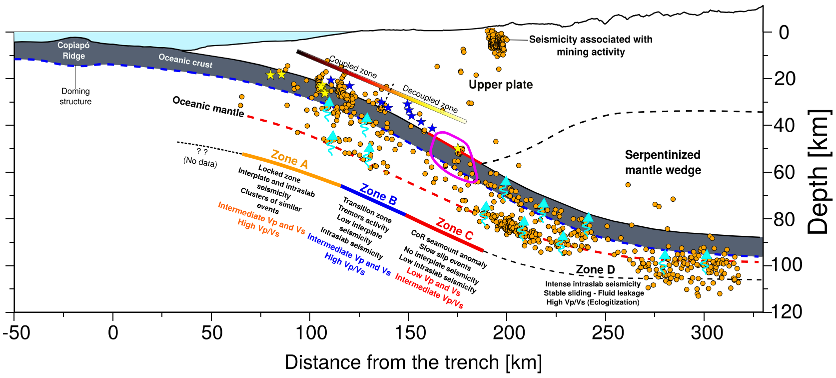

Figure 4. Representation of seismic and aseismic slip zones along-dip in t he CoR subduction zone. Inter plate and intraslab seismicity (or ange dots), clusters of similar events (yellow stars), NVTs (blue stars) and SSE (solid red line). The pink line indicates the potential seamount doming anomal y which coincides with the SSE and without seismicity. The lightblue arrows indicate the presence and leakage of fluids. More intense seismicity between 60 and 110 km depth indicating possible eclogitization metamorphic reactions.

3. Discussion

Based on the seismicity distribution, clusters of similar events, NVTs activity and the velocity anomalies obtained from our Vp and Vs models, and Vp/Vs ratio (Figures 2b and 3) we inferred a clear and marked picture along-dip heterogeneity of the plate interface. From 20 to 35 km depths (zone A in Figure 4), interplate seismicity is concentrated in clusters up to a depth of approximately 32 km, coinciding precisely with high coupling values reported by geodetic studies (coupling >0.7, Figure S1 in Supporting Information S1). Intraslab seismicity presents some clusters potentially related to the re-activation of faults in the oceanic crust and also tends to form a seismicity plane toward the bottom of the oceanic crust. Clusters of similar events were identified in this zone at depths from 18 to 29 km (Figure 2b), close to the seismic swarms (Figures 1 and 2a) and in a zone with low coupling values (Figure S1 in Supporting Information S1).

Similar and repeating events inside seismic swarms have been observed in the past (Pastén-Araya et al., 2018; Poli et al., 2017; Tréhu et al., 2015; Valenzuela-Malebrán et al., 2021). Several studies have proposed that these events might be caused by heterogeneities in the subduction zone due to the subduction of bathymetric features such as: (a) seamounts associated with oceanic ridges (Bilek & Lay, 2018; Valenzuela-Malebrán et al., 2021) and (b) more local structures like fractured zones, which are capable of transporting a greater quantity of fluids to the interface (Moreno et al., 2014; Poli et al., 2017). In this zone A, the Vp and Vs values are moderate and the Vp/Vs ratio is high, with values between 1.78 and 1.82 (Figure 3) suggesting the presence of fluids. According to Nishikawa and Ide (2018), fluid-rich zones are prone to exhibit aseismic slip and host seismic swarms with clusters of similar and repeating events. Therefore, our observations suggest that in zone A there are zones with different seismic behavior: zones with seismic slip characterized by elevated rates of ordinary seismicity with high coupling values (coupling >0.6; Figure S1 in Supporting Information S1) and zones with aseismic slip, characterized by low coupling (coupling <0.5; Figure S1 in Supporting Information S1), low seismicity rate, clusters of similar events, greater presence of fluids and regular seismic swarms (Figure 4). Subduction of seamounts or oceanic ridges can produce fracturing in the oceanic and upper crust and changes in frictional sliding or ductile deformation at the interface (Wang & Bilek, 2014). Between 20 and 35 km depths, clusters of similar events and swarms are spatially correlated with the subduction path of the CoR (Figures 1 and 2a). In addition, these similar events are located in less coupled zones (Figure S1 in Supporting Information S1). Mochizuki et al. (2008) and recently Chesley et al. (2021) established the subduction of seamounts, with their different geometries, widths and altitudes can influence that the distribution of seismicity, produce low coupling above these structures and can trigger clustered repeating earthquakes and similar events. Plata-Martinez et al. (2021) related the distribution of slow earthquakes in the Mexico subduction zone to the difference in relief produced by the subduction of seamounts. Therefore, we propose that the geometric heterogeneities of the seamounts of CoR could influence the diverse seismic behaviors observed in this zone.

In zone B or transition zone (Figure 4), ordinary interplate seismicity is scarce, and NVTs activity is detected (Figures 2a and 2b). This boundary between interplate seismicity and the zone where the NVTs occurs is characterized as a transition between a zone of high coupling, unstable and rate-weakening friction and a zone of low coupling, stable and rate-strengthening friction (Figure S1 in Supporting Information S1; Im et al., 2020). Under the assumption that zones hosting slow slip phenomena such as NVTs and SSEs may impede the propagation of seismic ruptures (Nishikawa et al., 2019; Rolandone et al., 2018), this boundary permits a rough estimation of the along-dip extent of potential future subduction earthquake ruptures that can be nucleated in the locked seismogenic zone. The low values of Vp and Vs and values of Vp/Vs ratio between 1.78 and 1.80 (Figure 3) indicate the presence of fluids in this zone and low normal stress, both factors favor the presence of NVTs (Shelly et al., 2006). Nishikawa et al. (2019) recognized NVTs activity in the southern segment of the Japan subduction zone associated to the subduction of seamounts. NVTs activity is mainly located updip of SSE and a little in zone A, similar to what has been observed recently in the Mexico subduction zone (Plata-Martinez et al., 2021). Moreover, NVTs activity is spatially correlated with CoR subduction (Figure 2a). Therefore we do not discard that the subduction of the CoR seamounts could affect the frictional properties in the zone hosting the NVTs activity.

Between 42 and 60 km depth (zone C in Figure 4), both Vp and Vs models potentially represent a large doming structure anomaly in the plate interface and in the oceanic crust (Figure 3). This anomaly presents low Vp and Vs velocities and a Vp/Vs ratio between 1.76 and 1.78. Kato et al. (2010) recognized an anomaly with similar characteristics with low velocities in the Japan subduction zone, which they attributed to the subduction of an oceanic ridge. Therefore, we tentatively attribute this anomaly to the subduction of a large seamount associated with the CoR. This anomaly coincides precisely, along-strike and down-dip, with the slip of the SSE (Figures S33a-S33b in Supporting Information S1) and a notable lack of interplate seismicity (Figures 3 and 4). The low Vp and Vs velocities and Vp/Vs ratio suggest the presence of fluids, which could be brought through the ridge and released at these depths (Chesley et al., 2021). This idea is consistent with our observations, as fluid abundance is one of the possible causes of aseismic slip (Bürgmann, 2018; Nishikawa & Ide, 2018). These observations propose a change in the rheology of this zone, promoting an aseismic slip behavior at the interface without seismicity. Temperature variation could be another factor in the lack of interplate seismicity. Some studies suggest an increase in temperature due to crustal thickening caused by subduction of ocean ridges (Kato et al., 2010; Tsuru et al., 2002; Wang & Bilek, 2014). This increase in temperature would produce ductile deformation, which could also explain the lack of interplate seismicity.

Finally, the zone between 60 and 110 km depth (zone D in Figure 4) corresponds to the zone below the mantle wedge with stable sliding. There is an increase of the Vp and Vs velocities and the Vp/Vs ratio and a drastic increase of intraslab seismicity. We interpret this increase in seismicity as the onset of the eclogitization metamorphic reaction, due to the dehydration of hydrated minerals in the basaltic oceanic crust and serpentinized upper oceanic mantle (Behr & Bürgmann, 2021; Calvert et al., 2020; Ferrand et al., 2017). The fluids released by the eclogitization could migrate into the mantle wedge enhancing serpentinization in that zone (Hyndman & Peacock, 2003). Our Vp/Vs ratio values ∼1.80 (Figure 3) and absolute velocity values of Vp ∼ 7.2 km/s and Vs ∼ 4.0 km/s (Figure S34 in Supporting Information S1) support this interpretation.

4. Conclusion

Through seismicity analysis and a 3-D tomography model, we studied the along-dip influence of the CoR subduction in the Atacama region, North-Central Chile. The observed distribution of seismicity, the occurrence of clusters of similar events, NVTs and the Vp, Vs and Vp/Vs ratio anomalies allowed us to identify diverse behaviors with different zones along-dip hosting seismic and aseismic slip (Figure 4). These observations are spatially related with the subduction of the Copiapó ridge, a process that could promote along-strike and along-dip changes and favor different slip behavior. Our results present novel observations shedding light on how subduction of large bathymetric features can influence the distribution of seismicity, aseismic slip and the likely extent of along-dip megathrust seismic ruptures in the North-Central Chilean subduction zone.

Data Availability Statement

The seismological catalog, station information, travel time data used to make the tomography model and information for searching and locating the NVTs can be obtained from the following repository: https://doi.org/10.34691/FK2/91GHJE ("Copiapó_ Experiment_Data"). Data obtained from Centro Sismológico Nacional (CSN) are directly available at http://www.sismologia.cl. Data from the Strasbourg University stations (Zigone et al., 2019) can be downloaded from the RESIF data portal (https://seismology.resif.fr). Figures were made using Generic Mapping Tool (GMT) and other open access software.

Acknowledgments
This work is funded by the Fondecyt project N°1200779 and by the Programa de Riesgo Sísmico (PRS), Universidad de Chile. This work has also received funding from the Agence Nationale de la Recherche (projects ANR-19-CE31-0003) and the European Research Council (ERC, under the European Union's Horizon 2020 research and innovation programme under grant agreement No. 805256). F. Pastén-Araya grateful to Marcos Aros and Daniela Calle-Gardella for their help in the field work and to Emilie Klein, Javier Ojeda and Nicole Krumm for their help during the preparation of this manuscript. L. Cabrera was supported by the European Union Horizon 2020 Research and Innovation Programme (grant agreement, 802777-MONIFAULTS). F. Aden-Antoniów acknowledges support from the United States Geological Survey under Grant No. G21AP10035. Most of the computations presented in this paper was performed using the GRICAD infrastructure (https://gricad.univ-grenoble-alpes.fr), which is supported by Grenoble research communities. Finally, we thank the editor Dr German Prieto and the reviewers A. M. Tréhu and anonymous for their constructive comments to improve the manuscript.

References

Baba, S., Takemura, S., Obara, K., & Noda, A. (2020). Slow earthquakes illuminating interplate coupling heterogeneities in subduction zones. *Geophysical Research Letters*, *47*(14), e2020GL088089. https://doi.org/10.1029/2020gl088089

Bassett, D., Sandwell, D. T., Fialko, Y., & Watts, A. B. (2016). Upper-plate controls on co-seismic slip in the 2011 magnitude 9.0 Tohoku-oki earthquake. *Nature*, *531*(7592), 92–96. https://doi.org/10.1038/nature16945

Bassett, D., & Watts, A. B. (2015a). Gravity anomalies, crustal structure, and seismicity at subduction zones: 1. Seafloor roughness and subducting relief. *Geochemistry, Geophysics, Geosystems*, *16*(5), 1508–1540. https://doi.org/10.1002/2014gc005684

Bassett, D., & Watts, A. B. (2015b). Gravity anomalies, crustal structure, and seismicity at subduction zones: 2. Interrelationships between forearc structure and seismogenic behavior. *Geochemistry, Geophysics, Geosystems*, *16*(5), 1541–1576. https://doi.org/10.1002/2014gc005685

Beck, S., Barrientos, S., Kausel, E., & Reyes, M. (1998). Source characteristics of historic earthquakes along the central Chile subduction Askew et Alzone. *Journal of South American Earth Sciences*, *11*(2), 115–129. https://doi.org/10.1016/s0895-9811(98)00005-4

Behr, W. M., & Bürgmann, R. (2021). What's down there? The structures, materials and environment of deep-seated slow slip and tremor. *Philosophical Transactions of the Royal Society A*, *379*, 20200218. https://doi.org/10.1098/rsta.2020.0218

Bilek, S. L., & Lay, T. (2018). Subduction zone megathrust earthquakes. *Geosphere*, *14*(4), 1468–1500. https://doi.org/10.1130/ges01608.1

Bloch, W., Kummerow, J., Salazar, P., Wigger, P., & Shapiro, S. A. (2014). High-resolution image of the north Chilean subduction zone: Seismicity, reflectivity and fluids. *Geophysical Journal International*, *197*(3), 1744–1749. https://doi.org/10.1093/gji/ggu084

Bürgmann, R. (2018). The geophysics, geology and mechanics of slow fault slip. *Earth and Planetary Science Letters*, *495*, 112–134. https://doi.org/10.1016/j.epsl.2018.04.062

Calvert, A. J., Bostock, M. G., Savard, G., & Unsworth, M. J. (2020). Cascadia low frequency earthquakes at the base of an overpressured subduction shear zone. *Nature Communications*, *11*(1), 1–10. https://doi.org/10.1038/s41467-020-17609-3

Chesley, C., Naif, S., Key, K., & Bassett, D. (2021). Fluid-rich subducting topography generates anomalous forearc porosity. *Nature*, *595*(7866), 255–260. https://doi.org/10.1038/s41586-021-03619-8

Comte, D., Dorbath, L., Pardo, M., Monfret, T., Haessler, H., Rivera, L., et al. (1999). A double-layered seismic zone in Artica, northern Chile. *Geophysical Research Letters*, *26*(13), 1965–1968. https://doi.org/10.1029/1999gl900447

Comte, D., Haessler, H., Dorbath, L., Pardo, M., Monfret, T., Lavenu, A., & Hello, Y. (2002). Seismicity and stress distribution in the Copiapo, northern Chile subduction zone using combined on-and off-shore seismic observations. *Physics of the Earth and Planetary Interiors*, *132*(1–3), 197–217. https://doi.org/10.1016/s0031-9201(02)00052-3

Comte, D., Tassara, A., Farias, M., & Boroschek, R. (2006). *Copiapo Chile seismic swarm analysis: Mapping the interplate contact*. AGU Fall Meeting Abstracts (pp. S53B–1327).

Contreras-Reyes, E., & Carrizo, D. (2011). Control of high oceanic features and subduction channel on earthquake ruptures along the Chile–Peru subduction zone. *Physics of the Earth and Planetary Interiors*, *186*(1–2), 49–58. https://doi.org/10.1016/j.pepi.2011.03.002

Ferrand, T. P., Hilairet, N., Incel, S., Deldicque, D., Labrousse, L., Gasc, J., et al. (2017). Dehydration-driven stress transfer triggers intermediate-depth earthquakes. *Nature Communications*, *8*(1), 1–11. https://doi.org/10.1038/ncomms15247

Gibbons, S. J., & Ringdal, F. (2006). The detection of low magnitude seismic events using array-based waveform correlation. *Geophysical Journal International*, *165*(1), 149–166. https://doi.org/10.1111/j.1365-246x.2006.02865.x

Hansen, P. C. (1992). Numerical tools for analysis and solution of Fredholm integral equations of the first kind. *Inverse Problems*, *8*(6), 849–872. https://doi.org/10.1088/0266-5611/8/6/005

Havskov, J., & Ottemöller, L. (2008). *SEISAN: The earthquake analysis software for windows, solares, linux and macosx*. Institute of Solid Earth Science, University of Bergen. version 8.2. 1.

Hayes, G. P., Moore, G. L., Portner, D. E., Hearne, M., Flamme, H., Furtney, M., & Smoczyk, G. M. (2018). Slab2, a comprehensive subduction zone geometry model. *Science*, *362*(6410), 58–61. https://doi.org/10.1126/science.aat4723

Henstock, T. J., McNeill, L. C., Bull, J. M., Cook, B. J., Gulick, S. P., Austin, J. A., Jr, et al. (2016). Downgoing plate topography stopped rupture in the AD 2005 Sumatra earthquake. *Geology*, *44*(1), 71–74. https://doi.org/10.1130/g37258.1

Holtkamp, S. G., Pritchard, M. E., & Lohman, R. B. (2011). Earthquake swarms in south America. *Geophysical Journal International*, *187*(1), 128–146. https://doi.org/10.1111/j.1365-246x.2011.05137.x

Hyndman, R. D., & Peacock, S. M. (2003). Serpentinization of the forearc mantle. *Earth and Planetary Science Letters*, *212*(3–4), 417–432. https://doi.org/10.1016/s0012-821x(03)00263-2

Ide, S. (2010). Striations, duration, migration and tidal response in deep tremor. *Nature*, *466*(7304), 356–359. https://doi.org/10.1038/nature09251

Ide, S. (2012). Variety and spatial heterogeneity of tectonic tremor worldwide. *Journal of Geophysical Research*, *117*(B3). https://doi.org/10.1029/2011jb008840

Igarashi, T. (2020). Catalog of small repeating earthquakes for the Japanese Islands. *Earth Planets and Space*, *72*, 1–8. https://doi.org/10.1186/s40623-020-01205-2

Im, K., Saffer, D., Marone, C., & Avouac, J. P. (2020). Slip-rate-dependent friction as a universal mechanism for slow slip events. *Nature Geoscience*, *13*(10), 705–710. https://doi.org/10.1038/s41561-020-0627-9

Ji, S., Li, L., Motra, H. B., Wuttke, F., Sun, S., Michibayashi, K., & Salisbury, M. H. (2018). Poisson's ratio and auxetic properties of natural rocks. *Journal of Geophysical Research: Solid Earth*, *123*(2), 1161–1185. https://doi.org/10.1002/2017jb014606

Kanamori, H., Rivera, L., Ye, L., Lay, T., Murotani, S., & Tsumura, K. (2019). New constraints on the 1922 Atacama, Chile, earthquake from historical seismograms. *Geophysical Journal International*, *219*(1), 645–661. https://doi.org/10.1093/gji/ggz302

Kato, A., Iidaka, T., Ikuta, R., Yoshida, Y., Katsumata, K., Iwasaki, T., et al. (2010). Variations of fluid pressure within the subducting oceanic crust and slow earthquakes. *Geophysical Research Letters*, *37*(14). https://doi.org/10.1029/2010gl043723

Kennett, B. L., Engdahl, E. R., & Buland, R. (1995). Constraints on seismic velocities in the Earth from traveltimes. *Geophysical Journal International*, *122*(1), 108–124. https://doi.org/10.1111/j.1365-246x.1995.tb03540.x

Klein, E., Duputel, Z., Zigone, D., Vigny, C., Boy, J. P., Doubre, C., & Meneses, G. (2018). Deep transient slow slip detected by survey GPS in the region of Atacama, Chile. *Geophysical Research Letters*, *45*(22), 12–263. https://doi.org/10.1029/2018gl080613

Klein, E., Metois, M., Meneses, G., Vigny, C., & Delorme, A. (2018). Bridging the gap between north and central Chile: Insight from new GPS data on coupling complexities and the Andean sliver motion. *Geophysical Journal International*, *213*(3), 1924–1933. https://doi.org/10.1093/gji/ggy094

Klein, E., Potin, B., Pasten-Araya, F., Tissandier, R., Azua, K., Duputel, Z., et al. (2021). Interplay of seismic and a-seismic deformation during the 2020 sequence of Atacama, Chile. *Earth and Planetary Science Letters*, *570*, 117081. https://doi.org/10.1016/j.epsl.2021.117081

Kodaira, S., Iidaka, T., Kato, A., Park, J. O., Iwasaki, T., & Kaneda, Y. (2004). High pore fluid pressure may cause silent slip in the Nankai Trough. *Science*, *304*(5675), 1295–1298. https://doi.org/10.1126/science.1096535

Lallemand, S., Peyret, M., van Rijsingen, E., Arcay, D., & Heuret, A. (2018). Roughness characteristics of oceanic seafloor prior to subduction in relation to the seismogenic potential of subduction zones. *Geochemistry, Geophysics, Geosystems*, *19*(7), 2121–2146. https://doi.org/10.1029/2018gc007434

Latorre, D., Virieux, J., Monfret, T., Monteiller, V., Vanorio, T., Got, J. L., & Lyon-Caen, H. (2004). A new seismic tomography of Aigion area (Gulf of Corinth, Greece) from the 1991 data set. *Geophysical Journal International*, *159*(3), 1013–1031. https://doi.org/10.1111/j.1365-246x.2004.02412.x

Liu, X., & Zhao, D. (2018). Upper and lower plate controls on the great 2011 Tohoku-oki earthquake. *Science Advances*, *4*(6), eaat4396. https://doi.org/10.1126/sciadv.aat4396

Maksymowicz, A. (2015). The geometry of the Chilean continental wedge: Tectonic segmentation of subduction processes off Chile. *Tectonophysics*, *659*, 183–196. https://doi.org/10.1016/j.tecto.2015.08.007

Maksymowicz, A., Ruiz, J., Vera, E., Contreras-Reyes, E., Ruiz, S., Arraigada, C., et al. (2018). Heterogeneous structure of the Northern Chile marine forearc and its implications for megathrust earthquakes. *Geophysical Journal International*, *215*(2), 1080–1097. https://doi.org/10.1093/gji/ggy325

Marot, M., Monfret, T., Pardo, M., Ranalli, G., & Nolet, G. (2013). A double seismic zone in the subducting juan fernandez ridge of the Nazca plate (32 S), central Chile. *Journal of Geophysical Research: Solid Earth*, *118*(7), 3462–3475. https://doi.org/10.1002/jgrb.50240

Mochizuki, K., Yamada, T., Shinohara, M., Yamanaka, Y., & Kanazawa, T. (2008). Weak interplate coupling by seamounts and repeating M ~ 7 earthquakes. *Science*, *321*(5893), 1194–1197. https://doi.org/10.1126/science.1160250

Moreno, M., Haberland, C., Oncken, O., Rietbrock, A., Angiboust, S., & Heidbach, O. (2014). Locking of the Chile subduction zone controlled by fluid pressure before the 2010 earthquake. *Nature Geoscience*, *7*(4), 292–296. https://doi.org/10.1038/ngeo2102

Nishikawa, T., & Ide, S. (2018). Recurring slow slip events and earthquake nucleation in the source region of the M 7 Ibaraki-Oki earthquakes revealed by earthquake swarm and foreshock activity. *Journal of Geophysical Research: Solid Earth*, *123*(9), 7950–7968. https://doi.org/10.1029/2018jb015642

Nishikawa, T., Matsuzawa, T., Ohta, K., Uchida, N., Nishimura, T., & Ide, S. (2019). The slow earthquake spectrum in the Japan Trench illuminated by the S-net seafloor observatories. *Science*, *365*(6455), 808–813. https://doi.org/10.1126/science.aax5618

Paige, C. C., & Saunders, M. A. (1982). LSQR: An algorithm for sparse linear equations and sparse least squares. *ACM Transactions on Mathematical Software (TOMS)*, *8*(1), 43–71. https://doi.org/10.1145/355984.355989

Pastén-Araya, F., Salazar, P., Ruiz, S., Rivera, E., Potin, B., Maksymowicz, A., & Shapiro, S. A. (2018). Fluids along the plate interface influencing the frictional regime of the Chilean subduction zone, northern Chile. *Geophysical Research Letters*, *45*(19), 10–378. https://doi.org/10.1029/2018GL079283

Plata-Martínez, R., Ide, S., Shinohara, M., Garcia, E. S., Mizuno, N., Dominguez, L. A., et al. (2021). Shallow slow earthquakes to decipher future catastrophic earthquakes in the Guerrero seismic gap. *Nature Communications*, *12*(1), 1–8. https://doi.org/10.1038/s41467-021-24210-9

Podvin, P., & Lecomte, I. (1991). Finite difference computation of traveltimes in very contrasted velocity models: A massively parallel approach and its associated tools. *Geophysical Journal International*, *105*(1), 271–284. https://doi.org/10.1111/j.1365-246x.1991.tb03461.x

Poli, P., Maksymowicz, A., & Ruiz, S. (2017). The Mw 8.3 Illapel earthquake (Chile): Preseismic and postseismic activity associated with hydrated slab structures. *Geology*, *45*(3), 247–250. https://doi.org/10.1130/g38522.1

Potin, B. (2016). *Les Alpes occidentales: Tomographie, localisation de séismes et topographie du Moho (Doctoral dissertation, université Grenoble Alpes (ComUE))*.

Rolandone, F., Nocquet, J. M., Mothes, P. A., Jarrin, P., Vallée, M., Cubas, N., et al. (2018). Areas prone to slow slip events impede earthquake rupture propagation and promote afterslip. *Science Advances*, *4*(1), eaao6596. https://doi.org/10.1126/sciadv.aao6596

Ruiz, S., & Madariaga, R. (2018). Historical and recent large megathrust earthquakes in Chile. *Tectonophysics*, *733*, 37–56. https://doi.org/10.1016/j.tecto.2018.01.015

Sáez, M., Ruiz, S., Ide, S., & Sugioka, H. (2019). Shallow nonvolcanic tremor activity and potential repeating earthquakes in the Chile triple junction: Seismic evidence of the subduction of the active Nazca–Antarctic spreading center. *Seismological Research Letters*, *90*(5), 1740–1747.

Shelly, D. R., Beroza, G. C., Ide, S., & Nakamula, S. (2006). Low-frequency earthquakes in Shikoku, Japan, and their relationship to episodic tremor and slip. *Nature*, *442*(7099), 188–191. https://doi.org/10.1038/nature04931

Tarantola, A., & Valette, B. (1982). Generalized nonlinear inverse problems solved using the least squares criterion. *Reviews of Geophysics*, *20*(2), 219–232. https://doi.org/10.1029/rg020i002p00219

Thurber, C. H. (1983). Earthquake locations and three-dimensional crustal structure in the Coyote Lake area, central California. *Journal of Geophysical Research*, *88*(B10), 8226–8236. https://doi.org/10.1029/jb088ib10p08226

Tréhu, A. M., Blakely, R. J., & Williams, M. C. (2012). Subducted seamounts and recent earthquakes beneath the central Cascadia forearc. *Geology*, *40*(2), 103–106.

Tréhu, A. M., Braunmiller, J., & Davis, E. (2015). Seismicity of the central Cascadia continental margin near 44.5 N: A decadal view. *Seismological Research Letters*, *86*(3), 819–829.

Tsuru, T., Park, J. O., Miura, S., Kodaira, S., Kido, Y., & Hayashi, T. (2002). Along-arc structural variation of the plate boundary at the Japan Trench margin: Implication of interplate coupling. *Journal of Geophysical Research*, *107*(B12), ESE-11. https://doi.org/10.1029/2001jb001664

Uchida, N. (2019). Detection of repeating earthquakes and their application in characterizing slow fault slip. *Progress in Earth and Planetary Science*, *6*(1), 1–21. https://doi.org/10.1186/s40645-019-0284-z

Uchida, N., & Matsuzawa, T. (2013). Pre-and postseismic slow slip surrounding the 2011 Tohoku-oki earthquake rupture. *Earth and Planetary Science Letters*, *374*, 81–91. https://doi.org/10.1016/j.epsl.2013.05.021

Valenzuela-Malebrán, C., Cesca, S., Ruiz, S., Passarelli, L., Leyton, F., Hainzl, S., et al. (2021). Seismicity clusters in central Chile: Investigating the role of repeating earthquakes and swarms in a subduction region. *Geophysical Journal International*, *224*(3), 2028–2043.

Vergely, J. L., Valette, B., Lallement, R., & Raimond, S. (2010). Spatial distribution of interstellar dust in the sun's vicinity-comparison with neutral sodium-bearing gas. *Astronomy & Astrophysics*, *518*, A31. https://doi.org/10.1051/0004-6361/200913962

Wang, K., & Bilek, S. L. (2011). Do subducting seamounts generate or stop large earthquakes? *Geology*, *39*(9), 819–822. https://doi.org/10.1130/g31856.1

Wang, K., & Bilek, S. L. (2014). Invited review paper: Fault creep caused by subduction of rough seafloor relief. *Tectonophysics*, *610*, 1–24. https://doi.org/10.1016/j.tecto.2013.11.024

Wolfe, C. J. (2002). On the mathematics of using difference operators to relocate earthquakes. *Bulletin of the Seismological Society of America*, *92*(8), 2879–2892. https://doi.org/10.1785/0120010189

Zigone, D., Duputel, Z., Rivera, L., Thore, J. Y., Klein, E., Vigny, C., & Ruiz, S. (2019). *Copiapo temporary deployment*. International Federation of Digital Seismograph Networks. https://doi.org/10.7914/SN/9C_2019

3.4 Señales Ordinarias Asociadas a la Ocurrencia de Terremotos Lentos

3.4.1.1 Manifestaciones sísmicas ordinarias asociadas a deslizamientos lentos en el Sistema de Falla Liquiñe-Ofqui

El objetivo de esta investigación era comprender que tipos de manifestaciones sísmicas es capaz de generar la porción sur del Sistema de Fallas Liquiñe-Ofqui. En particular, se analizó la zona comprendida entre los -44°S y -46°S, la cual ha sido afectada por grandes y destructivos terremotos, como la réplica mayor del terremoto de Valdivia M_w 7.7 ocurrida el 6 de junio del año 1960 (Kanamori & Rivera, 2017) y los terremotos M_w 6.1 y M_w 6.2 ocurridos el año 2007 durante la secuencia sísmica de Aysén (Agurto et al., 2012; Legrand et al., 2011; Mora et al., 2010).

Para el desarrollo de la investigación se utilizaron 17 estaciones banda ancha desplegadas en la zona de estudio por el Centro Sismológico Nacional (CSN) y el Observatorio Volcanológico de los Andes Sur (OVDAS).

En el trabajo se detectó y localizó la sismicidad ordinaria ocurrida entre los años 2018 y 2019. Adicionalmente, se identificó la presencia de manifestaciones ordinarias asociadas a terremotos lentos como son la ocurrencia de terremotos repetitivos y enjambres sísmicos. El trabajo desarrollado concluye que el sistema de fallas Liquiñe-Ofqui presenta diversas ramas sísmicamente activas capaces de generar una variedad de manifestaciones sísmicas, y expone por primera vez la ocurrencia de terremotos repetitivos en la zona.

El trabajo realizado durante la investigación consistió en el desarrollo de la hipótesis de trabajo, procesamiento de datos, análisis de resultados y escritura del artículo. A continuación, se presenta el articulo científico publicado, en el cual, participé como primer autor.

Revealing the seismic behavior of the southern portion of the Liquiñe-Ofqui fault zone

Miguel Sáez, Department of Geophysics, Universidad de Chile, Santiago, Chile, misaez@uchile.cl

Sergio Ruiz, Department of Geophysics, Universidad de Chile, Santiago, Chile, sruiz@uchile.cl

Francisco Pastén-Araya, Department of Civil Engineering, Universidad Católica del Maule, Talca, Chile, fpa007@ucn.cl

Sebastian Carrasco, Bensberg Observatory, University of Cologne, Bergisch Gladbach, Germany, acarrasc@uni-koeln.de

Rogelio Torres, Department of Geophysics, Universidad de Chile, Chile, rogelio.torres@ug.uchile.cl

Corresponding author: Miguel Sáez Arias

Abstract

The Liquiñe-Ofqui Fault Zone (LOFZ) is a complex dextral strike-slip fault system that extend for more than 1,200 km in southern Chile. Historically, the LOFZ has generated large and destructive earthquakes that have caused the death of people and significant economic and social damage. These destructive earthquakes have been generated mainly in the southern portion of the LOFZ where 5 earthquakes with M_s greater than 6.0 have occurred since 1927, including the largest aftershocks (M_w 7.7) of the giant Valdivia 1960 earthquake. Despite its seismogenic potential, seismicity along this portion of the LOFZ has been poorly characterized mainly due to adverse weather conditions and the lack of permanent seismological networks in the area. In this study, we used the data recorded between 2018 and 2019 by a permanent seismic network deployed in the southern area of the LOFZ. Using the LTA/STA algorithm and template matching, we detected more than 7.200 earthquakes with M_l ranging from -3.0 to 3.6 that occur at depths generally less than 25 km. The spatial distribution and focal mechanism of the detected earthquakes are compatible with slip of different faults belonging to the LOFZ. In particular, the occurrence of ordinary earthquakes, repeating earthquakes, volcano activity and swarm-type activity in different zones of the LOFZ were detected. From our analyses, we conclude that the LOFZ has several seismically active faults capable of generating a variety of seismic signatures ranging from ordinary earthquakes to slow earthquakes.

Keywords

Liquiñe-Ofqui system zone, strike-slip fault, ordinary earthquakes, repeating earthquakes,

1. Introduction

The Liquiñe-Ofqui Fault Zone (LOFZ) is a complex dextral strike-slip fault system produced by the oblique subduction of the Nazca plate (N77°E) beneath the South America plate at 6.6 cm/year (Angermann et al., 1999; Cembrano et al., 1996a; Easton et al., 2013). LOFZ extend for more than 1,200 km (38°S-48°S), starting in the vicinity of the Copahue Volcano and ending in the Golfo de Penas (Figure 1). The fault system is composed of two NNE trending parallel lineaments with dextral and dextral-reverse kinematics, connected by at least four NE trending en échelon lineaments that define a strike-slip duplex (Cembrano et al., 1996b, 1996a; Pérez-Estay et al., 2020; Villalobos et al., 2020).

Historically, the LOFZ has been involved is some large earthquakes which have caused significant human and financial losses. From 1927 to date, five earthquakes with magnitudes greater than Ms 6.0 have been associated with the seismic and volcanic activity of the LOFZ (Figure 1a), including the largest aftershocks (Mw 7.7) of the giant Mw 9.5 Valdivia 1960 earthquake (Kanamori & Rivera, 2017).

The first documented event occurred in 1927. Only the magnitude (MGR 7.1) and location (-44.5° and -73°) of this event are known (Gutenberg & Richter, 1954). On November 28, 1965, a shallow earthquake Ms 6.1 occurred at -45.77° and –72.90°. The event was attributed to an eruption of the Hudson volcano (Lange et al., 2008; Rosenau et al., 2006) and had a strike-slip mechanism compatible with a slip on the LOFZ (S. E. Barrientos & Acevedo-Aránguiz, 1992; Chinn & Isacks, 1983). Subsequently, on June 6, 1960, the largest aftershock of the giant megathrust Valdivia earthquake occurred (Cifuentes, 1989). Initially, the surface wave magnitude of this event was estimated at MS 6.9 (Rothé, 1969). According to (Kanamori & Stewart, 1979), this event generated surface waves with an amplitude larger than expected for an event of its magnitude. Recently, using strain seismogram recorded at Isabella, California, (Kanamori & Rivera, 2017) re-examined the source characteristics of the June 6 earthquake and confirm that the event was a slow earthquake, with a magnitude of Mw 7.7 and right-lateral strike-slip mechanism compatible with a slip on the Liquiñe-Ofqui Fault Zone.

The last two important earthquakes associated to the LOFZ occurred in 2007, during the Aysén Fjord seismic sequence (Figure 1b). The sequence took place in the central portion of the LOFZ and was characterized by swarm-like activity with more than 7200 earthquakes recorded between January and June 2007 (Legrand et al., 2011). The peak of this seismic sequence occurred in April with the earthquakes of 2 April (Mw 6.1) and 21 April (Mw 6.2) (Agurto et al., 2012). The latter events generated series of landslides, local tsunamis, damage to the salmon industry and the death of 10 people (Naranjo et al., 2009; Sepúlveda et al., 2010, 2022; Sepúlveda & Serey, 2009).

The occurrence of these destructive earthquakes has been concentrated in the southern portion of the LOFZ, between ~-45°S and ~-46°S. This zone is immersed in a complex tectonic-seismic environment due to the oblique subduction of the Nazca plate and its proximity to the Chile Triple Junction (CTJ), location where the spreading center between the Antarctic and Nazca plates (Chile Rise) is currently subducting under the South American plate (Maksymowicz et al., 2012). The combined effect of the oblique subduction and the collision of the ridge with South America would explain the presence of a slab window, distribution of volcanoes in the Southern Volcanic Zone (SVZ) and the location of the main LOFZ trace (master fault) (Breitsprecher & Thorkelson, 2009; Cembrano et al., 1996a; Cembrano & Herve, 1993; De Pascale et al., 2021). Recently, slip rates of 11.6-24.6 mm/year have been measured by mapping paleo-surface ruptures, offsets, and lithological separation along the master faults (De Pascale et al., 2021). These high slip rates would be sufficient to explain the occurrence of destructive earthquakes such as the 2007 Mw 6.2 Aysén earthquake and the 1960 Mw 7.7 Valdivia aftershock. But is it only through large earthquakes that seismic energy is released in the LOFZ? Are there other seismic manifestations?

Despite the historical background, the seismic-volcanic hazard, and the proximity to populated cities, seismicity along the southern portion of the LOFZ (-43.75°S to -46.25°S and -74° to -72°) had been scarcely studied. From 2012 to 2017, the National Seismological Center (CSN) reported the occurrence of only 28 earthquakes for this zone (Figure 2a and Figure 2b).

In this work, we analyzed the seismic activity generated in the southern portion of the LOFZ, where the largest and most destructive earthquakes have occurred. We analyzed the data collected by a permanent seismic network composed of 17 broadband stations, which were continuously recording during 2018 and 2019 (see Figure 1). We focused on identifying the branches of the LOFZ that present seismic activity as well as understanding what type of seismic manifestations are generated in the study area.

2. Previous Seismic Studies

Most of the research carried out along the LOFZ has focused on its north-central portion (-36°S to -43°S). The interest in this area is mainly due to the presence of many volcanoes and geothermal sources that are of interest for the sustainable energy development of Chile. Work in this area has focused mainly on understanding the relationship between crustal faults, seismicity, and volcanic activity (Sielfeld et al., 2019 and reference therein). On the other hand, the seismic activity of the southern portion of the LOFZ has been scarcely studied, mainly due to the complex climatic-access conditions in the Aysén fjords, the lack of dense and permanent seismological networks and the absence of large earthquakes. From 1990 to 2012, only temporary seismic arrays have been deployed in this portion of the LOFZ.

(Murdie et al., 1993) installed a network of nine sensors around the CTJ to study the seismic signals generated by the Chilean ridge before and after its subduction. They located 50 events with magnitude between 0 and 4 occurring in the vicinity CTJ. (Miller et al., 2005) installed 60 broadband seismometers east of the CTJ from ~44.6°S to ~48.3°S to study the seismicity, plate geometry, velocity and attenuation structure of this region. They detected seismicity associated with the LOFZ, the Chile Ridge and the Hudson volcano.

(Comte et al., 2007) deployed a dense seismic array which allowed recording the initial phase of the Aysén 2007 seismic sequence. These data were additionally used by (Gallego et al., 2013) and (Ide, 2012) to study the occurrence of non-volcanic tremor north of the CTJ. After the Aysén 2007 sequence, the interest in monitoring and understanding the seismic behavior of the LOFZ increased. Between 2007 and 2012, some temporal networks were deployed around the Aysén 2007 area, to study its tectonic origin as well as to infer a 1D velocity model for the zone (Agurto et al., 2012; Legrand et al., 2011; Mora et al., 2010; Russo et al., 2011).

Since 2012, the National Seismological Center (CSN) and the Southern Andes Volcanological Observatory (OVDAS) deployed a permanent seismic network along the LOFZ. From 2012 to 2017, the CSN reported a total of 28 earthquakes with magnitudes between Mw 1.8 and 4.9 and depths varying between 3.0-34 km (see Figure 1c).

(Agurto-Detzel et al., 2014) reanalyzes the data collected by (Miller et al., 2005) between 2004 and 2005 to study the local seismicity generated in the vicinity of the CTJ. They located 276 events with magnitudes between 0.5 and 3.4 occurring at shallow depths and do not detect events in the area where the 2007 Aysén sequence occurs.

Combining tectonic observations with local seismicity data, (Villalobos et al., 2020) studied the temporal and spatial evolution of the Aysén 2007 seismic sequence. They concluded that three faults were progressively activated during the seismic sequence, one of them reached surface rupture while the other two reached partial rupture.

Finally, (Pérez-Estay et al., 2020) installed a temporal seismic network for ten months, to study the seismicity around the Puyuhuapi volcano area, located at ~-44°S in the SVZ. Authors located 81 events with magnitudes between Mw 2.1 and 4.1 and depths between 0.7 and 12.5 km.

To date, the different works that have been carried out in the southern portion of the LOFZ, have reported scarce seismic activity, mainly associated with volcanic activity and manifestations of tectonic origin by the LOFZ. With the exception of the Aysén 2007 swarm, seismic activity in the southern portion of the LOFZ is characterized by magnitudes less than Mw 5.0 and depths less than 35 km.

3. The 2007 Aysén Seismic Sequence

The 2007 Aysén seismic sequence took place in the Aysén fjords and was composed of more than 7200 events that developed in an area of approximately 50x25 km2 (Legrand et al., 2011; Villalobos et al., 2020) (Figure 2c). The sequence begins on January 10, 2007 with a Ml 3.9 earthquake occurring at a depth of ~10 km. Scarce seismicity of small magnitude developed until January 23, when an earthquake of magnitude Mw 5.2 struck the Aysén fjords, triggering a series of events whose magnitudes increased from Mw 5.1 to 6.2. The sequence had two main events, the first of magnitude Mw 6.1 occurred on April 2nd while the second of magnitude Mw 6.2 occurred on April 21st. In general, the focal mechanisms of the larger events, including the main Mw 6.2 event, were strike-slip, which are compatible with the local and regional kinematics of the LOFZ (Legrand et al., 2011; Russo et al., 2011), supporting the idea that faults belonging to the LOFZ were responsible for the seismic sequence (Easton et al., 2013). The only exception is the normal-type focal mechanism of event Mw 6.1, however, this mechanism is compatible with the presence of normal faults in the area (Villalobos et al., 2020). According to (Agurto et al., 2012), the critical phase of the sequence culminated with the Mw 6.2 earthquake. This shallow earthquake (depth 8.0) triggered hundreds of landslides around the epicentral zone generating multiple rockslides, rock falls and rock avalanches (Sepúlveda & Serey, 2009). These landslides generated local tsunamis, causing damage to the salmon industry, hydroelectric plants and ten fatalities (Naranjo et al., 2009; Sepúlveda et al., 2022).

Initially, the tectonic or volcanic origin of the sequence was debated. By analyzing b-value, time-magnitude distribution, the presence of monogenic volcanic cones and focal mechanisms, (Legrand et al., 2011) proposes that the Aysén 2007 sequence had a tectonic-volcanic origin. On the other hand, (Mora et al., 2010) analyzed the initial phase of the sequence, suggesting from the focal mechanisms a tectonic origin. Subsequently, (Agurto-Detzel et al., 2014) analyzed the aftershocks of the sequence, showing that the seismicity extended for more than 50 km in lineaments that coincide with the trace of the LOFZ, suggesting a tectonic origin.

Through the analysis of high-resolution reflection seismic and bathymetric data, (Villalobos et al., 2020) infers that the temporal and spatial distribution of the 2007 Aysén seismic sequence was controlled by the rupture of three main structures: Quitralco fault (QF), Rio Cuervo fault (RCF) and Punta Cola fault (PC). The authors suggest a tectonic origin for the sequence and propose that the RCF and QF faults represent a major source of seismic hazard since they did not reach a surface rupture during the sequence.

4. Data

In this work we used the data collected by a permanent network deployed by the CSN and OVDAS along the LOFZ. The array consists of seismic stations equipped with a broadband Trillium 120-s period sensor, a Marmot data logger system, and a Quanterra Q330 digitizer. The stations recorded continuously the north-south (NS), the east-west (EW) and the vertical (Z) directions a rate of 100 samples per seconds.

For this work, we used the data recorded by 17 broadband stations located in the south-central portion of the LOFZ (-43.75° to -46.25° and -74° to -72°). Due to environmental conditions and access problems to the sites, station maintenance is complex. Therefore, during the period of operation of the network (from 2012), there are long periods of time where some stations were not operational. For this reason, we decided to analyze the data recorded between 2018 and 2019. This period shows the highest number of stations operating simultaneously. Despite the above, there are several days where the availability of stations is scarce (see Figure 3).

5. Methodology

5.1. Detection and location of ordinary earthquakes

Ordinary earthquakes detection was performed in a multi-stage process using the STA/LTA algorithm (Trnkoczy, 2009). The main goal of the developed methodology is the detection and localization of local seismicity associated with the tectonic and volcanic activity of the LOFZ.

MGDN and CHAC stations were used in this process, since they were the most stable stations during the period analyzed and the ones with the highest number of days recorded (see Figure 3).

In the first stage, the raw data were divided into daily traces, all gaps were filled with white noise, the trend and mean were removed, and the data were filtered between 1 and 20 Hz. This frequency range was used to enhance the seismic signal of small earthquakes (Ml<4) with respect to the anthropogenic noise.

In the second stage, we run the STA/LTA algorithm on the data from MGDN and CHAC stations, using a STA value of 2 seg and LTA value of 60 seg. Windows with an STA/LTA greater than 10(trigger threshold level) were considered as a potential detection.

In the third stage, we used the detection times to generate the horizontal and vertical traces at each available station. The traces were cut 40 s before and after the detection time. Subsequently, the horizontal and vertical traces were correlated between each available station pair, generating the horizontal (CCH) and vertical (CCV) correlation coefficients, respectively. A detection was considered as a potential earthquake if in at least 3 or more station pairs the CCH and CCV values were greater than 0.4. A total of 840 detections were classified as potential earthquakes and were subjected to a manual picking process to identify the S- and P-wave arrival time at each available station. Finally, location of earthquakes was carried out by using the software SEISAN (Havskov & Ottemoller, 1999) and a 1D velocity model developed in the vicinity of the Chile Triple Junction (Agurto-Detzel et al., 2014). Figure 4 shows some examples of waveforms associated with earthquakes occurring in the study area and recorded by CHAC station. In general, the difference between the P- and S-wave arrival times (tS-P) is less than 12 s, indicating a short distance between the stations and the earthquakes.

The resulting catalog (initial catalog) is composed of 751 events. To complete this catalog, we used the events reported by the CSN between 2018 and 2019. In the case of having an earthquake detected twice, the location proposed by the

CSN was chosen. Finally, the initial catalog is composed of 780 events whose spatial and temporal distribution is shown in Figure 5a and 5b, respectively.

5.2. Local Magnitudes

Local magnitudes (Ml) were calculated using the expressions of (Lahr, 1999):

$$M_l = \log_{10}(A) + b * \log_{10}(D) - c \qquad \text{Ec. (1)}$$

Where D is the epicentral distance in km, A is the maximum displacement peak-to-peak amplitude in mm, b and c are constants that depend on the epicentral distance:

$$b = 0.15; c = 0.80\ for\ 1\ km \leq D < 200\ km \qquad \text{Ec. (2)}$$

$$b = 3.38; c = 1.50\ for\ 200\ km \leq D < 600\ km \qquad \text{Ec. (3)}$$

The expressions described above were applied for each station used in the localization process. The final local magnitude was calculated from the median of these values. The time evolution of the magnitudes is shown in Figure 5c, while Figure 5d shows the cumulative frequency-magnitude distribution. The magnitude for the initial catalog varies between Ml -0.9 and 3.6.

5.3. Extended Catalog: Template Matching

Template matching (TM) is a novel computational technique widely used in seismology. This high-resolution method uses a known signal (template) to detect in continuous seismic records events similar to the template (Gibbons & Ringdal, 2006).

TM has been used in different tectonic environments to detect, locate, and characterize weak seismic signals such as small magnitude earthquakes (Cabrera et al., 2022; Ross et al., 2019), non-volcanic tremors (Brown et al., 2008; Shelly et al., 2007), fractures in geothermal fields (Li & Zhan, 2018), icequakes (Röösli et al., 2014), among others.

The use of TM has made it possible to extend seismic catalogs by a factor of ~10 (Cabrera et al., 2022; Essing & Poli, 2022; Ross et al., 2019) allowing to improve the magnitude of completeness and reduce localization errors, generating extremely detailed catalogs.

In this study, the TM was applied to the data following the next steps:

i. The continuous daily traces (EW, NS and ZZ) are detrended, demeaned, filtered between 2 and 8 Hz using a Butterworth filter and resampled to 20 Hz. This frequency range was chosen according to the observed local magnitudes to enhance the seismic signals over the ambient noise.
ii. In the second step, for all earthquakes in the initial catalog, a template per component is generated for each station used in the localization process. The template waveform is defined as a 10 s time window starting 1 s before the arrival of the P-wave at the station. This selection resulted in 11148 templates. Additionally, we calculated the signal to noise ratio (SNR) for each template as the ratio between the root-mean-square (RMS) during the 2*(tS-P) seconds before the arrival of the P-wave (noise windows) and the RMS during the 2*(tS-P) seconds after the arrival of the P-wave (signal windows).
iii. We calculated the cross-correlation between the templates and the daily continuous data, considering a one-sample moving window. The daily cross-correlation function (CC) over the three components was calculated using the Fast Matched Filter algorithm (Beaucé et al., 2018). For the calculation of the CC, we assign a weight to each station according to the following expression:

$$SNR_i = \frac{\sum_{k=1}^{3} SNR_{i,k}}{\sum_{i=1}^{n} \sum_{k=i}^{3} SNR_{i,k}} \qquad \text{Ec. (4)}$$

iv. Where SNRi,k is the signal-to-noise ratio for the "k" component of the station "i". For more detail on the methodology used in the calculation of CC, see (Beaucé et al., 2018).
v. We calculated the median absolute deviation (MAD) of the CC function averaged over all station and components. We defined a new detection when the MAD value of the daily CC is greater than 15. This threshold value minimizes false detections.
vi. We order the events according to their detection time. We merge consecutive detections with interevent times less than the window length of the template (10 s). The detection with the highest correlation coefficient is considered as the final event.
vii. We calculate the magnitude of the new detections from the amplitude ratio between detection and its template for two-time windows containing the P and S-wave, respectively. We consider a 2 s long time window starting 0.3 before the arrival of the P-wave and S-wave. The final magnitude was estimated from the median value over all amplitude ratios and assuming that a difference of 10 in amplitude corresponds to a unit magnitude difference (Peng & Zhao, 2009; Ross et al., 2017).

The proposed methodology leads to a final catalog of 7,219 events, which represents an extension of the initial catalog by a factor of ~9.3. Similar factors have been obtained in other studies where a similar criterion has been used (Cabrera et al., 2022; Frank et al., 2017; Ross et al., 2019). Figure 6 shows the temporal properties of the extended catalog.

6. Results

6.1. Initial Catalog and Local Seismicity

The initial catalog is composed of 780 earthquakes with local magnitudes ranging from M_l -0.9 to 3.6 and depths less than 59 km. The magnitude of completeness (M_c) of the catalog is M_l = 1.0 with a b-value of 1.03 (Figure 4c), similar M_c (M_c=1.1) and b-values (b=1.11) have been obtained in the northern portion of the LOFZ between 38°S-40°S (Sielfeld et al., 2019). The initial catalog represents a

4.3-fold increase over the 180 earthquakes reported by the CSN for the same period (2018-2019).

The temporal distribution (Figure 5b) shows that the seismic activity is persistent with a rate of 1.07 earthquakes per day. Because during the analyzed period some stations had operating problems, it is very likely that some events have not been detected and therefore the rate of seismic activity is higher.

For most days, 1-3 events were identified (background seismicity). Some seismicity bursts with more than five events per day were identified in isolation, except between May 12 and June 12, 2018, where the seismicity rate increases to 10 events per day reaching a maximum of 24 events on May 16. During this period, 315 earthquakes occurred, which represents 40% of the initial catalog. Because the spatial distribution of these events was concentrated in the area where the 2007 Aysén seismic sequence occurred, we named this burst of seismicity as “The Aysén 2018 Seismic Sequence”. This sequence will be discussed later in this section.

The spatial distribution (Figure 4a) shows that most of the hypocenters tends to be clustered mainly along major geomorphologic lineaments belonging to different branches of LOFZ and around the location of volcanoes (Figure 5). This observation is supported by the calculated focal mechanisms, most of which show strike-slip components consistent with the long-term deformation field along the LOFZ (Iturrieta et al., 2017; Lavenu & Cembrano, 1999). In a second order, some focal mechanisms of normal type were identified mainly in the Aysén fjords, where previous studies have identified the presence of local faults with normal kinematics (Easton et al., 2013; Villalobos et al., 2020).

Most of this seismicity corresponds to shallow crustal events occurring in the South American Plate at depths less than 25 km. This value constrains the depth of the seismogenic zone for the study area and agrees with the values reported by other authors which vary between 15 and 40 km for nearby zones (Agurto-Detzel et al., 2014; Pérez-Estay et al., 2020; Sielfeld et al., 2019). Hypocenters with depths greater than 30 km are concentrated towards the west side of the study area, where the Nazca plate is subducting beneath the South American plate and therefore subduction-associated earthquakes are expected to occur. In this zone, we detected earthquakes with depths of up to 59 km, which is consistent with the limit of the wadati-benioff zone which ranges from 50-60 km to -45°S (Ide, 2012).

The detected seismicity corresponds to small earthquakes with magnitudes less than M_l 3.6 (Figure 5b). These values coincide with the magnitudes reported in the north-central (M_w<3.8) (Lange et al., 2008; Sielfeld et al., 2019), south-central (M_w<4.1) (Pérez-Estay et al., 2020) and southern (M_l<3.4) (Agurto-Detzel et al., 2014) portions of the LOFZ.

According to their spatial distribution and the origin of the seismicity, we group the events into three types of clusters:

- Cluster type A: Events with a tectonic origin and associated with LOFZ seismic activity.
- Cluster type B: Events related to volcanic activity.
- Cluster type C: Events of tectonic origin and associated with the subduction of the Nazca plate beneath South American plate.

We defined a total of 8 clusters, 4 type A, 3 type B and 1 type C. The spatial distribution of the clusters is shown in Figure 5a, while the characteristics of each cluster are discussed in section 6.4.

6.2. Extended Catalog

From 780 templates, we were able to detect 6.540 new events, which represents an extension of the initial catalog by about 9.3 times. In Figure 6a we compare the temporal evolution of the extended and initial catalog. In general, both catalogs share a similar temporal evolution, although the extended catalog shows seismicity peaks not observed in the initial catalog especially for the second half of 2019. This is because in that period the CHAC and AYSN stations present a significant information gap (Figure 3a).

The extended catalog reaffirms that seismicity in the study area is persistent with a rate of 10 earthquakes per day and tends to be clustered in time and space, identifying several days where the seismicity rate exceeds 20 earthquakes per day. The peak of seismicity occurs between May and July 2018 during the 2018 Aysén seismic sequence. In this period, more than 4000 earthquakes are detected with a maximum seismicity rate reaching 131 events per day on May 16 and 23, 2018.

Figure 6b shows the temporal distribution of the magnitudes for the extended catalog, which vary between M_l -3.0 and 3.6, which results in a sustainable improvement of this catalog in the detection of small magnitude events. The median magnitude is 0.6 showing that seismicity is characterized mainly by the occurrence of small magnitude events.

In addition, Figure 5b shows the frequency-magnitude distribution for the extended catalog. The estimated b-value is of 1.12 which is similar to the b-value for the initial catalog and consistent with a tectonic origin of the seismicity (Farrell et al., 2009; Frohlich & Davis, 1993). On the other hand, the magnitude of completeness decreased from M_l 1.0 for the initial catalog to M_l 0.6 for the extended catalog.

The correlation coefficient of the detections that compose the extended catalog varies between 0.22 and 1.0, the latter value being associated with the auto-detection of the template. On the other hand, the number of detections per template varies between 1 (auto-detection) and 307 (Template #477) with an average of 10. Figure 6b shows the number of detections per template while Figure 6a shows its spatial distribution. From Figure 6b it is possible to observe that multiples templates detected more than 50 new events in the analyzed period. These new detections have locations close to the templates (Cabrera et al., 2022; Ross et al., 2019), showing that there are zones in the LOFZ with a high seismic productivity. Figure 6c shows the events detected with Templates #349 which share similar arrival time for the S and P, confirming that they are generated in an area very close to the template.

6.3. Similar Events and Repeating Earthquakes

Because some templates have multiple detections with high correlation coefficients, we look for the presence of similar events and repeating earthquakes. Similar events are earthquakes that generate almost identical waveforms at a common station, implying that both events share similar locations and focal mechanisms (Schaff & Richards, 2004). When similar events are co-located and their rupture area overlaps by at least 50%, these events are called repeating earthquakes (Gao et al., 2023), which represent repetitive ruptures of the same fault patch at different times (Uchida, 2019; Uchida & Bürgmann, 2019). Repeating earthquakes are generated in seismic patches that are loaded to the failure by a surrounding aseismic slip (creeping) (Nadeau & Johnson, 1998; Nadeau & McEvilly, 1999; Nakajima & Hasegawa, 2023) and are used for indicator of slow slip (Uchida, 2019). Repeating earthquakes have been detected on other major strike-slip faults, such as, San Andreas (North America) (Nadeau et al., 1995; Templeton et al., 2008), Haiyuan Fault System (Tibetan Plateau) (Deng et al., 2020), Anatolian Fault (Turkey) (Uchida et al., 2019) and Queen Charlotte Fault (Canada) (Hayward & Bostock, 2017) showing that a significant portion of the slip is accommodated by fault creep (Uchida & Bürgmann, 2019).

In the first stage, we searched for families of similar events following the next steps:

i. For each template, we selected from the extended catalog all the detections that have a correlation coefficient greater than 0.65.
ii. For each available station, we generate waveforms for the template and its detection considering a time window of 2ts-p [s], starting 1 [s] before the arrival of the P-wave.
iii. We filtered the traces between 2 and 12 Hz using a Butterworth filter. Similar frequency ranges have been used to identify repeating earthquakes of events with similar magnitudes (~Ml 1-2) (De Barros et al., 2020; Hayward & Bostock, 2017; Konca et al., 2021; Zhou et al., 2022).
iv. We calculate the cross-correlation between the template and its detections. If the correlation coefficient is greater than 0.90 in all

components for at least one station, the detection is considered as a similar event.

After calculating the cross-correlation between all the templates and their detections, we grouped the events into families. We use the term family to refer to a set of events that have highly similar waveforms (correlation coefficient C.C.>0.9) in at least one station, which indicates that the focal mechanism and location of events are similar (Robinson et al., 2007; Snieder & Vrijlandt, 2005).

We defined the families using the “chain-like method”. This method considers that if event A has a high correlation coefficient with event B, and event B correlates highly with event C, then it is assumed that event A and C will also have a high correlation and therefore events A, B and C belong to the same family (Got et al., 1994; Igarashi et al., 2003; Peng & Ben-Zion, 2005).

Figure 7 shows an example of events with highly similar waveforms occurring at different times (family of similar events). We identify a total of 103 families that have at least two events with similar waveforms and occur at different times. The spatial distribution of the families is shown in Figure 8a. We consider the location of the template with the lowest error as the representative location of the family.

The occurrence of the families over time is shown in Figure 8b, while Figure 8c shows the number of times each family was identified. The number of events per family varied between 2 and 554 (Family #18) with a median value of 3 events. Figure 8c shows the traces associated with the family #18, where it is possible to observe that the 554 events share similar waveforms and S-P arrival times. This confirms that the members of a family share similar locations and focal mechanisms.

A total of 1077 events were grouped into families, representing 15% of all detected seismicity. On the other hand, the time between two consecutive events for each family varies between 65 seconds (Family #12) and 398 days (Family #92). Families of similar events are distributed throughout the study area with recurrence times averaging less than 9 days, demonstrating that an important part of the seismicity in the LOFZ tends to cluster in time and space.

To understand whether similar events are generated by the same seismic patch or the rupture of nearby patches, we look for repeating earthquakes (RE) which are interpreted as seismic evidence of aseismic slip (Igarashi et al., 2003; Liu et al., 2022; Uchida & Bürgmann, 2019).

Different methodologies have been proposed to identify repeating earthquakes, the most common of which are based on finding events that generate similar waveforms at one or more stations. However, in recent years, several authors have shown that this condition is not sufficient to ensure that two events represent the repetitive rupture of a seismic patch, suggesting that events with an overlapping area between 50-70% can be considered RE (Ellsworth & Bulut, 2018; Gao et al., 2021, 2023). The latter condition requires dense seismic arrays capable of accurately measuring the delay times between arriving P and S waves of the different events.

Because many stations have significant data gaps during the analyzed period, we employed the coda wave interferometry method to constrain the source separation between events (Hayward & Bostock, 2017; Robinson et al., 2007; Snieder & Vrijlandt, 2005). This approach uses the cross-correlation of the coda waves generated by two events at the same station to constrain their separation. The main advantage of this approach over other traditional methods, such as the double-difference method (Waldhauser & Ellsworth, 2000), is that it requires only one station and does not require a velocity model (Robinson et al., 2007; Snieder, 2006; Snieder & Vrijlandt, 2005).

The methodology used to identify ER follows the next steps:

i. In each family of similar events, we selected those with a correlation coefficient greater than 0.97 in at least two stations.
ii. We divide the event signals into 1.0 s windows and compute the cross correlation as a function of time by sliding the time window along the waveforms.
iii. We calculate the source separation between events using equation (53)

of (Snieder & Vrijlandt, 2005) and assuming that the events are generated by a double couple source. We consider a Vp of 8.0 km/s and a Vs of 3.5 m/s.

iv. If the source separation is less than 50 m, the events are considered as repeating earthquakes. The threshold (50m) was selected by considering a circular rupture with constant stress drop ($\Delta\sigma$) of 3MPa and a rupture radius of (Kanamori & Anderson, 1975):

$$r = \left(\frac{7M_0}{16\Delta\sigma}\right)^{\frac{1}{3}} \qquad \text{Ec. (5)}$$

Where, the moment-magnitude (M_0) is related to the local magnitude through the following expression (Hanks & Kanamori, 1979):

$$\log\left(M_0\right) = 16.1 + 1.5M_l \qquad \text{Ec. (6)}$$

If we consider a M_l~ 1.9, the diameter of the rupture would be of the order of 100 m, showing that a source separation of less than 50 m suggests a significant overlap (>50%).

Figure 10 show an example of repeating earthquakes, where their traces have a correlation coefficient greater than 0.97 (Figure 10a and Figure 10b) and the source separation is less than 50 m (Figure 10c). We identified a total of 108 repeating earthquakes, which were grouped into 33 families using the chain method. The number of events per family varies between 2 and 19 (Family #14). The spatial distribution of the families (Figure 11a) shows that repeating earthquakes are mainly concentrated in the Aysén area where 26 families are identified. The remaining families are identified in the vicinity of the Cay volcano (two families), in the western portion of the study area (subduction zone) (two families) and in the vicinity of different branches belonging to the LOFZ (three families). The temporal distribution of the families (Figure 11b) shows that most of the events occur in May during the 2018 Aysén seismic sequence. In this period, the families with the highest number of events occur in time intervals of less than 17 days (Family #10, Family #11 y Family #14). The interevent time between subsequent events varies between ~0.01 and ~336 days (Figure 11 d) with a median value of ~16 hr, showing that most families tend to occur in burst-type sequences.

6.4. The 2018 Aysén Seismic Sequence

During 2018 and 2019, we identified in the Aysén Fjords, the occurrence of 478 earthquakes in an area of approximately 25x25 km2. The number earthquakes increase to more than 4000 when considering the detections of the final catalog. This seismic activity, accounting for 67% of the total seismicity detected in the initial catalog, primarily takes place between the months of May and June of 2018 in the same region where the 2007 Aysén seismic sequence occurred. The spatial distribution of events is shown in Figure 12, where it is possible to observe that seismic activity in the area tends to occur at depths shallower than 30 km and is primarily associated with the Punta Cola, Rio Cuervo, and Quitralco faults, which were involved in the 2007 Aysén seismic sequence (Easton et al., 2013; Villalobos et al., 2020). The temporal evolution (Figure 13a) demonstrates that seismicity in the area is persistent between 2018 and 2019, with an average of 6 events per day and local magnitudes that varies between Ml -3.0 and 3.6 (Figure 13b). During the months of August and November 2019, there is a decrease in the number of detections due to operational issues with the CHAC and AYSN stations (Figure 3a). The seismic activity shows a notorious change since the end of April, when more than 10 earthquakes per day were detected for the first time. Subsequently, between the months of May and June, the peak of detected events was reached with a maximum of 109 events per day (May 16). In addition, the largest events (Ml 3.5 and Ml 3.6) occur in this period.

Subsequently, seismicity begins to cease, identifying isolated days in the months of July, September, October, and November 2018 where the seismicity rate exceeds 20 events per day. During 2019, seismicity rate returns to background seismicity with an average of 1 event per day. Because more than 60% of the seismicity occurs between May and June 2018, we refer to this period as the 2018 Aysén seismic sequence.

7. Conclusions

We used a permanent network of 17 broadband stations to study the seismic behavior of the southern portion of the LOFZ between 2018 and 2019. Historically, this area has been hit by large earthquakes which have generated considerable economic and infrastructure damage and loss of human lives.

During the analyzed period, we detected the occurrence of more than 7000 earthquakes with magnitudes ranging between Ml -3.0 and 3.6 and depths generally less than 30 km. The spatial distribution and calculated focal mechanisms indicate that different branches of the LOFZ are the main source of seismic activity in the area. In general, the detected seismicity tends to be cluster in space and time, in families of events that share similar locations and focal mechanisms and occur in periods of time that vary between 1 min and 400 days.

One of the most significant findings was the detection of a seismic swarm between the months of May and June 2018, where nearly 50% of the total detected seismicity occurred. The swarm took place in the Aysen fjords, in the same area where the 2007 Aysén seismic sequence occurred. The swarm was characterized by the occurrence of more than 3000 earthquakes with magnitudes less than Ml 3.6 and depths shallower than 20 km. The temporal and spatial evolution of seismicity suggests that the seismic swarm was driven by a diffusive process. The presence of repetitive earthquakes with interevent times shorter than 10 days confirms the presence of fluids as the triggering mechanism of the swarm.

Our observations suggest that LOFZ is a complex system with several seismically active branches capable of generating a variety of seismic manifestations including ordinary earthquakes, volcano-related seismicity, seismic swarms, and repeating earthquakes.

Considering the findings presented in this study, the available historical background and the proximity of some branches to populated areas, it is essential to re-evaluate the seismic hazard along the LOFZ.

References

Agurto, H., Rietbrock, A., Barrientos, S., Bataille, K., & Legrand, D. (2012). Seismotectonic structure of the Aysén Region, Southern Chile, inferred from the 2007 M w= 6.2 Aysén earthquake sequence. *Geophysical Journal International*, *190*(1), 116–130. https://doi.org/10.1111/j.1365-246X.2012.05507.x

Agurto-Detzel, H., Rietbrock, A., Bataille, K., Miller, M., Iwamori, H., & Priestley, K. (2014). Seismicity distribution in the vicinity of the Chile Triple Junction, Aysén Region, southern Chile. *Journal of South American Earth Sciences*, *51*, 1–11. https://doi.org/10.1016/j.jsames.2013.12.011

Angermann, D., Klotz, J., & Reigber, C. (1999). Space-geodetic estimation of the Nazca-South America Euler vector. *Earth and Planetary Science Letters*, *171*(3), 329–334.

Barrientos, S., Bataille, K., Aranda, C., Legrand, D., Báez, J. C., Agurto, H., Pavez, A., Genrich, J., Vigny, C., & Bondoux, F. (2007). Complex sequence of earthquakes in Fjordland, Southern Chile. *Proceedings Geosur*, *21*.

Barrientos, S. E., & Acevedo-Aránguiz, P. S. (1992). Seismological aspects of the 1988–1989 Lonquimay (Chile) volcanic eruption. *Journal of Volcanology and Geothermal Research*, *53*(1–4), 73–87.

Barrientos, S. E., & Ward, S. N. (1990). The 1960 Chile earthquake: inversion for slip distribution from surface deformation. *Geophysical Journal International*, *103*(3), 589–598.

Beaucé, E., Frank, W. B., & Romanenko, A. (2018). Fast matched filter (FMF): An efficient seismic matched-filter search for both CPU and GPU architectures. *Seismological Research Letters*, *89*(1), 165–172.

Breitsprecher, K., & Thorkelson, D. J. (2009). Neogene kinematic history of Nazca–Antarctic–Phoenix slab windows beneath Patagonia and the Antarctic Peninsula. *Tectonophysics*, *464*(1–4), 10–20.

Brown, J. R., Beroza, G. C., & Shelly, D. R. (2008). An autocorrelation method to detect low frequency earthquakes within tremor. *Geophysical Research Letters*, *35*(16). https://doi.org/10.1029/2008GL034560

Cabrera, L., Poli, P., & Frank, W. B. (2022). Tracking the spatio-temporal evolution of foreshocks preceding the Mw 6.1 2009 L'Aquila earthquake. *Journal of Geophysical Research: Solid Earth*, *127*(3), e2021JB023888.

Cembrano, J., & Herve, F. (1993). The Liquiñe-Ofqui fault zone: A major Cenozoic strike-slip duplex in the Southern Andes. *International Symposium on Andean Geodynamics*, *2*, 175–178.

Cembrano, J., Hervé, F., & Lavenu, A. (1996a). The Liquiñe Ofqui fault zone: A long-lived intra-arc fault system in southern Chile. *Tectonophysics*, *259*(1-3 SPEC. ISS.), 55–66. https://doi.org/10.1016/0040-1951(95)00066-6

Cembrano, J., Hervé, F., & Lavenu, A. (1996b). The Liquiñe Ofqui fault zone: A long-lived intra-arc fault system in southern Chile. *Tectonophysics*, *259*(1-3 SPEC. ISS.), 55–66. https://doi.org/10.1016/0040-1951(95)00066-6

Chinn, D. S., & Isacks, B. L. (1983). Accurate source depths and focal mechanisms of shallow earthquakes in western South America and in the New Hebrides island arc. *Tectonics*, *2*(6), 529–563.

Cifuentes, I. L. (1989). The 1960 Chilean earthquakes. *Journal of Geophysical Research*, *94*(B1), 665–680. https://doi.org/10.1029/JB094iB01p00665

Comte, D., Gallego, A., Russo, R., Mocanu, V., Murdie, R., & VanDecar, J. (2007). The Aysen (Southern Chile) 2007 seismic swarm: volcanic or tectonic origin? *AGU Spring Meeting Abstracts*, *2007*, S43C-04.

De Barros, L., Cappa, F., Deschamps, A., & Dublanchet, P. (2020). Imbricated Aseismic Slip and Fluid Diffusion Drive a Seismic Swarm in the Corinth Gulf, Greece. *Geophysical Research Letters*, *47*(9). https://doi.org/10.1029/2020GL087142

De Pascale, G. P., Froude, M., Penna, I., Hermanns, R. L., Sepúlveda, S. A., Moncada, D., Persico, M., Easton, G., Villalobos, A., & Gutiérrez, F. (2021). Liquiñe-Ofqui's fast slipping intra-volcanic arc crustal faulting above the subducted Chile Ridge. *Scientific Reports*, *11*(1). https://doi.org/10.1038/s41598-021-86413-w

Deng, Y., Peng, Z., & Liu-Zeng, J. (2020). Systematic search for repeating earthquakes along the Haiyuan fault system in northeastern Tibet. *Journal of Geophysical Research: Solid Earth*, *125*(7), e2020JB019583.

Easton, G. V., Rebolledo, S., Sepúlveda, S. A., Lahsen, A., Thiele, R., Townley, B., Padilla, C., Rauld, R., Herrera, M. J., & Lara, M. (2013). Submarine earthquake rupture, active faulting and volcanism along the major Liquiñe-Ofqui Fault Zone and implications for seismic hazard assessment in the Patagonian Andes. *Andean Geology*, *40*(1), 141–171.

Ellsworth, W. L., & Bulut, F. (2018). Nucleation of the 1999 Izmit earthquake by a triggered cascade of foreshocks. *Nature Geoscience*, *11*(7), 531–535.

Essing, D., & Poli, P. (2022). Spatiotemporal Evolution of the Seismicity in the Alto Tiberina Fault System Revealed by a High-Resolution Template Matching Catalog. *Journal of Geophysical Research : Solid Earth*, *127*, 10. https://doi.org/10.1029/2022JB024845ï

Farrell, J., Husen, S., & Smith, R. B. (2009). Earthquake swarm and b-value characterization of the Yellowstone volcano-tectonic system. *Journal of Volcanology and Geothermal Research*, *188*(1–3), 260–276. https://doi.org/10.1016/j.jvolgeores.2009.08.008

Frank, W. B., Poli, P., & Perfettini, H. (2017). Mapping the rheology of the Central Chile subduction zone with aftershocks. *Geophysical Research Letters*, *44*(11), 5374–5382.

Frohlich, C., & Davis, S. D. (1993). Teleseismic b values; or, much ado about 1.0. *Journal of Geophysical Research: Solid Earth*, *98*(B1), 631–644.

Gallego, A., Russo, R. M., Comte, D., Mocanu, V., Murdie, R. E., & Vandecar, J. C. (2013). Tidal modulation of continuous nonvolcanic seismic tremor in the Chile triple junction region. *Geochemistry, Geophysics, Geosystems*, *14*(4), 851–863. https://doi.org/10.1002/ggge.20091

Gao, D., Kao, H., & Liu, J. (2023). Identification of Repeating Earthquakes: Controversy and Rectification. *Seismological Research Letters*, *94*(6), 2655–2665.

Gao, D., Kao, H., & Wang, B. (2021). Misconception of Waveform Similarity in the Identification of Repeating Earthquakes. *Geophysical Research Letters*, *48*(13). https://doi.org/10.1029/2021GL092815

Gibbons, S. J., & Ringdal, F. (2006). The detection of low magnitude seismic events using array-based waveform correlation. *Geophysical Journal International*, *165*(1), 149–166.

Got, J., Fréchet, J., & Klein, F. W. (1994). Deep fault plane geometry inferred from multiplet relative relocation beneath the south flank of Kilauea. *Journal of Geophysical Research: Solid Earth*, *99*(B8), 15375–15386.

Gutenberg, B., & Richter, C. (1954). Seismicity of the earth and associated phenomena. *Priceton NJ: Priceton Univ. Pr*, 1–310.

Hanks, T. C., & Kanamori, H. (1979). A moment magnitude scale. *Journal of Geophysical Research: Solid Earth*, *84*(B5), 2348–2350.

Havskov, J., & Ottemoller, L. (1999). SEISAN earthquake analysis software. *Seismol. Res. Lett*, *70*(5), 532–534.

Hayward, T. W., & Bostock, M. G. (2017). Slip Behavior of the Queen Charlotte Plate Boundary Before and After the 2012, MW 7.8 Haida Gwaii Earthquake: Evidence From Repeating Earthquakes. *Journal of Geophysical Research: Solid Earth*, *122*(11), 8990–9011. https://doi.org/10.1002/2017JB014248

Ide, S. (2012). Variety and spatial heterogeneity of tectonic tremor worldwide. *Journal of Geophysical Research: Solid Earth*, *117*(3). https://doi.org/10.1029/2011JB008840

Idehara, K., Yabe, S., & Ide, S. (2014). Regional and global variations in the temporal clustering of tectonic tremor activity. *Earth, Planets and Space*, *66*(1), 1–10.

Igarashi, T., Matsuzawa, T., & Hasegawa, A. (2003). Repeating earthquakes and interplate aseismic slip in the northeastern Japan subduction zone. *Journal of Geophysical Research: Solid Earth*, *108*(B5).

Iturrieta, P. C., Hurtado, D. E., Cembrano, J., & Stanton-Yonge, A. (2017). States of stress and slip partitioning in a continental scale strike-slip duplex: Tectonic and magmatic implications by means of finite element modeling. *Earth and Planetary Science Letters*, *473*, 71–82.

Kanamori, H., & Anderson, D. L. (1975). Theoretical basis of some empirical relations in seismology. *Bulletin of the Seismological Society of America*, *65*(5), 1073–1095.

Kanamori, H., & Rivera, L. (2017). An Mw = 7.7 slow earthquake in 1960 near the Aysén Fjord region, Chile. *Geophysical Journal International*, *211*(1), 93–106. https://doi.org/10.1093/GJI/GGX292

Kanamori, H., & Stewart, G. S. (1979). A slow earthquake. *Physics of the Earth and Planetary Interiors*, *18*(3), 167–175.

Konca, A. Ö., Karabulut, H., Güvercin, S. E., Eskiköy, F., Özarpacı, S., Özdemir, A., Floyd, M., Ergintav, S., & Doğan, U. (2021). From Interseismic Deformation With Near-Repeating Earthquakes to Co-Seismic Rupture: A Unified View of the 2020 Mw6.8 Sivrice (Elazığ) Eastern Turkey Earthquake. *Journal of Geophysical Research: Solid Earth*, *126*(10). https://doi.org/10.1029/2021JB021830

Lahr, J. C. (1999). *HYPOELLIPSE: A computer program for determining local earthquake hypocentral parameters, magnitude, and first motion pattern*. Citeseer.

Lange, D., Cembrano, J., Rietbrock, A., Haberland, C., Dahm, T., & Bataille, K. (2008). First seismic record for intra-arc strike-slip tectonics along the Liquiñe-Ofqui fault zone at the obliquely convergent plate margin of the southern Andes. *Tectonophysics*, *455*(1–4), 14–24. https://doi.org/10.1016/j.tecto.2008.04.014

Lavenu, A., & Cembrano, J. (1999). Compressional-and transpressional-stress pattern for Pliocene and Quaternary brittle deformation in fore arc and intra-arc zones (Andes of Central and Southern Chile). *Journal of Structural Geology*, *21*(12), 1669–1691.

Legrand, D., Barrientos, S., Bataille, K., Cembrano, J., & Pavez, A. (2011). The fluid-driven tectonic swarm of Aysen Fjord, Chile (2007) associated with two earthquakes (Mw=6.1 and Mw=6.2) within the Liquiñe-Ofqui Fault Zone. *Continental Shelf Research*, *31*(3–4), 154–161. https://doi.org/10.1016/j.csr.2010.05.008

Li, Z., & Zhan, Z. (2018). Pushing the limit of earthquake detection with distributed acoustic sensing and template matching: A case study at the Brady geothermal field. *Geophysical Journal International*, *215*(3), 1583–1593. https://doi.org/10.1093/gji/ggy359

Liu, M., Li, H., Li, L., Zhang, M., & Wang, W. (2022). Multistage nucleation of the 2021 Yangbi MS 6.4 earthquake, Yunnan, China and its foreshocks. *Journal of Geophysical Research: Solid Earth*, *127*(5), e2022JB024091.

Maksymowicz, A., Contreras-Reyes, E., Grevemeyer, I., & Flueh, E. R. (2012). Structure and geodynamics of the post-collision zone between the Nazca-Antarctic spreading center and South America. *Earth and Planetary Science Letters*, *345–348*, 27–37. https://doi.org/10.1016/j.epsl.2012.06.023

Miller, M., Bataille, K., Priestley, K., Iwamori, H., & Calisto, I. (2005). Seismic imaging of a subducted ridge, southern Chile. *AGU Fall Meeting Abstracts*, *2005*, S51A-0982.

Mora, C., Comte, D., Russo, R., Gallego, A., & Mocanu, V. (2010). Aysén seismic swarm (January 2007) in southern Chile: Analysis using Joint Hypocenter

Determination. *Journal of Seismology*, *14*(4), 683–691. https://doi.org/10.1007/s10950-010-9190-y

Murdie, R. E., Prior, D. J., Styles, P., Flint, S. S., Pearce, R. G., & Agar, S. M. (1993). Seismic responses to ridge-transform subduction: Chile triple junction. *Geology*, *21*(12), 1095–1098.

Nadeau, R. M., Foxall, W., & McEvilly, T. V. (1995). Clustering and periodic recurrence of microearthquakes on the San Andreas fault at Parkfield, California. *Science*, *267*(5197), 503–507.

Nadeau, R. M., & Johnson, L. R. (1998). Seismological studies at Parkfield VI: Moment release rates and estimates of source parameters for small repeating earthquakes. *Bulletin of the Seismological Society of America*, *88*(3), 790–814.

Nadeau, R. M., & McEvilly, T. V. (1999). Fault slip rates at depth from recurrence intervals of repeating microearthquakes. *Science*, *285*(5428), 718–721.

Nakajima, J., & Hasegawa, A. (2023). Prevalence of Repeating Earthquakes in the Continental Crust and Subducting Slabs: Triggering of Earthquakes by Aseismic Slip. *Journal of Geophysical Research: Solid Earth*, *128*(2). https://doi.org/10.1029/2022JB024667

Naranjo, J. A., Arenas, M., Clavero, J., & Muñoz, O. (2009). Mass movement-induced tsunamis: main effects during the Patagonian Fjordland seismic crisis in Aisén (45° 25’S), Chile. *Andean Geology*, *36*(1), 137–145.

Peng, Z., & Ben-Zion, Y. (2005). Spatiotemporal variations of crustal anisotropy from similar events in aftershocks of the 1999 M 7.4 Izmit and M 7.1 Düzce, Turkey, earthquake sequences. *Geophysical Journal International*, *160*(3), 1027–1043.

Peng, Z., & Zhao, P. (2009). Migration of early aftershocks following the 2004 Parkfield earthquake. *Nature Geoscience*, *2*(12), 877–881.

Pérez-Estay, N., Yáñez, G., Crempien, J., Roquer, T., Cembrano, J., Valdenegro, P., Aravena, D., Arancibia, G., & Morata, D. (2020). Seismicity in a Transpressional

Volcanic Arc: The Liquiñe-Ofqui Fault System in the Puyuhuapi Area, Southern Andes, Chile (44°S). *Tectonics*, *39*(11). https://doi.org/10.1029/2020TC006391

Robinson, D. J., Snieder, R., & Sambridge, M. (2007). Using coda wave interferometry for estimating the variation in source mechanism between double couple events. *Journal of Geophysical Research: Solid Earth*, *112*(12). https://doi.org/10.1029/2007JB004925

Röösli, C., Walter, F., Husen, S., Andrews, L. C., Lüthi, M. P., Catania, G. A., & Kissling, E. (2014). Sustained seismic tremors and icequakes detected in the ablation zone of the Greenland ice sheet. *Journal of Glaciology*, *60*(221), 563–575.

Rosenau, M., Melnick, D., & Echtler, H. (2006). Kinematic constraints on intra-arc shear and strain partitioning in the southern Andes between 38°S and 42°S latitude. *Tectonics*, *25*(4). https://doi.org/10.1029/2005TC001943

Ross, Z. E., Hauksson, E., & Ben-Zion, Y. (2017). Abundant off-fault seismicity and orthogonal structures in the San Jacinto fault zone. *Science Advances*, *3*(3), e1601946.

Ross, Z. E., Trugman, D. T., Hauksson, E., & Shearer, P. M. (2019). Searching for hidden earthquakes in Southern California. *Science*, *364*(6442), 767–771.

Rothé, J.-P. (1969). The seismicity of the earth, 1953-1965= La séismicité du globe 1953-1965. *(No Title)*.

Russo, R. M., Gallego, A., Comte, D., Mocanu, V. I., Murdie, R. E., Mora, C., & VanDecar, J. C. (2011). Triggered seismic activity in the Liquiñe-Ofqui fault zone, southern Chile, during the 2007 Aysen seismic swarm. *Geophysical Journal International*, *184*(3), 1317–1326. https://doi.org/10.1111/j.1365-246X.2010.04908.x

Sáez, M., Ruiz, S., Ide, S., & Sugioka, H. (2019). Shallow nonvolcanic tremor activity and potential repeating earthquakes in the Chile triple junction: Seismic evidence of the subduction of the active Nazca–Antarctic spreading center. *Seismological Research Letters*, *90*(5), 1740–1747. https://doi.org/10.1785/0220180394

Schaff, D. P., & Richards, P. G. (2004). Repeating seismic events in China. *Science*, *303*(5661), 1176–1178.

Sepúlveda, S. A., Ochoa-Cornejo, F., & Serey, A. (2022). Earthquake-Induced Landslides and Ground Failure in Chile: The Aysen 2007 and Maule 2010 Earthquakes. In *Coseismic Landslides: Phenomena, Long-Term Effects and Mitigation* (pp. 41–57). Springer.

Sepúlveda, S. A., & Serey, A. (2009). Tsunamigenic, earthquake-triggered rock slope failures during the April 21, 2007 Aisén earthquake, southern Chile (45.5 S). *Andean Geology*, *36*(1), 131–136.

Sepúlveda, S. A., Serey, A., Lara, M., Pavez, A., & Rebolledo, S. (2010). Landslides induced by the April 2007 Aysén Fjord earthquake, Chilean Patagonia. *Landslides*, *7*(4), 483–492. https://doi.org/10.1007/s10346-010-0203-2

Shelly, D. R., Beroza, G. C., & Ide, S. (2007). Non-volcanic tremor and low-frequency earthquake swarms. *Nature*, *446*(7133), 305–307. https://doi.org/10.1038/nature05666

Siebert, L., & Simkin, T. (2013). *Volcanoes of the world: An illustrated catalog of Holocene volcanoes and their eruptions*.

Sielfeld, G., Lange, D., & Cembrano, J. (2019). Intra-Arc Crustal Seismicity: Seismotectonic Implications for the Southern Andes Volcanic Zone, Chile. *Tectonics*, *38*(2), 552–578. https://doi.org/10.1029/2018TC004985

Snieder, R. (2006). The theory of coda wave interferometry. *Pure and Applied Geophysics*, *163*, 455–473.

Snieder, R., & Vrijlandt, M. (2005). Constraining the source separation with coda wave interferometry: Theory and application to earthquake doublets in the Hayward fault, California. *Journal of Geophysical Research: Solid Earth*, *110*(4), 1–15. https://doi.org/10.1029/2004JB003317

Templeton, D. C., Nadeau, R. M., & Bürgmann, R. (2008). Behavior of repeating earthquake sequences in central California and the implications for subsurface fault creep. *Bulletin of the Seismological Society of America*, *98*(1), 52–65.

Trnkoczy, A. (2009). Understanding and parameter setting of STA/LTA trigger algorithm. In *New manual of seismological observatory practice (NMSOP)* (pp. 1–20). Deutsches GeoForschungsZentrum GFZ.

Uchida, N. (2019). Detection of repeating earthquakes and their application in characterizing slow fault slip. In *Progress in Earth and Planetary Science* (Vol. 6, Issue 1). Springer Berlin Heidelberg. https://doi.org/10.1186/s40645-019-0284-z

Uchida, N., & Bürgmann, R. (2019). Repeating earthquakes. *Annual Review of Earth and Planetary Sciences*, *47*, 305–332.

Uchida, N., Kalafat, D., Pinar, A., & Yamamoto, Y. (2019). Repeating earthquakes and interplate coupling along the western part of the North Anatolian Fault. *Tectonophysics*, *769*, 228185.

Villalobos, A., Easton, G., Maksymowicz, A., Ruiz, S., Lastras, G., De Pascale, G. P., & Agurto-Detzel, H. (2020). Active faulting, submarine surface rupture, and seismic migration along the Liquiñe-Ofqui Fault System, Patagonian Andes. *Journal of Geophysical Research: Solid Earth*, *125*(9), e2020JB019946.

Waldhauser, F., & Ellsworth, W. L. (2000). A double-difference earthquake location algorithm: Method and application to the northern Hayward fault, California. *Bulletin of the Seismological Society of America*, *90*(6), 1353–1368.

Zhou, Y., Xu, L., Wu, J., Li, C., Fang, L., & Pan, Z. (2022). Seismicity of the repeating earthquake clusters in the northern Xiaojiang fault zone and its implications. *Frontiers in Earth Science*, *10*. https://doi.org/10.3389/feart.2022.917635

Figure captions

Figure 1. Seismotectonic of the Chile trench between -42°S and -48°S. Red line represent the Chile Ridge spreading center. The continuous black, red, and purple lines represent the surface trace of the LOFZ, the Chile Ridge spreading center and the estimated rupture extent of the Mw 9.5 1960 Valdivia giant megathrust earthquake (S. E. Barrientos & Ward, 1990). Dots are epicenters of events from the CSN catalog from 2005 to 2017. Diamonds represent the epicenters of the non-volcanic tremors (NVT) according to the catalogs of (Ide, 2012; Idehara et al., 2014; Sáez et al., 2019). The color bar is related to the hypocentral depth of the earthquakes and NVT. Stars represent the epicentral location of historical earthquakes with a magnitude greater than Ms 6.0. Focal mechanisms were obtained from (Agurto et al., 2012; Kanamori & Rivera, 2017; Lange et al., 2008). Volcanoes are plotted as cyan triangles (Siebert & Simkin, 2013). The blue box indicates the study area.

Figure 2. (a) Study area, seismic arrays, and epicenter's location. Blue squares show the location of broadband stations. Dots represents the distribution of earthquakes according to the CSN catalog from 2005 to 2017. Volcanoes are plotted as cyan triangles. The red box indicates the Aysén 2007 seismic sequence area. (b) Temporal distribution of earthquakes. The purple solid line indicates the period from which the CSN in conjunction with OVDAS deployed a permanent seismic array in the study area. (c) Aysén 2007 seismic sequence. The circles represent the epicentral distribution of earthquakes according to the CSN, (Agurto et al., 2012; S. Barrientos et al., 2007; Legrand et al., 2011). The focal mechanisms for the main events were obtained from (Agurto et al., 2012). For figures (a) and (b) the solid black line represents the surface trace of the LOFZ while the colored bar indicates the hypocentral depth of the earthquakes.

Figure 3. Seismic Array. (a) Availability of stations per day. (b) Total days recorded for each station.

Figure 4. Example of earthquake waveforms generated in the study area and recorded by the CHAC station. Figure 2a shows the location of the stations. The waveforms are associated with earthquakes that have time differences between the arrival of the S-wave and the P-wave (S-P_{time}) at the CHAC station of: (a) S-P_{time} ~3[s]; (b) S-P_{time} ~4.5[s]; (c) S-P_{time} ~6.6[s] and (d) S- P_{time} ~11[s]. Each graph shows the east-west (HE), north-south (NS) and vertical components (ZZ). Traces were filtered between 2 and 8 [Hz].

Figure 5. Local seismicity detected in this work. (a) Epicentral distribution of the 780 earthquakes reported in the initial catalog. The size of the circles is proportional to the local magnitude while the color scale is related to the depth of the earthquakes. (b) Temporal distribution of earthquakes reported by the CSN between 2018-2019 (blue bars and lines) and the initial catalog developed in the present study (black bars and lines). (c) Temporal distribution of the local magnitude. (d) Magnitude-frequency histogram for the initial catalog. Bars indicates numbers of earthquakes each 0.2 units-of-magnitude bins.

Figure 6. Extended catalog. (a) Number of earthquakes detected per day according to the CSN catalog (red bars), initial catalog (blue bars) and extended catalog (black bars). (b) Temporal distribution for the local magnitude of the extended catalog. (c) Cumulative frequency-magnitude distribution for the initial catalog (red circles) and extended catalog (blue circles).

Figure 7. Detections per Template. (a) Spatial distribution of the number of detections per Template. The color scale indicates the number of detections per template and is saturated at a maximum of 100. (b) Number of detections per template. (c) In the panel above, all waveforms associated with the 349 template detections are presented. In the bottom panel, the blue line shows the waveform

associated to the template while the red line shows the stacking of the waveforms associated to the new detections.

Figure 8. Example of events with highly similar waveforms (CC>0.90) or family events. (a) East-West waveform, (b) North-South waveforms and (c) Vertical waveforms

Figure 9. Families of events with similar waveforms. (a) Circles show the spatial distribution of the families that have at least two events with a C.C. greater than 0.9 in at least one station. The color of the circles indicates the numbering of each family while the size is proportional to the number of events that make up each family. (b) Temporal distribution of the events of each family. (c) Frequency distribution of families. (d) Vertical trace of events belonging to Family #18 and recorded at station AYSN.

Figure 10. Example of repeating earthquakes. (a) Red line shows event occurred on May 12, 2018 at 00:43:41.40 while blue line shows event occurred on May 13, 2018 at 05:49:41.24. Traces were filtered between 2 and 12 Hz using. (b) Temporal evolution of the cross-correlation coefficient in a 1.0 s long windows. (c) Source separation between events calculated from expression (53) of (Snieder & Vrijlandt, 2005).

Figure 11. Families of repeating earthquakes. (a) Circles show the spatial distribution of the families while the color indicates the numbering of each family, and the size is proportional to the number of events that make up each family (b) Temporal distribution of the events of each family (d) Interevent time between subsequent events in each family.

Figure 12. The 2018 Aysén Seismic Sequence. Circles and squares represent the spatial distribution of ordinary earthquakes detected in the initial catalog and families of repeating events, respectively. The size of the symbols is proportional to their local magnitude. Stars show the main events of the 2007 Aysén seismic sequence (2007-AYSS) according to (Agurto et al., 2012). Faults are from (Villalobos et al., 2020).

Figure 13. Seismicity in the Aysén Fjords between 2018 and 2019. (a) Number of earthquakes detected per day according to the final catalog (blue bars) and initial catalog (red bars). (b) Temporal distribution of local magnitudes according to initial (red dots) and final catalog (blue dots).

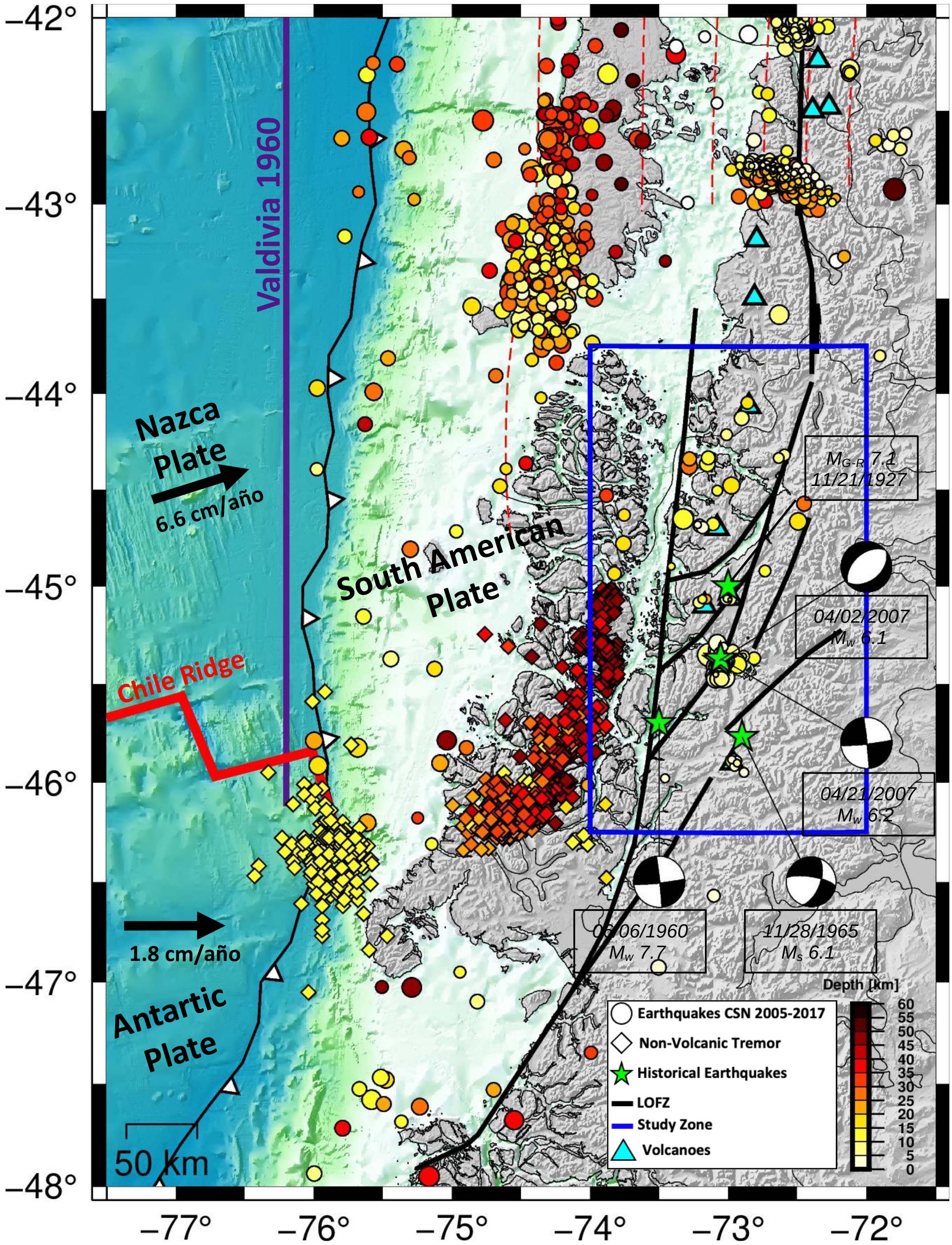

Figure 1. Seismotectonic of the Chile trench between -42°S and -48°S. Red line represent the Chile Ridge spreading center. The continuous black, red, and purple lines represent the surface trace of the LOFZ, the Chile Ridge spreading center and the estimated rupture extent of the Mw 9.5 1960 Valdivia giant megathrust earthquake (S. E. Barrientos & Ward, 1990). Dots are epicenters of events from the CSN catalog from 2005 to 2017. Diamonds represent the

epicenters of the non-volcanic tremors (NVT) according to the catalogs of (Ide, 2012; Idehara et al., 2014; Sáez et al., 2019). The color bar is related to the hypocentral depth of the earthquakes and NVT. Stars represent the epicentral location of historical earthquakes with a magnitude greater than Ms 6.0. Focal mechanisms were obtained from (Agurto et al., 2012; Kanamori & Rivera, 2017; Lange et al., 2008). Volcanoes are plotted as cyan triangles (Siebert & Simkin, 2013). The blue box indicates the study area.

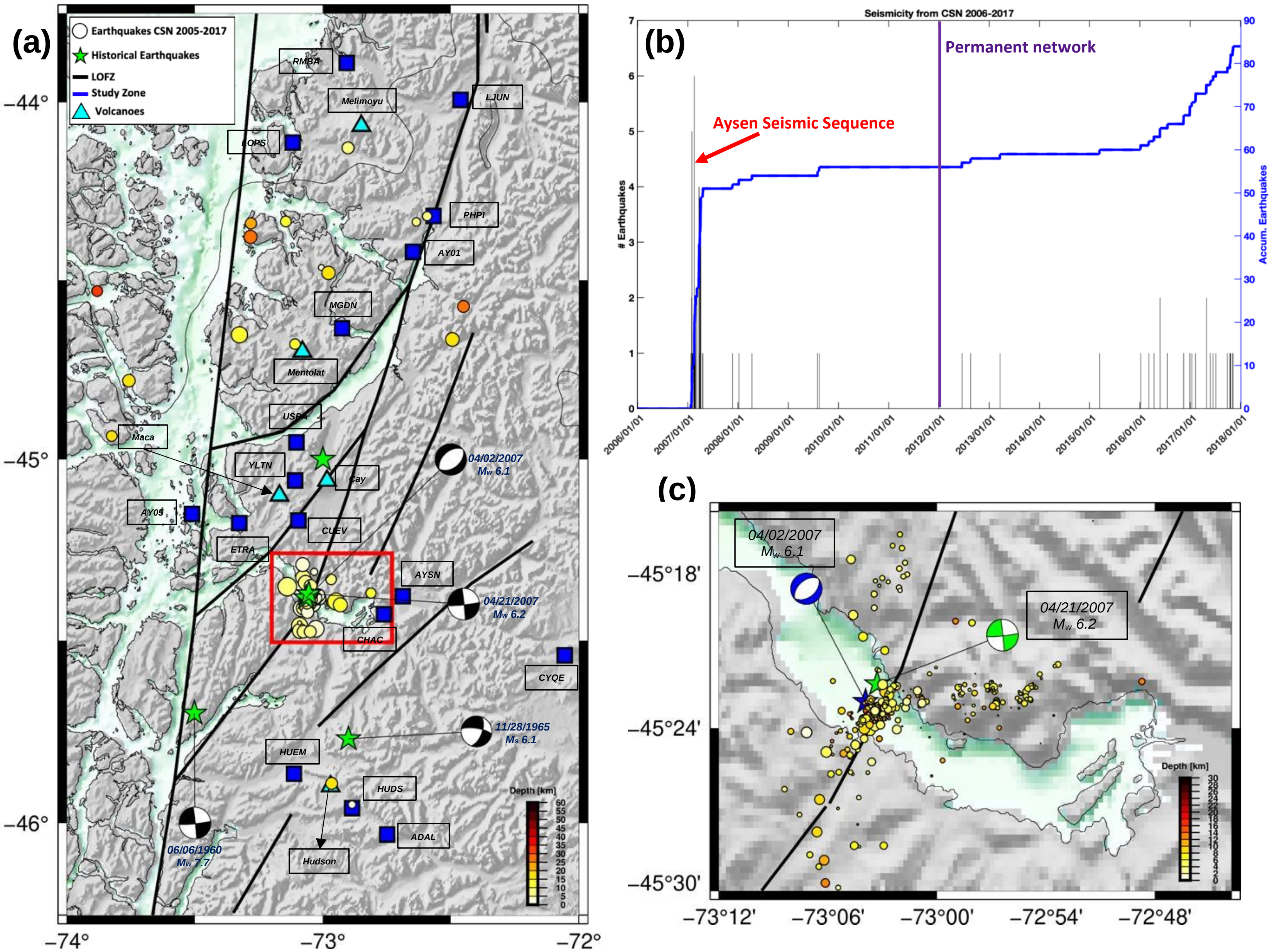
(a)
Earthquakes CSN 2005-2017
Historical Earthquakes
LOFZ
Study Zone
Volcanoes
RMBA
Melimoyu
LJUN
LOPS
PHPI
AY01
MGDN
Mentolat
USPA
Maca
YLTN
Cay
AY05
ETRA
CUEV
AYSN
CHAC
CYQE
HUEM
HUDS
Hudson
ADAL
04/02/2007
Mw 6.1
04/21/2007
Mw 6.2
11/28/1965
Ms 6.1
06/06/1960
Mw 7.7
Depth [km]
-44°
-45°
-46°
-74°
-73°
-72°
(b)
Seismicity from CSN 2006-2017
Permanent network
Aysen Seismic Sequence
Earthquakes
Accum. Earthquakes
(c)
-45°18'
-45°24'
-45°30'
-73°12'
-73°06'
-73°00'
-72°54'
-72°48'

Figure 2. (a) Study area, seismic arrays, and epicenter's location. Blue squares show the location of broadband stations. Dots represents the distribution of earthquakes according to the CSN catalog from 2005 to 2017. Volcanoes are plotted as cyan triangles. The red box indicates the Aysén 2007 seismic sequence area. (b) Temporal distribution of earthquakes. The purple solid line indicates the period from which the CSN in conjunction with OVDAS deployed a permanent seismic array in the study area. (c) Aysén 2007 seismic sequence. The circles represent the epicentral distribution of earthquakes according to the CSN, (Agurto et al., 2012; S. Barrientos et al., 2007; Legrand et al., 2011). The focal mechanisms for the main events were obtained from (Agurto et al., 2012). For figures (a) and (b) the solid black line represents the surface trace of the LOFZ while the colored bar indicates the hypocentral depth of the earthquakes.

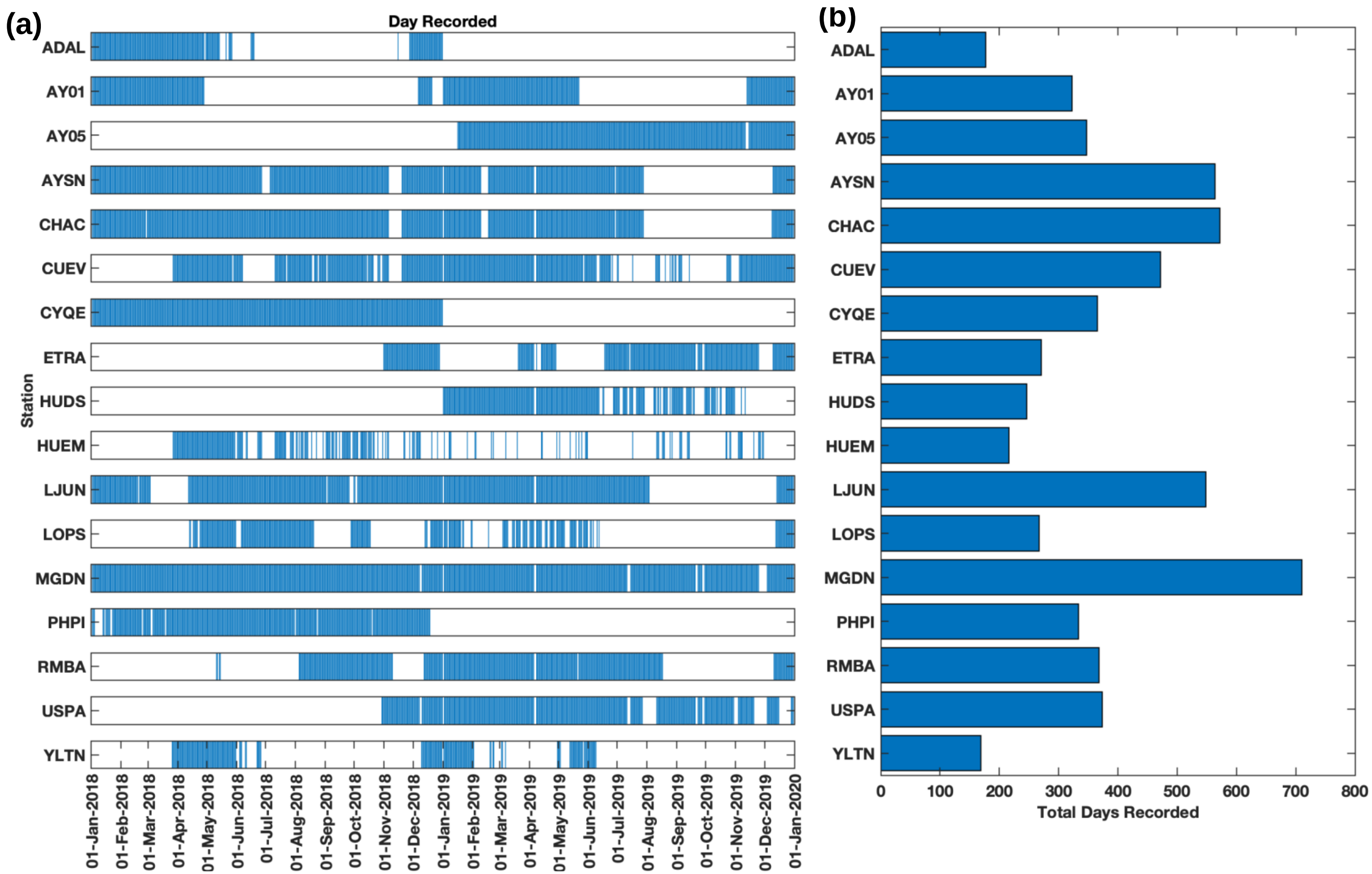

Figure 3. Seismic Array. (a) Availability of stations per day. (b) Total days recorded for each station.

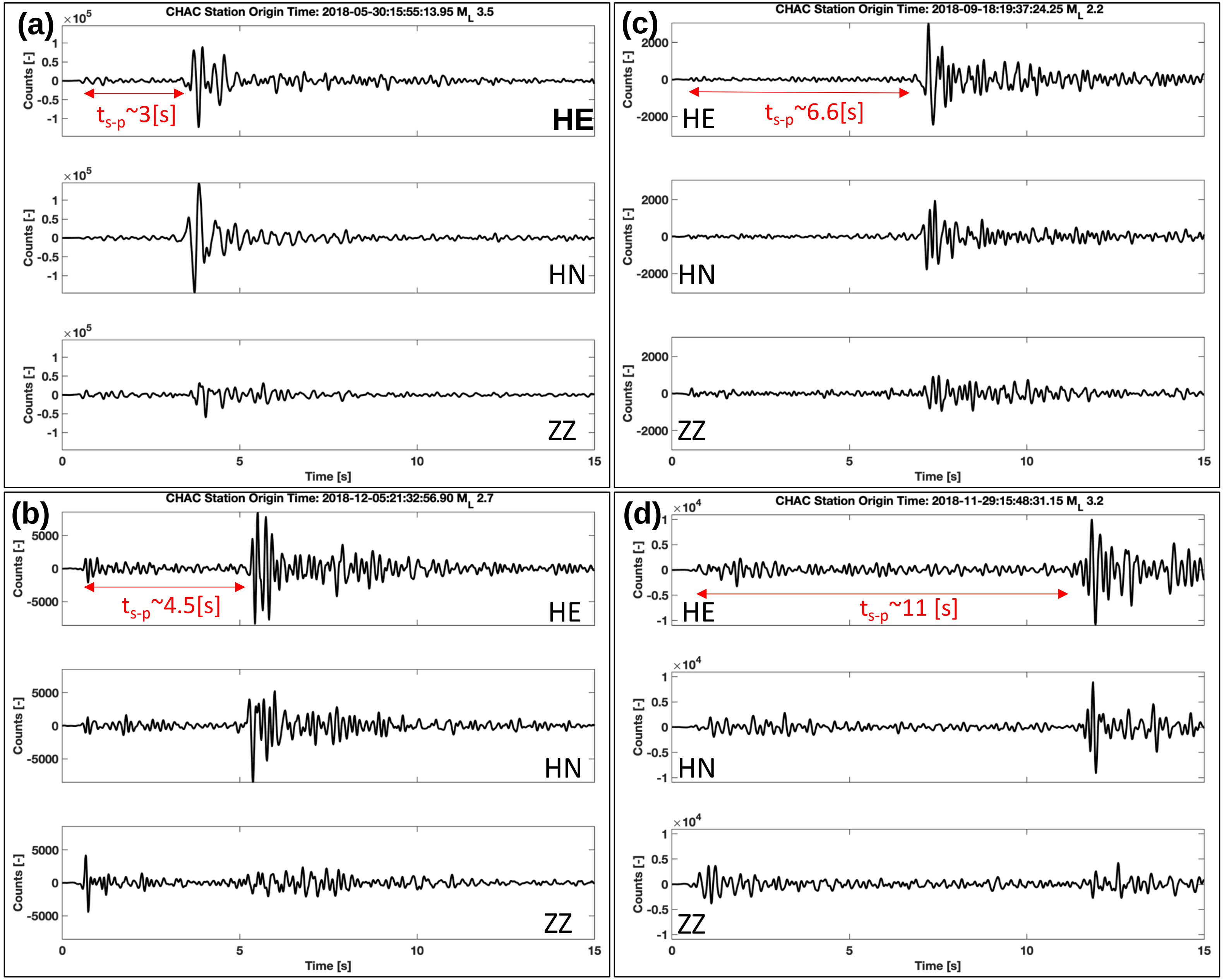
(a)
CHAC Station Origin Time: 2018-05-30:15:55:13.95 M_L 3.5
t_{s-p}~3[s]
HE
HN
ZZ
Counts [-]
Time [s]
(b)
CHAC Station Origin Time: 2018-12-05:21:32:56.90 M_L 2.7
t_{s-p}~4.5[s]
HE
HN
ZZ
(c)
CHAC Station Origin Time: 2018-09-18:19:37:24.25 M_L 2.2
t_{s-p}~6.6[s]
HE
HN
ZZ
(d)
CHAC Station Origin Time: 2018-11-29:15:48:31.15 M_L 3.2
t_{s-p}~11 [s]
HE
HN
ZZ

Figure 4. Example of earthquake waveforms generated in the study area and recorded by the CHAC station. Figure 2a shows the location of the stations. The waveforms are associated with earthquakes that have time differences between the arrival of the S-wave and the P-wave (S-Ptime) at the CHAC station of: (a) S-Ptime ~3[s]; (b) S-Ptime ~4.5[s]; (c) S-Ptime ~6.6[s] and (d) S- Ptime ~11[s]. Each graph shows the east-west (HE), north-south (NS) and vertical components (ZZ). Traces were filtered between 2 and 8 [Hz].

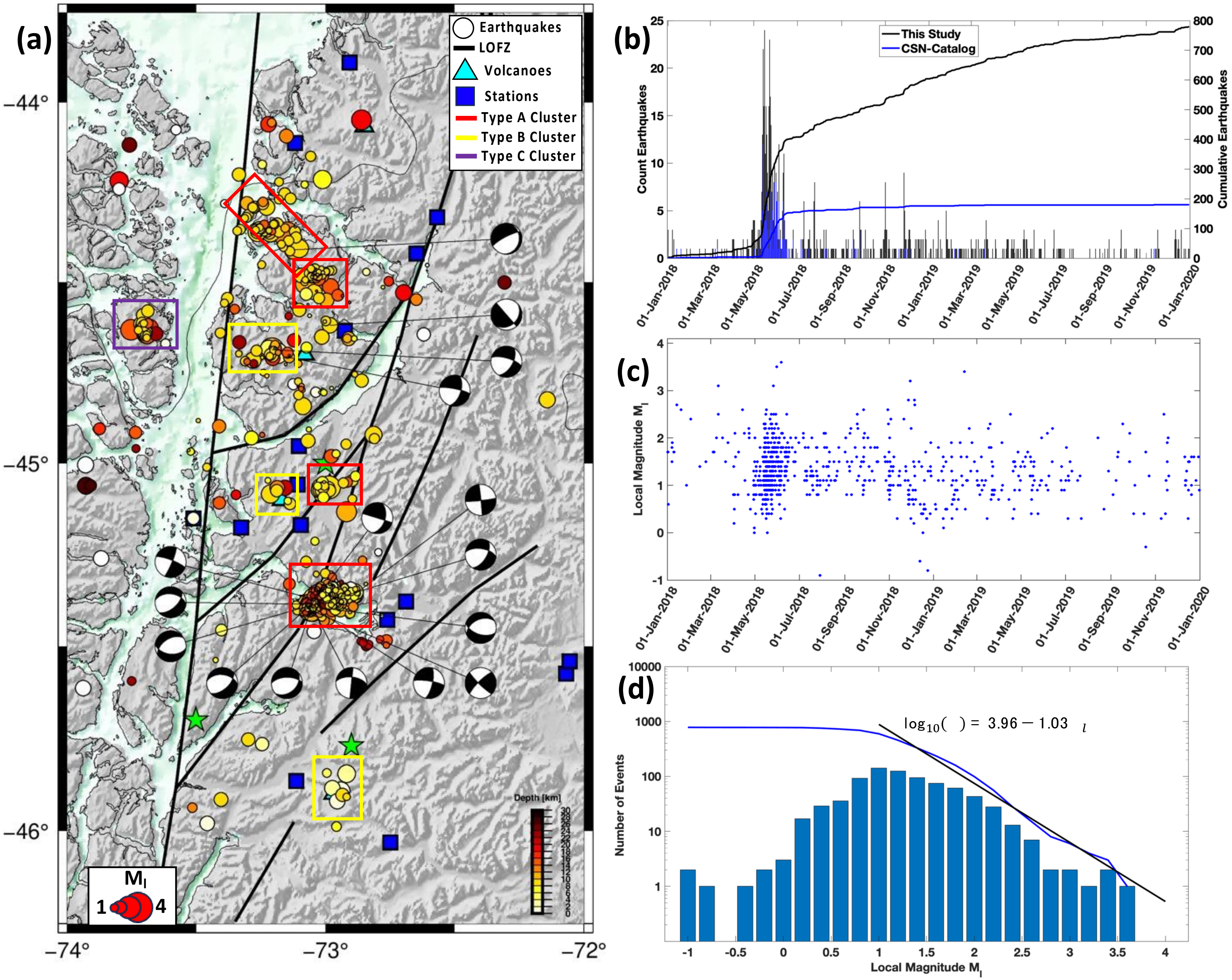
(a)
Earthquakes
LOFZ
Volcanoes
Stations
Type A Cluster
Type B Cluster
Type C Cluster
-44°
-45°
-46°
-74°
-73°
-72°
Depth [km]
M_l
1
4
(b)
This Study
CSN-Catalog
Count Earthquakes
Cumulative Earthquakes
(c)
Local Magnitude M_l
(d)
$\log_{10}(\ ) = 3.96 - 1.03\ _l$
Number of Events
Local Magnitude M_l

Figure 5. Local seismicity detected in this work. (a) Epicentral distribution of the 780 earthquakes reported in the initial catalog. The size of the circles is proportional to the local magnitude while the color scale is related to the depth of the earthquakes. (b) Temporal distribution of earthquakes reported by the CSN between 2018-2019 (blue bars and lines) and the initial catalog developed in the present study (black bars and lines). (c) Temporal distribution of the local magnitude. (d) Magnitude-frequency histogram for the initial catalog. Bars indicates numbers of earthquakes each 0.2 units-of-magnitude bins.

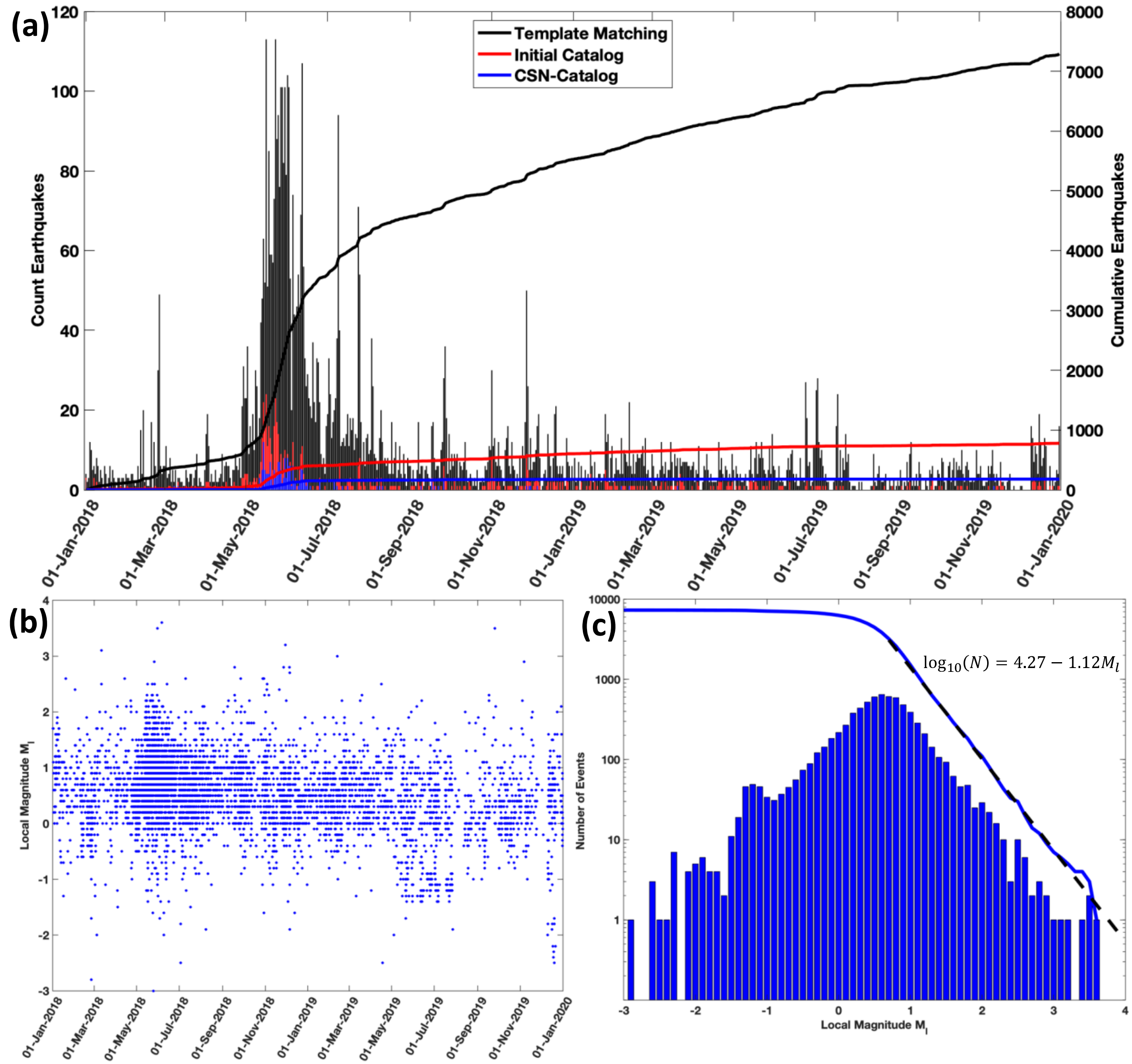

(a)
Template Matching
Initial Catalog
CSN-Catalog
Count Earthquakes
Cumulative Earthquakes
(b)
Local Magnitude M_l
(c)
$\log_{10}(N) = 4.27 - 1.12M_l$
Number of Events
Local Magnitude M_l

Figure 6. Extended catalog. (a) Number of earthquakes detected per day according to the CSN catalog (red bars), initial catalog (blue bars) and extended catalog (black bars). (b) Temporal distribution for the local magnitude of the extended catalog. (c) Cumulative frequency-magnitude distribution for the initial catalog (red circles) and extended catalog (blue circles).

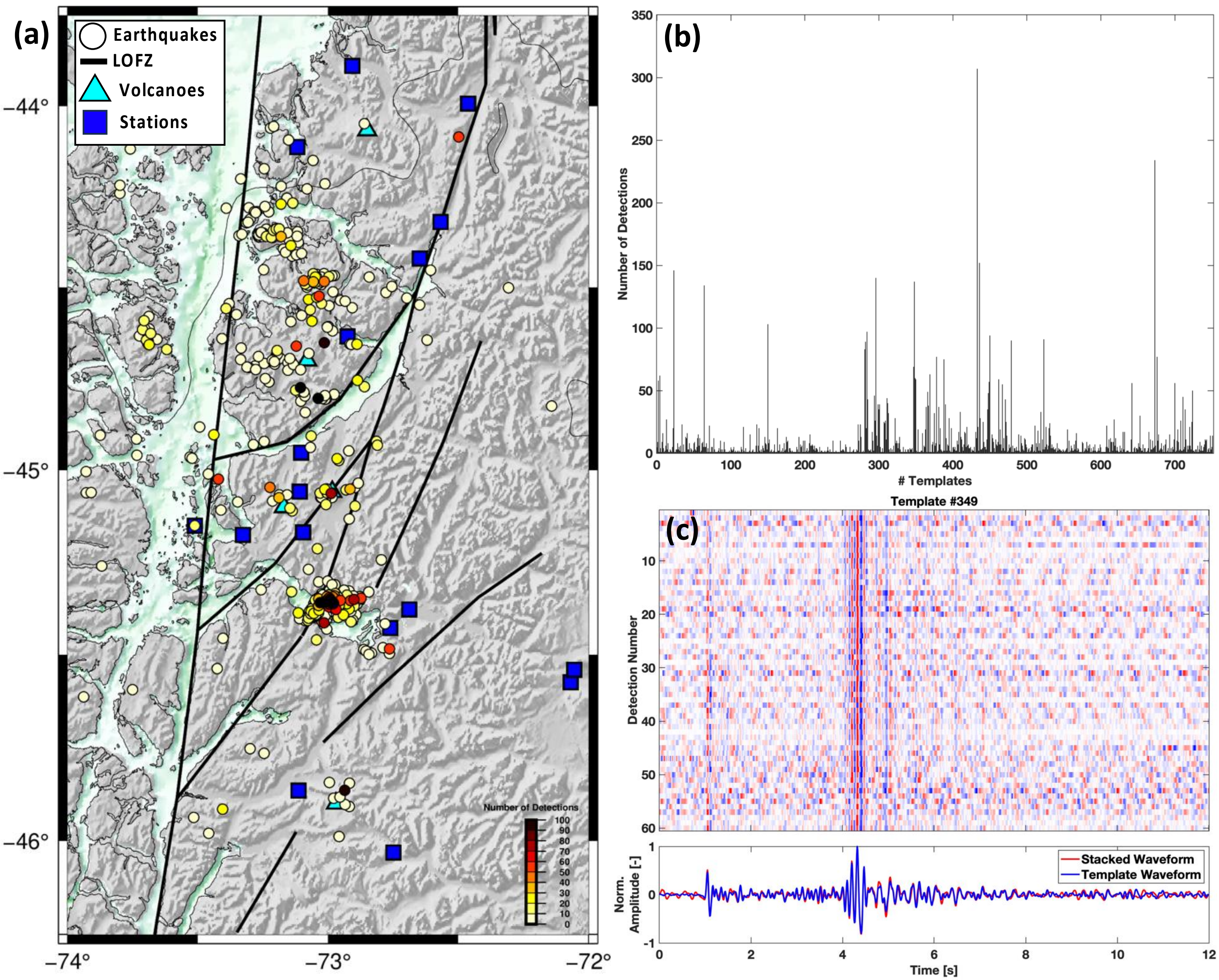
(a)
Earthquakes
LOFZ
Volcanoes
Stations
Number of Detections
-44°
-45°
-46°
-74°
-73°
-72°
(b)
Number of Detections
Templates
Template #349
(c)
Detection Number
Norm. Amplitude [-]
Stacked Waveform
Template Waveform
Time [s]

Figure 7. Detections per Template. (a) Spatial distribution of the number of detections per Template. The color scale indicates the number of detections per template and is saturated at a maximum of 100. (b) Number of detections per template. (c) In the panel above, all waveforms associated with the 349 template detections are presented. In the bottom panel, the blue line shows the waveform associated to the template while the red line shows the stacking of the waveforms associated to the new detections.

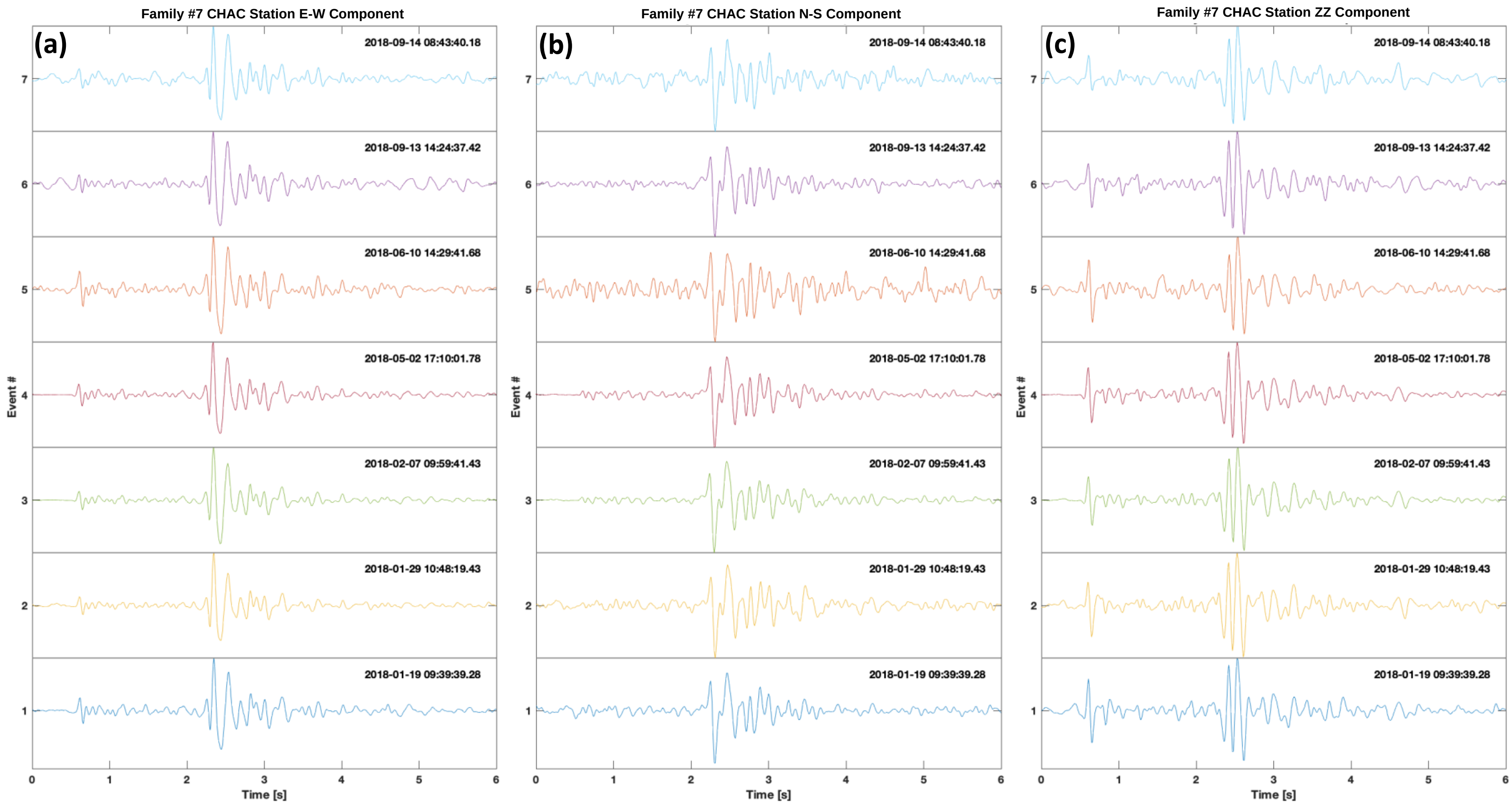

Figure 8. Example of events with highly similar waveforms (CC>0.90) or family events. (a) East-West waveform, (b) North-South waveforms and (c) Vertical waveforms

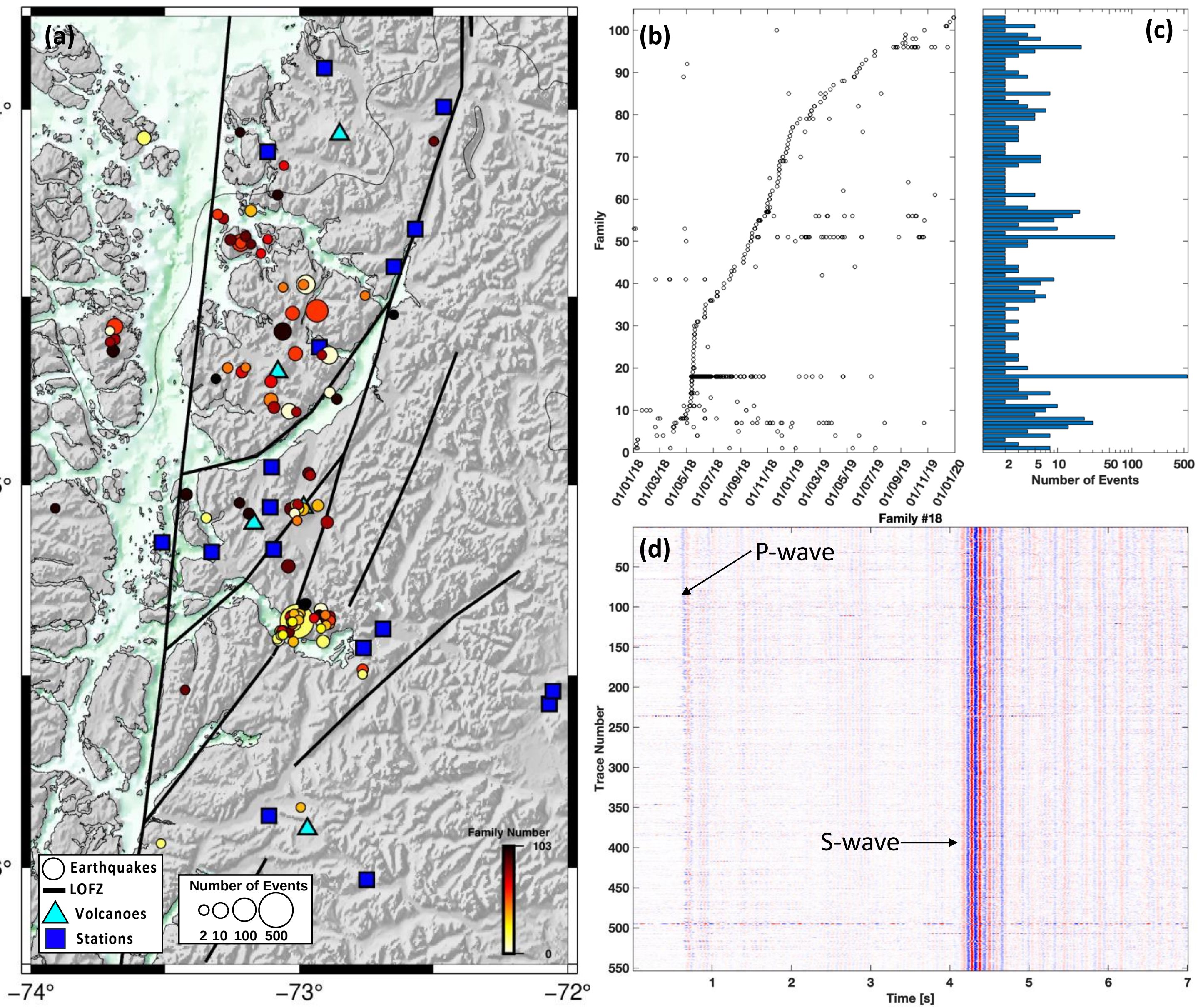
(a)
−44°
−45°
−46°
−74°
−73°
−72°
Earthquakes
LOFZ
Volcanoes
Stations
Number of Events
2 10 100 500
Family Number
103
0
(b)
Family
Family #18
(c)
Number of Events
(d)
P-wave
S-wave
Trace Number
Time [s]

Figure 9. Families of events with similar waveforms. (a) Circles show the spatial distribution of the families that have at least two events with a C.C. greater than 0.9 in at least one station. The color of the circles indicates the numbering of each family while the size is proportional to the number of events that make up each family. (b) Temporal distribution of the events of each family. (c) Frequency distribution of families. (d) Vertical trace of events belonging to Family #18 and recorded at station AYSN.

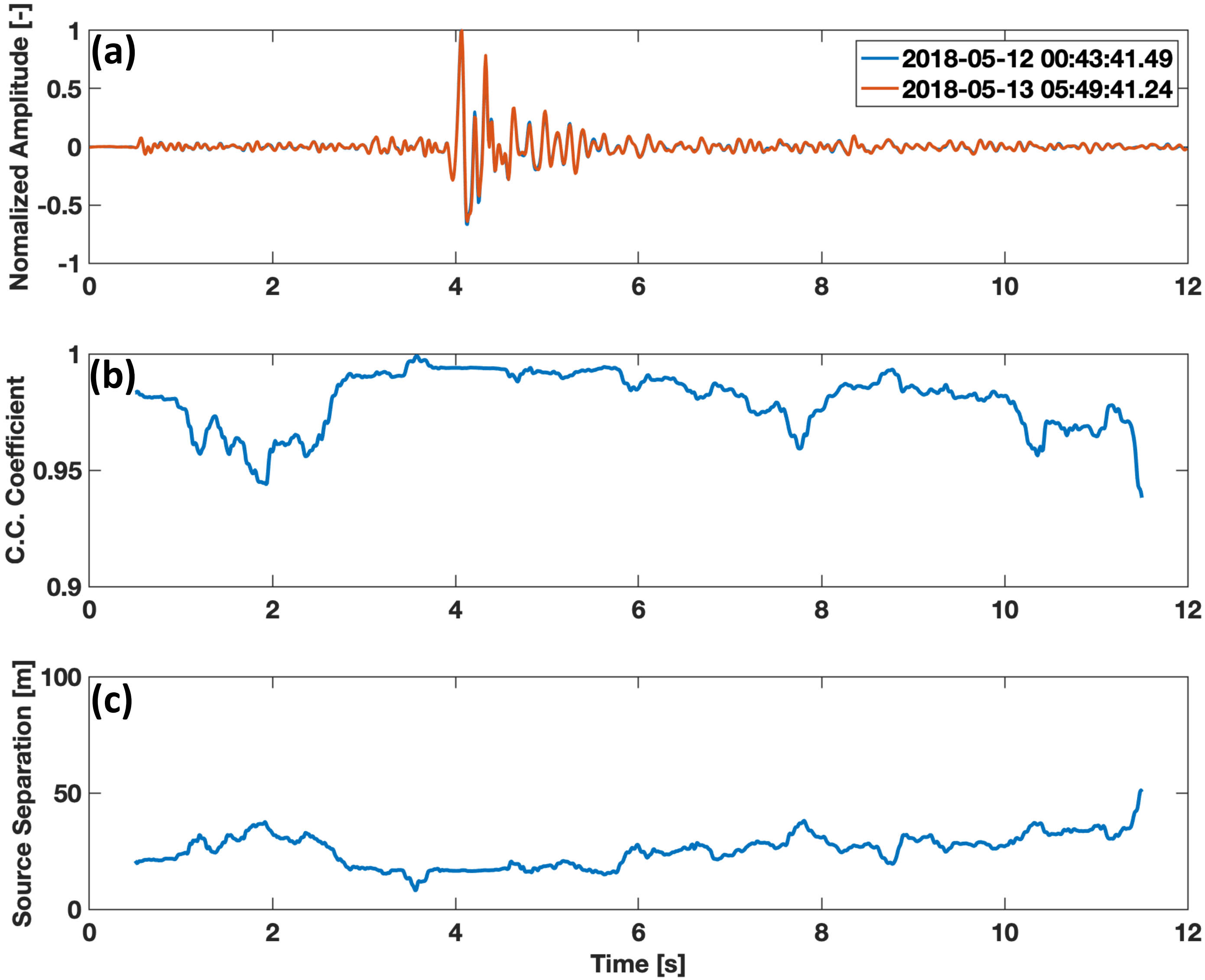
(a)
2018-05-12 00:43:41.49
2018-05-13 05:49:41.24
Nomalized Amplitude [-]
(b)
C.C. Coefficient
(c)
Source Separation [m]
Time [s]

Figure 10. Example of repeating earthquakes. (a) Red line shows event occurred on May 12, 2018 at 00:43:41.40 while blue line shows event occurred on May 13, 2018 at 05:49:41.24. Traces were filtered between 2 and 12 Hz using. (b) Temporal evolution of the cross-correlation coefficient in a 1.0 s long windows. (c) Source separation between events calculated from expression (53) of (Snieder & Vrijlandt, 2005).

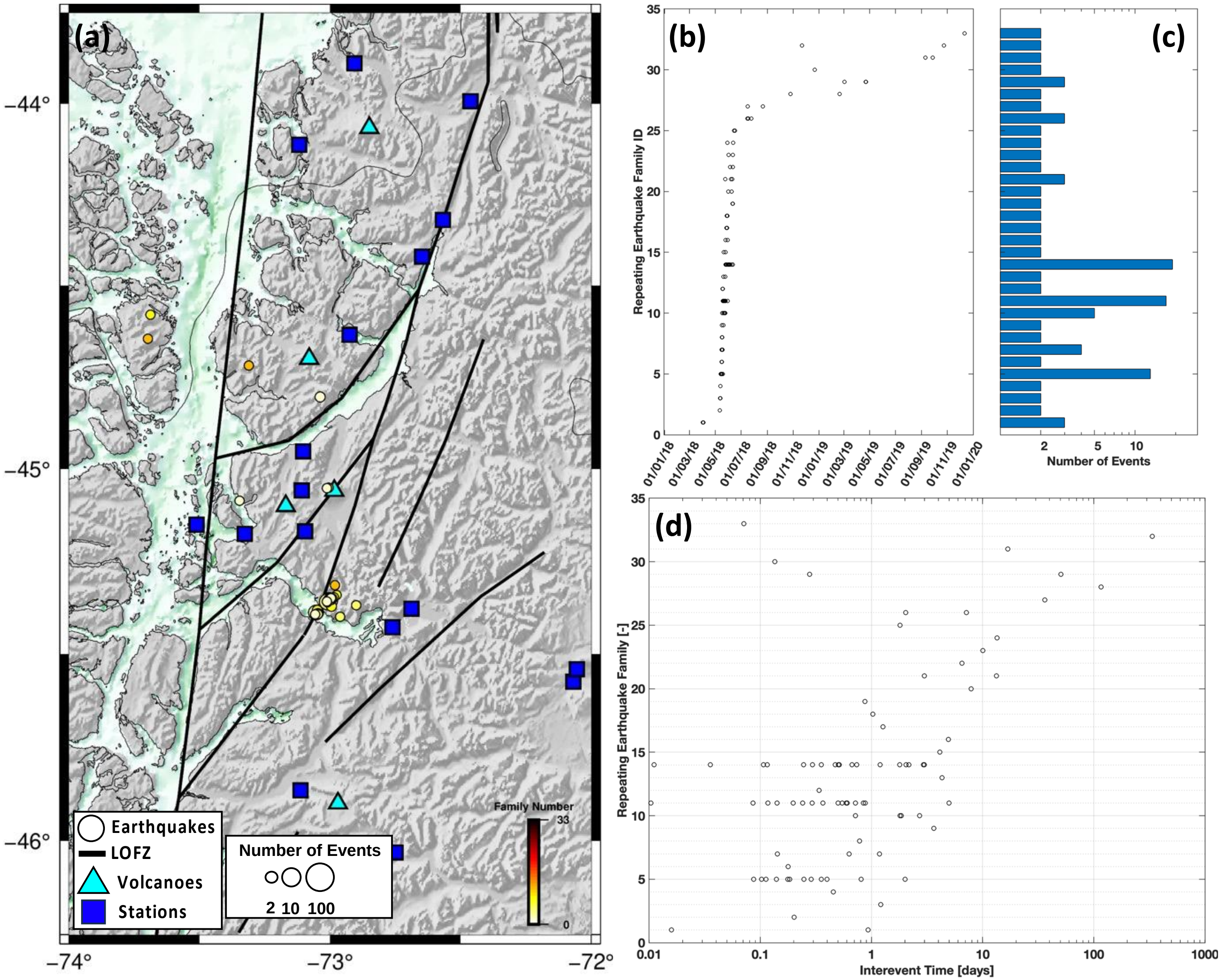

(a)
(b)
(c)
(d)
-44°
-45°
-46°
-74°
-73°
-72°
Earthquakes
LOFZ
Volcanoes
Stations
Number of Events
2 10 100
Family Number
33
0
Repeating Earthquake Family ID
01/01/18
01/03/18
01/05/18
01/07/18
01/09/18
01/11/18
01/01/19
01/03/19
01/05/19
01/07/19
01/09/19
01/11/19
01/01/20
Number of Events
Repeating Earthquake Family [-]
Interevent Time [days]

Figure 11. Families of repeating earthquakes. (a) Circles show the spatial distribution of the families while the color indicates the numbering of each family, and the size is proportional to the number of events that make up each family (b) Temporal distribution of the events of each family (d) Interevent time between subsequent events in each family.

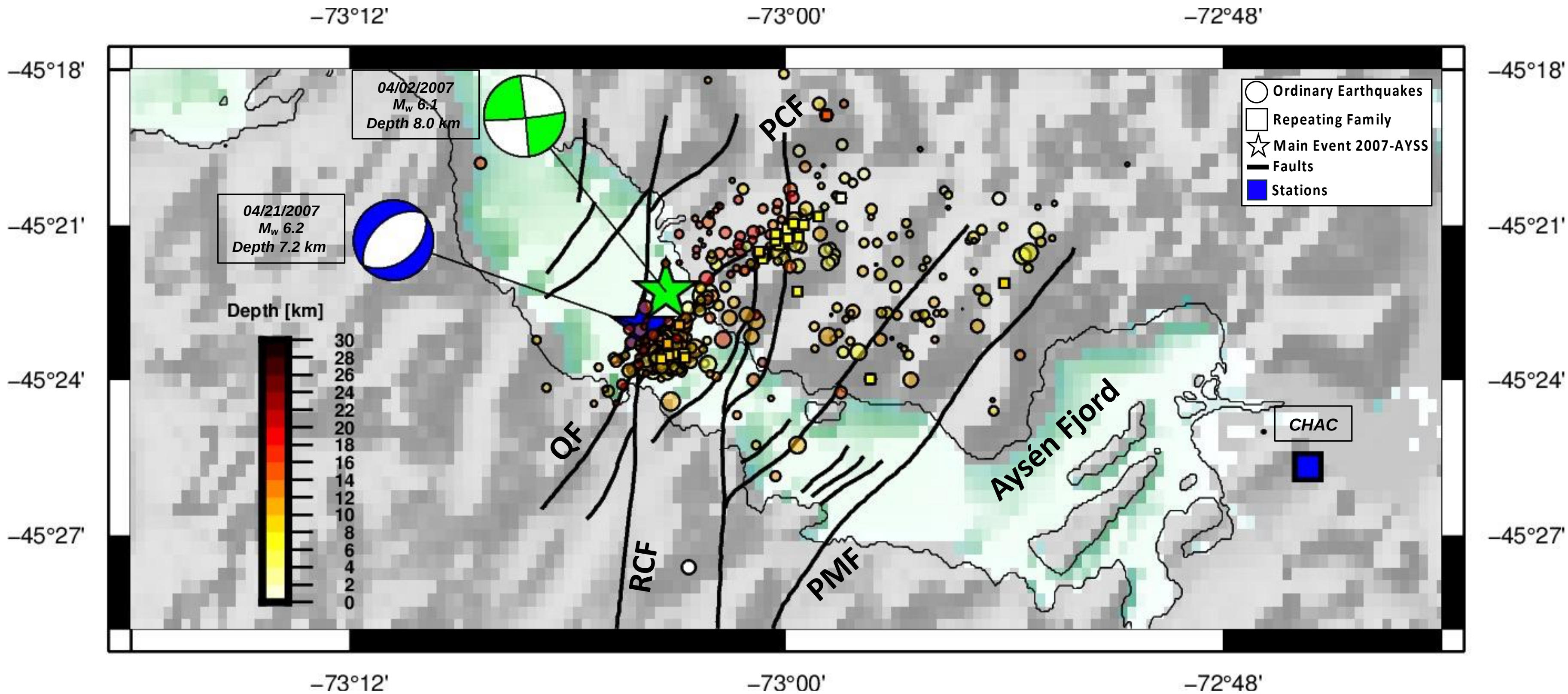

Figure 12. The 2018 Aysén Seismic Sequence. Circles and squares represent the spatial distribution of ordinary earthquakes detected in the initial catalog and families of repeating events, respectively. The size of the symbols is proportional to their local magnitude. Stars show the main events of the 2007 Aysén seismic sequence (2007-AYSS) according to (Agurto et al., 2012). Faults are from (Villalobos et al., 2020), QF (Quitralco Fault), RCF (Rio Cuervo Fault), PCF (Punta Cola Fault) and PMF (Punta Mano Fault).

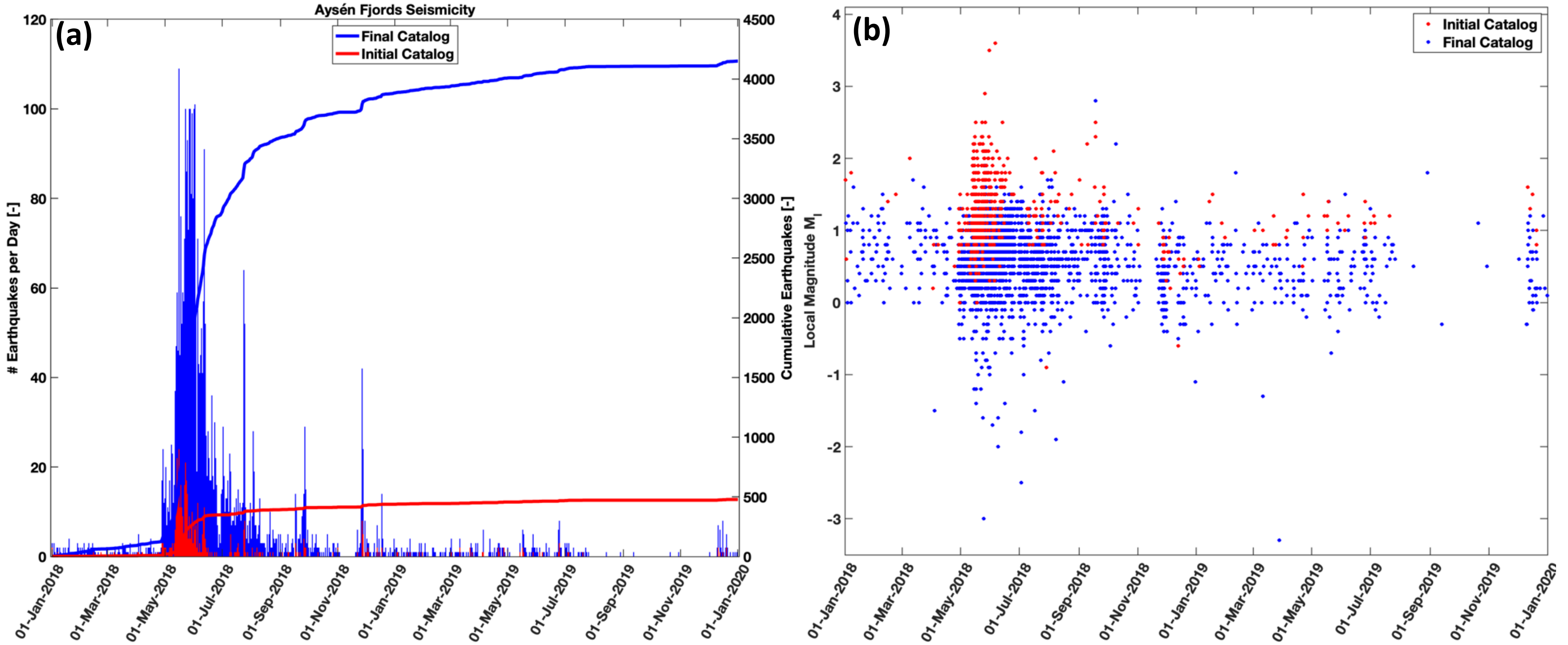

Figure 13. Seismicity in the Aysén Fjords between 2018 and 2019. (a) Number of earthquakes detected per day according to the final catalog (blue bars) and initial catalog (red bars). (b) Temporal distribution of local magnitudes according to initial (red dots) and final catalog (blue dots).

4 Resumen y Conclusiones Particulares

El objetivo de la presente investigación fue la búsqueda, localización y caracterización de señales sísmicas lentas en el margen chileno. La búsqueda de estas señales se realizó en datos recopilados por redes sismológicas desplegadas en la zona norte, centro-sur y sur de Chile. Las redes utilizadas se detallan a continuación:

1) En la zona sur se analizaron dos redes. La primera compuesta por cinco estaciones de periodo corto (1s) desplegadas en el fondo del mar (OBS) bajo el punto triple chileno. Esta red registró de forma continua entre los meses de marzo y octubre del 2009. La segunda red, corresponde a estaciones sismológicas desplegadas por el OVDAS y el CSN a lo largo del sistema de fallas Liquiñe-Ofqui. Esta red está compuesta por 17 estaciones banda ancha (120 s) y registraron de forma continua entre los años 2018 y 2019.
2) En la zona centro-sur se analizaron los datos recopilados por diez estaciones de periodo corto (1s) desplegadas en el fondo del mar frente a las costas de Pichilemu. Esta red registró de forma continua entre mayo del 2012 y marzo del 2013.
3) En la zona norte se analizaron los datos recopilados por diez estaciones banda ancha (120s) desplegadas en tierra en torno a la ciudad de Copiapó, las cuales registraron de forma continua entre junio del 2019 y enero del 2020.

Las redes sismológicas analizadas permitieron detectar por primera vez la ocurrencia de señales sísmicas lentas superficiales en el margen chileno, así como también la ocurrencia de terremotos repetitivos en el sistema de fallas Liquiñe-Ofqui. A continuación, se presentan las conclusiones particulares obtenidas de cada investigación:

4.1 Shallow Nonvolcanic Tremor Activity and Potential Repeating Earthquakes in the Chile Triple Junction: Seismic Evidence of the Subduction of the Active Nazca–Antarctic Spreading Center (Sáez et al., 2019).

En esta investigación estudiamos las manifestaciones sísmicas de tipo lenta y ordinaria que genera la subducción del Ridge de Chile bajo la placa sudamericana. En la investigación se muestra por primera vez la ocurrencia de tremores tectónicos superficiales en el margen chileno. Estas señales están caracterizadas por un contenido de frecuencia entre 2-8 [Hz] y un carácter no impulsivo. Propiedades similares han sido identificados en otros ambientes tectónicos. Durante el periodo analizado, se identificaron tremores tectónicos por períodos de tiempo superiores a 1 día. Utilizando la técnica S-P fue posible concluir que estas señales eran generadas por una fuente ubicada a un tiempo $t_{s\text{-}p}$ (diferencia entre el tiempo de llegada de la onda S y onda P) de aproximadamente 2 segundos. Por otro lado, al analizar la sismicidad ordinaria pudimos identificar terremotos ordinarios y repetitivos de pequeñas amplitudes con tiempos $t_{s\text{-}p} \sim 2$ s. A partir de estas observaciones, concluimos que existe una zona bajo el punto triple chileno capaz de romper de forma frágil (generando sismicidad ordinaria) y dúctil (generando tremores y terremotos repetitivos). Esta zona sería el prisma de acreción el cual podría tener un comportamiento sísmico dual (frágil y dúctil) debido a la presencia de fluidos.

4.2 Post-seismic response of the outer accretionary prism after the 2010 Maule earthquake, Chile (Tréhu et al., 2019).

En esta investigación se muestra como estudiar la respuesta dinámica que se genera en el prisma de acreción luego de un gran terremoto como el del Maule 2010 M_w 8.8. Para estudiar el comportamiento sísmico del prisma se analizó la sismicidad ordinaria que ocurre a menos de 125 km del arreglo y se buscó evidencias de posibles deslizamientos asísmicos. La investigación muestra que la mayor parte de la sismicidad ocurre cerca del límite entre el prisma de acreción activo y el basamento continental o en la elevación exterior hacia la fosa. La sismicidad detectada generalmesnte está acompañada de T-Phase, lo anterior dificultó la detección de tremores tectónicos, debido a que ambas señales comparten el mismo contenido de frecuencia y poseen formas no impulsivas similares. A pesar de lo anterior, el día 16 de diciembre se detectó una señal que cumple con los criterios para ser clasificada como tremor tectónico (velocidad de propagación cercana a los 3.5 km/s). Las observaciones sísmicas desarrolladas junto con las detecciones de eventos transientes permiten concluir que la respuesta post-sísmica del prisma de acreción está controlada por deformaciones sísmicas y asísmicas.

4.3 Along-Dip Segmentation of the Slip Behavior and Rheology of the Copiapó Ridge Subducted in North-Central Chile (Pastén-Araya et al., 2022)

En esta investigación se muestra como la subducción del ridge de Copiapó controla el comportamiento sísmico en la región de Atacama. Para dicho propósito se desarrolla un catálogo sísmico detallado que incluye el picado de múltiples fases S y P, las cuales, a su vez, son utilizadas para la construcción de un modelo tomográfico 3D de la zona. Adicionalmente, se identifica la ocurrencia de eventos repetitivos y tremores tectónicos. A partir de la distribución espacial de las distintas manifestaciones sísmicas y su correlación con los modelos tomográficos, la investigación concluye que la subducción del ridge induce una segmentación de la sismicidad en profundidad. En particular, se propone la presencia de una zona superficial “bloqueada” (50-65 km de profundidad) y caracterizada por razones de Vp/Vs elevadas. En esta zona se desarrollan las manifestaciones ordinarias y terremotos repetitivos. Entre los 65 y 85 km de profundidad se propone la presencia de una zona de transición con valores intermedios de V_p/V_s. En esta zona se genera sismicidad ordinaria de tipo intraplaca y se identifica la presencia de tremores tectónicos. Finalmente, entre 80 y 100 km de profundidad se propone la presencia de una zona asísmica, caracterizada por valores intermedios de V_p/V_s y en donde se desarrollan deslizamientos lentos.

A pesar de que la investigación propone la presencia de tremores tectónicos, las velocidades de propagación de estas señales (~2.0 km/s) no corresponden a las esperadas (~3.5 km/s). Por otro lado, se descarta que las señales sean T-Phase, debido a que estas ondas se atenúan fuertemente al entrar el contacto con el continente y su velocidad de propagación es cercana a los 1.45 km/s (Sáez & Ruiz, 2018). Por lo tanto, estas señales deberán ser estudiadas cuidadosamente para comprender su origen.

4.4 Revealing the seismic behavior of the southern portion of the Liquiñe-Ofqui fault zone (Sáez et al., 2024 en preparación).

La investigación se centra en estudiar las manifestaciones sísmicas que se generan en la porción sur del sistema de fallas Liquiñe-Ofqui (-44°S y -46°S). En la primera etapa del estudio se desarrolló una metodología de detección automática para identificar terremotos locales (t_{s-p}<12 s) los cuales posteriormente fueron localizados mediante un proceso de picado manual. Este catálogo inicial fue utilizado para generar plantillas de terremotos, las cuales fueron utilizadas para extender el catálogo inicial, aplicando para ello la metodología de template matching. En total se identificaron más de 7200 terremotos, los cuales poseen magnitudes locales inferiores a 3.6 y ocurren a profundidades menores a 30 km. La distribución espacial y temporal de la sismicidad demuestra que el sistema de fallas liquiñe-ofqui es la principal fuente de sismicidad en la zona. En un segundo orden se identificaron eventos relacionados con la actividad volcánica de la zona, así como también, terremotos relacionados con la subducción de la placa de Nazca bajo Sudamerica. Estos últimos caracterizados por profundidades mayores a 30 km.

Los resultados del template matching fueron utilizados para detectar familias de eventos similares, los cuales comparten ubicaciones y mecanismos focales similares, aunque no necesariamente representan la ruptura del mismo parche sísmico (evento repetitivo). Estas familias representan más del 15% de la sismicidad total detectada, demostrando que una fracción importante de la actividad sísmica tiende a agruparse en tiempo y espacio.

Uno de los hallazgos más importantes de la investigación fue la identificación de un enjambre sísmico en la misma zona donde tuvo lugar la secuencia sísmica de Aysén en el año 2007. Este enjambre, nombrado secuencia sísmica de Aysén 2018, estuvo caracterizado por la ocurrencia de más de 3000 terremotos entre los meses de mayo y julio del 2018, los cuales presentaron magnitudes menores a M_l 3.6 y profundidades inferiores a 25 km. Al evaluar la distribución temporal de la sismicidad se concluye que las fallas Punta Cola, Rio Cuervo y Quitralco fueron las responsables de la ocurrencia del enjambre sísmico. Adicionalmente, durante esta secuencia se identificaron la ocurrencia de terremotos repetitivos con tiempos de recurrencia menores a 10 días (actividad tipo burst).

Al evaluar la evolución temporal y espacial de la sismicidad es posible identificar que el enjambre estuvo modulado por un proceso difusivo, lo que sumado a la presencia de terremotos repetitivos de tipo burst permite concluir que la presencia de fluidos es el mecanismo que gatilla el enjambre.

A partir de las observaciones desarrolladas durante esta investigación se concluye que el sistema de fallas Liquiñe-Ofqui presenta varias ramas sísmicamente activas, capaces de generar una variedad de señales sísmicas de tipo ordinaria (terremotos ordinarios de pequeña y gran magnitud) y ordinaria-lenta (terremotos repetitivos y enjambres sísmicos).

5 Conclusiones Generales

A continuación, se listan las conclusiones generales obtenidas a partir de la investigación desarrollada y los antecedentes disponibles a la fecha:

- Las últimas observaciones sismológicas, nos han permitido entender que la liberación de la energía sísmica en Chile es un proceso complejo, que puede ocurrir a través de terremotos ordinarios, lentos o una combinación de estos.

- A la fecha, se han detectado manifestaciones geodésicas (Long and Short-Term Slow Slip), señales sísmicas lentas (L.F.E y tremores tectónicos), y ordinarias-lentas (enjambres y terremotos repetitivos) tanto en la parte superficial como profunda del contacto. Adicionalmente, se detectó por primera vez señales ordinarias-lentas en un sistema de falla superficial (LOFZ). En la Figura 5-1 se presenta un resumen con las manifestaciones de tipo lenta detectadas en el margen chileno hasta el año 2024.

- Las características de las señales sísmicas lentas chilenas son similares a las observadas en otras zonas del mundo. En particular, los tremores tectónicos superficiales detectados, son ondas de tipo no-impulsiva, de duración promedio de 150 [s] y ricas en un contenido de frecuencia entre 2-8 [Hz].

- Dos observaciones pertenecientes a la familia de terremotos lentos aún no han sido detectadas en el margen chileno: terremotos de muy baja frecuencia (VLFE) y señales geodésicas acompañadas de señales sísmicas lentas (Episodic Tremor and Slip).

- Las observaciones realizadas en el margen chileno muestran que la presencia de fluidos es un factor de primer orden para la generación señales sísmicas lentas. Las fuentes aportantes de estos fluidos dependerá de la zona donde se desarrolle la manifestación lenta. En el caso de señales lentas asociadas a la parte superficial del contacto entre placas, la deshidratación de los sedimentos y minerales subductados forman parte de las fuentes aportantes de fluidos, mientras que, para la zona profunda, la presencia de estratos saturados de baja velocidad sobre la placa subductante y reacciones metamórficas de deshidratación son las principales fuentes de fluido. En el caso del sistema de fallas Liquiñe-Ofqui, la presencia de fuentes hidrotermales y/o la actividad volcánica de la zona son la principal fuente de fluidos. Por otro lado, rasgos geomorfológicos que faciliten el movimiento de fluidos o alteren las propiedades friccionantes de los materiales (ej: subducción de ridge, montes submarinos, etc) favorecen la generación de T.L. en profundidad.

- En la zona norte y centro de Chile, terremotos lentos han sido detectados previo a la ruptura de un gran terremoto, mientras que, en la zona sur, señales sísmicas de tipo lenta se detectan de forma periódica sin la ocurrencia de un terremoto principal.

- Es de esperar que la densificación de redes sismológicas a lo largo del territorio nacional y el aumento de los periodos observacionales permita detectar otras zonas del país donde se desarrollen terremotos lentos y con ello mejorar nuestra compresión sobre estas señales.

- Queda mucho por entender, el estudio de los terremotos lentos debe ser una prioridad del país, debido a su relación con la ocurrencia de mega terremotos. Los esfuerzos se deben centrar en generar políticas que permitan mejorar las redes sismológicas y geodésicas a lo largo del país.

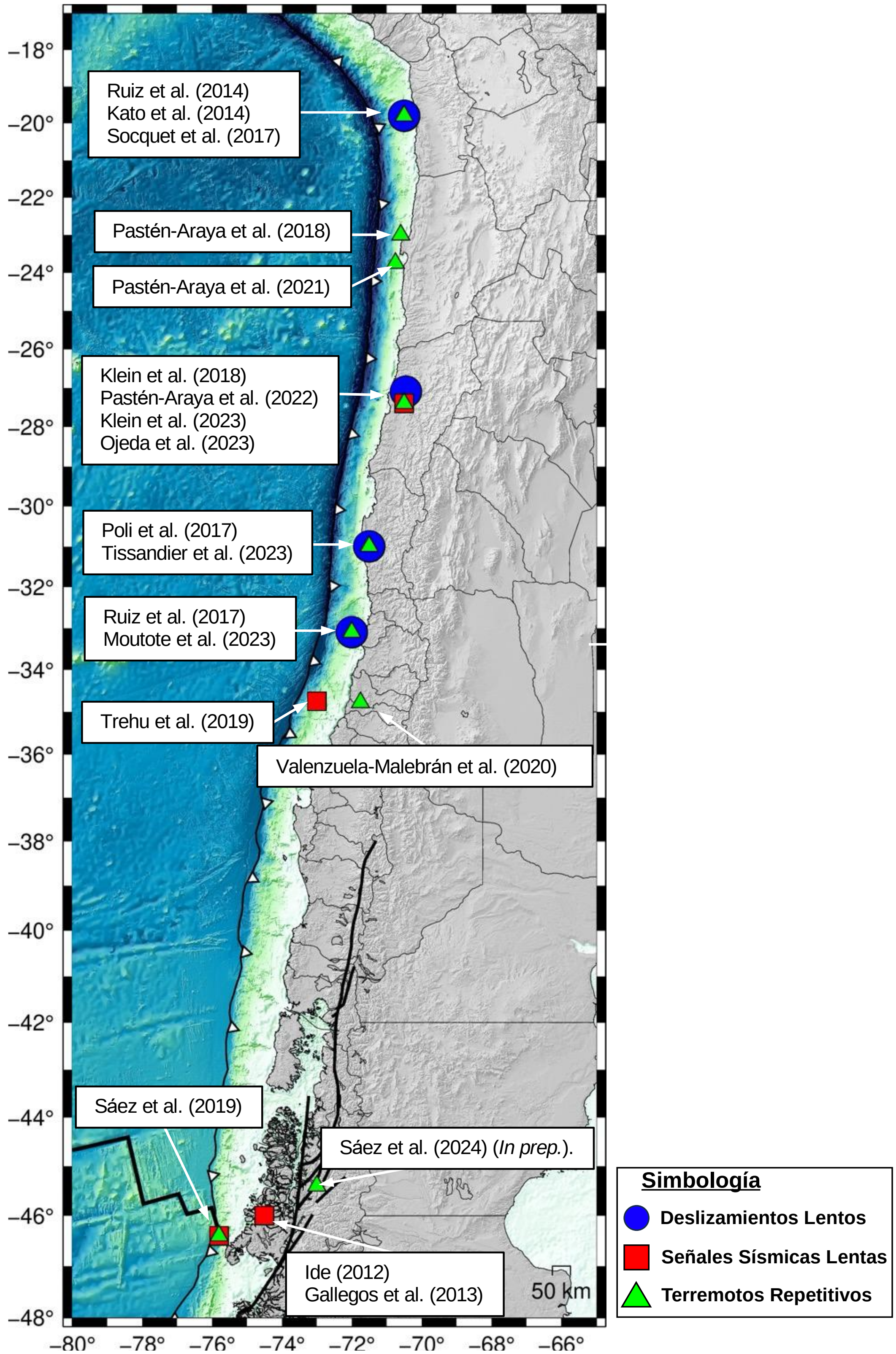

Figura 5-1: Resumen manifestaciones de terremotos lentos detectados en el margen chileno al año 2024.

6 Recomendaciones

Si bien el trabajo realizado en la presente investigación supone un avance en la detección y estudio de señales sísmicas lentas, tanto superficiales como profundas, en el margen chileno, existen diversos tópicos que podrían ser abordados por trabajos futuros para comprender de mejor manera cómo se desarrollan estas manifestaciones y cómo se relacionan con la ocurrencia de terremotos ordinarios de gran magnitud. A continuación, se presentan una serie de recomendaciones:

- Instalación de redes sismológicas densas compuestas por estaciones banda ancha y estaciones GPS en sitios de interés a nivel nacional. En este sentido, se debería priorizar aquellas zonas del país donde se han inidentificado previamente algún tipo de manifestación sísmica lenta. En este punto, es importante enfatizar la necesidad de establecer redes sismológicas que permitan monitorear periodos extensos de tiempo (mayores a 10 años), y con ello tener la posibilidad de detectar deslizamientos lentos de corta y larga duración junto con la ocurrencia de algún terremoto ordinario de gran magnitud.

- La relación entre las distintas manifestaciones sísmicas de tipo lenta es un tema sin dilucidar a nivel nacional. En otros ambientes subductivos a nivel mundial se ha observado de formas clara y recurrente, una correlación temporal y espacial entre los distintos tipos de señales. En el caso de Chile, aún no ha sido posible observar directamente la ocurrencia de un deslizamiento lento con alguna señal sísmica de tipo lenta. Por lo tanto, se recomienda, densificar las estaciones geodésicas disponibles en la zona sur del margen chileno, donde se han identificado señales sísmicas de tipo lenta pero no así la ocurrencia de deslizamientos lentos. Por otro lado, dada la alta tasa de sismicidad presente en la zona norte del país, no ha sido posible identificar la ocurrencia de señales sísmicas lentas, pero sí, deslizamientos lentos de larga y corta duración. En este sentido, los trabajos futuros deberían estar enfocados en estudiar zonas como la región de Atacama, donde ya se han identificados deslizamientos lentos cada 5 años. En dichas zonas, se recomienda analizar de forma detallada la sismicidad ordinaria que ocurre en periodos donde se identifiquen deslizamientos lentos, además de buscar manifestaciones sísmicas lentas. Para la anterior, resulta crucial el uso de redes densas compuestas por instrumentos banda ancha. El desarrollo de metodología de aprendizaje automático que permitan discriminar sismicidad ordinaria respecto de otros tipos de señales también debería ser unos de los tópicos a desarrollar en la zona norte de Chile.

- La investigación realizada en el presente trabajo expuso por primera vez la ocurrencia de señales sísmicas lentas (tremores tectónicos) y ordinarias de tipo lenta (potenciales terremotos repetitivos) en la parte superficial del contacto entre placas. A pesar de lo anterior, señales asociadas a terremotos de baja (LFE) y muy baja frecuencia (VLF) en esta parte del contacto aún no han sido detectadas. Es por ello, que se recomienda la búsqueda de este tipo de señales tanto en la zona norte como sur del margen chileno. En este sentido, los datos recopilados por una red de sensores OBS desplegados sobre el punto triple chileno entre enero del año 2019 y 2021 (A. Ito et al., 2023) son una oportunidad única para estudiar este tipo de manifestaciones y comprender cuál es su relación.

- Si bien el trabajo realizado propone que el prisma de acreción es capaz de romper de manera frágil (generando terremotos ordinarios) y dúctil (generando tremores tectónicos y terremotos repetitivos), se deben desarrollar estudios geológicos y geofísicos que permitan validar esta observación. En particular, el desarrollo de tomografías sísmicas y perfiles de reflexión sobre el punto triple permitirán dilucidar los factores que controlan este comportamiento bimodal y el rol que juegan los fluidos. En este sentido, un análisis detallado de la evolución temporal y espacial de la sismicidad ordinaria y lenta permitirán constreñir de mejor manera la relación que existe entre ambos tipos de señales y comprender si son generadas por una misma fuente. Para finalizar este punto, se recomienda el desarrollo de modelos locales que permitan comprender la variación de las mareas sobre el punto triple y junto con ello, estudiar si existe una relación entre estas variaciones y la generación de sismicidad ordinaria y lenta en la zona.

- En la zona sur, los tremores tectónicos han sido identificados entre los -45°S y -46°S. En esta zona se recomienda utilizar las redes permanentes desplegadas por el CSN y el OVDAS para extender hacia el norte la búsqueda de estas señales. Adicionalmente, se recomienda utilizar estas redes compuestas por instrumentos banda ancha para la búsqueda de LFE y VLFE. Por último, se recomienda estudiar la sismicidad ordinaria asociada a la subducción de la placa de Nazca bajo Sudamérica y comprender la relación espacial y temporal que existe con las señales sísmicas de tipo lenta identificadas en la zona.

- En la Liquiñe-Ofqui se recomienda como primer punto la instalación de redes sísmicas densas, multiparamétricas y por un largo periodo de tiempo. Lo anterior, con el propósito de detectar y localizar con gran detalle la sismicidad generada a lo largo del sistema de fallas, y con ello poder identificar de manera clara cuales son las ramas de este sistema que se encuentran sísmicamente activas y podrían presentar un riesgo para los asentamientos urbanos ubicados en sus alrededores. En este sentido, se hace urgente la necesidad de monitorear de manera permanente el sector donde se desarrolló la secuencia sísmica de Aysén 2007 y Aysén 2018.

- Este trabajo permitió detectar por primera vez la ocurrencia de terremotos repetitivos en el sistema de fallas Liquiñe-Ofqui. En general, los tiempos de recurrencia detectados para estos eventos es inferior a 10 días y estarían controlados por la presencia de fluidos, los cuales facilitarían este tipo de rupturas. Se recomienda que investigaciones futuras se centren en la búsqueda de terremotos repetitivos en otras zonas del sistema de fallas y analicen periodos de tiempos superiores a 10 años. Lo anterior, permitirá comprender y caracterizar las zonas del sistema de fallas que liberan el estress acumulado en forma asísmica además de poder estimar tasas de deslizamiento lento (creep). Estos estudios tendrán que ser complementados con campañas geológicas y geofísicas locales que permitan comprender las diferencias que existen entre las zonas que liberan la energía de forma asísmica versus aquellas que rompen de manera ordinaria.

- Finalmente, se recomienda la búsqueda de manifestaciones sísmicas lentas (tremores tectónicos, LFE y VLFE) en el sistema de falla Liquiñe-Ofqui.

7 Bibliografía

Agurto, H., Rietbrock, A., Barrientos, S., Bataille, K., & Legrand, D. (2012). Seismo-tectonic structure of the Aysén Region, Southern Chile, inferred from the 2007 M w= 6.2 Aysén earthquake sequence. *Geophysical Journal International*, *190*(1), 116–130. https://doi.org/10.1111/j.1365-246X.2012.05507.x.

Aki, K. (1967). Scaling law of seismic spectrum. *Journal of Geophysical Research*, *72*(4), 1217–1231. https://doi.org/10.1029/JZ072i004p01217.

Aki, K. (1972). Scaling law of earthquake source time-function. *Geophysical Journal International*, *31*(1–3), 3–25. https://doi.org/10.1111/j.1365-246X.1972.tb02356.x

Audet, P., & Kim, Y. H. (2016). Teleseismic constraints on the geological environment of deep episodic slow earthquakes in subduction zone forearcs: A review. In *Tectonophysics* (Vol. 670, pp. 1–15). Elsevier. https://doi.org/10.1016/j.tecto.2016.01.005.

Behr, W. M., & Bürgmann, R. (2021). What's down there? The structures, materials and environment of deep-seated slow slip and tremor. In *Philosophical Transactions of the Royal Society A: Mathematical, Physical and Engineering Sciences* (Vol. 379, Issue 2193). Royal Society Publishing. https://doi.org/10.1098/rsta.2020.0218.

Beroza, G. C., & Ide, S. (2011). Slow earthquakes and nonvolcanic tremor. *Annual Review of Earth and Planetary Sciences*, *39*, 271–296. https://doi.org/10.1146/annurev-earth-040809-152531.

Brodsky, E. E., & Mori, J. (2007). Creep events slip less than ordinary earthquakes. *Geophysical Research Letters*, *34*(16). https://doi.org/10.1029/2007GL030917.

Brown, J. R., Beroza, G. C., & Shelly, D. R. (2008). An autocorrelation method to detect low frequency earthquakes within tremor. *Geophysical Research Letters*, *35*(16). https://doi.org/10.1029/2008GL034560.

Brudzinski, M. R., Schlanser, K. M., Kelly, N. J., DeMets, C., Grand, S. P., Márquez-Azúa, B., & Cabral-Cano, E. (2016). Tectonic tremor and slow slip along the northwestern section of the Mexico subduction zone. *Earth and Planetary Science Letters*, *454*, 259–271. https://doi.org/10.1016/j.epsl.2016.08.004.

Bürgmann, R. (2018). The geophysics, geology and mechanics of slow fault slip. *Earth and Planetary Science Letters*, *495*, 112–134. https://doi.org/10.1016/j.epsl.2018.04.062.

Caballero, E., Chounet, A., Duputel, Z., Jara, J., Twardzik, C., & Jolivet, R. (2021). Seismic and Aseismic Fault Slip During the Initiation Phase of the 2017 MW = 6.9 Valparaíso Earthquake. *Geophysical Research Letters*, *48*(6). https://doi.org/10.1029/2020GL091916.

Carrasco, S., Ruiz, S., & Sáez, M. (2019). Earthquakes felt in the Juan Fernandez Islands: Where are they coming from? *Seismological Research Letters*, *91*(1), 262–271. https://doi.org/10.1785/0220190151.

Chao, K., Peng, Z., Frank, W. B., Prieto, G. A., & Obara, K. (2019). Isolated triggered tremor spots in South America and implications for global tremor activity. *Seismological Research Letters*, *90*(5), 1726–1739. https://doi.org/10.1785/0220190009.

Chao, K., Peng, Z., Wu, C., Tang, C. C., & Lin, C. H. (2012). Remote triggering of non-volcanic tremor around Taiwan. *Geophysical Journal International*, *188*(1), 301–324. https://doi.org/10.1111/j.1365-246X.2011.05261.x.

Dragert, H., Wang, K., & James, T. S. (2001). A silent slip event on the deeper Cascadia subduction interface. *Science*, *292*(5521), 1525–1528. https://doi.org/10.1126/science.1060152.

Fukuda, J. (2018). Variability of the Space-Time Evolution of Slow Slip Events Off the Boso Peninsula, Central Japan, From 1996 to 2014. *Journal of Geophysical Research: Solid Earth*, *123*(1), 732–760. https://doi.org/10.1002/2017JB014709.

Gallego, A., Russo, R. M., Comte, D., Mocanu, V., Murdie, R. E., & Vandecar, J. C. (2013). Tidal modulation of continuous nonvolcanic seismic tremor in the Chile triple junction region. *Geochemistry, Geophysics, Geosystems*, *14*(4), 851–863. https://doi.org/10.1002/ggge.20091.

Hill, D. P. (1977). A model for earthquake swarms. *Journal of Geophysical Research*, *82*(8), 1347–1352. https://doi.org/10.1029/JB082i008p01347.

Hirose, H., & Obara, K. (2005). Repeating short-and long-term slow slip events with deep tremor activity around the Bungo channel region, southwest Japan. In *Earth Planets Space* (Vol. 57). https://doi.org/10.1186/BF03351875.

Holtkamp, S. G., & Brudzinski, M. R. (2011). Earthquake swarms in circum-Pacific subduction zones. *Earth and Planetary Science Letters*, *305*(1–2), 215–225. https://doi.org/10.1016/j.epsl.2011.03.004.

Hutchison, A. A., & Ghosh, A. (2016). Very low frequency earthquakes spatiotemporally asynchronous with strong tremor during the 2014 episodic tremor and slip event in Cascadia. *Geophysical Research Letters*, *43*(13), 6876–6882. https://doi.org/10.1002/2016GL069750.

Ide, S. (2010). Striations, duration, migration and tidal response in deep tremor. *Nature*, *466*(7304), 356–359. https://doi.org/10.1038/nature09251.

Ide, S. (2012). Variety and spatial heterogeneity of tectonic tremor worldwide. *Journal of Geophysical Research: Solid Earth*, *117*(3). https://doi.org/10.1029/2011JB008840.

Ide, S. (2014). Modeling fast and slow earthquakes at various scales. In *Proceedings of the Japan Academy Series B: Physical and Biological Sciences* (Vol. 90, Issue 8, pp. 259–277). Japan Academy. https://doi.org/10.2183/pjab.90.259.

Ide, S., Beroza, G. C., Shelly, D. R., & Uchide, T. (2007). A scaling law for slow earthquakes. *Nature*, *447*(7140), 76–79. https://doi.org/10.1038/nature05780.

Ide, S., Shelly, D. R., & Beroza, G. C. (2007). Mechanism of deep low frequency earthquakes: Further evidence that deep non-volcanic tremor is generated by shear slip on the plate interface. *Geophysical Research Letters*, *34*(3). https://doi.org/10.1029/2006GL028890.

Ishihara, Y. (2003). Major existence of very low frequency earthquakes in background seismicity along subduction zone of south-western Japan. *AGU Fall Meeting Abstracts*, *2003*, S41C-0107.

Ito, A., Shiobara, H., Miller, M., Sugioka, H., Ojeda, J., Tassara, C., Shinohara, M., Kinoshita, M., & Iwamori, H. (2023). Long-term array observation by ocean bottom seismometers at the Chile Triple Junction. *Journal of South American Earth Sciences*, *124*, 104285. https://doi.org/10.1016/j.jsames.2023.104285.

Ito, Y., Hino, R., Suzuki, S., & Kaneda, Y. (2015). Episodic tremor and slip near the Japan Trench prior to the 2011 Tohoku-Oki earthquake. *Geophysical Research Letters*, *42*(6), 1725–1731. https://doi.org/10.1002/2014GL062986.

Ito, Y., Obara, K., Shiomi, K., Sekine, S., & Hirose, H. (2007). Slow earthquakes coincident with episodic tremors and slow slip events. *Science*, *315*(5811), 503–506. https://doi.org/10.1126/science.1134454.

Kanamori, H., & Rivera, L. (2017). An Mw = 7.7 slow earthquake in 1960 near the Aysén Fjord region, Chile. *Geophysical Journal International*, *211*(1), 93–106. https://doi.org/10.1093/GJI/GGX292.

Kaneko, L., Ide, S., & Nakano, M. (2018). Slow Earthquakes in the Microseism Frequency Band (0.1–1.0 Hz) off Kii Peninsula, Japan. *Geophysical Research Letters*, *45*(6), 2618–2624. https://doi.org/10.1002/2017GL076773.

Katakami, S., Yamashita, Y., Yakihara, H., Shimizu, H., Ito, Y., & Ohta, K. (2017). Tidal Response in Shallow Tectonic Tremors. *Geophysical Research Letters*, *44*(19), 9699–9706. https://doi.org/10.1002/2017GL074060.

Kato, A., Fukuda, J., Kumazawa, T., & Nakagawa, S. (2016). Accelerated nucleation of the 2014 Iquique, Chile Mw 8.2 Earthquake. *Scientific Reports*, *6*. https://doi.org/10.1038/srep24792.

Kato, A., & Nakagawa, S. (2014). Multiple slow-slip events during a foreshock sequence of the 2014 Iquique, Chile Mw 8.1 earthquake. *Geophysical Research Letters*, *41*(15), 5420–5427. https://doi.org/10.1002/2014GL061138.

Kato, A., Obara, K., Igarashi, T., Tsuruoka, H., Nakagawa, S., & Hirata, N. (2012). Propagation of slow slip leading up to the 2011 M w 9.0 Tohoku-Oki earthquake. *Science*, *335*(6069), 705–708. https://doi.org/10.1126/science.1215141.

Katsumata, A., & Kamaya, N. (2003). Low-frequency continuous tremor around the Moho discontinuity away from volcanoes in the southwest Japan. *Geophysical Research Letters*, *30*(1), 20–21. https://doi.org/10.1029/2002GL015981

Khoshmanesh, M., Shirzaei, M., & Uchida, N. (2020). Deep slow-slip events promote seismicity in northeastern Japan megathrust. *Earth and Planetary Science Letters*, *540*. https://doi.org/10.1016/j.epsl.2020.116261.

Klein, E., Duputel, Z., Zigone, D., Vigny, C., Boy, J. P., Doubre, C., & Meneses, G. (2018). Deep Transient Slow Slip Detected by Survey GPS in the Region of Atacama, Chile. *Geophysical Research Letters*, *45*(22), 12,263-12,273. https://doi.org/10.1029/2018GL080613.

Klein, E., Vigny, C., Duputel, Z., Zigone, D., Rivera, L., Ruiz, S., & Potin, B. (2023). Return of the Atacama deep Slow Slip Event: The 5-year recurrence confirmed by continuous GPS. *Physics of the Earth and Planetary Interiors*, *334*. https://doi.org/10.1016/j.pepi.2022.106970.

Lay, T., & Bilek, S. (2007). 15. Anomalous Earthquake Ruptures at Shallow Depths on Subduction Zone Megathrusts. In *The seismogenic zone of subduction thrust faults* (pp. 476–511). Columbia University Press. https://doi.org/10.7312/dixo13866-015.

Lay, T., Kanamori, H., Ammon, C. J., Koper, K. D., Hutko, A. R., Ye, L., Yue, H., & Rushing, T. M. (2012). Depth-varying rupture properties of subduction zone megathrust faults. *Journal of Geophysical Research: Solid Earth*, *117*(4). https://doi.org/10.1029/2011JB009133.

Legrand, D., Barrientos, S., Bataille, K., Cembrano, J., & Pavez, A. (2011). The fluid-driven tectonic swarm of Aysen Fjord, Chile (2007) associated with two earthquakes (Mw=6.1 and Mw=6.2) within the Liquiñe-Ofqui Fault Zone. *Continental Shelf Research*, *31*(3–4), 154–161. https://doi.org/10.1016/j.csr.2010.05.008.

Masuda, K., Ide, S., Ohta, K., & Matsuzawa, T. (2020). Bridging the gap between low-frequency and very-low-frequency earthquakes. In *Earth, Planets and Space* (Vol. 72, Issue 1). Springer. https://doi.org/10.1186/s40623-020-01172-8.

Meng, L., Huang, H., Bürgmann, R., Ampuero, J. P., & Strader, A. (2015). Dual megathrust slip behaviors of the 2014 Iquique earthquake sequence. *Earth and Planetary Science Letters*, *411*, 177–187. https://doi.org/10.1016/j.epsl.2014.11.041.

Métois, M., Vigny, C., & Socquet, A. (2016). Interseismic Coupling, Megathrust Earthquakes and Seismic Swarms Along the Chilean Subduction Zone (38°–18°S). *Pure and Applied Geophysics*, *173*(5), 1431–1449. https://doi.org/10.1007/s00024-016-1280-5.

Mora, C., Comte, D., Russo, R., Gallego, A., & Mocanu, V. (2010). Aysén seismic swarm (January 2007) in southern Chile: Analysis using Joint Hypocenter Determination. *Journal of Seismology*, *14*(4), 683–691. https://doi.org/10.1007/s10950-010-9190-y.

Moreno, M., Rosenau, M., & Oncken, O. (2010). 2010 Maule earthquake slip correlates with pre-seismic locking of Andean subduction zone. *Nature*, *467*(7312), 198–202. https://doi.org/10.1038/nature09349.

Moutote, L., Itoh, Y., Lengliné, O., Duputel, Z., & Socquet, A. (2023). Evidence of a transient aseismic slip driving the 2017 Valparaiso earthquake sequence, from foreshocks to aftershocks. *Journal of Geophysical Research: Solid Earth*, *128*(9), e2023JB026603. https://doi.org/10.1029/2023JB026603

Müller, R. D., Sdrolias, M., Gaina, C., & Roest, W. R. (2008). Age, spreading rates, and spreading asymmetry of the world's ocean crust. *Geochemistry, Geophysics, Geosystems*, *9*(4). https://doi.org/10.1029/2007GC001743.

Nadeau, R. M., & Dolenc, D. (2005). Nonvolcanic tremors deep beneath the San Andreas Fault. *Science*, *307*(5708), 389. https://doi.org/10.1126/science.1107142.

Nishide, N., Hashimoto, T., Funasaki, J., Nakazawa, H., Oka, M., Ueno, H., Yamada, N., Sasakawa, I., Maeda, K., & Sugimoto, K. (2000). Nationwide activity of low-frequency earthquakes in the lower crust in Japan. *Abstr. Jpn. Earth and Planet. Sci. Joint Meeting*.

Nishikawa, T., Ide, S., & Nishimura, T. (2023). A review on slow earthquakes in the Japan Trench. In *Progress in Earth and Planetary Science* (Vol. 10, Issue 1). Springer Science and Business Media Deutschland GmbH. https://doi.org/10.1186/s40645-022-00528-w.

Nishikawa, T., Nishimura, T., & Okada, Y. (2021). Earthquake Swarm Detection Along the Hikurangi Trench, New Zealand: Insights Into the Relationship Between Seismicity and Slow Slip Events. *Journal of Geophysical Research: Solid Earth*, *126*(4). https://doi.org/10.1029/2020JB020618.

Obana, K., & Kodaira, S. (2009). Low-frequency tremors associated with reverse faults in a shallow accretionary prism. *Earth and Planetary Science Letters*, *287*(1–2), 168–174. https://doi.org/10.1016/j.epsl.2009.08.005.

Obara, K. (2002). Nonvolcanic deep tremor associated with subduction in southwest Japan. *Science*, *296*(5573), 1679–1681. https://doi.org/10.1126/science.1070378.

Obara, K. (2020). Characteristic activities of slow earthquakes in Japan. In *Proceedings of the Japan Academy Series B: Physical and Biological Sciences* (Vol. 96, Issue 7, pp. 297–315). Japan Academy. https://doi.org/10.2183/PJAB.96.022.

Obara, K., Hirose, H., Yamamizu, F., & Kasahara, K. (2004). Episodic slow slip events accompanied by non-volcanic tremors in southwest Japan subduction zone. *Geophysical Research Letters*, *31*(23), 1–4. https://doi.org/10.1029/2004GL020848.

Obara, K., & Ito, Y. (2005). Very low frequency earthquakes excited by the 2004 off the Kii peninsula earthquakes: A dynamic deformation process in the large accretionary prism. In *LETTER Earth Planets Space* (Vol. 57). https://doi.org/10.1186/BF03352570

Obara, K., & Kato, A. (2016). Connecting slow earthquakes to huge earthquakes. *Science*, *353*(6296), 253–257. https://doi.org/10.1126/science.aaf1512.

Ojeda, J., Morales-Yáñez, C., Ducret, G., Ruiz, S., Grandin, R., Doin, M. P., Vigny, C. & Nocquet, J. M. (2023). Seismic and aseismic slip during the 2006 Copiapó swarm in North-Central Chile. *Journal of South American Earth Sciences*, 123, 104198. https://doi.org/10.1016/j.jsames.2023.104198.

Pasten-Araya, F., Salazar, P., Ruiz, S., Rivera, E., Potin, B., Maksymowicz, A., ... & Shapiro, S. A. (2018). Fluids along the plate interface influencing the frictional regime of the Chilean subduction zone, northern Chile. *Geophysical Research Letters, 45(19), 10-378*. https://doi.org/10.1029/2018GL079283.

Pastén-Araya, F., Potin, B., Ruiz, S., Zerbst, L., Aden-Antoniów, F., Azúa, K., ... & Fuenzalida, A. (2021). Seismicity in the upper plate of the Northern Chilean offshore forearc: Evidence of splay fault south of the Mejillones Peninsula. *Tectonophysics, 800, 228706.* https://doi.org/10.1016/j.tecto.2020.228706

Pastén-Araya, F., Potin, B., Azúa, K., Sáez, M., Aden-Antoniów, F., Ruiz, S., Cabrera, L., Ampuero, J. P., Nocquet, J. M., Rivera, L., & Duputel, Z. (2022). Along-Dip Segmentation of the Slip Behavior and Rheology of the Copiapó Ridge Subducted in North-Central Chile. *Geophysical Research Letters*, *49*(4). https://doi.org/10.1029/2021GL095471.

Peacock, S. M. (2009). Thermal and metamorphic environment of subduction zone episodic tremor and slip. *Journal of Geophysical Research: Solid Earth*, *114*(B8). https://doi.org/10.1029/2008JB005978.

Peacock, S. M., Christensen, N. I., Bostock, M. G., & Audet, P. (2011). High pore pressures and porosity at 35 km depth in the Cascadia subduction zone. *Geology*, *39*(5), 471–474. https://doi.org/10.1130/G31649.1.

Peng, Z., & Chao, K. (2008). Non-volcanic tremor beneath the Central Range in Taiwan triggered by the 2001 Mw 7.8 Kunlun earthquake. *Geophysical Journal International*, *175*(2), 825–829. https://doi.org/10.1111/j.1365-246X.2008.03886.x.

Peng, Z., & Gomberg, J. (2010). An integrated perspective of the continuum between earthquakes and slow-slip phenomena. In *Nature Geoscience* (Vol. 3, Issue 9, pp. 599–607). https://doi.org/10.1038/ngeo940.

Perez-Silva, A., Kaneko, Y., Savage, M., Wallace, L., Li, D., & Williams, C. (2022). Segmentation of Shallow Slow Slip Events at the Hikurangi Subduction Zone Explained by Along-Strike Changes in Fault Geometry and Plate Convergence Rates. *Journal of Geophysical Research: Solid Earth*, *127*(1). https://doi.org/10.1029/2021JB022913.

Poli, P., Maksymowicz, A., & Ruiz, S. (2017). The Mw 8.3 Illapel earthquake (Chile): Preseismic and postseismic activity associated with hydrated slab structures. Geology, 45(3), 247-250. https://doi.org/10.1130/G38522.1

Plata-Martinez, R., Ide, S., Shinohara, M., Garcia, E. S., Mizuno, N., Dominguez, L. A., Taira, T., Yamashita, Y., Toh, A., Yamada, T., Real, J., Husker, A., Cruz-Atienza, V. M., & Ito, Y. (2021). Shallow slow earthquakes to decipher future catastrophic earthquakes in the Guerrero seismic gap. *Nature Communications*, *12*(1). https://doi.org/10.1038/s41467-021-24210-9.

Radiguet, M., Perfettini, H., Cotte, N., Gualandi, A., Valette, B., Kostoglodov, V., Lhomme, T., Walpersdorf, A., Cabral Cano, E., & Campillo, M. (2016). Triggering of the 2014 Mw 7.3 Papanoa earthquake by a slow slip event in Guerrero, Mexico. *Nature Geoscience*, *9*(11), 829–833. https://doi.org/10.1038/ngeo2817.

Rogers, G., & Dragert, H. (2003). Episodic tremor and slip on the Cascadia subduction zone: The chatter of silent slip. *Science*, *300*(5627), 1942–1943. https://doi.org/10.1126/science.1084783.

Romanet, P., & Ide, S. (2019). Ambient tectonic tremors in Manawatu, Cape Turnagain, Marlborough, and Puysegur, New Zealand. *Earth, Planets and Space*, *71*(1). https://doi.org/10.1186/s40623-019-1039-1.

Rousset, B., Campillo, M., Lasserre, C., Frank, W. B., Cotte, N., Walpersdorf, A., Socquet, A., & Kostoglodov, V. (2017). A geodetic matched filter search for slow slip with application to the Mexico subduction zone. *Journal of Geophysical Research: Solid Earth*, *122*(12), 10,498-10,514. https://doi.org/10.1002/2017JB014448.

Rousset, B., Fu, Y., Bartlow, N., & Bürgmann, R. (2019). Week-Long and Year-Long Slow Slip and Tectonic Tremor Episodes on the South Central Alaska Megathrust. *Journal of Geophysical Research: Solid Earth*, *124*(12), 13392–13403. https://doi.org/10.1029/2019JB018724.

Rubinstein, J. L., La Rocca, M., Vidale, J. E., Creager, K. C., & Wech, A. G. (2008). Tidal modulation of nonvolcanic tremor. *Science*, *319*(5860), 186–189. https://doi.org/10.1126/science.1150558.

Rubinstein, J. L., Shelly, D. R., & Ellsworth, W. L. (2010). Non-volcanic tremor: A window into the roots of fault zones. *New Frontiers in Integrated Solid Earth Sciences*, 287–314. https://doi.org/10.1007/978-90-481-2737-5_8.

Ruiz, S., Aden-Antoniow, F., Baez, J. C., Otarola, C., Potin, B., del Campo, F., Poli, P., Flores, C., Satriano, C., Leyton, F., Madariaga, R., & Bernard, P. (2017). Nucleation Phase and Dynamic Inversion of the Mw 6.9 Valparaíso 2017 Earthquake in Central Chile. *Geophysical Research Letters*, *44*(20), 10,290-10,297. https://doi.org/10.1002/2017GL075675.

Ruiz, S., & Madariaga, R. (2018). Historical and recent large megathrust earthquakes in Chile. In *Tectonophysics* (Vol. 733, pp. 37–56). Elsevier B.V. https://doi.org/10.1016/j.tecto.2018.01.015.

Ruiz, S., Metois, M., Fuenzalida, A., Ruiz, J., Leyton, F., Grandin, R., Vigny, C., Madariaga, R., & Campos, J. (2014). Intense foreshocks and a slow slip event preceded the 2014 Iquique Mw8.1 earthquake. *Science*, *6201*, 1165–1169. https://doi.org/10.1126/science.1256074.

Sáez, M., & Ruiz, S. (2018). Controls on the T Phase Energy Fluxes Recorded on Juan Fernandez Island by Continental Seismic Wave Paths and Nazca Bathymetry. *Geophysical Research Letters*, *45*(6), 2610–2617. https://doi.org/10.1002/2017GL076790.

Sáez, M., Ruiz, S., Ide, S., & Sugioka, H. (2019). Shallow nonvolcanic tremor activity and potential repeating earthquakes in the Chile triple junction: Seismic evidence of the subduction of the active Nazca–Antarctic spreading center. *Seismological Research Letters*, *90*(5), 1740–1747. https://doi.org/10.1785/0220180394.

Schwartz, S. Y., & Rokosky, J. M. (2007). Slow slip events and seismic tremor at circum-pacific subduction zones. In *Reviews of Geophysics* (Vol. 45, Issue 3). https://doi.org/10.1029/2006RG000208.

Shelly, D. R., Beroza, G. C., & Ide, S. (2007). Non-volcanic tremor and low-frequency earthquake swarms. *Nature*, *446*(7133), 305–307. https://doi.org/10.1038/nature05666.

Shelly, D. R., Beroza, G. C., Ide, S., & Nakamula, S. (2006). Low-frequency earthquakes in Shikoku, Japan, and their relationship to episodic tremor and slip. *Nature*, *442*(7099), 188–191. https://doi.org/10.1038/nature04931.

Socquet, A., Valdes, J. P., Jara, J., Cotton, F., Walpersdorf, A., Cotte, N., Specht, S., Ortega-Culaciati, F., Carrizo, D., & Norabuena, E. (2017). An 8 month slow slip event triggers progressive nucleation of the 2014 Chile megathrust. *Geophysical Research Letters*, *44*(9), 4046–4053. https://doi.org/10.1002/2017GL073023.

Talandier, J., & Okal, E. A. (1998). On the Mechanism of Conversion of Seismic Waves to and from T Waves in the Vicinity of Island Shores. In *Bulletin of the Seismological Society of America* (Vol. 88, Issue 2). https://doi.org/10.1785/BSSA0880020621

Tang, C., Peng, Z., Chao, K., Chen, C., & Lin, C. (2010). Detecting low-frequency earthquakes within non-volcanic tremor in southern Taiwan triggered by the 2005 Mw8. 6 Nias earthquake. *Geophysical Research Letters*, *37*(16). https://doi.org/10.1029/2010GL043918.

Thomas, A. M., Nadeau, R. M., & Bürgmann, R. (2009). Tremor-tide correlations and near-lithostatic pore pressure on the deep San Andreas fault. *Nature*, *462*(7276), 1048–1051. https://doi.org/10.1038/nature08654.

Thorp, W. H. (1965). Deep-ocean sound attenuation in the sub-and low-kilocycle-per-second region. *The Journal of the Acoustical Society of America*, *38*(4), 648–654. https://doi.org/10.1121/1.1909768.

Tilmann, F., Zhang, Y., Moreno, M., Saul, J., Eckelmann, F., Palo, M., Deng, Z., Babeyko, A., Chen, K., Baez, J. C., Schurr, B., Wang, R., & Dahm, T. (2016). The 2015 Illapel earthquake, central Chile: A type case for a characteristic earthquake? *Geophysical Research Letters*, *43*(2), 574–583. https://doi.org/10.1002/2015GL066963.

Tissandier, R., Nocquet, J. M., Klein, E., Vigny, C., Ojeda, J., & Ruiz, S. (2023). Afterslip of the Mw 8.3 2015 Illapel earthquake imaged through a time-dependent inversion of continuous and survey GNSS data. *Journal of Geophysical Research: Solid Earth*, 128(2), e2022JB024778. https://doi.org/10.1029/2022JB024778.

Todd, E. K., Schwartz, S. Y., Mochizuki, K., Wallace, L. M., Sheehan, A. F., Webb, S. C., Williams, C. A., Nakai, J., Yarce, J., Fry, B., Henrys, S., & Ito, Y. (2018). Earthquakes and Tremor Linked to Seamount Subduction During Shallow Slow Slip at the Hikurangi Margin, New Zealand. *Journal of Geophysical Research: Solid Earth*, *123*(8), 6769–6783. https://doi.org/10.1029/2018JB016136.

Tonegawa, T., Takemura, S., Yabe, S., & Yomogida, K. (2022). Fluid Migration Before and During Slow Earthquakes in the Shallow Nankai Subduction Zone. *Journal of Geophysical Research: Solid Earth*, *127*(3). https://doi.org/10.1029/2021JB023583.

Tréhu, A. M., de Moor, A., Madrid, J. M., Sáez, M., Chadwell, C. D., Ortega-Culaciati, F., Ruiz, J., Ruiz, S., & Tryon, M. D. (2020). Post-seismic response of the outer accretionary prism after the 2010 Maule earthquake, Chile. *Geosphere*, *16*(1), 13–32. https://doi.org/10.1130/GES02102.1.

Uchida, N. (2019). Detection of repeating earthquakes and their application in characterizing slow fault slip. In *Progress in Earth and Planetary Science* (Vol. 6, Issue 1). Springer Berlin Heidelberg. https://doi.org/10.1186/s40645-019-0284-z.

Uchida, N., & Bürgmann, R. (2019). Repeating earthquakes. *Annual Review of Earth and Planetary Sciences*, *47*, 305–332. https://doi.org/10.1146/annurev-earth-053018-060119

Valdés-Pineda, R., Cañón, J., & Valdés, J. B. (2018). Multi-decadal 40- to 60-year cycles of precipitation variability in Chile (South America) and their relationship to the AMO and PDO signals. *Journal of Hydrology*, *556*, 1153–1170. https://doi.org/10.1016/j.jhydrol.2017.01.031.

Valenzuela-Malebrán, C., Cesca, S., Ruiz, S., Passarelli, L., Leyton, F., Hainzl, S., ... & Dahm, T. (2021). Seismicity clusters in Central Chile: Investigating the role of repeating earthquakes and swarms in a subduction region. *Geophysical Journal International*, 224(3), 2028-2043. https://doi.org/10.1093/gji/ggaa562.

Vigny, C., Rudloff, A., Ruegg, J. C., Madariaga, R., Campos, J., & Alvarez, M. (2009). Upper plate deformation measured by GPS in the Coquimbo Gap, Chile. *Physics of the Earth and Planetary Interiors*, *175*(1–2), 86–95. https://doi.org/10.1016/j.pepi.2008.02.013.

Wallace, L. M. (2020). Slow Slip Events in New Zealand. *Annual Review of Earth and Planetary Sciences*. https://doi.org/10.1146/annurev-earth-071719.

Wallace, L. M., & Eberhart-Phillips, D. (2013). Newly observed, deep slow slip events at the central Hikurangi margin, New Zealand: Implications for downdip variability of slow slip and tremor, and relationship to seismic structure. *Geophysical Research Letters*, *40*(20), 5393–5398. https://doi.org/10.1002/2013GL057682.

Wallace, L. M., Kaneko, Y., Hreinsdóttir, S., Hamling, I., Peng, Z., Bartlow, N., D'Anastasio, E., & Fry, B. (2017). Large-scale dynamic triggering of shallow slow slip enhanced by overlying sedimentary wedge. *Nature Geoscience*, *10*(10), 765–770. https://doi.org/10.1038/ngeo3021.

Walter, J. I., Schwartz, S. Y., Protti, M., & Gonzalez, V. (2013). The synchronous occurrence of shallow tremor and very low frequency earthquakes offshore of the Nicoya Peninsula, Costa Rica. *Geophysical Research Letters*, *40*(8), 1517–1522. https://doi.org/10.1002/grl.50213.

Wech, A. G., Boese, C. M., Stern, T. A., & Townend, J. (2012). Tectonic tremor and deep slow slip on the Alpine Fault. *Geophysical Research Letters*, *39*(10). https://doi.org/10.1029/2012GL051751.

Yamashita, T. (1998). Simulation of seismicity due to fluid migration in a fault zone. *Geophysical Journal International*, *132*(3), 674–686. https://doi.org/10.1046/j.1365-246X.1998.00483.x.

Yokota, Y., & Ishikawa, T. (2020). Shallow slow slip events along the Nankai Trough detected by GNSS-A. *Science Advances*, *6*(3), eaay5786. https://doi.org/10.1126/sciadv.aay5786.

8 Anexos

8.1 Anexo A: Controls on the T-Phases Energy Fluxes Recorded on Juan Fernandez Island by Continental Seismic Wave Paths and Nazca Bathymetry

Check for updates

AGU PUBLICATIONS

Geophysical Research Letters

RESEARCH LETTER
10.1002/2017GL076790

Key Points:
- Broadband station deployed on Juan Fernandez Island detected T phases from South American earthquakes
- T phase energy fluxes of the Valparaíso and Illapel earthquakes depend on their depths along the dip and the bathymetry along their travel paths
- Tectonic characteristics near the trench control the T phase efficiencies of interplate thrust events

Supporting Information:
- Supporting Information S1
- Table S1

Correspondence to:
M. Sáez,
msaez@dgf.uchile.cl

Citation:
Sáez, M., & Ruiz, S. (2018). Controls on the T phase energy fluxes recorded on Juan Fernandez Island by continental seismic wave paths and Nazca bathymetry. Geophysical Research Letters, 45, 2610–2617. https://doi.org/10.1002/2017GL076790

Received 12 DEC 2017
Accepted 22 FEB 2018
Accepted article online 28 FEB 2018
Published online 23 MAR 2018

Controls on the T Phase Energy Fluxes Recorded on Juan Fernandez Island by Continental Seismic Wave Paths and Nazca Bathymetry

Miguel Sáez[1,2] and Sergio Ruiz[1]

[1]Geophysics department, Universidad de Chile, Santiago, Chile, [2]Geology department, Universidad de Chile, Santiago, Chile

Abstract T phases from 54 South American earthquakes with $M_w > 5.2$ are observed at a broadband station on Juan Fernandez Island. We computed the T phase energy flux (TPEF) values of the seismograms. The TPEF values show a large dispersion that can be explained by considering the tectonic characteristics of the South American plate and the Nazca plate bathymetry. The TPEFs generated by the 2015 Illapel and 2017 Valparaíso seismic sequences were controlled by the positions of the interface events along the dip. The central and downdip interplate earthquakes were more efficient in the generation of T phases than the near-trench interplate earthquakes (depths of < 15 km). The variations in the generation efficiency with depth are explained by the continental raypaths of the body waves and the incidence angles of waves entering the sound fixing and ranging channel. Additionally, we observed differences in the TPEFs from both earthquake sequences that were controlled by seamounts atop the Nazca plate along the T phase paths.

1. Introduction

Since 2015, the National Seismological Center (CSN) has operated the continuously recording broadband station VA04 on Juan Fernandez Island (JFI), which is located 700 km from the South American coast. Station VA04 has consequently recorded most of the larger events that occurred throughout South America (see Figure 1a). Due to the large hypocentral distances between these events and station VA04, the resulting high-frequency body waves are strongly attenuated; nevertheless, T phases are clearly observed in the records (Matsumoto et al., 2016). T phases are high-frequency acoustic waves (2–8 Hz) that are generated by the conversion of seismic waves trapped within the sound fixing and ranging (SOFAR) channel (Talandier & Okal, 1998). The SOFAR channel is a low-velocity channel located 1,200 m below the sea surface that acts as a waveguide for T phases, thereby allowing them to travel long distances without anelastic attenuation (Thorp, 1965). The low attenuation property of T phases has been utilized to study the source properties of distant earthquakes (Okal & Talandier, 1997), underwater landslides (Fryer et al., 2004), and low-magnitude seismic swarms (Ito et al., 2012) and to differentiate between nuclear explosions and earthquakes (Talandier & Okal, 2001). On the receiver side, T phases are converted from acoustic to seismic waves, being strongly attenuated by continental raypaths and the conversion process (Kosuga, 2011; Walker et al., 1992). Despite this, Buehler and Shearer (2015) showed that it is possible to observe them at coastal stations using stacking methods. For simplicity, we refer to seismic waves recorded on seismograms after the conversion process as "T phases." Despite its multiple uses, the mechanism through which T phases are generated is a complex process that is not well understood; this is primarily due to differences in a multitude of factors, including variations in the bathymetry, sizes, and types of earthquakes; continental and oceanic raypaths; and frequency content (Williams et al., 2006), which affect their formation.

We analyzed 54 earthquakes with magnitudes larger than M_w 5.2 (Table S1 in the supporting information). These earthquakes are associated with the subduction of the Nazca plate beneath the South American plate and primarily occur along the plate interface, along which Lay et al. (2012) proposed three different seismic domains that generate high-frequency content. Events from shallower depths (< 15 km) are characterized by source spectra with low high-frequency contents (Ye et al., 2013), and they are deficient in the generation of T phases (Okal et al., 2003). Meanwhile, events generated at moderate depths (15–30 km) along the central plate interface have modest high-frequency content in their source spectra. Finally, interface events from greater downdip depths (35–60 km) are characterized by earthquakes with source spectra rich in high-frequency content (Lay et al., 2012; Ye et al., 2013, among others). In this study, we compared the T phase energy flux (TPEF) values and high-frequency seismic source spectrum content recorded at broadband

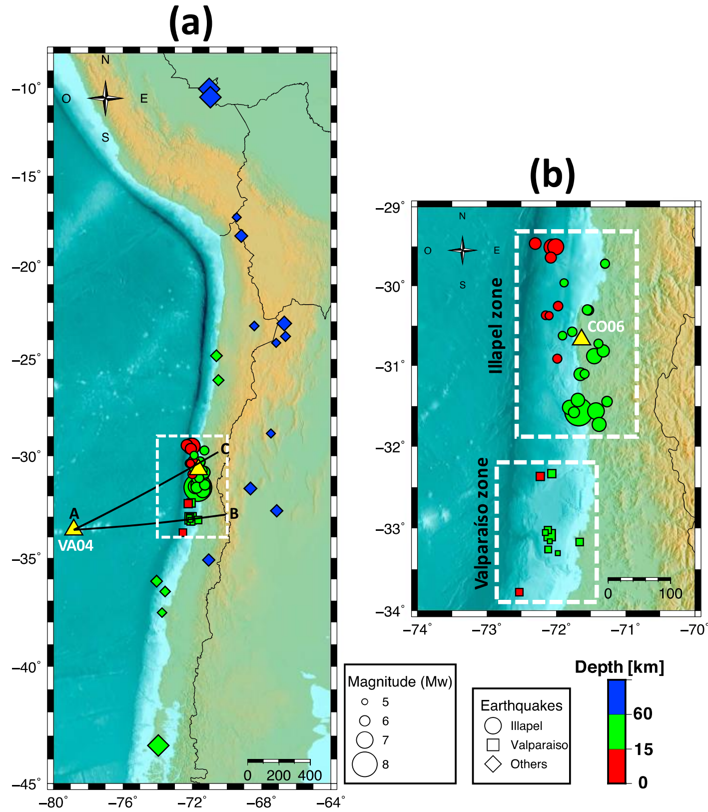

Figure 1. Spatial distribution of the 54 earthquakes analyzed in this study. The sizes and colors of the markers are proportional to the M_w and depth of each event, respectively. (a) South American earthquakes ($M_w > 5.2$) that occurred between February 2015 and May 2017 recorded by station VA04 on Juan Fernandez Island and station CO06 in the city of Coquimbo. The largest events considered are the 2015 Illapel M_w 8.3, 2017 Chiloé M_w 7.6, 2015 deep Peru M_w 7.6, and 2017 Valparaíso M_w 6.9 earthquakes. (b) Magnified view of the white box shown in (a). The circles are events associated with the 2015 Illapel seismic sequence, and the squares represent the 2017 Valparaíso seismic sequence.

station VA04 on JFI with those recorded at the coastal broadband station CO06 (see Figure 1). We focused on the seismic sequences of the 2015 M_w 8.3 Illapel and 2017 M_w 6.9 Valparaíso earthquakes (Ruiz et al., 2016; Ruiz, Aden-Antoniow, et al., 2017) because their foreshocks and aftershocks were located over the entire plate interface. Our results show that the TPEFs observed at JFI depend on the body waves produced by continental raypaths, the incidence angle into the SOFAR channel and the bathymetry of the Nazca plate.

2. Data and Methodology

2.1. JFI and Chilean Coastal CSN Broadband Stations

Stations VA04 and CO06 are located on JFI and on the Chilean coast at 90 and 200 m above sea level, respectively (see Figure 1). We considered South American earthquakes that occurred between February 2015 and May 2017, during which time VA04 was operating continuously. Figure 1a shows the epicenters from the CSN catalog for the Chilean events and those from the United States Geological Survey catalog for the other earthquakes. Table S1 shows the magnitude (ranging from M_w 5.2 to M_w 8.3), epicenter location, and focal

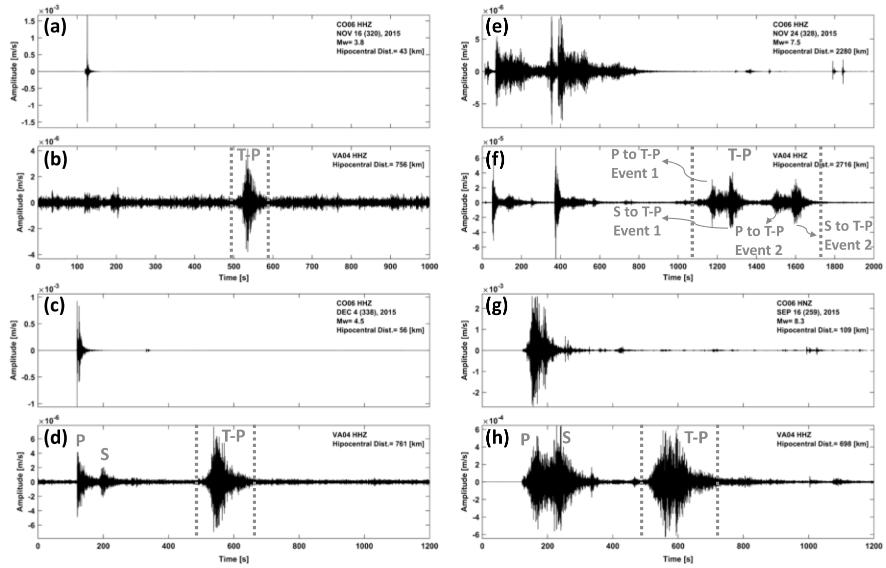

Figure 2. Four seismograms filtered between 2 and 8 Hz of earthquakes recorded simultaneously at stations VA04 and CO06. (a, c, e, and g) Seismograms recorded at station CO06. (b, d, f, and h) Seismograms recorded at station VA04. The gray dashed lines represent the windows that contain the *T* phases (T-P).

depth (ranging from 10 to 620 km) of each event. Stations VA04 and C006 are equipped with a broadband Trillium 120-s period sensor, a Marmot data logger system, and a Quanterra Q330 digitizer. The broadband stations recorded continuously at a rate of 100 samples per second.

2.2. *T* Phases Observed at the JFI and Chilean Coastal Stations

We filtered the up-down components using a fourth-order Butterworth band-pass filter with corner frequencies of 2 and 8 Hz. Figure 2 shows filtered traces generated in VA04 and CO06 stations for four different earthquakes. The *T* phases recorded at station VA04 have amplitudes greater than or similar to those of *P* or *S* waves (Figures 2b and 2d). The *T* phases of the deep Peru 2015 earthquakes (Ruiz, Tavera, et al., 2017) exhibit conversions from both *P* and *S* phases to *T* phases (Figure 2f), similar to the conversions from the deep Bolivian 1994 M_w 8.2 earthquake observed by Okal and Talandier (1997) at other broadband stations placed on islands throughout the Pacific Ocean. Although the distance between station CO06 and the 1,200 m isobath is only 16 km, the *T* phases are strongly attenuated by the continental raypath, and thus, it is impossible to distinguish their arrivals in the filtered traces (Figures 2a, 2c, 2e, and 2g).

2.3. *T* Phase Energy Flux

The TPEF generated by a *T* phase at a receiver is defined as follows (Okal et al., 2003):

$$\mathrm{TPEF} = \rho\alpha\int_W [\dot{u}(t)]^2 dt \tag{1}$$

where $\dot{u}(t)$ is the vertical ground velocity motion, W is the *T* phase duration, and ρ and α are the density and *P* wave velocity at the site where the station is located, respectively.

After filtering the records, we followed the steps listed hereafter to calculate the TPEF.

1. We calculated the theoretical arrival times of the *T* phases. Considering the travel time of *P* and *S* waves from the hypocenter to the continental slope and the travel times of *T* phases in the SOFAR channel, we used average velocities of 8, 4.6, and 1.484 km/s, respectively (Talandier & Okal, 1998).
2. Utilizing the theoretical *T* phase arrival time at station VA04, we visually selected the *T* phase time windows. We performed this process manually due to the frequent seismicity detected at VA04 during the seismic sequences of 2015 Illapel and 2017 Valparaíso earthquakes.

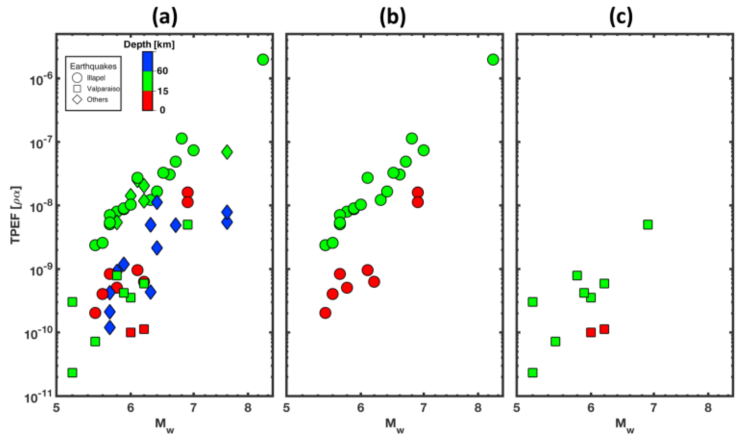

Figure 3. *T* phase energy flux (TPEF) as a function of the magnitude M_W. (a) TPEF versus M_W for the 54 South American earthquakes shown in Figure 1. (b) TPEF versus M_W for the Illapel events. (c) TPEF versus M_W for the Valparaíso events.

3. We divided the *T* phase records into windows with a length of 1 s and calculated their root mean square (rms) in each available window, thereby generating an rms curve.
4. The rms curve was normalized according to its maximum value and then smoothed using a moving average of 5 points (Figure S1 in the supporting information).
5. We calculated the TPEF according to equation (1) by considering the *T* phase duration (*W*) where the rms-normalized amplitude is equal to or greater than 0.6 as the record portion (Figure S1). Finally, our computed TPEF values are normalized by ρ and α.

3. Results

3.1. TPEF Efficiency

Figure 3a shows the TPEF values generated at station VA04 by the earthquakes shown in Figure 1a. The TPEF values scale according to the event magnitudes, as was proposed originally by Okal et al. (2003). The data dispersion between the TPEF and the magnitude decreases when we separate the values associated with each seismic sequence (see Figures 3b and 3c). The Illapel and Valparaíso seismic sequences show that near-trench earthquakes (<15 km depth) have TPEF values lower than those of deeper earthquakes (15–60 km depth). Intraplate intermediate-depth earthquakes (>60 km depth) have a higher TPEF dispersion, but this can be explained by the diverse depths and zones in which those events occurred (Figure 1). In addition, the Valparaíso seismic sequence generated smaller TPEF values than the Illapel earthquakes, even though their epicentral distances to JFI are smaller.

3.2. High-Frequency Fourier Spectrum Variations

We computed the Fourier amplitude spectra of the Illapel earthquakes recorded at stations VA04 and CO06 by considering time windows beginning with the first *P* wave arrivals and ending 30 s after the *S* wave arrivals. We chose this time window because of the relationship between the body waves and the conversion from seismic to acoustic waves (Balanche et al., 2009; Talandier & Okal, 1998). To compare the events with different magnitudes, we decided to normalize the Fourier spectra at 1 Hz, as their corner frequencies are all less than 1 Hz. The Fourier spectra associated with the Illapel events recorded at station VA04 (Figure 4a) show an important frequency content between 2 and 8 Hz independent of the event depths. Meanwhile, the Fourier spectra associated with the Illapel earthquakes recorded at station CO06 show variations in the frequency content with respect to their focal depths. The shallower events (<15 km depth) have lower high-frequency spectral amplitudes between 2 and 8 Hz compared with those of the deeper events (15–60 km depth).

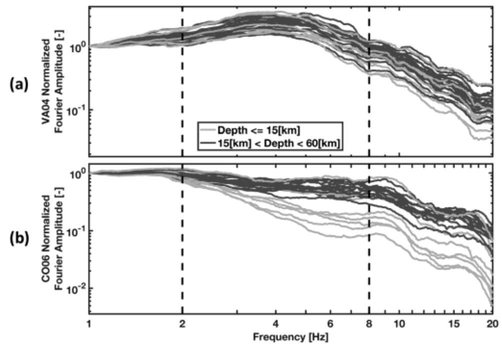

Figure 4. Fourier amplitude spectra of the Illapel earthquakes normalized to 1 Hz. (a) VA04 records. (b) CO06 records. Frequencies between 2 and 8 Hz for near-trench interface events are more attenuated at station CO06 than at station VA04. The gray and black lines represent normalized Fourier amplitude of near trench (depth ≤ 15 km) and central and downdip earthquakes (15 km < depth ≤ 60), respectively.

4. Discussion

4.1. High-Frequency Variations in the Plate Interface Events Along Dip

Okal et al. (2003) first suggested the presence of a dip-dependent variation in the efficiencies of generated *T* phases after observing lower TPEF values for tsunami earthquakes. According to Okal (2008), these types of events are deficient in the generation of *T* phases due to their low spectral frequency contents above 1 Hz. This dip-dependent difference in the source spectra for plate interface events was corroborated by Lay et al. (2012), and other authors, who studied the source spectra of recent megathrust subduction earthquakes. In this study, we compared the Fourier spectra of the 2015 Illapel earthquakes in the frequency band from 2 to 8 Hz. Figure 4 shows different high-frequency properties between the broadband records of stations VA04 and CO06. While the Fourier spectra recorded at VA04 from the shallow, central, and downdip interface events do not display evident differences, the Fourier spectra for the shallower earthquakes recorded at CO06 exhibit a lower high-frequency spectral content than the deeper ones. We propose that the greater high-frequency attenuation observed at station CO06 is associated with the continental raypaths of the body waves. The shallower earthquakes generated body waves that traveled from the near-trench area to the coast through an eroded and fractured wedge that probably serves as a low-pass filter (Figure 5a). This wedge has previously been observed along the Chilean subduction zone, and it is characterized by a low-velocity zone relative to the continental basement (Contreras-Reyes et al., 2012, 2014; León-Ríos et al., 2016). Meanwhile, the central and downdip interplate events generated body waves that traveled through the continental basement (Figure 5a), which would attenuate high-frequency waves relatively less. In the case of station VA04, the raypaths of the body waves' path did not travel through the eroded and fractured wedge because they traveled directly to JFI without traversing the South American plate (Figure 5a). We propose that the observed deficiency of *T* phases from shallower earthquakes can be partially explained by the high-frequency attenuation of body waves produced by their paths through the wedge to the continental slope where the seismic-acoustic conversion occurred.

4.2. *T* Phase Incidence Angles of Waves Entering the SOFAR Channel

Another reason for the depth-dependent *T* phase efficiency for the Valparaíso and Illapel earthquakes could be due to the incidence angles of the acoustic waves entering the SOFAR channel. The shallower events generated body waves with incidence angles that were almost vertical with respect to the continental slope; these waves would require a considerable number of reflections to reach a horizontal angle (~12°) suitable for penetrating the SOFAR channel (Okal, 2008; Talandier & Okal, 1998). These multiple reflections make the seismic-acoustic conversion relatively inefficient (Talandier & Okal, 1998). In contrast, the deeper events generated seismic rays with relatively horizontal incidence angles in comparison with the shallower earthquakes; these rays required fewer reflections to enter the SOFAR channel, and therefore, the generation of *T* phases was more efficient (Talandier & Okal, 1998). This explanation is schematically summarized in Figure 5b.

4.3. *T* Phase Path Bathymetry

Although the Valparaíso earthquakes have a smaller epicentral distance with respect to JFI (Figure 1), they generated TPEF values that were 1 order of magnitude lower than those of the Illapel earthquakes (Figures 3b and 3c). These different TPEF versus M_w trends can be explained by the complex Nazca bathymetry along the raypaths between the Valparaíso earthquakes and JFI compared with the smooth Nazca bathymetry between the Illapel earthquakes and JFI. The bathymetry along profile A′-B′ (Figure 5b) extracted from Becker et al. (2009) and Smith and Sandwell (1997) is characterized by several seamounts belonging to the Juan Fernandez Ridge with heights greater than 1,200 m (Figure 5c). These seamounts penetrate the SOFAR channel; therefore, they acted as a barrier to the propagation of *T* phases (Walker et al., 1992) between the 2017 Valparaíso earthquakes and JFI. In contrast, the smooth bathymetry of profile A′-C′ (Figure 5c) favored the efficient propagation of *T* phases between the 2015 Illapel earthquakes and JFI. Despite of the presence of

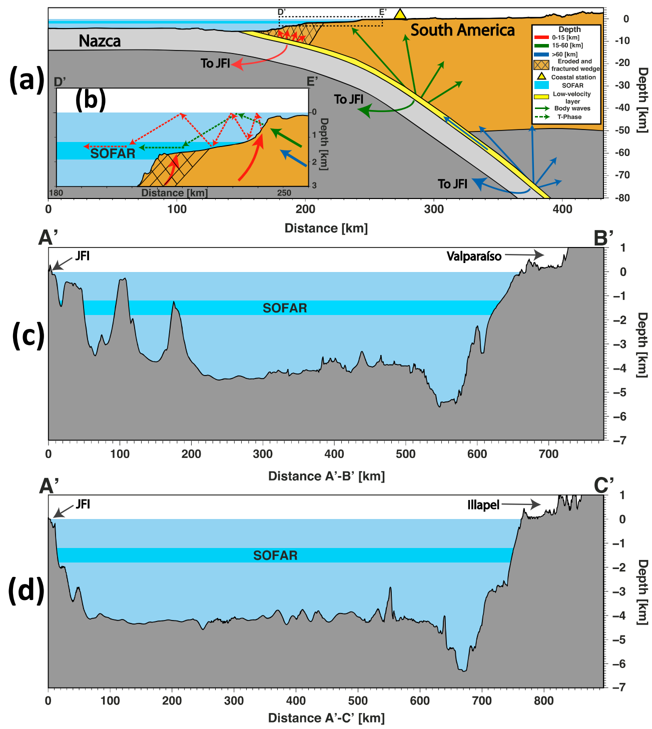

Figure 5. (a) Schematic illustration of body waves rays generated from near-trench interface events (red line), central and downdip interplate events (green line), and intraplate intermediate-depth earthquakes (blue line). The sound fixing and ranging channel is located at 1,200 m. The low-velocity layer is based in the scheme suggested for the Northern Chile by Garth and Rietbrock (2017). (b) Scheme of the generation of *T* phases. (c) Bathymetry of profile A′-B′ in Figure 1b representative of the Valparaíso-Juan Fernandez Island (JFI) raypaths (Figure 1b). (d) Bathymetry of profile A′-C′ in Figure 1b representative of the Illapel-JFI raypaths (Figure 1b).

seamounts along profile A′-B′, we were not able to detect reversed propagation of *T* phases (Obara & Maeda, 2009) due to the high rate of aftershocks detected during the 2017 Valparaíso seismic sequence.

4.4. Intraplate Intermediate-Depth Events

Intraplate intermediate-depth earthquakes occur at depths greater than 60 km throughout most of the South American subduction zone. The presence of a low-velocity layer at the top of the subducting oceanic crust (Garth & Rietbrock, 2017; Martin et al., 2003) and the scattering due to small-scale heterogeneities within the subducted plate (Furumura & Kennett, 2005) have been proposed as waveguides for high frequency. Despite this, the TPEFs calculated for intraplate intermediate-depth events are similar to those of the shallower Illapel earthquakes and the Valparaíso central and downdip interface events (Figure 3a). Additional data and research are needed to interpret the TPEFs values of these types of events, especially because we considered events located in different zones (Figure 1a) characterized by different conditions of *T* phase generation and different Nazca bathymetry paths.

5. Conclusions

We showed that *T* phases produced by various South American earthquakes were recorded at the broadband station deployed on JFI. The situation was different for the coastal station CO06, where very weak *T* phases were recorded due to strong attenuation along the continental raypath. The TPEFs generated by the South American earthquakes recorded at JFI increased with M_w. For the 2015 Illapel and 2017 Valparaíso seismic sequences, the TPEF values were controlled mainly by the Nazca bathymetry along the oceanic raypaths and the hypocentral depths of the earthquakes. The complex bathymetry between the 2017 Valparaíso earthquakes and JFI reduced the continuity of the SOFAR channel relative to that along the raypaths from the 2015 Illapel earthquakes to JFI; thus, the *T* phases were able to propagate more efficiently between the latter. In addition, we observed that the *T* phase efficiency varied with the dip. The central and downdip earthquakes (depths ranging from 15 to 60 km) were more efficient in the generation of *T* phases than near-trench earthquakes (depths less than 15 km). This depth dependency of the efficiency can be explained by two reasons: (1) higher seismic wave attenuation along continental wedge raypaths in comparison with those through the continental basement and (2) the incidence angles of waves entering the SOFAR channel. We expect that future seismicity in South America will generate *T* phases that follow the pattern exposed herein, for which JFI can be used as a natural place for continuous monitoring.

Acknowledgments
We thank CSN, National Seismological Center of the Universidad de Chile, for providing us the raw data of VA04 and CO06 stations, which are available at CSN or Incorporated Research Institutions for Seismology Data Management (IRIS). Miguel Sáez thanks the scholarship PCHA/Doctorado Nacional/2017-21171480, granted by CONICYT. This work was partially funded by PRS (Programa de Riesgo Sísmico, Universidad de Chile) and FONDECYT 1170430. We also thank R. Madariaga for his helpful advice and the two anonymous reviewers whose comments helped to improve this article.

References

Balanche, A., Guennou, C., Goslin, J., & Mazoyer, C. (2009). Generation of hydroacoustic signals by oceanic subseafloor earthquakes: A mechanical model. *Geophysical Journal International*, *177*(2), 476–480. https://doi.org/10.1111/j.1365-246X.2009.04146.x

Becker, J. J., Sandwell, D. T., Smith, W. H. F., Braud, J., Binder, B., Depner, J., et al. (2009). Global bathymetry and elevation data at 30 arc seconds resolution: SRTM30_PLUS. *Marine Geodesy*, *32*(4), 355–371. https://doi.org/10.1080/01490410903297766

Buehler, J. S., & Shearer, P. M. (2015). T phase observations in global seismogram stacks. *Geophysical Research Letters*, *42*, 6607–6613. https://doi.org/10.1002/2015GL064721

Contreras-Reyes, E., Becerra, J., Kopp, H., Reichert, C., & Díaz-Naveas, J. (2014). Seismic structure of the north-central Chilean convergent margin: Subduction erosion of a paleomagmatic arc. *Geophysical Research Letters*, *41*, 1523–1529. https://doi.org/10.1002/2013GL058729

Contreras-Reyes, E., Jara, J., Grevemeyer, I., Ruiz, S., & Carrizo, D. (2012). Abrupt change in the dip of the subducting plate beneath North Chile. *Nature Geoscience*, *5*(5), 342–345. https://doi.org/10.1038/ngeo1447

Fryer, G. J., Watts, P., & Pratson, L. F. (2004). Source of the great tsunami of 1 April 1946: A landslide in the upper Aleutian forearc. *Marine Geology*, *203*(3–4), 201–218. https://doi.org/10.1016/S0025-3227(03)00305-0

Furumura, T., & Kennett, B. L. N. (2005). Subduction zone guided waves and the heterogeneity structure of the subducted plate: Intensity anomalies in northern Japan. *Journal of Geophysical Research*, *110*, B10302. https://doi.org/10.1029/2004JB003486

Garth, T., & Rietbrock, A. (2017). Constraining the hydration of the subducting Nazca plate beneath Northern Chile using subduction zone guided waves. *Earth and Planetary Science Letters*, *474*, 237–247. https://doi.org/10.1016/j.epsl.2017.06.041

Ito, A., Sugioka, H., Suetsugu, D., Shiobara, H., Kanazawa, T., & Fukao, Y. (2012). Detection of small earthquakes along the Pacific-Antarctic Ridge from T-waves recorded by abyssal ocean-bottom observatories. *Marine Geophysical Research*, *33*(3), 229–238. https://doi.org/10.1007/s11001-012-9158-0

Kosuga, M. (2011). Localization of T-wave energy on land revealed by a dense seismic network in Japan. *Geophysical Journal International*, *187*(1), 338–354. https://doi.org/10.1111/j.1365-246X.2011.05143.x

Lay, T., Kanamori, H., Ammon, C. J., Koper, K. D., Hutko, A. R., Ye, L., et al. (2012). Depth-varying rupture properties of subduction zone megathrust faults. *Journal of Geophysical Research*, *117*, B04311. https://doi.org/10.1029/2011JB009133

León-Ríos, S., Ruiz, S., Maksymowicz, A., Leyton, F., Fuenzalida, A., & Madariaga, R. (2016). Diversity of the 2014 Iquique's foreshocks and aftershocks: Clues about the complex rupture process of a Mw 8.1 earthquake. *Journal of Seismology*, *20*(4), 1059–1073. https://doi.org/10.1007/s10950-016-9568-6

Martin, S., Rietbrock, A., Haberland, C., & Asch, G. (2003). Guided waves propagating in subducted oceanic crust. *Journal of Geophysical Research*, *108*(B11), 2536. https://doi.org/10.1029/2003JB002450

Matsumoto, H., Haralabus, G., Zampolli, M., & Özel, N. M. (2016). T-phase and tsunami pressure waveforms recorded by near-source IMS water-column hydrophone triplets during the 2015 Chile earthquake. *Geophysical Research Letters*, *43*, 12,511–12,519. https://doi.org/10.1002/2016GL071425

Obara, K., & Maeda, T. (2009). Reverse propagation of T waves from the Emperor seamount chain. *Geophysical Research Letters*, *36*, L08304. https://doi.org/10.1029/2009GL037454

Okal, E. A. (2008). The generation of T waves by earthquakes. *Advances in Geophysics*, *49*, 1–65. https://doi.org/10.1016/S0065-2687(07)49001-X

Okal, E. A., Alasset, P.-J., Hyvernaud, O., & Schindelé, F. (2003). The deficient T waves of tsunami earthquakes. *Geophysical Journal International*, *152*(2), 416–432. https://doi.org/10.1046/j.1365-246X.2003.01853.x

Okal, E. A., & Talandier, J. (1997). T waves from the great 1994 Bolivian deep earthquake in relation to channeling of S wave energy up the slab. *Journal of Geophysical Research*, *102*(B12), 27,421–27,437. https://doi.org/10.1029/97JB02718

Ruiz, S., Aden-Antoniow, F., Baez, J. C., Otarola, C., Potin, B., Campo, F., et al. (2017). Nucleation phase and dynamic inversion of the Mw 6.9 Valparaíso 2017 earthquake in Central Chile. *Geophysical Research Letters*, *44*, 10,290–10,297. https://doi.org/10.1002/2017GL075675

Ruiz, S., Klein, E., Del Campo, F., Rivera, E., Poli, P., Metois, M., et al. (2016). The seismic sequence of the 16 September 2015 Mw 8.3 Illapel, Chile, earthquake. *Seismological Research Letters*, *87*, 789–799.

Ruiz, S., Tavera, H., Poli, P., Herrera, C., Flores, C., Rivera, E., & Madariaga, R. (2017). The deep Peru 2015 doublet earthquakes. *Earth and Planetary Science Letters*, *478*, 102–109. https://doi.org/10.1016/j.epsl.2017.08.036

Smith, W. H. F., & Sandwell, D. T. (1997). Global Sea floor topography from satellite altimetry and ship depth soundings. *Science*, *277*(5334), 1956–1962. https://doi.org/10.1126/science.277.5334.1956

Talandier, J., & Okal, E. A. (1998). On the mechanism of conversion of seismic waves to and from T waves in the vicinity of island shores. *Bulletin of the Seismological Society of America*, *88*(2), 621–632.

Talandier, J., & Okal, E. A. (2001). Identification criteria for sources of T waves recorded in French Polynesia. *Pure and Applied Geophysics*, *158*, 567–603.

Thorp, W. H. (1965). Deep-ocean sound attenuation in the sub-and low-kilocycle-per-second region. *The Journal of the Acoustical Society of America*, *38*(4), 648–654. https://doi.org/10.1121/1.1909768

Walker, D. A., Mccreery, C. S., & Hiyoshi, Y. (1992). T-phase spectra, seismic moments, and tsunamigenesis. *Bulletin of the Seismological Society of America*, *82*(3), 1275–1305.

Williams, C. M., Stephen, R. A., & Smith, D. K. (2006). Hydroacoustic events located at the intersection of the Atlantis (30°N) and Kane (23°40′N) transform faults with the mid-Atlantic ridge. *Geochemistry, Geophysics, Geosystems*, *7*, Q06015. https://doi.org/10.1029/2005GC001127

Ye, L., Lay, T., & Kanamori, H. (2013). Ground shaking and seismic source spectra for large earthquakes around the megathrust fault offshore of northeastern Honshu, Japan. *Bulletin of the Seismological Society of America*, *103*(2B), 1221–1241. https://doi.org/10.1785/0120120115

8.2 Anexo B: Earthquakes Felt in the Juan Fernandez Islands: Where Are They Coming From?

Earthquakes Felt in the Juan Fernandez Islands: Where Are They Coming from?

Sebastián Carrasco*[1,2], Sergio Ruiz[3], and Miguel Sáez[3]

Abstract

The Juan Fernandez Islands (JFI) are located in the Pacific Ocean 675 km west of the Chilean coast. This archipelago has historically been affected by large tsunamis. Robinson Crusoe Island (RCI), the main island of the JFI, was first inhabited in 1749. Since then, several tsunamis have destroyed RCI port structures and sometimes caused deaths. Ground shaking perceived by the inhabitants has preceded some tsunami arrivals. Seismological instrumentation was temporarily deployed on RCI in 1999, and a permanent station has been operating since 2014. Here, we use these data to characterize the seismic waves that arrive at the JFI and to determine whether shaking perception could be used as a tsunami early warning system. We compute peak ground accelerations (PGAs) from *P*, *S*, and *T* waves generated by Peruvian and Chilean earthquakes and find that the largest ground shakings are mostly related to *T*-wave arrivals, which correlate with macroseismic modified Mercalli intensities lower than III. From the analysis of PGAs and macroseismic intensities, we conclude that shaking perception can be associated with large megathrust earthquakes, subduction events generated in the deep zone of seismogenic contact, and local seismicity. Unfortunately, potential tsunami earthquakes that occur on the Chilean coast will not be felt on RCI. Consequently, ground shaking in the JFI would not be a good proxy for tsunami warning, and a robust tsunami early warning system is necessary for RCI.

Cite this article as Carrasco, S., S. Ruiz, and M. Sáez (2019). Earthquakes Felt in the Juan Fernandez Islands: Where Are They Coming from? *Seismol. Res. Lett.* **91**, 262–271, doi: 10.1785/0220190151.

Supplemental Material

Introduction

The Juan Fernandez Islands (JFI) are intraplate volcanic islands located at latitude 33° S, longitude 79° W, ~675 km west of central Chile. They rise from the Juan Fernandez ridge (JFR), a discontinuous array of volcanic centers aligned approximately east–west, whose origin has been attributed to an active hot spot located west of Robinson Crusoe Island (RCI), as shown in Figure 1 (Von Huene *et al.*, 1997). The JFI have been devastated by tsunamis produced by earthquakes generated along the Chilean margin. Written reports exist since 1749, when the Spanish crown ordered the building of the Saint Barbara Fortress and the populating of RCI. The first reports of earthquake-related activity dates back to 1751, when the tsunami generated by the 1751 Concepción megathrust earthquake reached the coast of RCI, causing 36 deaths and destroying houses, warehouses, the church, and the governor's house (Udías *et al.*, 2012; based on "Documents of the Archivo de Indias," located in Spain). The governor of JFI, Thomas Sutcliffe, reported the effects of the 20 February 1835 south-central Chile megathrust earthquake. This earthquake generated a large tsunami that reached the RCI, destroyed the harbor and triggered the eruption of a submarine volcano located near JFI, which generated a slight shaking felt on RCI (Sutcliffe, 1839; Montessus de Ballore, 1911/1916). During the twentieth century, three earthquakes were reported to occur in the area surrounding the RCI in the 1980s (Wysession *et al.*, 1991), and two of them were confirmedly felt by RCI inhabitants (E. Okal, personal comm., 2019). Between October and December 1998, earthquake shaking was reported by inhabitants of RCI, where macroseismic intensities (MsIs) reached III–IV modified Mercalli intensity (MMI). A quick deployment of seismological stations in March 1999 provided some information about local seismicity, and the most important outcome was the identification of *S-P* times even shorter than 3 s (Chilean National Emergency Office [ONEMI], 1999; see Fig. S1, available in the supplemental material to this article). During the 27 February 2010 Maule M_w 8.8 Chile megathrust earthquake (Ruiz and Madariaga, 2018), RCI inhabitants felt ground shaking before a tsunami arrived at the island, which finally destroyed most of the coastline buildings and left 18 fatalities and much damage (Fritz *et al.*, 2011). The 2015 Illapel M_w 8.3 earthquake, located due east of

1. National Seismological Center, Facultad de Ciencias Físicas y Matemáticas, Universidad de Chile, Santiago, Chile; 2. Now at Department of Earthquake Geology, Institute of Geology and Mineralogy, University of Cologne, Bergisch Gladbach, Germany; 3. Departamento de Geofísica, Facultad de Ciencias Físicas y Matemáticas, Universidad de Chile, Santiago, Chile

*Corresponding author: acarrasc@uni-koeln.de

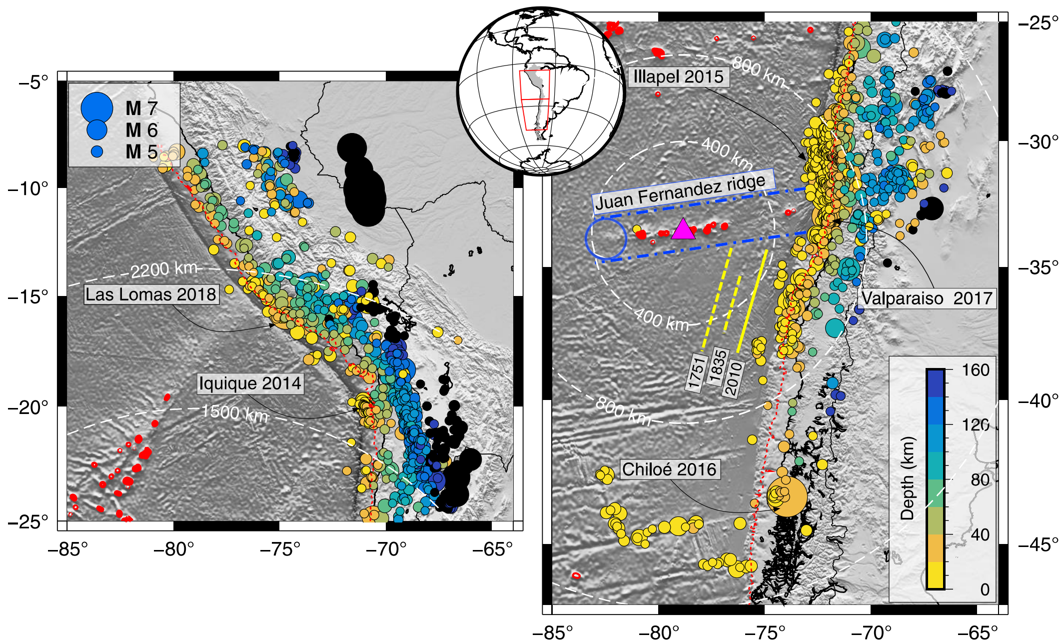

the JFI, was also felt by RCI inhabitants. Finally, ground shaking was reported by RCI inhabitants during the M_w 7.1 Las Lomas earthquake on 17 January 2018, which occurred more than 2000 km from the island and did not cause any fatalities or damage in the JFI. The rupture lengths of the three large earthquakes affecting RCI are illustrated in Figure 1, along with regional seismicity with $\mathbf{M} \geq 4.5$ located by the National Earthquake Information Center (NEIC) from June 2014 through January 2019.

A multiparametric seismological station of the National Seismological Center of University of Chile (CSN) has been running since 2014 on RCI. The strong-motion instrument and the broadband seismometer have recorded several large-magnitude earthquakes from the Chile–Peru trench such as the 2015 M_w 8.3 Illapel, 2016 M_w 7.6 Chiloé, and 2018 M_w 7.1 Las Lomas earthquakes and more than 180 earthquakes with $M_w \geq 5.5$ since its installation (see Fig. 1).

Currently, the perception of earthquakes by RCI inhabitants has been related to large tsunamigenic megathrust earthquakes. Here, we use these data from the CSN station to determine where the earthquakes felt in RCI originate. To achieve this goal, we consider 1803 earthquakes with magnitudes higher than 4.5 occurring along the Peruvian–Chilean margin and recorded on RCI to characterize the peak ground acceleration (PGA) generated by different seismic waves. Then we relate the PGA of the T phase to the MsI and compare this behavior with the T-phase energy flux (TPEF). We observe that

Figure 1. Seismological context of the Juan Fernandez Islands (JFI). Yellow solid line represents length of rupture area of the 2010 M_w 8.8 Maule earthquake. Dashed yellow line is the inferred rupture length of 1751 and 1835 earthquakes. Robinson Crusoe Island (RCI), one of the main islands of JFI and where VA04 station is installed, is illustrated by the magenta triangle. Solid circles correspond to regional seismicity studied in this work scaled by magnitude and filled according to hypocenter depth. Juan Fernandez ridge is delimited by the blue dashed-dotted lines, and its hot spot is noted by the open blue circle. Some large earthquakes are also noted. Isoepicentral distances contours from VA04 station at 400, 800, 1500, and 2200 km are drawn with white dashed lines. Topographic features in the Nazca plate where bathymetry reaches 1200 m below sea level are illustrated by red polygons. The 1200 m depth level in the continental slope is denoted by the red dashed line. (Inset) Global map with the specified studied area. The color version of this figure is available only in the electronic edition.

the different kinds of earthquakes correlate in different forms with the PGA and MsI. Finally, we discuss whether this relation between PGA and MsI could be used as a potential tsunami warning.

Data and Methods

Seismological instruments

The high-frequency arrival of P and S waves and especially T phases are well recorded in seismological stations located on islands (Okal, 2011). Here, we use data from the VA04 seismological station on RCI (Fig. 1) to analyze these high-frequency waves (see Data and Resources). This station is maintained and operated by CSN and is located inside Juan Fernandez National Park at 117 m vertical elevation and ~220 m from the island coastline at a site characterized by partially eroded volcanic sequences (Leyton *et al.*, 2018). The station is equipped with a broadband Trillium 120 s period sensor and a strong-motion CMG-5T sensor with a 2.4g clip level, both continuously recording with a sample rate of 100 Hz. The operation time range started in June 2014, and only some small data gaps have occurred because of malfunction of the station (Fig. S1 shows the available data). According to this information, we consider earthquakes occurring from 6 June 2014 until 31 January 2019 (see Data and Resources). The earthquake catalog was retrieved from the NEIC-U.S. Geological Survey for an area delimited by 8°–58° S and 99°–64° W; our preliminary catalog contains 2137 events with magnitudes $\mathbf{M} \geq 4.5$.

Main seismic sequences recorded in the JFI

The VA04 station on RCI has been able to record seismic waves from earthquakes related to different seismic sequences occurring along the Peruvian–Chilean coast. These seismic sequences are mainly related to large subduction interface earthquakes ($\mathbf{M} > 7$), which provide events with a wide range of magnitudes at different locations along the subduction margin (Fig. 1). Among these sequences, we can highlight the aftershock sequence of the 2014 M_w 8.2 Iquique earthquake, which was located mainly in the up-dip region of the interface (Cesca *et al.*, 2016; León-Ríos *et al.*, 2016). In addition, the station recorded the whole Illapel sequence of 2015, including its mainshock, which has been proposed to have slipped along almost the entire thrust interface, and its aftershocks, which occurred mainly along the plate contact at depths ranging from shallow to ~50 km (e.g., Li *et al.*, 2016; Melgar *et al.*, 2016; Ruiz *et al.*, 2016; Tilmann *et al.*, 2016; Carrasco *et al.*, 2019, and references therein). The 2016 M_w 7.6 Chiloé earthquake occurred at ~35 km depth and was also recorded on RCI, but it had only one aftershock with a magnitude larger than 5 (Ruiz, Moreno, *et al.*, 2017; Lange *et al.*, 2018). On the other hand, the 2017 M_w 6.9 Valparaiso sequence included significant events with $\mathbf{M} \geq 5.5$ (e.g., Ruiz, Aden-Antoniow, *et al.*, 2017). Recently, the 2018 M_w 7.1 Las Lomas earthquake occurred at greater depth along the thrust interface (~40 km) and was also recorded with all its surrounding events distributed prior to and after the mainshock.

MsIs: instrumental and perception

The perception of earthquake shaking can be described through instrumental MsI, which is based on observational features during and after shaking. Instrumental MsI can be defined for peak ground motion parameters such as peak ground velocity or PGA. Here, we consider the PGA amplitudes to obtain the MMI using ground motion to intensity conversion equations (GMICEs; Cua *et al.*, 2010). In this way, a summary of several GMICEs shows that lower intensities can be reached from a wide range of PGAs. Because low shaking perception (MMI < V) is usually related to PGA values, PGA amplitudes recorded by strong-motion sensors provide a good estimate of MsI. Here, we estimate the MsI felt on RCI according to the equation proposed by Wald *et al.* (1999):

$$\mathrm{MMI} = 2.20 \log(\mathrm{PGA}) + 1.0, \qquad (1)$$

with PGA in cm/s/s.

The MsI is computed for each P and S waves and T phase. For this calculation, we computed the P- and S-wave theoretical arrival times with a Python implementation of Java TauP toolkit by Crotwell *et al.* (1999) through ObsPy package (Beyreuther *et al.*, 2010), assuming a 1D spherically symmetric Earth model given by ak135 model (Kennett *et al.*, 1995). However, the computation of T-phase arrival times cannot be obtained directly from TauP toolkit as P and S waves do because T phase correspond to a combination of a P (or S) wave traveling through solid Earth and a T wave traveling through water. The latter is originated when the corresponding P (or S) wave reaches the interface between water (usually ocean) and crust at depths where the sound fixing and ranging (SOFAR) channel is located (between 700 and 1300 m). Thus, to estimate the T-phase arrival times, we divided the procedure in two stages. First, we computed the travel time t_{Ph} of a P wave from the hypocenter to the SOFAR channel interface along the continental slope using the TauP toolkit. Second, we computed the travel time t_{TW} of a T-wave traveling at 1.5 km/s from the SOFAR channel interface to VA04 station and considering the epicentral distance between these two points. The T-phase arrival time t_{TP} is finally estimated as the simple summation of t_{Ph} and t_{TW}. We estimated the location of the SOFAR channel interface as the 1200 m depth level along the Peru–Chile continental slope obtained from the ETOPO1 grid (Amante and Eakins, 2009) as shown in Figure 1. From these theoretical arrival times, we selected a window of data for each type of wave. For P and S waves, the data window starts 30 s before respective arrival time and spans 180 s after it. If theoretical S-wave arrives before the end of the P-wave window, then the ending time of the latter is given by t_s −20 s. The T-phase data window starts 40 s before the theoretical arrival time t_{TP} explained previously and finishes 150 s after the arrival of the T phase related to the S wave. Each data window is selected and cut from strong-motion records. After selection, the baseline and instrument response are removed. For each component, the PGAs of P and S waves and T phases, without filtering, are computed. The final PGA amplitude corresponds to the maximum acceleration among the three components.

For the T-phase case, we computed the TPEF as defined by Okal *et al.* (2003):

$$\mathrm{TPEF} = \rho\alpha \int_W [\dot{u}(t)]^2 \mathrm{d}t, \qquad (2)$$

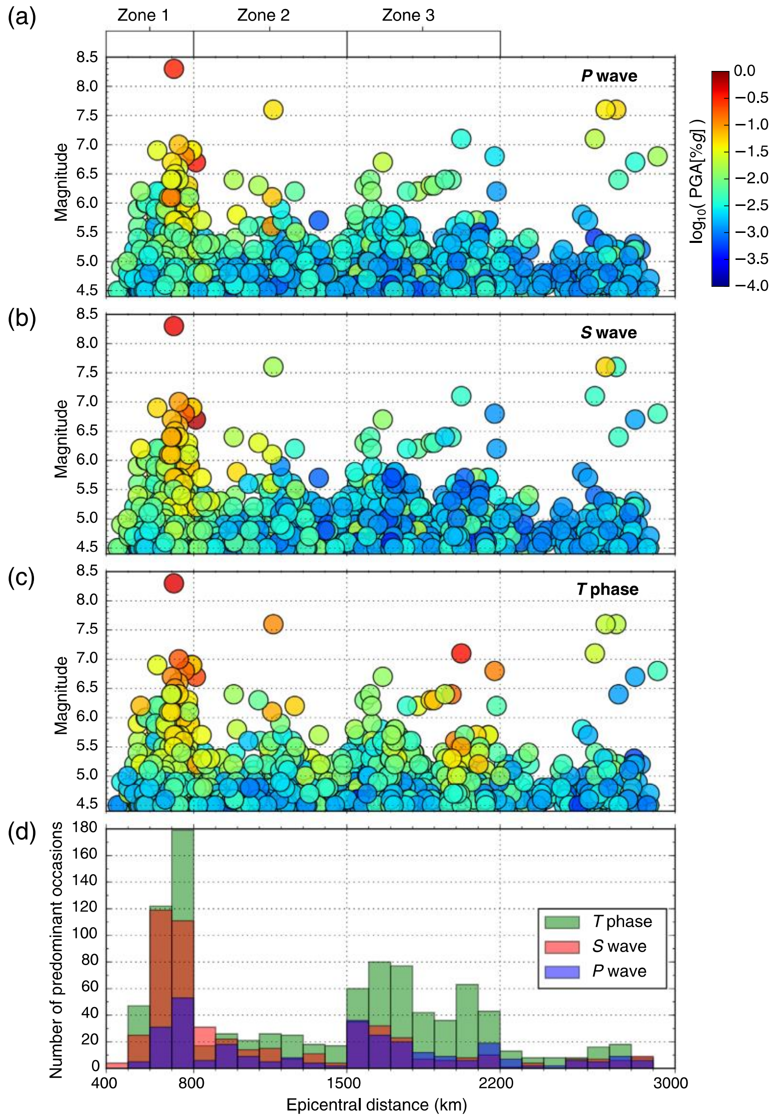

Figure 2. Distribution of earthquakes studied in this work as a function of epicentral distance from VA04 station and colored by $\log_{10}$ PGA related to each (a) *P* wave, (b) *S* wave, and (c) *T* phase. (d) Number of occasions when the PGA related to one type of wave is the largest one among the three types, computed in 100 km bins. Zones 1–3 are identified on top. PGA, peak ground acceleration. The color version of this figure is available only in the electronic edition.

in which $\dot{u}(t)$ is the vertical ground motion, W is the T-phase duration, and ρ and α are the density and P-wave velocity at the site where the ground motion is measured, respectively. We used the same time window obtained for the PGA computation and followed the same approach applied by Sáez and Ruiz (2018). Because we are working with just a single station, our final results are normalized by ρ and α.

Results

Influence of epicentral distance

Figure 2a–c shows the magnitude of all the earthquakes in our database versus epicentral distance and colored by its PGA amplitude for each *P* and *S* wave and T phase, where we can identify three main groups. We note that major contributions for short distances (zone 1, $\Delta < 800$ km) are mainly from *T* phases and *S* waves, accounting for almost 50% and 34% of the events, respectively. In this sense, the *P* wave is distinctly the minor contributor to the largest PGA in zone 1. In zone 2 ($800\text{ km} \leq \Delta < 1500$ km), its absolute contribution to largest PGA is less than its respective in zone 1, but it is in the same range of predominant occasions than *S* wave, which is even similar to *T*-phase contribution for this zone. A similar behavior is observed in zone 3 ($1500\text{ km} \leq \Delta < 2200$ km), where the absolute contribution of the three type of waves is larger than its respective in zone 2 because there are more earthquakes, but the *P*- and *S*-wave contribution are still in a similar range of predominant occasions. This similar range of *P*- and *S*-wave contribution at zones 2 and 3 can be related to anelastic attenuation of high frequencies along longer travel paths occurred in the upper mantle, where most of the anelastic losses occur in shear deformation (Der, 1998), thus generating low and similar PGA amplitudes for both

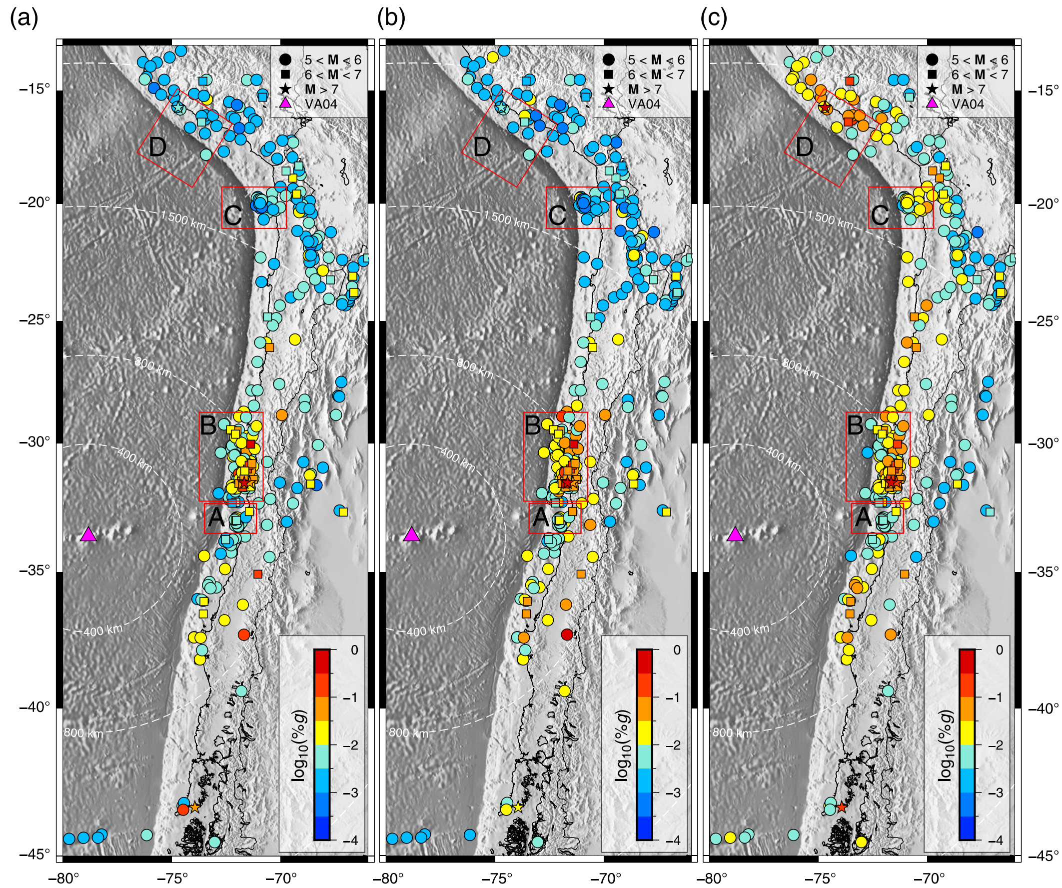

Figure 3. PGA amplitudes recorded at VA04 station (magenta triangle). The epicentral location of earthquakes is represented by symbols (square, circle, and star) according to magnitude range (**M** 5–6, **M** 6–7, and **M** > 7, respectively). Seismic sequences related to different large earthquakes are delimited by red boxes: (A) 2017 M_w 6.9 Valparaíso, (B) 2015 M_w 8.3 Illapel, (C) 2014 M_w 8.2 Iquique, and (D) 2018 M_w 7.1 Peru. Color scale is based on the logarithm of each PGA value (percent of gravity acceleration g). (a) PGA amplitudes associated with *P*-wave arrival. (b) PGA amplitudes associated with *S*-wave arrival. (c) PGA amplitudes associated with *T*-phase arrival. The same events are plotted on all three panels. White dashed circles denote epicentral distances from VA04 station. The color version of this figure is available only in the electronic edition.

P and *S* waves. Furthermore, Figure 3 shows the epicentral distribution of the same earthquake catalog as a function of PGA generated by *P* (Fig. 3a) and *S* waves (Fig. 3b) and *T* phases (Fig. 3c), which reveals that PGA amplitudes related to both *S* and *P* waves decrease with epicentral distance and do not depend on the event magnitude. However, PGA amplitudes associated with *T*-phase arrivals do not show dependence on epicentral distance, and they are mostly larger than their respective *P* and *S* waves (Figs. 2 and 3). This phenomenon can be explained as they mainly travel along the SOFAR channel rather than the upper mantle, where anelastic attenuation does not affect *T*-wave propagation (Thorp, 1965; Okal, 2008).

The PGA zones in Figure 2 can be related to different seismic sequences along the subduction margin. Earthquakes in zone 1 include the 2015 Illapel M_w 8.3 and the 2017 Valparaiso M_w 6.9 seismic sequences (B and A in Fig. 3), and their ground shaking is as large as 0.44%g, which is related to the *T*-phase arrival of the 2015 Illapel mainshock. As a whole, sequence A shows lower amplitudes of PGA at VA04 station than sequence B. Furthermore, zone 2 shows PGA amplitudes up to ~0.1%g, where the larger value is associated with the *T* phase generated by the 2016 M_w 7.6 Chiloé mainshock. This zone also includes

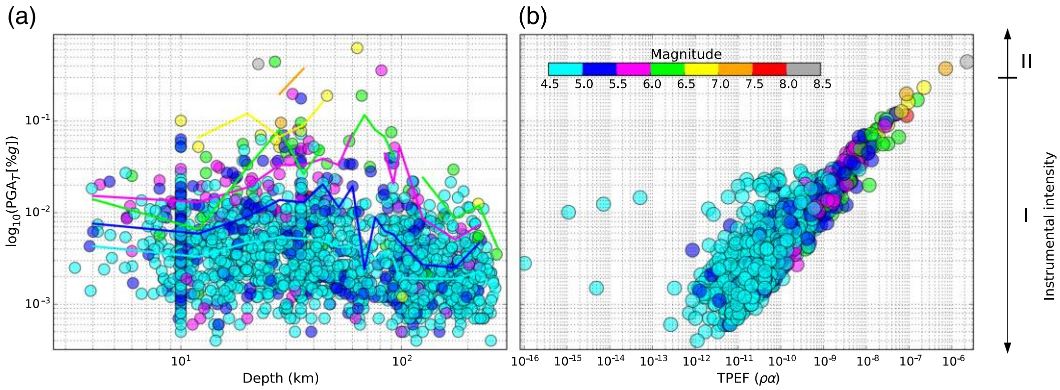

Figure 4. PGA records at VA04 station related to T-wave arrival as a function of (a) hypocentral depth and (b) T-phase energy flux (TPEF). Color curves in (a) correspond to the 50th percentile of data along 18 depth bins. Theoretical intensity ranges following Wald *et al.* (1999) are indicated in the right axis. The color version of this figure is available only in the electronic edition.

intraplate intermediate-depth events below the Andean Cordillera (at ~23° S; 68° W) at depths >70 km (as seen in Fig. 1), which show low PGA amplitudes. Finally, events occurring in zone 3 generate larger amplitudes of PGA than those in zone 2. This zone includes earthquakes mostly related to the 2014 Iquique aftershock sequence and to the Peruvian subduction zone, where the largest record is related to the T phase generated by the 2018 Las Lomas M_w 7.1 earthquake, which reached amplitudes as large as 0.37%g. The rest of the largest PGA amplitudes for this zone are mainly generated by T phases from earthquakes occurring in the area surrounding the 2018 M_w 7.1 Las Lomas mainshock (D in Fig. 3).

T phase and PGA values

T phases are the main contributors to large PGA amplitudes recorded at station VA04, and we studied the dependence of this variable on hypocentral parameters. We find a slight dependence of strong shaking related to T phases on the hypocentral depth of each event. Figure 4a shows an increase in recorded PGA amplitudes for earthquakes triggered at depths between 20 and 50 km, which mostly occur along the plate interface. We use equation (1) to estimate the intensities from PGAs due to arrival of the T phase at RCI (Fig. 4). These types of waves could generate detectable shaking on RCI, reaching MMIs of II–III. Indeed, according to intensity reports by ONEMI (Spanish acronym) and their respective association with PGA records during other earthquakes at different sites along the Chilean subduction zone, intensities larger than MMI III have been reported for PGA amplitudes as low as 0.1%g (see Table S2); thus, we consider that the T phase has the ability to generate ground shaking greater than MMI II.

Furthermore, our computations of TPEF values for each earthquake are in good agreement with its respective PGA reached by T-phase arrival, as shown in Figure 4b, where a direct relation between these parameters is evidenced, that is, larger PGA amplitudes are related to larger TPEF values. This observation is not clear when correlating the TPEF values with its respective PGA amplitudes from P and S waves (see Figs. S3 and S4) due to a higher dispersion of data.

Discussion

T phases

The largest PGA values are mainly related to T-wave arrivals from both near and far events. P and S waves make strong contributions to ground shaking when earthquakes occur near RCI, but their contributions vanish when the earthquakes occur far from the island, which can be explained by the attenuation of high-frequency of body waves with distance as they propagate through the oceanic lithosphere. Conversely, PGAs related to T-wave arrival do not depend on epicentral distance because they can travel long distances through the SOFAR channel without anelastic attenuation (Thorp, 1965; Okal, 2001); thus, high frequencies are preserved along the travel path and emerge at the station location, generating large PGA amplitudes. In particular, the 2018 M_w 7.1 Las Lomas earthquake was recorded at the VA04 station, and its T phase generated acceleration and velocity amplitudes larger than P- and S-wave arrivals, as shown in Figure 5. Moreover, the PGA amplitude of T-wave arrival was as large as 0.37%g at station VA04 and reached MMIs of II–III on RCI (F. Paredes, personal comm., 2018).

Some features of earthquake generation in subduction-zone processes can be inferred from PGA records of T-wave arrivals. The low PGA amplitudes generated by events related to the 2017 Valparaiso earthquake agree well with the respective low T-wave energy fluxes due to seamounts on top of the Nazca plate, which act as barriers for T-wave propagation (Walker

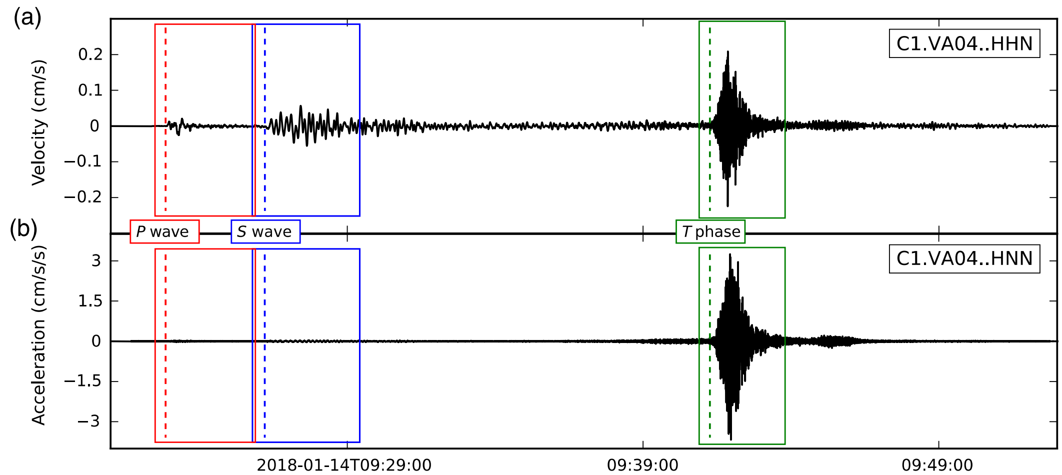

Figure 5. Ground-motion records at VA04 station due to the M_w 7.1 Las Lomas earthquake that occurred on 14 January 2018. (a) Nonfiltered ground velocity record from broadband seismometer; (b) nonfiltered ground acceleration record from accelerometer. In both panels, *P*-wave, *S*-wave, and *T*-phase observed arrival times are indicated with red, blue, and green segmented lines, respectively. According to the same color code, the data windows used for computation of each PGA (and TPEF for *T* phase only) are also indicated. The color version of this figure is available only in the electronic edition.

et al., 1992; Sáez and Ruiz, 2018). However, the aftershock seismicity of the 2015 M_w 8.3 Illapel earthquake, which was distributed along most of the plate interface, shows a dual behavior of PGA generation. In this sense, events occurring below the coastline, where depths between 30 and 45 km are expected, have larger PGA amplitudes than those occurring in the near-trench area for similar magnitude ranges. *T* waves generated by the latter events travel along similar paths, which do not evidence any topographic barrier for wave propagation reaching the SOFAR channel. This dual behavior can be explained by both a higher attenuation of seismic waves passing through the continental wedge (for shallow near-trench events) and a more effective incidence angle to the SOFAR channel for deeper earthquakes (Sáez and Ruiz, 2018). Nevertheless, it has been proposed that events occurring at deeper depths in the thrust interface have higher stress drop than those ones in the shallower part (e.g., Lay *et al.*, 2012; Yao *et al.*, 2013) meaning that they have an enriched high-frequency content, which would convert into larger PGA amplitudes, but further studies on this topic are required. Thus, a source effect cannot be discarded.

Furthermore, the *T* phases from the aftershock sequence of the 2014 Iquique earthquake present low PGAs at the VA04 station because these events occurred in the shallower portion of the plate contact zone, mainly between 5 and 25 km depth (León-Ríos *et al.*, 2016), where, although there is no topographic barrier for wave propagation (Fig. S3), the *T*-wave generation is less efficient because of the shallowness of these events. On the other hand, seismicity occurring in the area surrounding the 2018 Las Lomas earthquake (~16° S; 76° W) presents large PGAs for *T* waves reaching the VA04 station, mainly because these events were located in the deeper part of the plate contact (D in Fig. 3). Some of these PGA values are even larger than the largest PGA value in zone 2 (related to the *T* phase of Chiloé 2016 earthquake), which can be explained by differences in the morphology of the continental shelf, leading to different attenuation levels of incident *P* or *S* wave entering into the SOFAR channel. The continental shelf in the area of the 2016 Chiloé earthquake is ~60–100 km width (Contreras-Reyes *et al.*, 2010), which is wider than the continental shelf in the area of the 2018 Las Lomas earthquake in the Peruvian subduction zone (<30 km; Contreras-Reyes *et al.*, 2019). Thus, the lower attenuation in the latter area, together with the occurrence of deep events along the thrust interface, could lead to higher PGA values related to *T*-phase propagation in zone 3 rather than zone 2.

These observations have an important influence on ground-shaking assessment in the JFI because they demonstrate that earthquake perception is not always related to tsunami generation. The largest PGA values reached in JFI are usually related to *T*-phase arrival (Fig. 2d), and the TPEF values are in good correlation with PGA related to *T*-phase arrival (Fig. 4b). Then we could indicate that low PGA values can be expected for tsunami earthquakes because they feature strong deficiencies on the TPEF (Okal *et al.*, 2003; Okal, 2008). Tsunami earthquakes are events occurring in the shallow part of the thrust interface, whose rupture process is slower than ordinary subduction-zone

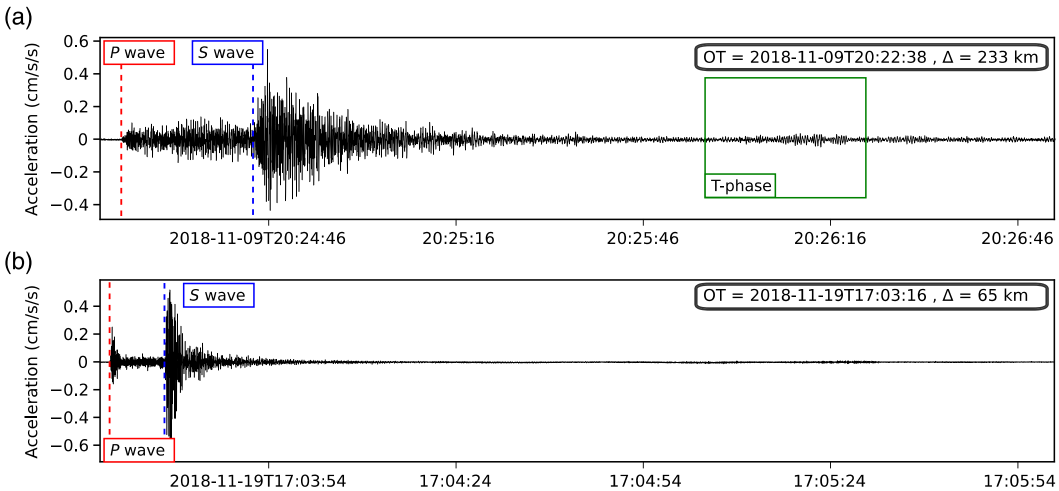

Figure 6. Accelerograms (east–west component) of nearby events recorded at VA04 station in RCI. (a) An m_b 4.9 event as reported by the National Seismological Center. (b) Local event located ~65 km southward away from RCI. Observed arrivals for *P* and *S* wave and *T* phase are indicated with red, blue, and green markers, respectively. The color version of this figure is available only in the electronic edition.

thrust earthquakes (Kanamori, 1972; Kanamori and Kikuchi, 1993; Tanioka *et al.*, 1997; Lay *et al.*, 2012), so they have large tsunami potential. Because the tsunami hazard is larger for shallow near-trench earthquakes and the PGA amplitudes related to these events are low, there is a chance that a tsunami earthquake could not be felt in RCI. In contrast, a large megathrust earthquake, breaking at least the B and C domains of the thrust interface, as indicated by Lay *et al.* (2012), can generate large PGA amplitudes on RCI, which would be felt by the population and would likely generate a large tsunami.

Other potential ground-shaking sources

In addition to feeling earthquakes that occur along the Chilean margin, inhabitants of RCI have reported perceptions of other events. In this sense, ground-shaking perception was reported late in 1998 with MMIs up to III and was related to seismicity generated by volcanic activity near the island (ONEMI, 1999). Recently, according to the CSN catalog (see Data and Resources), an m_b 4.9 tectonic earthquake occurred on 9 November 2018 at 20:22 UTC. Although the epicentral location of this event is hard to constrain because of scarce network coverage, the reported locations from both CSN and NEIC differ by ~30 km distance. Anyway, according to *S-P* time and phase observations on stations located along Chilean coast, we can confirm that this event comes from ~233 km to the west of RCI (Fig. 6a). According to this information, this event could be directly related to seismic activity surrounding the hot spot area (blue circle in Fig. 1) or to the progression of the JFR along the Nazca plate (Lara *et al.*, 2018). Days later, another seismic event was recorded on 19 November 2018 at 17:03 UTC with shorter *S-P* times of ~9 s, ~65 km from station VA04 (Fig. 6b), in the surrounding area of the RCI. Thus, although the JFR is considered an aseismic ridge (Von Huene *et al.*, 1997; Yáñez *et al.*, 2001), these recent events, together with seismicity recorded in the 1980s and in 1998, provide more evidence about the existence of intraplate seismicity in the surrounding area of the JFI. These events were not felt in RCI. Indeed, the PGA amplitudes were ~0.06%*g* and were related to the *S*-wave arrival rather than *T* phase, which is identified for the first event but is practically nonexistent for the second one (Fig. 6). Because the source mechanism and the characteristics of this seismicity are still unclear, it is not possible to confirm or dismiss the existence of any tsunamigenic source. Thus, we suggest that this surrounding area near JFI should be studied more in detail, making use of VA04 station data and one-single station seismic patterns searching techniques.

Conclusions

We assessed the ground acceleration related to the arrival of *P* and *S* waves and *T* phases from earthquakes along the Peru–Chile subduction zone at station VA04 on RCI. Our results show that the largest ground accelerations on RCI are <0.5%*g* and related to different types of waves; they generate enough ground shaking to be perceived by RCI inhabitants. The type of wave causing the large acceleration differs depending on the epicentral distance of the earthquake. The largest accelerations generated by earthquakes occurring closest to RCI, such as the 2015 Illapel earthquake, would be related to *S* waves, whereas the largest accelerations generated by distant events, such as the 2018 Las Lomas earthquake, would be associated with the arrival of T phases.

T phases with the largest accelerations are related to earthquakes occurring in the deeper part of the thrust interface, where highly efficient T-wave generation has been proposed, rather than in the shallower part. Consequently, ground-shaking perception on RCI will not always be related to imminent tsunami arrival because the hypocenter is more likely to occur in the deeper part of the interface, where low tsunami potential is expected. Indeed, tsunami earthquakes, which occur in the near-trench area, would not generate large PGA amplitudes on RCI, and people are more likely not to feel ground shaking but to be affected by the tsunami arrival. Finally, ground-shaking perception could also be generated by a large megathrust earthquake, which would slip along the shallower part of the thrust interface and generate a destructive tsunami such as the 2010 Maule earthquake. We revisited and showed evidence for the existence of surrounding intraplate seismicity near JFI. The source characteristics of this type of seismicity are still unclear, so it is not possible to dismiss the presence of any tsunamigenic source, but further research will be helpful to clarify this point.

Data and Resources

Seismological data from VA04 station were collected by the National Seismological Center (CSN, www.sismologia.cl, last accessed August 2019) and distributed by Incorporated Research Institutions for Seismology Data Management Center (IRIS-DMC). Waveforms can be reached through IRIS-DMC website at https://ds.iris.edu/ds/nodes/dmc/forms/breqfast-request (last accessed July 2019). The seismicity catalog was retrieved from National Earthquake Information Center–U.S. Geological Survey (NEIC-USGS) database at https://earthquake.usgs.gov/earthquakes/search (last accessed July 2019). Some plots were made using the Generic Mapping Tools v.5.2.1 (Wessel *et al.*, 2013). The supplemental material for this article includes figures and tables showing additional metadata information, P- and S-wave features, and official reported intensities in Chile for large earthquakes.

Acknowledgments

The authors thank the support of the Comisión Nacional de Investigación Científica y Tecnológica/Fondo Nacional de Desarrollo Científico y Tecnológico (CONICYT/FONDECYT) Project Number 1170430, CONICYT Programa de Investigación Asociativa (PIA)/Anillo de Investigación en Ciencia y Tecnología ACT172002, and Programa Riesgo Sísmico (Actividades de Interés Nacional [AIN], Universidad of Chile). The authors also thank Emile Okal, Kazushige Obara, and one anonymous reviewer for their very thoughtful suggestions.

References

Amante, C., and B. W. Eakins (2009). ETOPO1 1 arc-minute global relief model: Procedures, data sources and analysis, *NOAA Technical Memorandum NESDIS NGDC-24*, National Geophysical Data Center, NOAA, doi: 10.7289/V5C8276M.

Beyreuther, M., R. Barsch, L. Krischer, T. Megies, Y. Behr, and J. Wassermann (2010). ObsPy: A Python toolbox for seismology, *Seismol. Res. Lett.* **81,** no. 3, 530–533.

Carrasco, S., J. A. Ruiz, E. Contreras-Reyes, and F. Ortega-Culaciati (2019). Shallow intraplate seismicity related to the Illapel 2015 Mw 8.4 earthquake: Implications from the seismic source, *Tectonophysics* **766,** 205–218, doi: 10.1016/j.tecto.2019.06.011.

Cesca, S., F. Grigoli, S. Heimann, T. Dahm, M. Kriegerowski, M. Sobiesiak, C. Tassara, and M. Olcay (2016). The M_w 8.1 2014 Iquique, Chile, seismic sequence: A tale of foreshocks and aftershocks, *Geophys. J. Int.* **204,** no. 3, 1766–1780.

Chilean National Emergency Office (ONEMI) (1999). Informe "Misión a Archipiélago Juan Fernández, monitoreo sísmico y gestión de riesgos", available at http://repositoriodigitalonemi.cl/web/bitstream/handle/2012/117/ONE1145.pdf?sequence=1 (last accessed February 2019) (in Spanish).

Contreras-Reyes, E., E. R. Flueh, and I. Grevemeyer (2010). Tectonic control on sediment accretion and subduction off south central Chile: Implications for coseismic rupture processes of the 1960 and 2010 megathrust earthquakes, *Tectonics* **29,** no. 6, doi: 10.1029/2010TC002734.

Contreras-Reyes, E., P. Muñoz-Linford, V. Cortés-Rivas, J. P. Bello-González, J. A. Ruiz, and A. Krabbenhöft (2019). Structure of the collision zone between the Nazca ridge and the Peruvian convergent margin: Geodynamic and seismotectonic implications, *Tectonics* doi: 10.1029/2019TC005637.

Crotwell, H. P., T. J. Owens, and J. Ritsema (1999). The TauP toolkit: Flexible seismic travel-time and ray-path utilities, *Seismol. Res. Lett.* **70,** no. 2, 154–160.

Cua, G., D. J. Wald, T. I. Allen, D. Garcia, C. B. Worden, M. Gerstenberger, K. Lin, and K. Marano (2010). "Best practices" for using macroseismic intensity and ground motion-intensity conversion equations for hazard and loss models in GEM1 (p. 4), *GEM Technical Report 2010-4*, GEM Foundation, Pavia, Italy, available at https://cloud-storage.globalquakemodel.org/public/wix-new-website/pdf-collections-wix/publications/GEM-TechnicalReport_2010-4.pdf (last accessed October 2019).

Der, Z. A. (1998). *High-Frequency P-and S-Wave Attenuation in the Earth, in Q of the Earth: Global, Regional, and Laboratory Studies*, Birkhäuser, Basel, Switzerland, 273–310.

Fritz, H. M., C. M. Petroff, P. A. Catalán, R. Cienfuegos, P. Winckler, N. Kalligeris, R. Weiss, S. E. Barrientos, G. Meneses, C. Valderas-Bermejo, *et al.* (2011). Field survey of the 27 February 2010 Chile tsunami, *Pure Appl. Geophys.* **168,** no. 11, 1989–2010.

Kanamori, H. (1972). Mechanism of tsunami earthquakes, *Phys. Earth Planet. In.* **6,** 346–359.

Kanamori, H., and M. Kikuchi (1993). The 1992 Nicaragua earthquake: a slow tsunami earthquake associated with subducted sediments, *Nature* **361,** no. 6414, 714.

Kennett, B. L., E. R. Engdahl, and R. Buland (1995). Constraints on seismic velocities in the Earth from traveltimes, *Geophys. J. Int.* **122,** no. 1, 108–124.

Lange, D., J. Ruiz, S. Carrasco, and P. Manríquez (2018). The Chiloé M_w 7.6 earthquake of 2016 December 25 in Southern Chile and its relation to the M_w 9.5 1960 Valdivia earthquake, *Geophys. J. Int.* **213,** no. 1, 210–221.

Lara, L. E., J. Reyes, and J. Diaz-Naveas (2018). $^{40}Ar/^{39}Ar$ constraints on the age progression along the Juan Fernández Ridge, SE Pacific, *Front. Earth Sci.* **6,** 194.

Lay, T., H. C. J. Kanamori, K. D. Ammon, A. R. Koper Hutko, L. Ye, H. Yue, and T. M. Rushing (2012). Depth-varying rupture properties of subduction zone megathrust faults, *J. Geophys. Res.* **117,** no. B04311, doi: 10.1029/2011JB009133.

León-Ríos, S., S. Ruiz, A. Maksymowicz, F. Leyton, A. Fuenzalida, and R. Madariaga (2016). Diversity of the 2014 Iquique's foreshocks and aftershocks: clues about the complex rupture process of a M_w 8.1 earthquake, *J. Seismol.* **20,** no. 4, 1059–1073.

Leyton, F., A. Leopold, G. Hurtado, C. Pastén, S. Ruiz, G. Montalva, and E. Sáez (2018). Geophysical characterization of the Chilean seismological stations: First results, *Seismol. Res. Lett.* **89,** no. 2A, 519–525.

Li, L., T. Lay, K. F. Cheung, and L. Ye (2016). Joint modeling of teleseismic and tsunami wave observations to constrain the 16 September 2015 Illapel, Chile, M_w 8.3 earthquake rupture process, *Geophys. Res. Lett.* **43,** no. 9, 4303–4312.

Melgar, D., W. Fan, S. Riquelme, J. Geng, C. Liang, M. Fuentes, G. Vargas, R. M. Allen, P. Shearer, and E. J. Fielding (2016). Slip segmentation and slow rupture to the trench during the 2015, M_w 8.3 Illapel, Chile earthquake, *Geophys. Res. Lett.* **43,** no. 3, 961–966.

Montessus de Ballore, F. (1911/1916). *Historia Sísmica de los Andes Meridionales, al sur del Paralelo XVI*, Cervantes, Santiago de Chile, Chile (in Spanish).

Okal, E. A. (2001). T-phase stations for the International Monitoring System of the Comprehensive Nuclear-Test Ban Treaty: A global perspective, *Seismol. Res. Lett.* **72,** no. 2, 186–196.

Okal, E. A. (2008). The generation of T waves by earthquakes, *Adv. Geophys.* **49,** 1–65.

Okal, E. A. (2011). *T* waves, in *Encyclopedia of Solid Earth Geophysics*, H. Gupta (Editor), Earth Sciences Series, Springer, Dordrecht, The Netherlands, 1421–1423.

Okal, E. A., P. J. Alasset, O. Hyvernaud, and F. Schindelé (2003). The deficient *T* waves of tsunami earthquakes, *Geophys. J. Int.* **152,** no. 2, 416–432.

Ruiz, S., and R. Madariaga (2018). Historical and recent large megathrust earthquakes in Chile, *Tectonophysics* **733,** 37–56, doi: 10.1016/j.tecto.2018.01.015.

Ruiz, S., F. Aden-Antoniow, J. C. Baez, C. Otarola, B. Potin, F. del Campo, P. Poli, C. Flores, C. Satriano, F. Leyton, *et al.* (2017). Nucleation phase and dynamic inversion of the M_w 6.9 Valparaíso 2017 earthquake in Central Chile, *Geophys. Res. Lett.* **44,** 10,290–10,297, doi: 10.1002/2017GL075675.

Ruiz, S., E. Klein, F. del Campo, E. Rivera, P. Poli, M. Metois, C. Vigny, J. C. Baez, G. Vargas, F. Leyton, R. Madariaga, *et al.* (2016). The seismic sequence of the 16 September 2015 M_w 8.3 Illapel, Chile, earthquake, *Seismol. Res. Lett.* **87,** no. 4, 789–799.

Ruiz, S., M. Moreno, D. Melnick, F. del Campo, P. Poli, J. C. Baez, F. Leyton, and R. Madariaga (2017). Reawakening of large earthquakes in south central Chile: The 2016 M_w 7.6 Chiloé event, *Geophys. Res. Lett.* **44,** 6633–6640, doi: 10.1002/2017GL074133.

Sáez, M., and S. Ruiz (2018). Controls on the T phase energy fluxes recorded on Juan Fernandez Island by continental seismic wave paths and Nazca bathymetry, *Geophys. Res. Lett.* **45,** no. 6, 2610–2617.

Sutcliffe, T. (1839). *The Earthquake of Juan Fernandez, as It Occurred in the Year 1835*, Longman, Orme and Co., London, United Kingdom.

Tanioka, Y., L. J. Ruff, and K. Satake (1997). What controls the lateral variation of large earthquake occurrence along the Japan trench? *Island Arc* **6,** 261–266.

Thorp, W. H. (1965). Deep-ocean sound attenuation in the sub- and low-kilocycle-per-second region, *J. Acoust. Soc. Am.* **38,** no. 4, 648–654.

Tilmann, F., Y. Zhang, M. Moreno, J. Saul, F. Eckelmann, M. Palo, Z. Deng, A. Babeyko, K. Chen, J. C. Baez, *et al.* (2016). The 2015 Illapel earthquake, central Chile: A type case for a characteristic earthquake? *Geophys. Res. Lett.* **43,** no. 2, 574–583.

Udías, A., R. Madariaga, E. Buforn, D. Muñoz, and M. Ros (2012). The large Chilean historical earthquakes of 1647, 1657, 1730, and 1751 from contemporary documents, *Bull. Seismol. Soc. Am.* **102,** no. 4, 1639–1653.

Von Huene, R., J. Corvalán, E. R. Flueh, K. Hinz, J. Korstgard, C. R. Ranero, and W. Weinrebe (1997). Tectonic control of the subducting Juan Fernández Ridge on the Andean margin near Valparaiso, Chile, *Tectonics* **16,** no. 3, 474–488.

Wald, D. J., V. Quitoriano, T. H. Heaton, and H. Kanamori (1999). Relationships between peak ground acceleration, peak ground velocity, and modified Mercalli intensity in California, *Earthq. Spectra* **15,** no. 3, 557–564.

Walker, D. A., C. S. McCreery, and Y. Hiyoshi (1992). T-phase spectra, seismic moments, and tsunamigenesis, *Bull. Seismol. Soc. Am.* **82,** no. 3, 1275–1305.

Wessel, P., W. H. Smith, R. Scharroo, J. Luis, and F. Wobbe (2013). Generic Mapping Tools: Improved version released, *Eos Trans. AGU* **94,** no. 5, 409–410.

Wysession, M. E., E. A. Okal, and K. A. Miller (1991). Intraplate seismicity of the Pacific basin, 1913–1988, *Pure Appl. Geophys.* **135,** 261–359.

Yáñez, G. A., C. R. Ranero, R. von Huene, and J. Díaz (2001). Magnetic anomaly interpretation across the southern central Andes (32°–34° S): The role of the Juan Fernández Ridge in the late Tertiary evolution of the margin, *J. Geophys. Res.* **106,** no. B4, 6325–6345.

Yao, H., P. M. Shearer, and P. Gerstoft (2013). Compressive sensing of frequency-dependent seismic radiation from subduction zone megathrust ruptures, *Proc. Natl. Acad. Sci. Unit. States Am.* 110**,** no. 12, 4512–4517.

Manuscript received 27 June 2019
Published online 13 November 2019